ALMA MATER STUDIORUM

UNIVERSITY OF BOLOGNA

PhD in Physics

SC: 02/B1 - SSD: FIS/03

ION IMPLANTATION OF ORGANIC THIN FILMS AND ELECTRONIC DEVICES

Thesis Advisor:
Prof. Beatrice Fraboni

Presented by:
Alessandra Scidà

PhD Coordinator:
Prof. Fabio Ortolani

X X V C Y C L E - M A R C H 2 0 1 3

To my family
who always trusted
and supported me

Contents

Introduction

Organic semiconductors have great promise in the field of electronics due to their low cost in term of fabrication on large areas and their versatility to new devices, for these reasons they are becoming a great chance in the actual technologic scenery. Semiconductors derived from Carbon can be functionalized to obtain the requested properties, they have the advantage to be transparent and flexible and furthermore they can be used for medical devices cause they are compatible with biological tissues. One of the most simple fabrication methods is to print directly the semiconductors on a substrate to obtain electronic devices with an inkjet printer. The possible applications are countless: transparent solar cells, OLED displays, flexible screens and RFID tags. Taking advantage of their sensitivity to atmosphere or the gas composition of the surrounding environment, humidity or gas sensors can be built. The field of the sensors is not finished, there is the possibility to build also smart tissues and bio-medical patches able to inject a medicine in case of necessity. These new possibilities are the engine that make the challenge of this research so intriguing (Figure 1).

Figure 1: Some possible applications of Organic Semiconductors.

Actually organic semiconductors are not new. The first studies of the conductivity of Anthracene crystals (a prototype organic semiconductor) date back to the half of the 20th century[(1)]. Later, following the discovery of electroluminescence in the 1960s, molecular crystals were intensely investigated by many researchers. These investigations established the basic processes involved in optical excitation and charge carrier transport. Charge transport processed in organic semiconductors is substantially different from the inorganic ones, in fact the carriers move through the molecules by a

process called hopping and not by the band-to-band mechanism of inorganic semiconductors. This process leads to a small mobility and so less efficiency of the device. So, in spite of the principal demonstration of organic electroluminescent diodes, there were several reasons preventing practical use of these early devices. For example, neither sufficient current and light output nor satisfying stability could be achieved. The main obstacles were the high operating voltage as a consequence of the crystal thickness (in the millimeter range) together with the difficulties in scaling up crystal growth as well as preparing stable, injection-efficient contacts to them.

Since the 1970s, the successful synthesis and controlled doping of conjugated polymers established the second important class of organic semiconductors, which was honored with the Nobel Prize in Chemistry in the year 2000 [(2).] Together with organic photoconductors these conducting polymers have initiated the first applications of organic materials as conductive coatings or photoreceptors. The interest in undoped organic semiconductors revived in the 1980s due to the demonstration of an efficient photovoltaic cell incorporating an organic hetero-junction of p- and n-conducting materials as well as the first successful fabrication of thin film transistors from conjugated polymers and oligomers. The main impetus, however, came from the demonstration of high-performance electroluminescent diodes from vacuum-evaporated molecular films and from conjugated polymers. In the last 20 years the research in this field grows such a way that we can have now the first commercial products that are OLED displays. Other applications of organic semiconductors, as logic circuits with organic field-effect transistors (OFETs) or organic photovoltaic cells (OPVCs) are expected to follow in the near future [(3)].

As things stand now, some of the most important problems to investigate are the effects of surfaces and interfaces between semiconductor and metals, the changes caused by different deposition methods and temperature, the difficulty related to the charge transport modeling and finally a fast aging with time, bias, air and light, that can change the properties very easily. In order to find out some important features of these materials I also fabricated Organic Field Effect Transistors (OFETs), using them as characterization tools.

The focus of my research is to investigate the effects of ion implantation on organic semiconductors and on OFETs. Ion implantation is a technique widely used on inorganic semiconductors to modify their electrical transport properties through the controlled introduction of foreign atomic species in the semiconductor matrix. I pointed my attention on three major novel and interesting effects, that I observed for the first time following ion implantation of OFETs:

1) modification of the electrical conductivity;
2) introduction of stable charged species, electrically active with organic thin films;
3) stabilization of transport parameters (mobility and threshold voltage).

I examined 3 different semiconductors: Pentacene ($C_{22}H_{14}$), a small molecule constituted by 5 aromatic rings, Pentacene-TIPS, a more complex by-product of the first one, and finally a completely different organic material called Pedot PSS, that belongs to the branch of the conductive organic polymers. My research started with the analysis of ion implantation of Pentacene films and Pentacene OFETs, and apart from the last chapter, all the chapters are referred to this organic semiconductor. In chapter 7 instead, I will talk about totally inkjet printed OFETs made of Pentacene-TIPS or PEDOT-PSS, and the research will continue with the ion implantation on these new promising organic devices.

1 Fundamentals of Organic Field Effect Transistors (OFETs)

1.1 Device Structure

The Field Effect Transistor (FET) is a very common transistor used in microelectronic as a single block or in an integrated circuit. This device is a current generator controlled by the voltage of the Gate contact. Its structure is a superimposition of three layers: the substrate is a conductive layer that acts as the Gate contact, the second layer is a dielectric and on the top there is a film of semiconductor. The current flows between two metallic contacts placed at the sides (Source and Drain) due to the voltage applied between them (V_{DS}) and between Source and Gate (V_{GS}).

In an Organic FET (OFET) the semiconductor is organic, this kind of material is characterized by π bonds between double and single C-C bonds that constitute delocalized orbitals responsible of their electrical and optical features. Organic Semiconductors have a different energetic density of the states than inorganic, they have not a unique band gap but several levels permitted, for this reason it's useful to define the borders levels: the Highest Occupied Molecular Orbital (HOMO) and the Lowest Unoccupied Molecular Orbital (LUMO). The conductivity in these materials is surely lower than metals and also than inorganic semiconductor, in the better situation the charge carriers reach the mobility of the amorphous Silicon (for example in Pentacene $\mu \approx 5\ cm^2V^{-1}s^{-1}$) [4]. Usually organic semiconductors are simple to fabricate in very thin layer (~100 nm) at room temperature, with drop cast, spin coating or inkjet printing, to obtain better performance with low conductivity and maintain a low price. These are used to build devices called OTFTs (Organic Thin Film Transistors), they are OFETs with a layer of semiconductor very thin. A part from the inkjet printed OECT, described in the last chapter, I will talk always of this kind of devices, so I will use the term OFETs and OTFTs referring to the same concept.

The principle of operation of an OFET is similar to a capacitor (Figure 1.1): an electric field is generated from the Gate ($V_{GS} < 0$) to the semiconductor so that in it the charges (positive) migrate to the interface with the dielectric and beyond them remain a channel free of positive charges (p-channel). If a voltage ($V_{DS} < 0$) is applied from Drain to Source then a current of holes can flow in the channel generating the output signal (I_{DS}). In this way we can say that this FET works in accumulation mode. On the contrary, we can have an n-channel with a current of electrons, applying positive voltage V_{GS} and V_{DS}, this operation is called depletion mode and is often used with inorganic FETs but not with the organic ones.

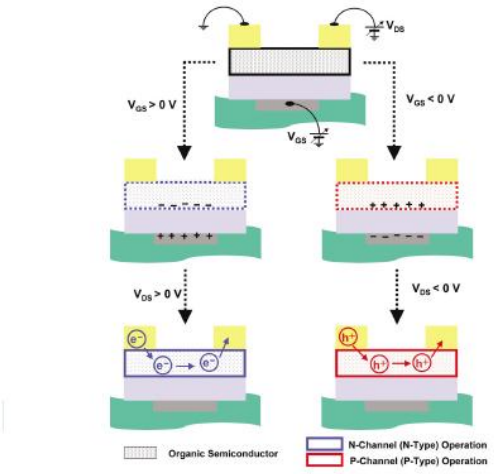

Figure 1.1: Schematic view of n-channel and p-channel operations in an OFET.

With the accumulation (or enhancement) mode for V_{DS} more negative than V_{GS}, I_{DS} tends to saturate (saturation regime) owing to the pinch-off of the accumulation layer. Most OFETs work in enhancement mode, and depending on the organic material and device configuration p-channel or n-channel behavior can be realized. To characterize the OFET behavior, a constant V_{GS} can be chosen and I_{DS} measured as a function of V_{DS}. For a set of different V_{GS} values this results in the output characteristics (I_{DS}–V_{DS} curves) exemplified in Figure 1.2. Assuming ohmic organic/source and drain contacts, the current can be described in the linear (I_{DS},lin) and saturation (I_{DS},sat) regions by Eq. 1 and Eq. 2:

$$I_{DS,lin} = \frac{W}{L} C_i \mu \left[(V_{GS} - V_{TH}) V_{DS} - \frac{V_{DS}^{\ 2}}{2} \right] \qquad \text{[Eq. 1]}$$

$$I_{DS,sat} = \frac{W}{2L} C_i \mu (V_{GS} - V_{TH})^2 \qquad \text{[Eq. 2]}$$

with channel width W, channel length L (see Figure 1.3), capacitance per unit area of the gate insulator C_i, the charge-carrier field-effect mobility μ, and the threshold voltage V_{TH}. The performance of an OFET can be tuned to some degree by using suitable geometries with short channel length or thin insulator layers of materials with high dielectric constant. V_{TH} is a parameter that describes the not ideal behavior of the device, that is, for cases where channel conductance is still considerably large for V_{GS}=0. Depending on the actual device, V_{TH} can be positive or negative, and includes effects related to un wanted doping, deep charge traps, or mismatches of energy levels at the organic/contact interfaces [(5)(6)]. For instance, a positive threshold voltage for p-channel devices may indicate the presence of (unwanted) p-dopants in the organic layer, thus a positive V_{GS} is needed to switch the device off (Figure 1.4).

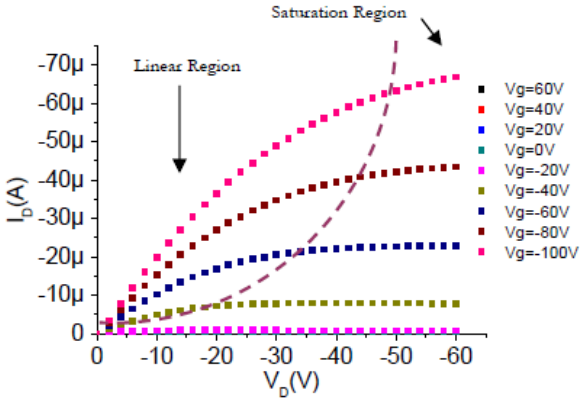

Figure 1.2: Example of I_{DS}-V_{DS} characteristics.

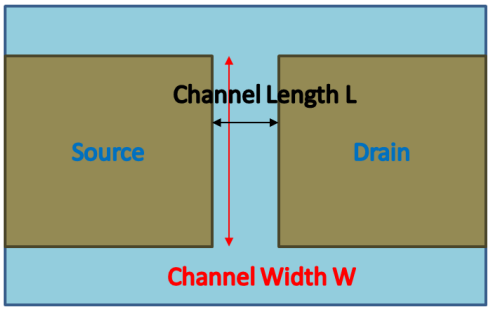

Figure 1.3: Top view of an OFET.

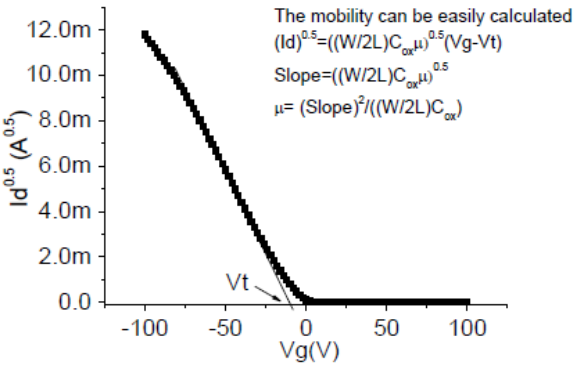

Figure 1.4: Transfer Characteristics of an OFET.

In the linear regime of OFET operation (Eq. 1), when V_{DS} is very smaller than (V_{GS}-V_{TH}), the carrier concentration within the channel is essentially independent of the position from source and drain contacts, and I_{DS} is proportional to V_{DS}. Increasing V_{DS} leads to a carrier concentration gradient within the channel (lower concentration near the drain), which leads to a deviation from linear behavior of the output curves. When

V_{DS} becomes equal to (V_{GS}-V_{TH}), the gate and the channel region right next to the drain are at the same electrical potential (the channel becomes "pinched"). If V_{DS} is further increased, the region of depletion from free charge carriers near the drain is shifted towards the source,[5] thus implying that I_{DS} does not increase with increasing V_{DS} (saturation regime; Figure 1.2). According to Eq.1 and Eq.2, the field-effect mobility can be calculated (e.g. from the slope of a plot $(I_{DS})^{1/2}$ vs V_{GS}; see Figure 1.4). However, μ values obtained in the saturation regime are frequently higher than those obtained from the linear regime, because the higher channel resistance in saturation decreases the importance of source/drain contact resistance. In view of the possible applications of OFETs, the following requirements for device properties can be derived. At present, high drain currents can only be achieved at rather high V_{GS} and V_{DS} values, typically several tens of volts, which is impractical for mobile applications that require low power consumption. Therefore, high charge-carrier mobility and gate-insulator capacitance are needed. This should be achieved for p-channel and n-channel device operation, as both modes of operation are needed for complementary circuit design.

It should be noted that p- and n-channel operation is in principle possible with most organic semiconductor materials. Yet, most presently available materials show exclusively, or at least predominantly, p-type behavior, and significant efforts are made to synthesize materials and fabricate device structures for efficient n-channel OFETs [6]. However, it has been convincingly shown that the limit for good n-channel performance is not necessarily an intrinsic material property; rather it is due to low stability against "doping" in air (by Oxygen or reactions with water) and electron trapping at the organic–insulator interface [7][8], where silanol, carbonyl, or hydroxyl functionalities can have damaging effects [7][9]. A step forward was the realization of an Ambipolar Transport Transistor [10], in this case both a electron and a hole current flow in the channel at different voltages using two different metals for source and drain, a low work function metal for electron injection and a high work function metal for hole injection. The solution seems possible only in N_2 atmosphere but not in air because there the low work function metal is not stable. This kind of device would be a great advance in organic electronic because they can be used to do CMOS-like inverters and multifunctional devices. This fact points the attention to the importance of the problem of the degrade of the devices caused by Oxygen and humidity, that is one of the problems I want to solve.

In Figure 1.5, we can see the decreasing of the voltage V_{GS} starting from the dielectric (insulator), coming to the interface and then in the semiconductor. If in the insulator there is a constant voltage V_{GS} exactly as it comes from the Gate, after the interface the voltage starts to decrease till to disappear near the external surface of the semiconductor. The Electric Field Effect in fact depends only on the first layers of semiconductor near the interface, where the voltage V_{GS} is still present. This concept

will be important as I will modify the surface of the semiconductor by ion implantation, to obtain better properties of the device, without affecting the interface with the dielectric and so without affecting the Field Effect. These devices are also excellent tools to study the charge transport in organic semiconductors just due to the capability of tuning the position of the quasi-Fermi level at the dielectric-semiconductor interface by applying a gate voltage [11].

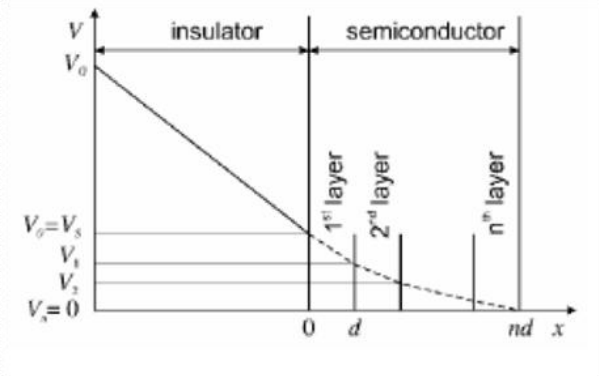

Figure 1.5: Voltage V_{GS} as a function of the distance from the Gate passing through the dielectric (insulator) and the semiconductor.

The structure of an OFET can be different as we can have the three contacts (Gate, Source and Drain) put on top of the device or in the bottom part (see Figure 1.6), we can use different solution depending on the situations.

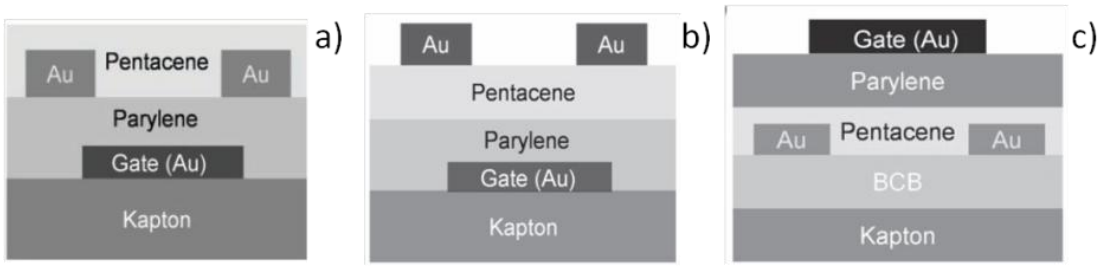

Figure 1.6: Three possible configuration of the contacts for an OFET: a) bottom contact-bottom gate, b) top contact-bottom gate, c) bottom contact-top gate [10].

The contact resistance is lower for transistors made in the top contact configuration because the area of contact between the electrodes and the semiconductor is larger. However, it is not always simple or convenient to make this structure because for a bottom gate OFET, it is usually easier to deposit the source and drain contacts in the bottom, because they tend to damage the organic material when deposited on top. Top gate OFETs, instead, have an advantage because the source and drain contacts are

deposited first in the staggered configuration so they cannot alter the organic material, but the counter-party is a rough semiconductor-dielectric interface that ruins the charge transport [10] [12]. My collaborators of the University of Cagliari created OTFTs with the configuration called bottom contact, bottom gate and then they were implanted with the ion implanter of the Los Alamos National Research laboratory in order to modify the superficial layer of the semiconductor.

1.2 Organic semiconductors properties

Carbon is an element able to share its electrons creating sp^3, sp^2 or sp orbitals with other Carbon atoms or other elements. For example, a Benzene ring (C_6H_6), that is the base of Pentacene ($C_{22}H_{14}$) and the other aromatic compounds, has 6 σ strong bonds in plane, and 12 π bonds weaker and out of plane; the electrons are delocalized, i.e. they can move easily along the molecule thanks to the overlap of the π orbitals of the atoms (Figure 1.7).

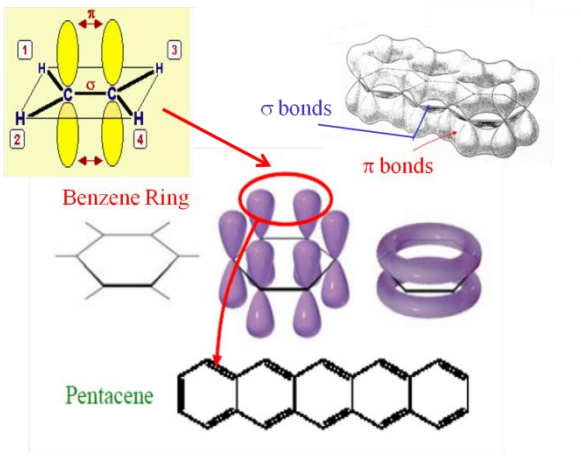

Figure 1.7: Structure of the benzene ring (C_6H_6) and of Pentacene ($C_{22}H_{14}$), showing σ and π bonds.

In a schematization, analogue to the inorganic semiconductors, we can represent the energetic levels of the molecule separated by a band gap, that is called HOMO-LUMO (Highest Occupied Molecular Orbital- Lowest Unoccupied Molecular Orbital) and by the two charge carriers, the hole and the electron. Most of the Organic Semiconductors have the gap in the visible range (from 1,5eV to 3eV) [3], this could seem in contrast with the evidence of transparency of some of these materials, but actually this propriety is due to the lower density of the organic with respect to inorganic crystals and to the different light absorption coefficient. Differently from

inorganic semiconductors, the band gap is constituted also by several internal levels of fundamental importance in the charge transport characterization.

The π electrons have higher energy, in fact they occupy the HOMO level, and due to the weak π bonds they are easily excitable to the LUMO, permitting an easy displacement of the electrons through the plane of the molecule. The movement of the carriers between molecules is not so easy. This transport mechanism is called hopping and most of all it depends on the structural order of the molecules. When movement of electrons or holes in an organic molecular solid is considered, one has to bear in mind that this involves ionic molecular states. In order to create a hole, e.g., an electron has to be removed to form a radical cation M^+ out of a neutral molecule M. This defect electron can then move from one molecule to the next. In the same way, electron transport involves negatively charged radical ions M^- (qualitatively, the same arguments hold for polymers, however, in this case charged states inside the HOMO-LUMO are usually termed positive or negative *polarons*.) As compared to isolated molecules in the gas phase, these ionic states are stabilized in the solid by polarization energies leading to an energy level diagram as shown in Figure 1.8 [(3)].

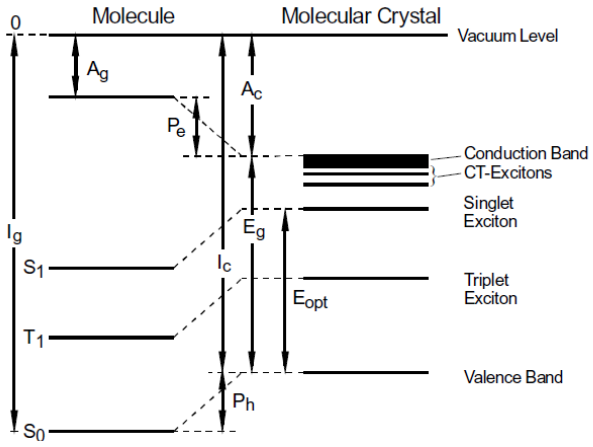

Figure 1.8: Energy levels of an isolated molecule (left) and a molecular crystal (right): I_g and A_g denote the ionization potential and electron affinity in the gas phase, I_c and A_c the respective quantities in the crystal. Due to the polarization energies P_h and P_e charged states are stabilized in the crystal. E_g is the single-particle gap being relevant for charge carrier generation, whereas E_{opt} denotes the optical gap measured in absorption and luminescence. Their difference is the so-called exciton binding energy [(3)].

Besides the small molecules, that are low-molecular weight materials, we must speak also of polymers and oligomers: they are all characterized by a conjugated p-electron system but an important difference between the two classes of materials lies in

the way how they are processed to form thin films. Whereas small molecules are usually deposited from the gas phase by sublimation or evaporation, conjugated polymers can only be processed from solution, e.g., by spin-coating or printing techniques [(3)]. An oligomer is a molecule that consists of a few monomer units, in contrast to a polymer that, at least in principle, consists of an unlimited number of monomers. Dimers, trimers, and tetramers are oligomers. Many oils are oligomeric, such as liquid paraffin. Plasticizers are oligomeric esters widely used to soften thermoplastics such as PVC. Polyisoprene of latex rubber and the polystyrene are examples of polymeric natural/biological and synthetic polymers, respectively. In biological contexts, essentially all biological macromolecules (proteins, nucleic acids, and polysaccharides) are purely polymeric, or are composed in large part of polymeric components. Organic Semiconductors with conjugated orbitals are divided in: molecular semiconductors, polymers, monodisperse oligomers. If the polymers are simple to produce, the oligomers instead are more crystalline and with very few defects. As already said, many polymers are not conductive, they must have a conjugated system with a backbone of double and single C-C alternate bonds. The polymers could also improve their conductivity with doping with appropriate inorganic compounds (discovery of MacDiarmid and Heeger in 1977). The name doping is used only to keep the analogy with inorganic semiconductors but in this situation the mechanism is not a substitutional but a redox process, so an electronic transfer. An important way to select a potentially conductive polymer is the facility to obtain an oxidized or reduced system in a reversible manner. The conductivity of the polymer depends on the length of conjugation, i.e. the number of repetitions of the base (monomer) and it depends also on the presence of defects both chemical or structural (Figure 1.10). The conductive polymer we will study in this research is PEDOT (Poly(3,4-ethylenedioxythiophene)), but due to its low solubility, it has to be mixed with PSS (Sodium Polystyrene Sulfonate) to form a soluble salt (Figure 1.9).

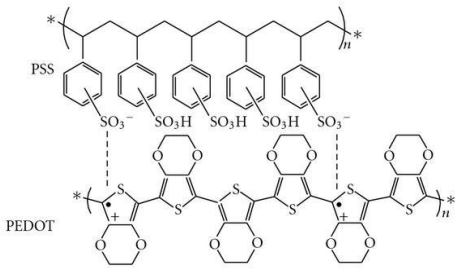

Figure 1.9: Chemical structure of PEDOT:PSS. The "dot" and "plus" represent the unpaired electron and positive charge on the PEDOT chain, respectively.

In an organic crystal we have strong overlap of the π orbitals and the electrons are delocalized all over the crystal. Instead in an amorphous or a polycrystalline film the molecules are bond with weaker Van der Waals interactions, so the distances between molecules (for example the chains of Pentacene in Figure 1.11) follow a casual distribution and in conclusion the mobility of the carriers decrease strongly.

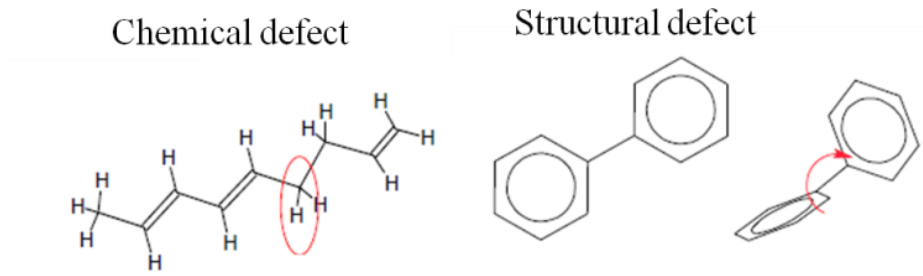

Figure 1.10: The conductivity of a polymer can be decreased by chemical or structural defects.

Figure 1.11: Schematization of the variable range hopping in an amorphous film of Pentacene.

As reported by Dimitrakopoulus [13], in the case of chain- or rod-like molecules, which have one molecular axis much longer than the other two, large p-conjugation length along the long axis and close molecular packing of the molecules along at least one of the short molecular axes are two important conditions for high carrier mobility. As shown in Figure 1.12, by growing amorphous films of Pentacene, which is achieved by keeping the substrate temperature low during deposition, they made a film that is practically insulating. When the substrate temperature is kept at room temperature during deposition, a very well-ordered film is deposited, and the mobility measured at room temperature is very high for an organic semiconductor (0.6 $cm^2 V^{-1} s^{-1}$). Since the structure of this thin film is different from the structure of single crystals of Pentacene, we must distinguish between a "thin-film phase" and a "single-crystal phase" of

Pentacene. When a mixture of the thin-film phase and the single-crystal phase is grown [14], the mobility is very low, possibly because of the high defect concentration resulting from the coexistence of the two phases.

Organic semiconductors have two important peculiarities as compared to their inorganic counterparts. One is the existence of well-defined spin states (singlet and triplet) as in isolated molecules which has important consequences for the photophysics of these materials (see Figure 1.8). Usually the ground state of an organic molecule is a singlet state (S_0) and absorption of a photon leads to the first excited singlet state (S_1). Typical lifetimes of the S_1 state are in the range 1–10 ns, thus leading to a rapid transition back to the S_0 ground state via fluorescence or non-radiative transitions. In the excited singlet state there is a small probability for intersystem crossing to the triplet state (T_1), from which the excitation energy can be released either by phosphorescence or non-radiatively. However, since intersystem crossing is a weak process, triplet lifetimes are usually in the millisecond range for pure aromatic hydrocarbons, and radiative decay via phosphorescence is usually not observed at room temperature. This also sets an upper limit for the electroluminescence quantum efficiency in OLEDs as about 75% of the excited states formed by the recombination of injected electrons and holes are in the triplet state [3] (Figure 1.13).

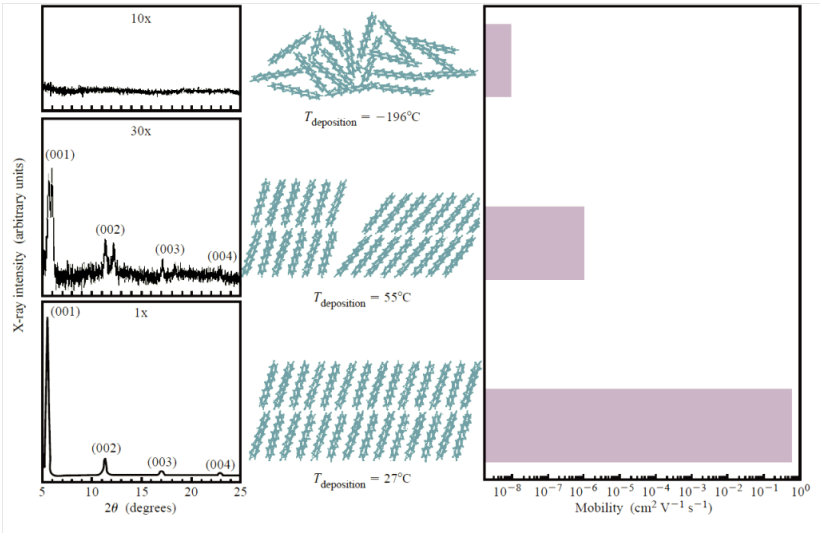

Figure 1.12: Comparison of X-ray diffraction patterns, schematic representations of structural order, and field-effect mobilities for three different phases of thin film Pentacene. an amorphous phase is achieved using a substrate temperature, T_{dep}=-196° C and a deposition rate DR=0,5 Hz. A single phase results at the temperature T_{dep}=27° C and DR=0,25 Hz, while T_{dep}=55° C and DR=0,25 Hz yields a double phase [13][14].

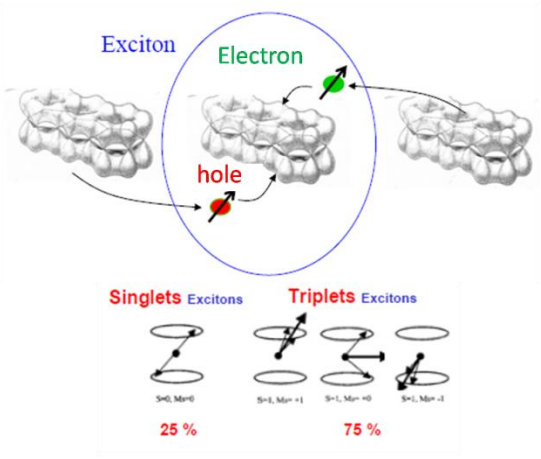

Figure 1.13: Charge recombination inside a molecule. Spin momentum conservation for radiative decay give certain probabilities to singlet and triplet excitons.

Triplet lifetimes can be considerably shorter in molecules incorporating heavy atoms, such as Pt or Ir. Therefore metal organic complexes incorporating these elements are becoming more and more important in OLEDs. A second important difference originates from the fact that optical excitations (*excitons*) are usually localized on one molecule and therefore have a considerable binding energy. A simple estimation of the Coulomb energy of an electron-hole pair, localized at a distance of 10 Å in a medium with a dielectric constant of 3, yields a value of about 0.5 eV for the *exciton* binding energy. In photovoltaic cells this binding energy has to be overcome before a pair of independent positive and negative charge carriers is generated [(3)].

1.3 Charge transport and hopping in organic thin films

Electronic transport usually is described by the (local) electric field-induced velocity component, $\langle v \rangle$, of the mobile charge carriers (superimposed on their random thermal motion as a time and ensemble average of a fast sequence of acceleration and scattering events) which is associated with a current density J:

$$J = en\langle v \rangle \qquad \text{[Eq. 3]}$$

where e is the electronic charge unit and n the local charge carrier density. The latter can be altered—in principle—by doping, injection, or photo-generation. The relation between $\langle v \rangle$ and the applied electric field E is usually linear for not too high fields (reflecting Ohm's law):

$$\langle v \rangle = \mu E \qquad \text{[Eq. 4]}$$

and it is obvious that μ, the charge carrier mobility, is the fundamental (intrinsic) electronic transport quantity that is specific of a given semiconductor material. Because of the usually lower than cubic symmetry of organic crystals, the vector relation [Eq. 4] is anisotropic in general, and μ is therefore a (polar) tensor of the second rank with six independent components μ_{ij} of the electron as well as of the hole contributions, that depend individually on temperature, T, and eventually (in the case of nonlinear transport) on the magnitude of E. Therefore, in more detail, the mobility components for given field components E_j are represented by the equation:

$$v_i = \mu_{ij}(T, \varphi, \chi, \theta; E) \cdot E_j \qquad \text{[Eq. 5]}$$

where the angles φ, χ, θ designate the orientation of the chosen coordinate system relative to the crystallographic one, v_i are the velocity components, (i, j = 1, 2, 3) and Einstein's summing convention has been implied. It is worth mentioning that even for macroscopically random (e.g. polycrystalline) materials the microscopic anisotropy is not simply averaged out. Grain boundaries in anisotropic materials lead to special problems that cannot be modeled without knowledge of the microscopic anisotropy(15). At present a theoretical prediction of $v_i = \mu_{ij}(T, \varphi, \chi, \theta; E) \cdot E_j$ for a given molecule in a given crystal structure is not possible. Therefore, first of all, reliable experimental data are required to find out, how large the transport parameters are, and under which conditions which kind of transport model can be applied.

A number of technical applications require high mobilities. For high purity single crystals, a high increase of mobilities towards low temperature has been found and traced back to temperature-dependent electron and hole masses, approaching the free electron mass at low temperature. With rising temperature, electron–phonon coupling, and therefore the effective masses, increase and coherent band transport is gradually destroyed; polaron-hopping transport evolves as a parallel channel and dominates at sufficiently high temperature [15]. The charge transport in crystalline organic semiconductors such as Pentacene may be described by assuming a *mobility edge* [15][16], which separates extended and localized states. The charge carriers are transported in the extended states above the *mobility edge*, but are trapped by and thermally released from localized trap states below the *mobility edge*. This may be identified with the valence or conduction-band edge. However, the parameters dominating charge transport are the trap densities as a function of energy relative to the *mobility edge*, the number of delocalized charge carriers above the *mobility edge*, and the mobility of the latter charge. For crystals with orientation disorder of the molecules band transport is precluded. In highly disordered organic semiconductors, a description of the charge transport by the method called *variable range hopping* [17] may be more appropriate. Importantly, this situation can be described by trap-controlled transport in a transport level with a distribution of localized states below the transport level and is thus very similar to the *mobility edge* picture [18].

In this study, however, I determine the mobility of the device using the saturation regime of the organic transistor as in the IEEE[19] standards (see Figure 1.14).

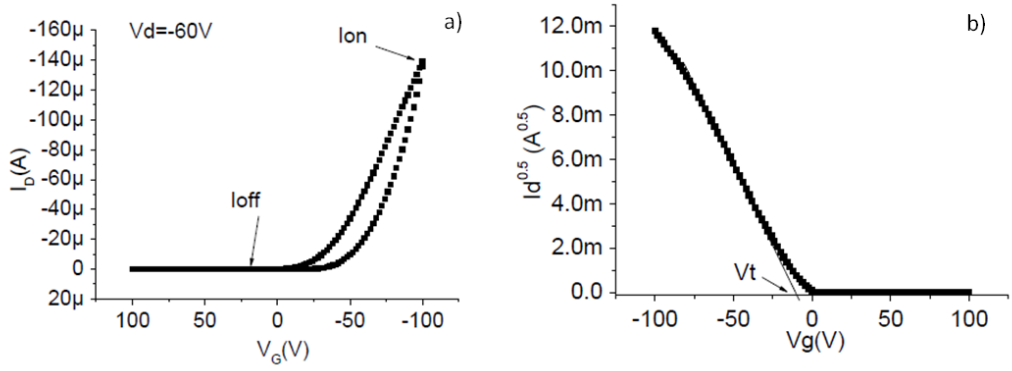

Figure 1.14: a) Transfer characteristic and b) its root square of an OTFT in the saturation regime.

The transconductivity can be calculated from a manipulation of:

$$I_{DS,sat} = \frac{W}{2L} C_i \mu (V_{GS} - V_{TH})^2 \qquad \text{[Eq. 6]}$$

$$\sqrt{I_{DS,sat}} = \sqrt{\frac{W}{2L} C_i \mu} (V_{GS} - V_{TH}) \qquad \text{[Eq. 7]}$$

by the acquisition of the slope of the linear part of the transfer characteristic:

$$g_{SAT} = \left. \frac{\partial I_{DS}}{\partial V_{GS}} \right|_{V_{DS}=cost} = \sqrt{\frac{W \mu C_i}{2L}} \qquad \text{[Eq. 8]}$$

and, μ_{SAT} can be approximated as:

$$\mu_{SAT} = \frac{2L g_{SAT}^{\ 2}}{W C_i} \qquad \text{[Eq. 9]}$$

This is true for every V_{DS} in the saturation region because I_{DS} is constant in that part of the characteristic.

The procedure to extract the mobility µ from the current-voltage data shows several difficulties: as a transistor has a two-dimensional geometry, Poisson's equation does not resolve to simple analytical solutions. Some researchers overcome this point with two simplifying assumptions:

1- carrier mobility in the conducting channel is constant;
2- the transverse field in the channel is much larger than the longitudinal field.
The latter condition corresponds to the so called gradual *channel approximation*, and allows one to reduce the two-dimensional to a local one-dimensional problem. However, condition 1 is not always fulfilled in organic devices, and in the general case

the mobility is not constant along the conducting channel. Horovitz measured the drain current I_{DS} at a low drain voltage V_{DS} (linear regime), so that the channel conductance g_d can be expanded to first-order, leading to Eq. 10:

$$g_d = \left.\frac{\partial I_{DS}}{\partial V_{DS}}\right|_{V_{GS}=cost} = \frac{W\mu C_i}{L}\left(V_G - V_{TH}\right) \qquad \text{[Eq. 10]}$$

A further improvement consists of taking account for the source and drain contact resistance R_S [(20)]:

$$g_d = \left(\frac{1}{\frac{W\mu C_i}{L}\left(V_G - V_{TH}\right)} + R_S\right)^{-1} \qquad \text{[Eq. 11]}$$

In practice, they first perform a least square fit of the data to Eq. 11 assuming a simple dependence of the mobility as a function of gate voltage. This gives them estimations of the series resistance and threshold voltage, which are then reintroduced in Eq. 10 to get the gate voltage dependent mobility. Typical results are given in Figure 1.15 for a Sexithiophene (6T) device. The mobility is calculated without and with correction for the contact resistance (Eq. 10 and Eq. 11, respectively). In the latter case, it increases quasi-linearly with gate voltage. Data obtained with a transistor built on a 6T single crystal are also shown in Figure 1.15. In this case, the uncorrected mobility decreases with gate voltage, while the corrected data are practically independent of the gate voltage.

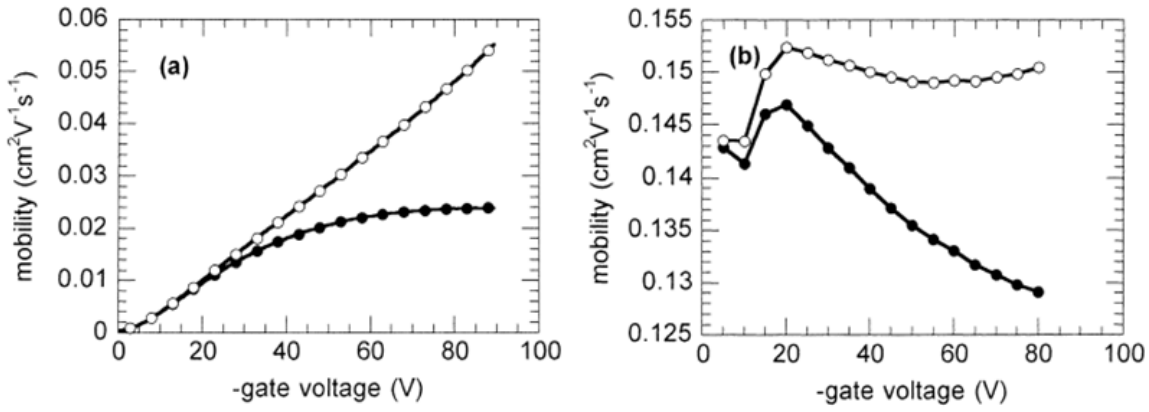

Figure 1.15: Charge mobility in a polycrystalline (a) and single crystal b) Sexithiophene at room temperature. Data are shown before (close circles) and after (open circles) correction for contact resistance [(20)].

Kalb [21] instead employs the μ_{eff} defined as the mobility obtained by the transcharacteristic when V_{DS} is in the linear regime, in the manner that the transconduttivity is:

$$g_{LIN} = \left.\frac{\partial I_{DS}}{\partial V_{GS}}\right|_{V_{DS}=\cos t} = \frac{W\mu C_i V_{DS}}{L} \qquad \text{[Eq. 12]}$$

While the mobility gives this result:

$$\mu_{LIN} = \frac{L g_{LIN}}{W C_i V_{DS}} \qquad \text{[Eq. 13]}$$

He also considered that in an organic field-effect transistor, a significant fraction of the drain voltage V_{DS} may drop at the contacts, which can introduce significant errors when extracting the field-effect conductivity and the field-effect mobility. From gated four terminal measurements, the conductivity can be derived without error considering (V_1-V_2) instead of V_{DS} (see Figure 1.16). P-type organic TFTs need a high work function metal, and Ag, Au, ITO and some others work well, while the lower work function metals give much higher contact resistance.

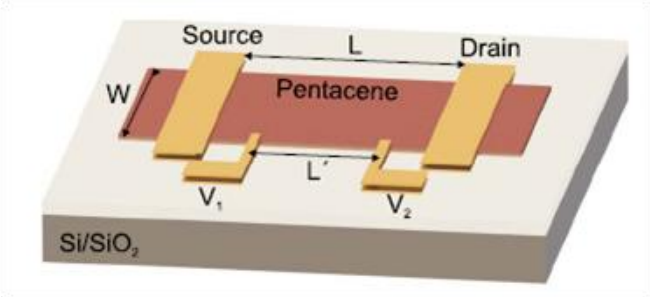

Figure 1.16: The transistor for the gated four-terminal measurements consists of a stripe of Pentacene with a width W. The distance between source and drain is L. The voltage-sensing electrodes are used to measure the potentials V_1 and V_2 with respect to the grounded source and were separated by L' [16].

I didn't find necessary to use the 4-contacts configuration because if we look at the measures of mobility executed by Kalb after 4 hours and after 140 hours (Figure 1.17), we can consider that after 140 hours the difference between 2-contacts and 4-contacts measures is not appreciable anymore. Thus, in first approximation to study the effect of aging and degrade of the OFETs, with or without ion implantation, we can reliably make use of the 2-contacts configuration

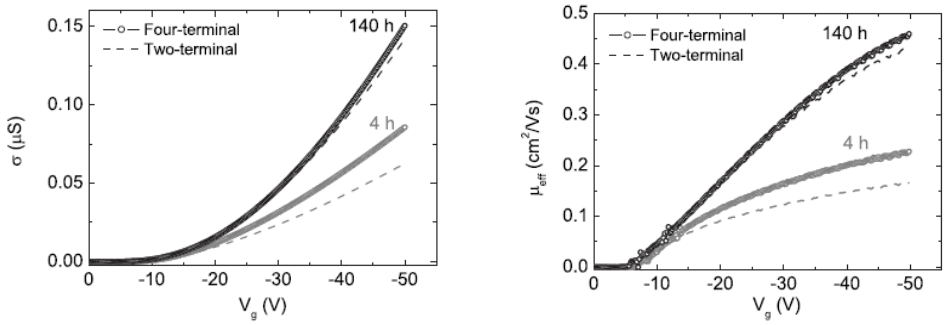

Figure 1.17: The four-terminal conductivity (a) and mobility (b) increase with time in vacuum. The graphs show the comparison between four-terminal and two-terminal conductivity (a) and mobility (b) after 4 hours and 140 hours.

1.4 Degradation

In this paragraph I will give a report of the current comprehension in the research landscape of the already discussed problem of the response degradation of the OTFTs. Several studies suggest that Oxygen acts as a p-type dopant in a variety of semiconducting polymers and small molecules, such as Pentacene [(22)]. Other studies show rather stable device operation under ambient conditions for weeks and months [(23)]. Therefore, a systematic investigation of doping and trapping effects is essential to clarify the picture. In particular, the threshold voltage of the transistor has to be stable to realize complex organic circuitry, which is required for applications. We can say that OTFTs show changes in the electrical characteristics due to several factors:

1. Bias stress;
2. Oxigen in the atmosphere;
3. Water vapor in the atmosphere;
4. Light.

As regards the changes in the threshold voltage, it is known that, applying a bias to the gate contact, V_{TH} tends to reach V_G [(24)(25)]. In particular, in ambient conditions, when you stress, for several hours, a p-OFET with negative Gate voltage, you can observe a shift of the V_{TH} toward negative voltages approaching the Gate voltage of the bias stress (Figure 1.18) as the research of Sharma confirmed [(24)]. An empirical result gets to the exponential function:

$$\Delta V_{TH}(t) = V_0\left(1 - \exp\left[-(t/\tau)^{\beta}\right]\right) \qquad \text{[Eq. 14]}$$

where V_0 is close to the absolute value of the applied gate voltage, τ is a relaxation time, and $0<\beta<1$ is an exponent.

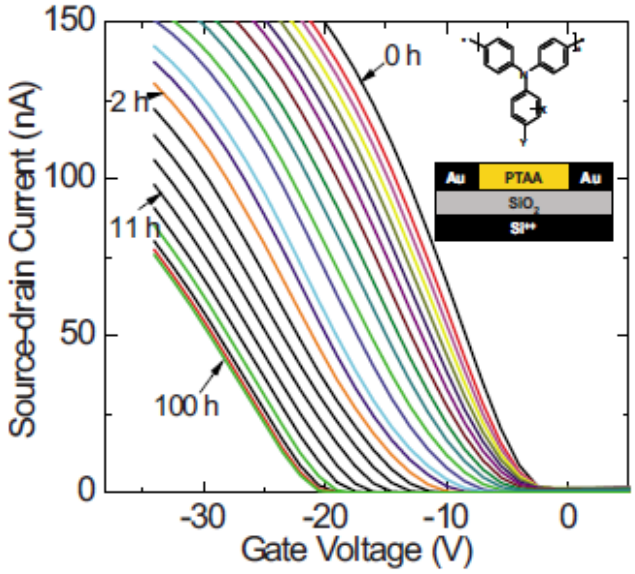

Figure 1.18: Transfer curves of a polytriarylamine (PTAA) transistor in ambient atmosphere at a temperature of 30 °C for different stressing times, indicated in hours (h): The gate bias during stressing is -20 V and the source-drain voltage during measurement of a transfer curve is 3 V. The inset shows a schematic cross section of the transistor and the chemical structure of PTAA, where X and Y are short alkyl side chains [(24)].

Other important but not understood observations are:

i. the effect is reversible: on grounding of the gate electrode of the transistor, V_{TH} shifts back toward its original value; this backward shift or "recovery," occurring on a similar time scale, also shows a stretched-exponential behavior;
ii. an increased humidity accelerates the effect;
iii. the effect is thermally activated with a semiconductor-independent activation energy of about 0,6 eV.

A possible explanation that Sharma [(24)] proposed for this phenomena is that water molecules, that are present in the air in the shape of vapor and that penetrate in the organic film, dissociate in protons and Deuterium by thermal activation and then the protons migrate to the dielectric interface causing the shift of the threshold voltage toward the gate voltage. This fact can also explain the possibility of a recovery when applying the gate to the ground. To strengthen the hypothesis, they increase the quantity of water and then an acceleration of the effect was measured. Furthermore, they also could establish the existence of the deuterium gas after the stress and the recovery of the device. This results are confirmed also by Puigdollers [(26)], they found a correspondence between a deep level at 0,49 eV upon the valence band and the absorption of water molecules. They also suppose that a thermal annealing at 110° for 1 hour in vacuum would be enough to remove most of the water content in the OTFT.

Knipp [25], with a different approach, studied the threshold voltage changes applying gate bias. The measures were carried out first in vacuum and at room temperature. The onset voltage of the drain current, defined as the gate voltage for which the drain current started to increase, was 0 V. Then the sample was stored for 30 minutes in a chamber with dry Oxygen (10^{-1} Pa), after that it was carried in vacuum and measured again. No changes were noted, also repeating the measures with different Oxygen pressure conditions and different storage time. A third set of experiments was carried out, in which a constant bias voltage was applied while exposing the devices to dry Oxygen for 30 min. Afterwards, the transistors were pumped back to high vacuum and characterized. Measurements were repeated for different biasing conditions. When the transistor was turned on (negative gate voltage, V_G) during the Oxygen exposure, no changes were observed in device characteristics. However, when the transistor was turned off (positive V_G) while exposing the device to Oxygen, distinct changes was observed. Transfer curves obtained after biasing the transistor in the off-state are shown in Figure 1.19. A significant shift of the onset voltage towards positive V_G values was observed as the V_G used during Oxygen exposure increased. Repeated measurements showed that the shift of the drain current is irreversible. Further experiments involving different exposure times revealed that the property changes occurred within the first few seconds. Afterwards no further changes were observed. The change of the onset behavior was likely caused by the acceptor states in the Pentacene film. The experiments described above suggested that exposure of Pentacene to Oxygen, under conditions in which the Fermi level is high in the Pentacene band gap (due to the positive V_G), can give rise to gap states which act as acceptors. These acceptors give rise to holes in the valence band, so that holes are present in the channel even when the V_G is zero. Knipp [25] studied several possible bonds or defects between Oxygen and Pentacene coming in conclusion that the defect under discussion is a Pn-2O-B complex, i.e. two atoms of Oxygen bonded with two Pentacene molecules as in Figure 1.20. An atomistic model was developed to individuate the energetic level of the defect with the result of a state in the gap located at 0,29 eV upon the valence band, this result is confirmed also by other researchers [16][26][27].

The experiments were also repeated without exposing the devices to Oxygen to ensure that bias stress effects did not cause the change; since the device characteristics remain unchanged, bias stress could be ruled out as the cause. This issue in not really cleared up, other studies of Wang and Li state that bias stress actually can modify the electrical parameters also in vacuum. The effect seems due to a change in the contact resistance, which effect becomes predominant compared to that of the channel resistance, this brings to a V_{TH} shift toward V_G and a mobility drop [28].

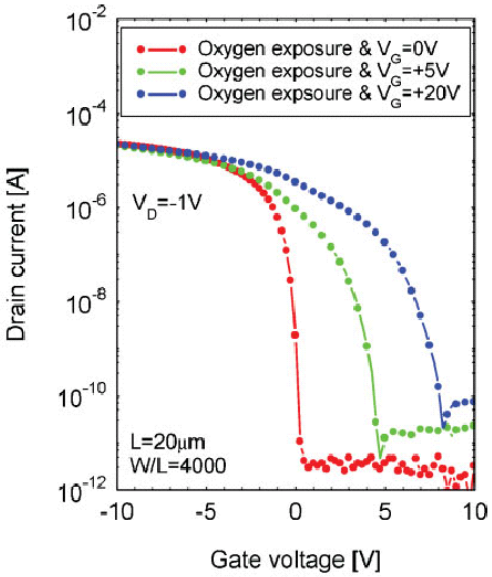

Figure 1.19: Measured transfer characteristics of a Pentacene TFT under vacuum with a drain voltage of V_D=-1 V. Prior to measurements, TFT was exposed to dry Oxygen for 30 min. while applying different magnitudes of V_G: 0 (red),+5 (green), and +20 V (blue). V_D was kept constant at -20 V. Applying a positive V_G while exposing the transistor to dry Oxygen led to the formation of gap states in the Pentacene film. The gap states behave like acceptor states, so that the onset of drain current shifts towards positive gate voltages [25].

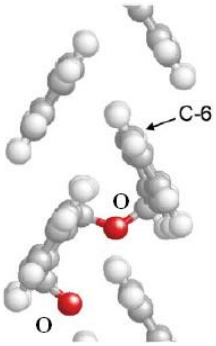

Figure 1.20: Pn-2O-B complex: One of the Oxygen atoms may form a second bond to a neighboring molecule. This complex has an acceptor level located about 0.29 eV above the HOMO[25].

Knipp found that this complex produces an acceptor level of E = 0.29 eV; this level is sufficiently close to the valence band to account for the p-type doping. The neutral defect may capture an electron from the valence band creating a negatively charged defect and a hole in the valence band. Thus, current may flow in the channel even when the gate-induced hole concentration is zero. The acceptor states are formed

in a very narrow region close to the interface. Consequently, the bulk conductivity of the Pentacene film was only slightly increased.

Nevertheless, the conductivity changes when the OTFT is exposed to Oxygen and water vapor for a long time. As the studies of Jurchescu [29] confirm, the density of current increases with time at room temperature in dry Oxygen environment compared to the measures in vacuum, but decreases in presence of water vapor (in ambient air), as it is shown in Figure 1.21.

The absorption of Oxygen, Nitrogen and Argon, both in dark and in white light, was studied with mass spectroscopy and the result is that the phenomena is reversible and not selective, i.e. all the gases are absorbed and released coming back in vacuum [29]. During the gas exposure there is also a DOS modification but not permanent, in fact, also in this case, coming back in vacuum there is no change in it [26] [30]. The only irreversible DOS modification due only to Oxygen exposure (so without electrical measures) happens when Pentacene is exposed to Oxygen combined with UV light; in this case Oxygen will dissociate in singlet Oxygen or in Ozone becoming very reactive with Pentacene. In this situation the structure of the film will be modified in an irreversible way [30].

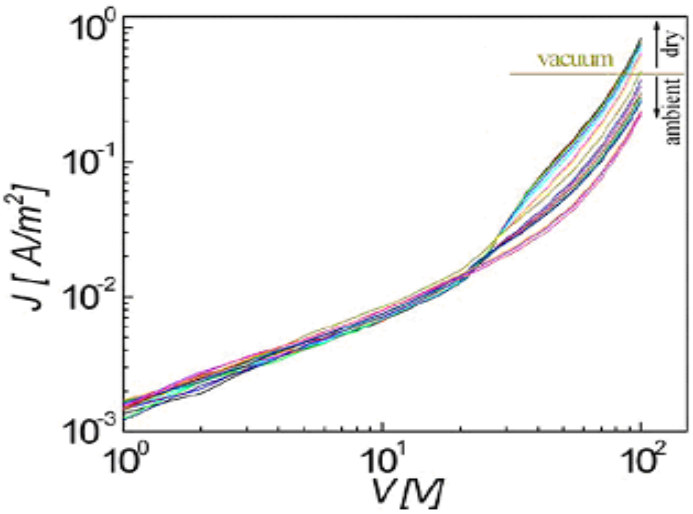

Figure 1.21: Current density J vs. applied voltage V for Pentacene single crystal at room temperature in vacuum and after exposure to dry air (increase in J) and ambient air (decrease in J). The different colors of the curves represent different exposure times. In pure air: (−250 min), (−200 min), (−150 min), (−100 min), (−50 min), (−10 min), (−0 min), (–in vacuum). In ambient air: (−0 min), (−10 min), (−20 min), (−30 min), (−50 min), (−100 min), (−150 min), (−200 min), (−250 min). The inset represents the evolution in time of the molar fraction of air in Pentacene upon exposure of single crystals to dry air at room temperature and the fit with a 1D diffusion model [29].

Talking about the electrical characteristic the problem is more complicated, only in the case of Oxygen, in fact, it was noticed that the density of current increases with the growing of the pressure of the gas (Figure 1.22a). The *I–V* curves are measured immediately after the desired pressure is reached. Once the system is at atmospheric pressure, the current continues to increase (Figure 1.22b) because the diffusion still continues. A comparison of the inset in Figure 1.21, with Figure 1.22b reveals a remarkable consistency. The time evolution of the electrical current is a sign of the Oxygen absorption. When venting with ambient air, both water vapor, and Oxygen are introduced into the chamber (Figure 1.22c and Figure 1.22d). They noticed that in ambient air, the effect of Oxygen exposure is counteracted by the exposure to water. Analyzing the magnitude of the induced changes in the current by combining Oxygen and water, one can distinguish two pressure regimes (Figure 1.22c). At low pressure ($p<10^{-2}$ mbar), the conduction is independent of air pressure. This leads us to conclude that the two effects are opposite and of the same magnitude. At $p=10^{-2}$ mbar, a sudden drop in the current is observed. Apparently, for $p>10^{-2}$ mbar the introduction of scattering sites exceeds the creation of holes, and this has a major effect on the conduction. This is reflected also in the results at atmospheric pressure, where diffusion of dry air causes a current increase of 25% (Figure 1.22b), whereas ambient air diffusion cause a drop of 45% (Figure 1.22d).

Figure 1.23 shows the evolution of the current under the same conditions, but now in the presence of light. The effect of Oxygen diffusion is stronger than in dark (Figure 1.23a and 20b). This is reflected in the increase of the current, which is a factor 2.4 larger in dry air than in ambient air. As the effect of water is independent of the presence of light, the total influence of ambient air on the crystal properties will be different in the presence of light. Consistent with the measurements in dark, we find two pressure regimes. At low pressure ($p<10^{-2}$ mbar), the Oxygen doping is the dominant factor of the conduction mechanism. At $p>10^{-2}$ mbar, the effect of Oxygen is decreased, and therefore a change in slope is observed (Figure 1.23c). However, the presence of Oxygen remains the most important factor, as the value of the current increases with pressure. After venting with ambient air, the doping caused by Oxygen, activated by illumination, gives a stronger effect than the trapping of charges by water [(29)].

The sensitivity to water of Pentacene OTFT can be otherwise useful to build sensors of Relative Humidity (RH) as Zhu did [(31)]. He demonstrates that the saturation current of a Pentacene TFT is a good parameter to monitor RH changes in the atmosphere, as it changes by as much as 80% when the RH changes from 0% to 30%. The effect is reversible and they found to depend on the thickness of the Pentacene film and attributed to changes in the hole mobility. The analysis of the $(I_{DS},sat)^{1/2}$ versus V_G curves reveals that the hole mobility decreases from $3x10^{-2}$ to $9x10^{-4}$ cm^2/Vs after a 30 min exposure to 72% RH. It's significant that nearly two orders of magnitude decrease in hole mobility does not translate into an equal change in the saturation current, which

merely changes by one order of magnitude as shown in Figure 1.24. This is due to the fact that both the off current and the voltage threshold of the OTFT change with RH, decreasing the dynamic range of the sensor.

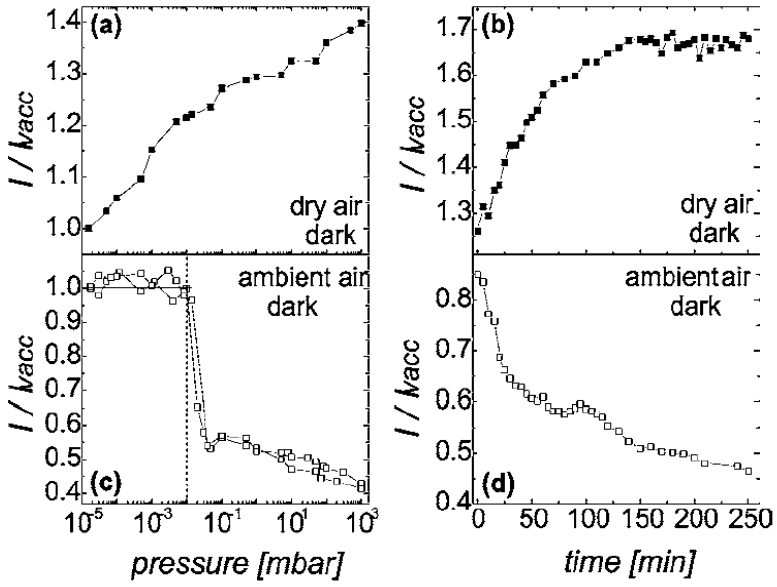

Figure 1.22: Pressure (a), (c) and time (b), (d) dependence of the current at fixed bias voltage for single crystal Pentacene in dark [29].

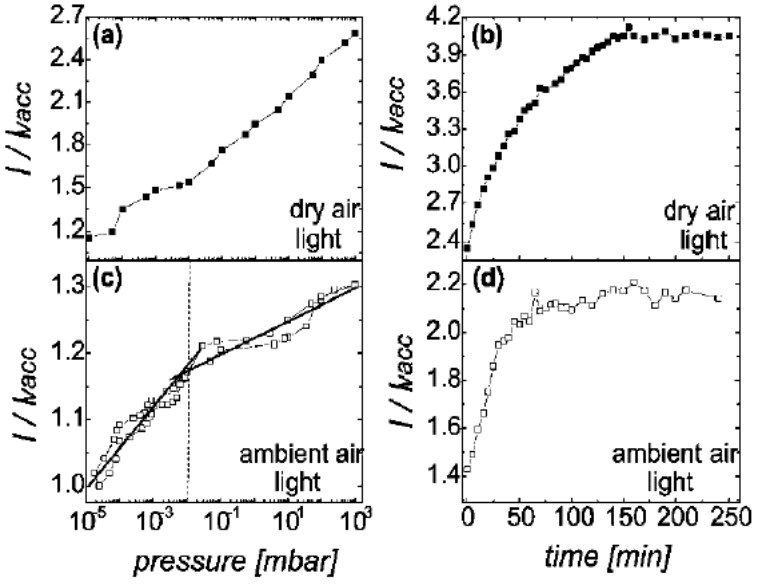

Figure 1.23: Dependence of the current at fixed bias voltage for single crystal Pentacene of pressure (a), (c) and time at normal pressure (b), (d) exposed ambient florescent light [29].

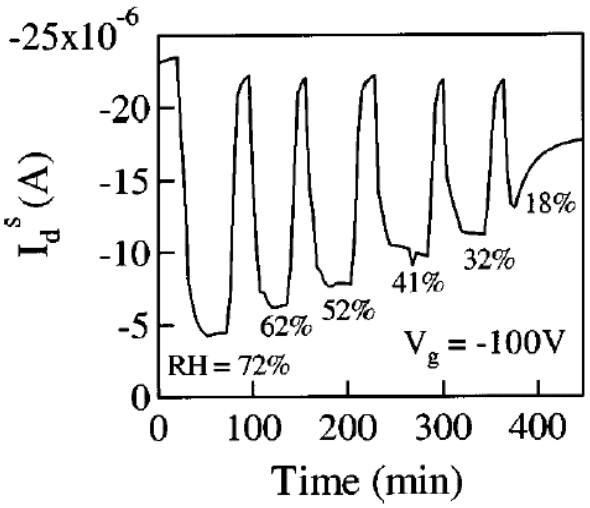

Figure 1.24: Time dependence of the saturation current measured at a gate voltage of -100 V and a drain voltage of -100 V. The OTFT was exposed to wet N_2 gas with different RH and vacuum, alternatively [(31)].

Also the mobility of an OTFT decreases due to Oxygen, as the studies of Kalb show [(16)] (Figure 1.25), both in presence of light both in dark, but the effect is accelerated with light. The measures were carried out in a chamber with only dry Oxygen (1 bar) and they commented also that several hours must be considered to have such an effect.

When Pentacene is exposed to oxygen, the gas migrates into the Pentacene film and interacts with the Pentacene molecules. This effect is expected to be accelerated if, in the presence of light, Oxygen is activated and its dissociation is aided. They observe significant and irreversible changes in the transfer characteristics (4-terminal I-V) and in the DOS caused by the Oxygen exposure leading to a broad peak of trap states centered at 0.28 eV (as in Knipp studies [(25)]).

Kalb suggests that the degradation mechanism is dominated by the creation of this specific oxygen-related defect for two reasons:

1- the decrease of the field effect mobility is due to the significantly smaller fraction of free holes in the channel (highly consistent with the density of the Oxygen related traps as estimated from the difference in the trap DOS prior and after Oxygen exposure);

2- the reduction of the mobility of the charge carriers might be due to scattering of charge carriers at the Oxygen defects.

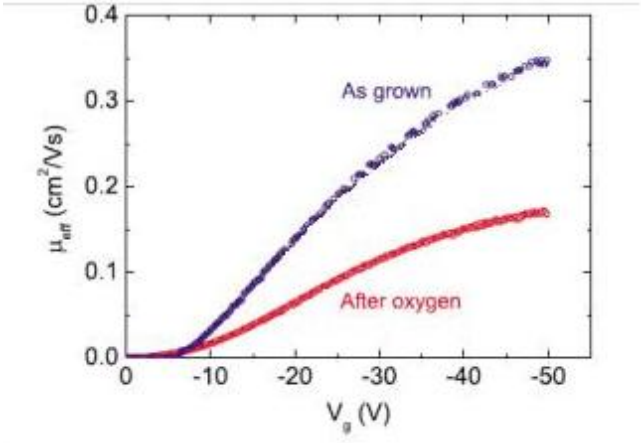

Figure 1.25: Four-terminal effective mobility from an as-grown sample (blue pentagons) and after the oxygen exposure (19 hours in dark and 4 hours in white light)(red circles). At V_G=−50 V for example, the contact-corrected field-effect mobility decreases from μ_{eff} =0.35 cm^2 /Vs to 0.17 cm^2 /Vs, i.e., it is reduced by a factor of 2.1 [16].

Experimental Conditions	**Effects**	**Reversibility**	**Ref.**
Absorption O_2	DOS changes	Reversible (coming back in vacuum + annealing)	(29) (30) (26)
Absorption H_2O			(26)
Absorption O_2+UV light		Irreversible	(30)
O_2+(V_G <0)	$V_{TH} \rightarrow V_G$	Reversible (with Gate grounded)	(24)
O_2 +(V_G >0)	$V_{TH} \rightarrow V_G$	Irreversible and immediate	(25)
I-V with O_2 (light accelerates the effect)	$I_{DS,sat}$ increases	Reversible	(29)
	μ decreases	Irreversible and not immediate	(16)(27)
I-V with H_2O	$I_{DS,sat}$ decreases	Reversible	(29) (31)
	μ decreases	?	(31)
Bias stress in vacuum	$V_{TH} \rightarrow V_G$ μ decreases	?	(32)

Table 1.1: Effects of bias, Oxygen, water vapor and light on OTFT.

In conclusion, the consequences of applying a bias, the exposure of Oxygen, water vapor, and light may influence the reliability of an OTFT in a strong way. It's important to know if the effect is reversible or not, in such a way to find a solution able to give us a reliable OTFT. In Table 1.1 we can summarize all the described effects and their possible reversibility. In Paragraph 4.2 I will discuss the changes in the DOS, with Photocurrent (PC) measurements, of my OTFT due to air effects, light and bias correlated with the electrical measurements. In paragraphs 6.1 and 6.2 I will show the stability of my devices ion implanted as regards V_{TH} and mobility and we will correlate that with PC spectra.

1.5 Encapsulation techniques

The problem of keeping safe the organic devices is a big issue and several researchers and industries are working to obtain the wished result. There are multiple choices of interventions, for example, if you want to prevent the effect of the bias stress (V_G = -10V) in presence of Oxygen, water and light, Cheng proposes a special gate insulators like a Cross-Linked Fluoropolymer (C-Cytop) [33]. This material is hydrophobic and hydroxyl free, further more the molecules of the solvent used (C_6-Si), when they condense, provide a physical network, embedding the Cytop chains. This is thought as the causes of the slower decrease of the drain-source current checked after bias stress in atmosphere compared with OTFT with other gate insulators. A similar device gave as a result a very small shift of the threshold voltage (ΔV_{TH} = 1,1 V) and no hysteresis despite the bias stress with V_G= -20 V [34].

Other approaches could be used to obtain stable electrical parameters in presence of air for a long time, Cho, in fact, tried to get the goal with an encapsulation layer of Titanium sub-oxide able to scavenge H_2O, O_2 and photoexcited electrons from the organic semiconductor [35]. Thin films of TiO_x are amorphous, transparent and smooth. When this barrier layer is deposed on the upper part of an OTFT (

*Figure 1.26*a), or another organic electronic device, the lifetime is improved by approximately two orders of magnitude. The further importance of this encapsulation film is that it can work also if the exposition of the organic semiconductor to Oxygen or water is already happened before the encapsulation. In

Figure *1.26*b we can see the recovery of the electrical characteristics of a FET device with or without TiO_x layer after exposure to air; in

Figure *1.26*c instead we can see the recovery of the threshold voltage and saturation current after dipping in water for 15s the device and then covered with the encapsulation layer. Finally, in

Figure *1.26*d, it's shown the effect of stabilization of the layer deposed after 12h of air exposure of the device and then covered with the TiO_x layer. As regard the mobility they obtain stability for 500 hours and one order of magnitude less after 2000 hours, the mobility of the unprotected device instead drop immediately (Figure 1.27).

A longer lifetime (100 days) is achieved by Kim with another transparent barrier made of two layers of SnO_2, one used as a buffer and the second, grown by Ion Beam-Assisted Deposition (IBAD), creates the barrier (Figure 1.28a) [(36)]. The buffer is used to preserve the organic layer from the ion beam possible damages, while the upper part establish a dense microstructure that has a very low Water Vapor Transmission Rate (WVTR), so it shuts out the water and the Oxygen. The IBAD technique in this case consists of an ion gun of Ar^+ ions used to increase SnO_2 ad-atom mobility (Figure 1.28b).

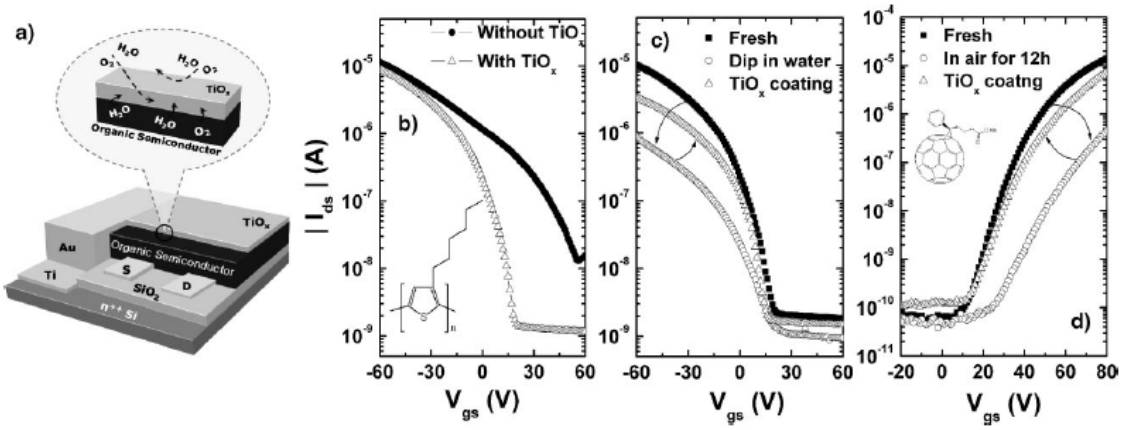

Figure 1.26: a) Schematic FET device structures with TiO_x active-passivation layer. b) Comparison between the transport characteristics of P3HT FETs with and without TiOx fabricated by spin-casting in air. c) Effect of TiOx layer on the degraded P3HT FET after being dipped into deionized water for 15 s. d) Effect of TiOx layer on the degraded PCBM FET after storage in air for 12 h [(35)].

In Figure 1.29 instead is shown the mobility and the I_{on}/I_{off} ratio (inset) as a function of the time of exposition to air for four Pentacene OTFTs: reference, with only SnO_2 buffer layer, with only IBAD SnO_2 layer and the last device with encapsulation made by both the layers. Only with the complete encapsulation there is a stable mobility and I_{on}/I_{off} ratio for at least 100 days. As the V_{TH} shift concerned, this method enable a better stability of the parameter, as shown in Figure 1.31 a and b, passing from a ΔV_{TH} = 9,4V to a ΔV_{TH} = 2,4V.

Other possible solutions are the multilayer barriers by multiple organic/inorganic layers (Figure 1.32). The inorganic layers are usually made of Aluminum Oxide deposited by DC reactive sputtering, 30-100nm thick. The organic layer instead is a monomer mixture of thickness of several μm for planarization and smoothing of the surface, the combination is repeated 4-5 times to achieve the desired hermeticity. Otherwise, other researchers use several compounds with dryer function through different appearances (Figure 1.33): tapes, dry paste and gel. The last idea is to insert nanoparticles of getter materials in a transparent layer.

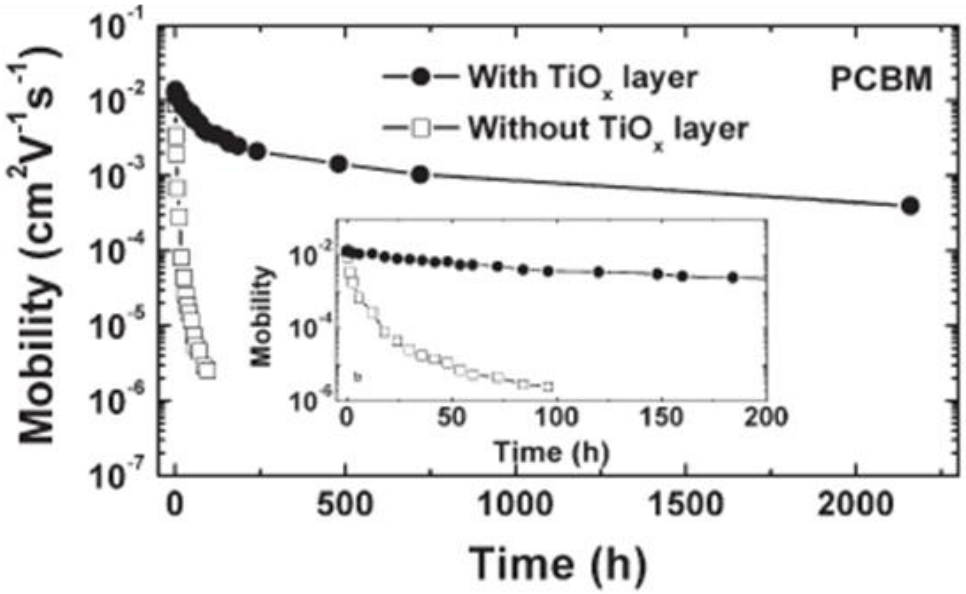

Figure 1.27: Comparison of the mobilities as a function of storage time in air for a n-type PCBM FET with and without the TiO_x layer [35].

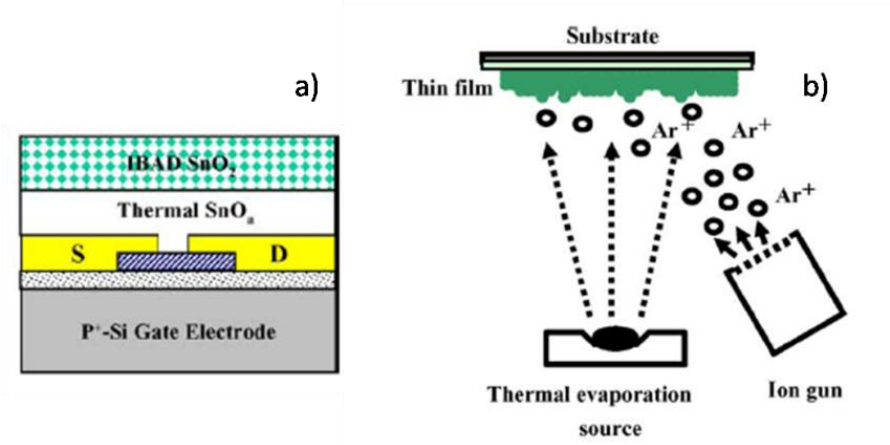

Figure 1.28 a) Cross-section of the device structure,b) schematic drawing of IBAD process [36].

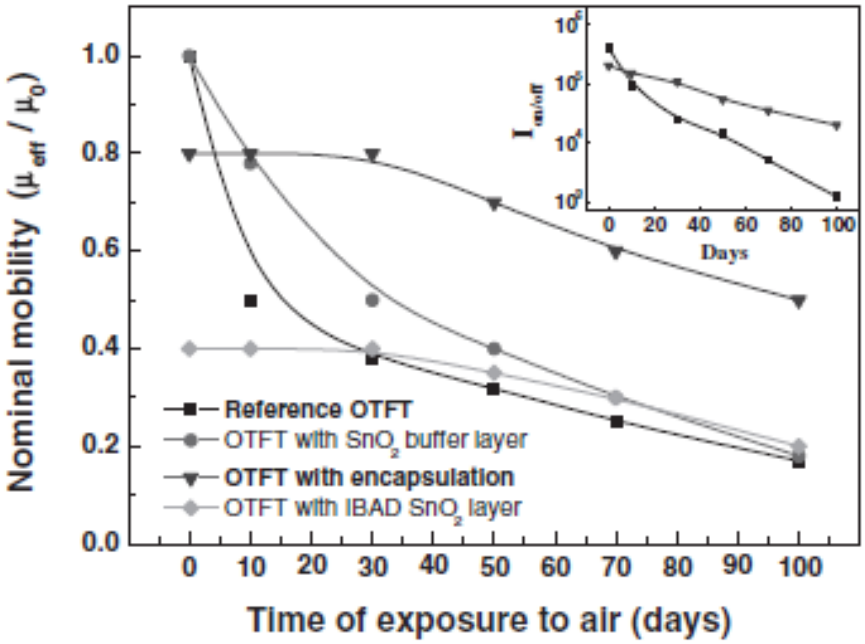

Figure 1.29: The property-endurance limit or aging effect with time of OTFTs in terms of field-effect mobility and I_{on}/I_{off} ratio [36].

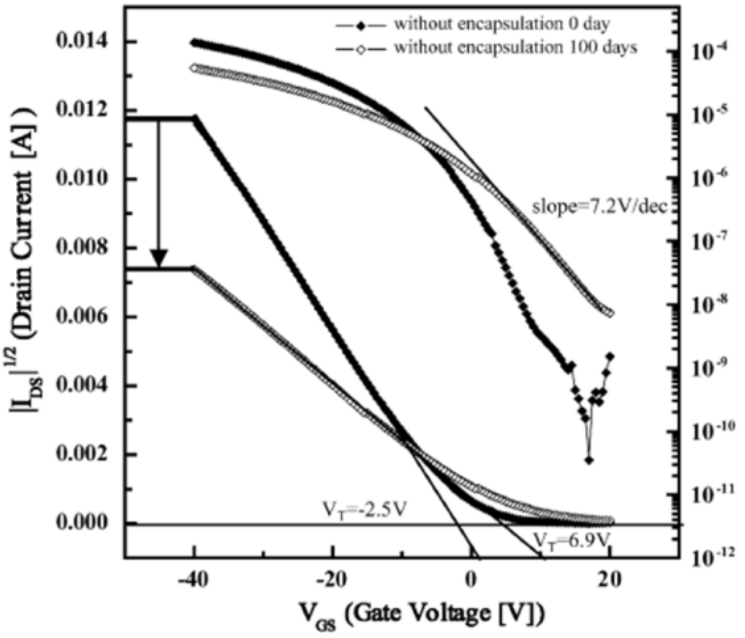

Figure 1.30: Plot of $\sqrt{-I_{DS}}$ vs. V_G and log10(- I_{DS}) vs. V_G for the OTFTs without encapsulation [36].

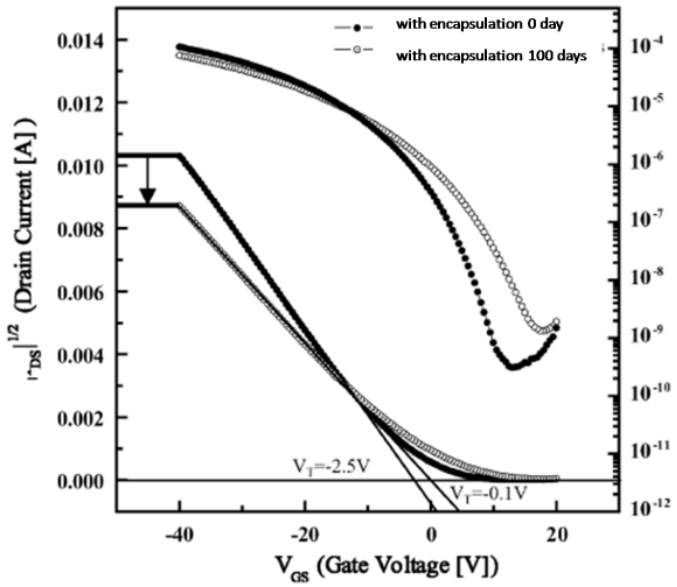

Figure 1.31: Plot of $\sqrt{-I_{DS}}$ *vs.* V_G *and* $log_{10}(-I_{DS})$ *vs.* V_G *for the OTFTs with encapsulation* [36].

However the actual two general ways undertaken by researchers and industries are: passivation layers or dessicant inside the device. These methods cover some requests but not all. In the Table 1.2 we can summarize the state of the art of the approaches to the degrade problem.

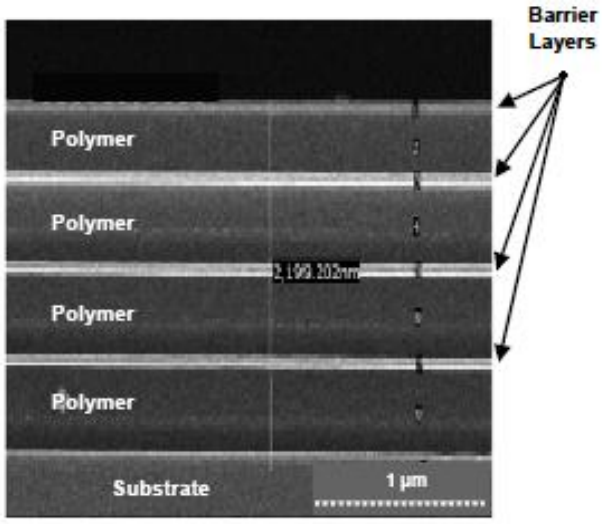

Figure 1.32: Multilayer polymer barrier producted by Vitex Systems.

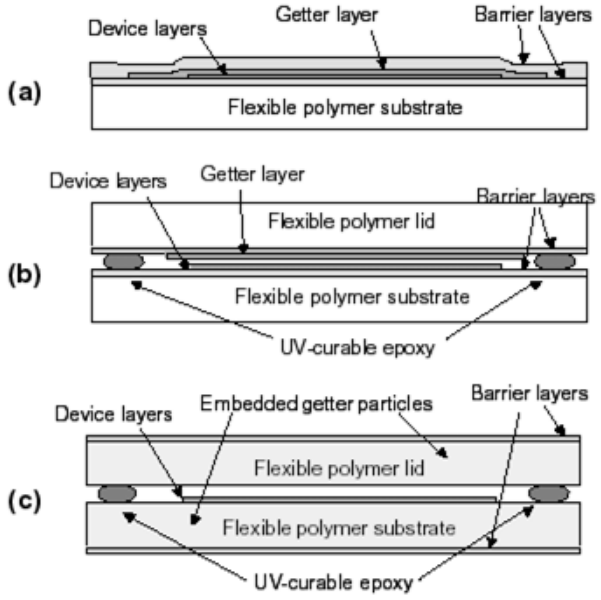

Figure 1.33: Other possible solutions of encapsulation layers: thin film of getter inside a) a monolithic barrier and b) a laminated barrier, c) nanoparticles of getter inside two coating polymer layers.

APPROACH	SCOPE	TECHNOLOGY ROADMAP	FEATURES	WEAK POINTS
Desiccant	Remove H_2O/O_2 already inside the device.	Reactants. Organics/inorganics chemicals.	Active component. Reduce risks of other approaches.	Host material. Transparency. Thickness. Cost. More process steps.
Barriers, Passivation, Adhesives	Prevent H_2O/O_2 entrance inside the device.	Multilayer structures. Hydrophobic compounds.	Passive/inert. Thin. Transparent.	Cost. Insufficient performances. Defect control.

Table 1.2: State of the art of the approaches to the degrade problem.

2 Ion implantation

Ion beam processing of materials results from the introduction of atoms into the surface layer of a solid substrate by bombardment of the solid with ions in the electron-volt to mega-electron-volt energy range. The solid-state aspects are particularly broad because of the range of physical properties that are sensitive to the presence of a trace amount of foreign atoms. Mechanical, electrical, optical, magnetic, and superconducting properties are all affected and, indeed, may even be dominated by the presence of such foreign atoms. The use of energetic ions affords the possibility of introducing a wide range of atomic species, independent of thermodynamic factors, thus making it possible to obtain impurity concentrations and distributions of particular interest; in many cases, these distributions would not be otherwise attainable [(37)].

Recent interest in ion beam processing has focused on the studies of ion implantation, ion beam mixing, ion induced phase transformations, and ion beam deposition. These interests have been stimulated by the possibilities of synthesizing novel materials with potential applications in the semiconductor, tribological, corrosion, and optical fields. Ion beam processing provides an alternative and non-equilibrium method of introducing dopant atoms into the lattice. In typical applications, a beam of dopant ions is accelerated through a potential of 10-100 kV. The implantation system shown in Figure 2.1 illustrates the basic elements required in this technique: ion source, acceleration column, mass separator, and target chamber. With different types of ion sources available, a wide variety of beams may be produced with sufficient intensity for implantation purposes for integrated circuit technology; 10^{14}-10^{15} ions/cm^2 (less than a monolayer) is a representative ion dose. Ion dose is defined as the number of ions per centimeter square implanted into the sample. Alternatively, the term fluence is used instead of dose. A mass-separating magnet is almost mandatory for semiconductor processing to eliminate unwanted species that often contaminate the extracted beam. However, for metallurgical processing, mass separation is not important, and as a result the basic instrumentation can be quite simple. In Figure 2.2, *Varian* implanter of Los Alamos National Laboratory, where the samples of my research were implanted, is shown.

The major features governing the successful exploitation of ion beam processing are the range distribution and the energetic ions, the amount and nature of the lattice disorder that is created, and the location of the energetic ions in the crystal lattice.

In paragraph 2.1 the main concepts necessary to comprehend the ion implantation are reported, without trying to be exhaustive, and the SRIM simulations used for the related calculations is explained in paragraph 2.2.

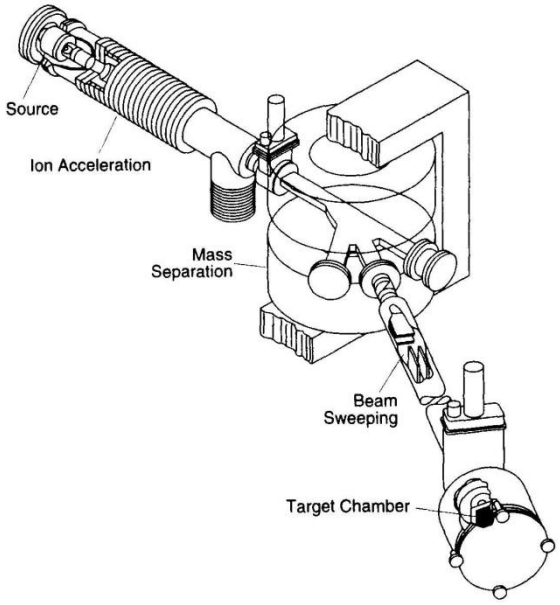

Figure 2.1: Schematic drawing of an ion implantation system. A mass-separating magnet is used to select the ion species (element and isotopes) of interest. Beam-sweeping facilities are required for large-area uniform implantations [(37)].

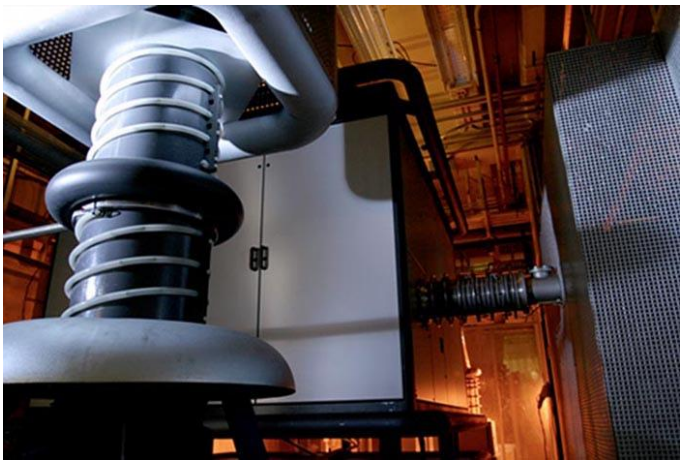

Figure 2.2: Ion implanter at Los Alamos national Laboratory.

In paragraphs 2.3-2.4-2.5 the focus is only on implanted polymers as these materials are organic compounds and also the more similar materials to the ones I studied that are represented in the literature of ion implantation. The interactions between ions and polymers are sketchily described in paragraph 2.3, the main effects of ion implantation on polymers in paragraph 2.4 whereas their possible applications in paragraph 2.5. Finally, paragraph 2.6 is related to Plasma Source Ion Implantation (PSII), one of the numerous techniques of ion implantation, that show several advantages like the lower

costs and the easier possibility to industrialize the process. In chapter 5 several of the effects described in paragraph 2.4 were found also for the samples of my research.

2.1 General concepts

When an energetic ion penetrates a solid, it undergoes a series of collisions with the atoms and electrons in the target. In these collisions the incident particle loses energy at a rate of *dE/dx* of a few to 100 electron-volts per nanometer, depending on the energy and mass of the ion as well as on the substrate material [37]. The total path length, also called range *R* of the ions (see Figure 2.3), is determined by the rate of energy loss along the path of the ion:

$$R = \int_{E_0}^{0} \frac{1}{dE/dx}\, dE \qquad \text{[Eq. 15]}$$

where E_0 is the incident energy of the ion as it penetrates the solid. The sign of *dE/dx* is negative, as it represents the energy loss per increment of path, although tabulated values are given as positive quantities.

The main parameters governing the range or energy-loss rate are the energy E_0 and atomic number Z_1 of the ion and atomic number Z_2 of the substrate if we exclude the effect of the orientation of the crystal lattice. As the incident ion penetrates the solid undergoing collisions with atoms and electrons, the distance traveled between collisions and the amount of energy lost per collision are random processes. Hence all ions of a given type and incident energy do not have the same range. Instead there is a broad distribution in the depths to which individual ions penetrate. The distribution in ranges is referred to as the range distribution or range straggling. Further, in ion implantation it is not the total distance *R* traveled by the ion that is of interest but the projection of *R* normal to the surface (i.e., the penetration depth or projected range R_P) (Figure 2.3).

Because the stopping of an ion is a stochastic (random) process, the collision sequence and subsequent ion deflection, and the ion's total path length in coming to rest vary randomly from ion to ion. As a result, ions with the same energy, incident with the same angle onto the sample surface, and into the same material, do not necessarily come to rest in the same place. Hence, all ions of a given type and incident energy do not necessarily have the same range. Instead, if one were to examine the range history of many ions, a statistically broad distribution in the depths to which ions penetrate would be observed, similar to that shown in Figure 2.4. The distribution in projected ranges is referred to as the range distribution or range straggling, with the most probable projected range referred to as the average or mean projected range.

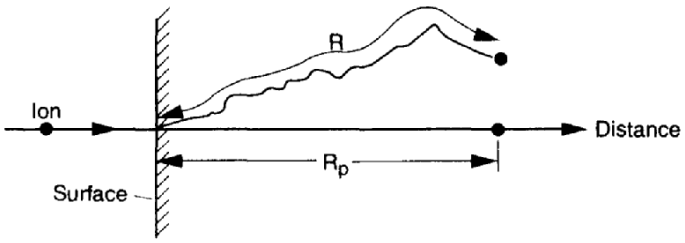

Figure 2.3: An ion incident on a semiconductor penetrates with a total path length, also called range R, which gives a projected range, R_P, along the direction parallel to that of the incident ion [37].

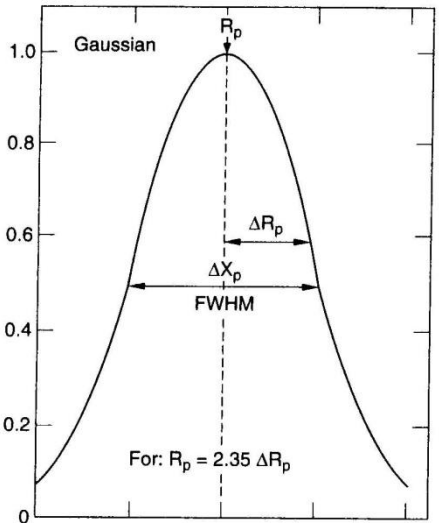

Figure 2.4: Gaussian range distribution for implanted ions with $R_P = 2.35\Delta R_P$, and a full width and half-maximum (FWHM) of ΔX_P [37].

Arbitrary distributions can be characterized by their moments. The first moment gives the mean value of a distribution, μ, and for a continuous distribution this is defined by:

$$\mu = \int_{-\infty}^{+\infty} xf(x)dx \qquad \text{[Eq. 16]}$$

where *f(x)* is the probability function for the random variable of interest. The second moment, σ^2, gives the variance of the distribution, and is defined as

$$\sigma^2 = \int_{-\infty}^{+\infty} (x-\mu)^2 f(x)dx \qquad \text{[Eq. 17]}$$

The standard deviation of a distribution is simply the square-root of the variance, σ. At low ion doses, and in the absence of crystal orientation effects, the range distribution and the projected range distributions are roughly Gaussian. The probability function for a Gaussian (normal) distribution, is:

$$f(x) = \frac{1}{\sigma(2\pi)^{1/2}} \exp\left[-\frac{1}{2}\left(\frac{x-\mu}{\sigma} \right)^2 \right] \qquad \text{[Eq. 18]}$$

The depth distribution, *N(x)* of implanted ions, normalized for an ion implantation dose ϕ_i, is given by the expression

$$N(x) = \frac{\phi_i}{\Delta R_P (2\pi)^{1/2}} \exp\left[-\frac{1}{2}\left(\frac{x-R_P}{\Delta R_P} \right)^2 \right] \qquad \text{[Eq. 19]}$$

where we have used Eq. 18, setting (i) the probability function, *f(x)*, equal to the ion distribution function *N(x)*, (ii) replacing the mean, μ, by the projected range, R_P, and (iii) replacing the standard deviation, σ, by the projected range straggling, ΔR_P. Assuming that all implanted ions are retained, the dose is related to the ion depth distribution as follows:

$$\phi_i = \int_{-\infty}^{+\infty} N(x)dx \qquad \text{[Eq. 20]}$$

The expression for peak atomic density in the ion implantation distribution is obtained by setting $x = R_P$ in Eq. 19:

$$N(R_P) \equiv N_P = \frac{\phi_i}{\Delta R_P (2\pi)^{1/2}} \cong \frac{0{,}4\phi_i}{\Delta R_P} \qquad \text{[Eq. 21]}$$

where N_P is in units of atoms per centimeter cubed for ϕ_i in units of atoms per centimeter squared and ΔR_P in centimeters. Consider a 100 keV N^+ implantation into Fe, where R_P = 106 nm and ΔR_P = 22 nm. For an implantation dose of $1 \cdot 10^{16}$ atoms/cm^2, the peak atomic density will be:

$N(R_P) = 0.4 \cdot 10^{16}$ (atoms/cm^2)/22 $\cdot 10^{-7}$ (cm) = 1.82 $\cdot 10^{21}$ (atoms/cm^3)

To obtain the atomic concentration resulting from this peak number of implanted ions requires knowing *N*, the atomic density of the substrate. The general relation for the concentration of the implanted species at the peak of the distribution is given by:

$$C_P = N_P/(N_P+N) \qquad \text{[Eq. 22]}$$

For the example above, as the atomic density of Fe is 8.5 $\cdot 10^{22}$ atoms/cm^3, the concentration of N^+ ions in Fe substrate is 0.18/(0.18 + 8.5) = 0.021 = 2.1%.

Higher moments are often necessary to describe the non-Gaussian ion depth distributions which occur at higher doses. Higher moments are usually taken about the projected range and have the general form:

$$m_i = \frac{1}{\phi}\int_{-\infty}^{+\infty}(x - R_P)^i N(x)dx \qquad \text{[Eq. 23]}$$

where *i* represents the order of the moment. The second, third, and fourth moments have special meanings in defining the ion distribution, with the second moment, as shown by Eq. 17, being related to the standard deviation or range straggling:

$$\sigma_P \equiv \Delta R_P = (m_2/\phi_i)^{1/2} \qquad \text{[Eq. 24]}$$

the third moment being related to the skewness:

$$\gamma_P = m_3/\sigma_P^3 \qquad \text{[Eq. 25]}$$

and the fourth moment being related to the kurtosis:

$$\beta_P = m_4/\sigma_P^4 \qquad \text{[Eq. 26]}$$

The skewness of the projected range distribution, γ_P, gives a measure of the asymmetry of the distribution, where a positive value locates the peak closer to the surface than R_P. In a Gaussian (normal) distribution, γ_P equals zero. The kurtosis, β_P, gives a measure of the flatness of the distribution, with a value $\beta_P = 3$ for a Gaussian distribution. The final concentration profile in the high-dose regime is the result of many processes occurring simultaneously. These processes include sputtering, radiation enhanced diffusion, compound formation, etc.

The energy-loss rate *dE/dx* of an energetic ion moving through a solid is determined by screened Coulomb interactions with the substrate atoms and electrons. It is customary to distinguish two different mechanisms of energy loss: (1) elastic nuclear collisions (or *nuclear stopping*), in which energy is transmitted as translatory motion to a target atom as a whole, and (2) inelastic electronic collisions (or *electronic stopping*), in which the moving particle excites or ejects atomic electrons [37]. For most purposes, this separation into elastic and inelastic collisions is a convenient one and, although not strictly true, it is a good approximation. The energy-loss rate *dE/dx* can be expressed as:

$$\frac{dE}{dx} = \left.\frac{dE}{dx}\right|_n + \left.\frac{dE}{dx}\right|_e \qquad \text{[Eq. 27]}$$

where the subscripts n and e denote nuclear and electronic collisions, respectively.

Nuclear collisions can involve large discrete energy losses and significant angular deflection of the trajectory of the ion (Figure 2.5). This process is responsible for the production of lattice disorder by the displacement of atoms from their positions in the lattice. Electronic collisions involve much smaller energy losses per collision, negligible deflection of the ion trajectory, and negligible lattice disorder. The relative importance of the two energy-loss mechanisms changes rapidly with the energy E and atomic number Z_1 of the particle: nuclear stopping predominates for low E and high Z_1,

whereas electronic stopping takes over for high E and low Z_1. Typical units for the energy loss rate are electron-volt per nanometer or kilo-electron-volt per micrometer.

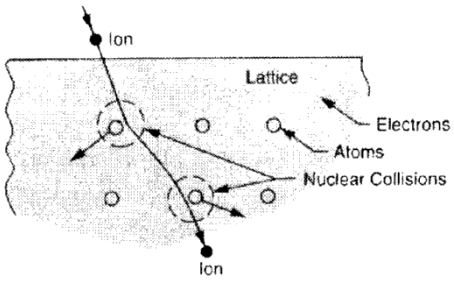

Figure 2.5: An ion incident on a crystal lattice is deflected in nuclear collisions with the lattice atoms, and also loses energy in collisions with electrons [(37)].

Bohr suggested that energetic ions would lose electrons whose orbital velocities were less than the ion velocity. Based on the Thomas-Fermi picture of the atom, Bohr suggested that the ion charge fraction, or the effective ion charge, should be given by:

$$\frac{Z^*}{Z} = \left(\frac{v_1}{v_0 Z_1^{2/3}} \right) \qquad \text{[Eq. 28]}$$

where Z is the total number of electrons which would surround the ion in its ground state (i.e. the atomic number), Z^* is the charge on the ion, v_1 is the ion velocity, and v_0 is the Bohr velocity of an electron in the innermost orbit of a hydrogen atom ($v_0 \approx 2.2 \cdot 10^8$ cm/s). The difference, Z-Z^*, is the number of electrons remaining on the ion. From the last equation, we have two extreme states for an energetic ion:

c

which implies that $Z^*/Z < 1$ and that the ion is not fully stripped, and

$$v > v_0 Z_1^{2/3}$$

implying that $Z^*/Z > 1$ and that the ion is fully stripped to a bare nucleus. Experimentally, it has been found that the ion charge fraction for heavy ions, i.e., $Z > Z_{He}$, more closely follows the form [(37)]:

$$\frac{Z^*}{Z} = 1 - \exp[-0{,}92 v_1 / (v_0 Z_1^{2/3})] \qquad \text{[Eq. 29]}$$

which expands approximately to the Bohr relation given in Eq. 17.

We have introduced the concepts of range and range distribution, and their associated quantities. To proceed, we must be able to calculate quantities for range, projected range, and projected range straggling. In range theory, the range distribution is regarded as a transport problem describing the slowing down of energetic ions in

matter. Two general methods for obtaining range quantities, one using simulations and the other employing analytical methods, have been developed over the years. In the next paragraph, we will focus on the simulation approach that will be used in my research (paragraph 5.1.1). The analytical method, instead, won't be discussed because it would go beyond the purpose of the thesis.

2.2 SRIM and TRIM simulations

Stopping and Range of Ions in Matter (SRIM)[38] is a group of computer programs which calculate interaction of ions with matter, the core of SRIM is the program: Transport of ions in matter (TRIM). The programs were developed by James F. Ziegler and Jochen P. Biersack around 1983 and are being continuously upgraded with the major changes occurring approximately every five years. SRIM is based on a Monte Carlo simulation method, namely the binary collision approximation with a random selection of the impact parameter of the next colliding ion. As the input parameters, it needs the ion type and energy (in the range 10 eV-2 GeV) and the material of one or several target layers.

TRIM was developed to determine ion range and damage distributions as well as angular and energy distributions of backscattered and transmitted ions. The program provides high computer efficiency while still maintaining accuracy. TRIM gives the amount of nuclear energy deposited in the primary collisions and recoil events.

TRIM gives the amount of nuclear energy deposited in the primary collisions and recoil events. Figure 2.6a shows a single trajectory (dashed line) of a 600 keV Kr ion (M = 84 amu) into NiAl. The subcascades generated by recoiling lattice atoms are distributed along the path of the Kr ion. Subsequent ion irradiation leads to the overlap of the ion trajectories and to the development of a more uniform distribution of subcascade damage.

Fig. 8.2(b) shows the number of target-atom displacements per ion per nanometer along the ion track. This result is a statistical value averaged over 7573 ion histories. The mean range of the Kr is 270 nm, and the peak in the displacement distribution occurs at a shallowed depth, about 180 nm. The integrated area under the curve gives the total number of displacements produced by one incident ion. Displaced target atoms will remain displaced when the collisional energy is sufficient to move the target atom far enough away from its lattice site to prevent spontaneous athermal recombination with its vacancy. Recombination of point defects can also occur during subsequent irradiation when damage regions overlap. This latter form of recombination is not typically considered in calculations such as TRIM, and as a result the information presented in Fig. 8.2(b) simply yields the number of lattice atoms which have

experienced displacement without reference to their final location. Therefore, the actual number of displaced atoms remaining in the lattice will be smaller than the calculated value. The term displacements per atom is based on calculations and is used as a relative measure of how much lattice damage has been imparted to the target for a given irradiation dose. The value indicates the statistical average of the fractional number of lattice atoms which have experienced a lattice displacement. If, for example, the calculated dpa for a given irradiation dose is 0.1 then, on average, 10% of the target atoms experienced displacement during the irradiation.

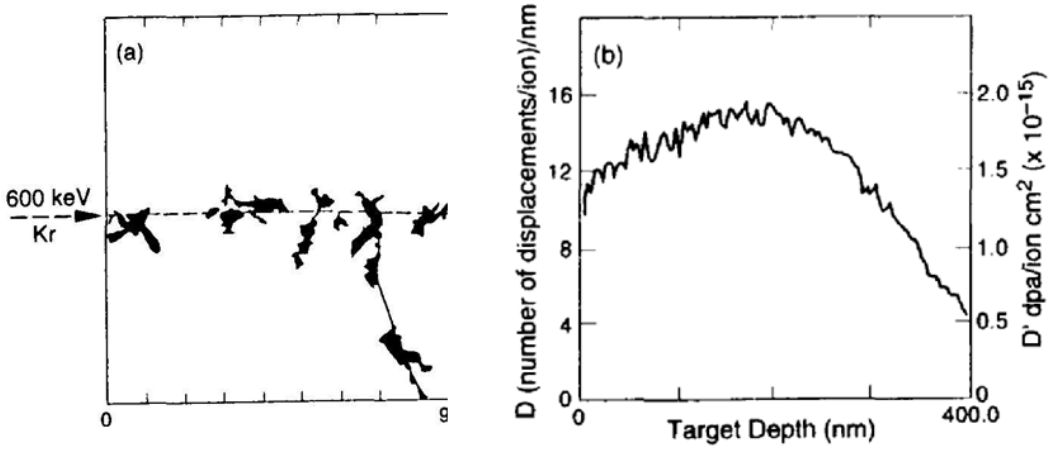

Figure 2.6: TRIM calculations for 600 keV Kr ions (7573 events) penetrating into NiAl with a range of 272 nm. (a) Subcascades (shaded) formed along the first 90 nm of the ion track. (b) The total number of target displacements per ion per nanometer (left axis), and in units dpa/ion cm^2 on the right axis [37].

In Fig. 8.2(b), the left-hand vertical axis, labeled *D,* is the number of dpa which occur in the equiatomic alloy NiAl at a given depth per incident Kr ion. For an irradiation with 600 keV Kr, there will be approximately ten atomic displacements per ion per nanometer at the NiAl surface. This value is converted into dpa per dose, *D',* on the right-hand scale, assuming a NiAl density $N = 8.37 \cdot 10^{22}$ atoms/cm. Then, an irradiation with, for example, 10^{14} Kr atoms/cm^2, gives a total surface dpa of 0.12. The conversions are:

$$dpa = D\left(\frac{10^7\, nm}{cm}\right)\left(\frac{dose(ions/cm^2)}{N(atoms/cm^3)}\right) \qquad \text{[Eq. 30]}$$

$$D = \frac{displacements/ion}{nm} = \frac{dpaN(atoms/cm^3)}{10^7\, nm/cm} \qquad \text{[Eq. 31]}$$

where the dose is given in ions per centimeter squared. The unit dpa is dimensionless and

$$D' \equiv \frac{dpa}{dose} = \frac{10^8 D}{N} \qquad \text{[Eq. 32]}$$

where N is the atomic density.

2.3 Ion beam-Polymer interactions

Despite the fact that ion beam techniques have been successfully applied to polymers to produce marked modifications of surface-sensitive mechanical properties, as well as other physical and chemical properties, the physical, chemical and structural alternations occurring during ion beam processing are still far from that being understood [39]. Consequently, the potential of ion beam surface modification of polymers cannot be fully realized without an in-depth understanding of the mechanisms underlying such property changes. High-energy ion bombardment (irradiation) can modify the structure, composition and properties of surface material in two ways: through the introduction of ion species (doping or chemical effect) and through irradiation-induced defects (radiation or defect effect). However, the defect effect is more important in surface modification for polymers than for metals and ceramics, and may mask any doping effect. This is because:

1- the ‘‘doping’’ effect is an ‘‘end-of-track’’ phenomenon and the implanted ion concentrations are generally very low, while the radiation effect operates throughout the whole range of ion track and produces a high yield;

2- the bond breakage of organic molecules results in the formation of an ensemble of smaller molecules, increasing the molecular weight, hardness and wear many of which may be volatile;

3- the ability to anneal out damage during the implantation becomes progressively worse in the order of metals, inorganic insulators and polymers.

In short, ion beam irradiation leads to irreversible changes in polymers, and hence it is important to understand the damage mechanisms in polymers. Essentially, radiation affects materials by the deposition of high-density energy. Energetic ions are slowed down in materials by momentum transfer to target atoms (*nuclear stopping*), and by exciting the electronic system of the target (*electronic stopping*)[39].

The displacement of target atoms by energetic collisions can cause permanent damage in a polymer mainly in the form of chain scission by displacing atoms from polymer chains (Figure 2.7a). If a bond that makes up part of the backbone of the molecule (such as C–C) breaks, this main chain scission results in degradation, with

products of a lower average molecular weight. Alternatively, the electronic excitation or removal of valence electrons (ionization) can result in the formation of free radicals that may readily cross-link the polymer chains (Figure 2.7b), thereby increasing the molecular weight, hardness and wear resistance [40]. Continued cross-linking causes the surface region to become a three-dimensional network, which becomes an infusible and insoluble gel [41]. It is worth noting, however, that incomplete reaction of free radicals may drastically increase chemical reactivity and thus promote detrimental oxidation, which leads to embrittlement of the polymer surface and thereby susceptibility to abrasive wear and fatigue wear [40].

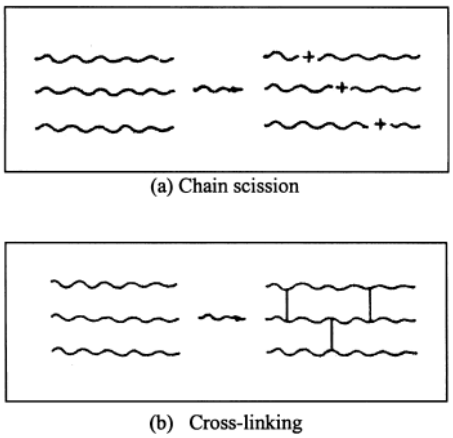

Figure 2.7 Schematic of random scission and cross-linking [40] .

In general, the random chain scissions (*nuclear stopping*) and cross-linking (*electronic stopping*) usually coexist, but one of these two events may prevail for a given polymer. Accordingly, polymers be divided into two groups, those in which cross-linking predominates (group I) and those in which chain scission is predominant (group II) [39].

The interaction of high energy ions with polymeric chains is different with respect to other ionizing radiations (as γ-rays, electrons, etc.) basically for two main factors: the high value of energy loss and the different spatial distribution of deposited energy. The energy loss for energetic ions ranges between 1 and 100 eV/nm, much higher than the one of γ-ray or electrons. This energy is transferred in a very short time ($\sim 10^{-13}$ s) to the electrons of the polymeric chains, within a small volume forming the ion track: the energy density is high and it can reach values of the order of 100 eV/atom [41].

The track size depends primarily on the ion velocity; it is determined by the secondary electrons (δray) that are generated along the primary ion track. For energetic

secondary electrons (~100 eV) the travelled distance is about 5 nm. Typical ion track radius (i.e. the region where is deposited most of the ion energy) is of the order of 10 nm for a 1.0 MeV/amu ion and of 50 nm for a 50 MeV/amu ion. The electronic energy deposition produces some intermediate species (as radicals), which may recombine themselves and react with the polymeric chains. Because the reactions involve molecular groups of the same ion track, the average distance of ionization events inside the track can be an important parameter for the final modifications. For photons or electrons this distance is high and only primary and linear effects are observed. In the case of ion irradiation, due to the high value of energy loss, this distance is very small (0.1-1 nm) and then reactions between different subionization events may occur producing non linear effects.

A general parameter to describe the effects of an ionizing radiation in a polymeric target is the chemical yield, G = number of events produced per 100 eV of adsorbed energy. In Table 2.1 are reported the chemical yield of crosslinks (G_{CL}) and scission (G_{SC}) for different polymers irradiated with ions and electrons (or γ-ray) [41]. The G values depend on the type of polymer and of irradiation. The dependence on the polymer species is due to the different chemical structure of each target. In all cases, the chemical yield for ion beams is higher than for electrons and γ-rays. This difference can be explained by considering that high energy loss particles (as ions) produce a high concentration of excited species and reactions between excited intermediates occur. For lightly ionizing radiations (electrons, γ-rays) reactions occur only between an excited molecule and a ground state one.

The effects of ion irradiation on polymers may be classified in a general way according to three characteristic fluence (or dose) ranges, in which different types of modifications occur. Moreover due to the different values of energy loss S_e = dE/dx (eV/cm), a more general parameter to follow these effects is the energy density $D_e = \phi S_e$ (eV/cm^3), given by the product of the ion fluence (ϕ = ions/cm^2) and energy loss.

Polymer	**Ion irradiation**		**Electrons or γ-rays**	
	G_{CL}	**G_{SC}**	**G_{CL}**	**G_{SC}**
PMMA	0,1	1,2	0,04	0,03
PS	0,07-0,55	0,01	0,04	0
PE	1,4	0	1,2	0

Table 2.1: Chemical yield of crosslinks (G_{CL}) and scission (G_{SC}) for ion and electron or γ-rays in different polymers [41].

At low energy density (~10^{23} eV/cm^3), new bonds (crosslinks) or chain scissions formation occurs in the polymer, inducing modifications in its solubility and molecular weight distribution. In addition, changes in the transport properties and in the polymer morphology are observed. Unsaturation is created and desorption of simple molecules occurs. In this energy density regime, the overlap between different tracks is almost negligible.

By increasing the energy density (~10^{24} eV/cm^3), the continuous bond rearrangement induces a complete change of the polymer molecular structure. The obtained material is a chemical system, characterized by new functional groups, different backbone and electronic structure and different physical properties. Formation and emission of new molecular species change the polymer composition.

At higher energy density (~10^{25} eV/cm^3) the complete overlap between the ion tracks produces a stable material whose properties are similar to that of hydrogenated amorphous carbon, in terms of optical absorbance, electrical properties, hardness and chemical inertness. Generally, at high energy density the polymer target loses memory of its original structure and stoichiometry.

2.4 Effects of ion implantation on polymers

Ion implantation, which is a surface modification technique, has become a common tool to modify the surface properties of polymer films to enhance their electrical, mechanical, wettable, optical, and magnetic properties through the interaction between energetic ions and atoms or electrons of polymer. Less common is the literature of ion implantation on small molecules organic semiconductors. Ion implantation onto organic polymers gives rise to a wide range of properties which are both technologically interesting and demanding. The reorganization of the polymer backbone at high ion dose following the polymer degradation induces modification in the pristine polymer properties. These properties are illustrated by several researchers and most of them were found also in our work with Pentacene thin films (chapter 5), granting the possibility to extend these properties of the polymers also to other organic composites as molecular semiconductors.

Compared with other modification methods, ion implantation technique has some unique advantages:

- Ion implantation could import any element, which is in the form of ion, into most of the polymer materials to obtain new-type polymer materials;
- Ion implantation process is a low temperature process in the vacuum, so the surface morphology of polymer materials or polymer devices could be hardly changed by ion implantation;

- Ion implantation is a faster doping method and has a superior controllability of doping depth to other chemical methods since the energy and dose of implanted ion could be selected freely.

The first structural change due to ion implantation, observed with FTIR and XPS measurements, is a carbonification of the superficial part of a polymer film. This effect is caused by the destruction of the C-H bonds, due to implantation, and to the new reorganization of the superficial bonds, sometimes, as a consequence, with expulsion of the volatile species, i.e. with a dehydrogenation of the layer [42][43][44][45][46][37]. Tretinnikov[42] found that the Polyethylene (PE) film irradiated with 100 keV of Ar^+ ions (HEIB: High-Energy Ion Beams) generate chemical changes extended to a depth of 1.4 μm from the outermost film surface and produce two distinct layers. The first outermost layer has a thickness of the order of 10 nm and, presumably, is composed of a graphite-like material. In this layer, ca. 75% of the carbon atoms are combined by graphitic sp^2 and diamond-like sp^3 bonds, and the remaining 25% have chemical links with oxygen atoms. Spectroscopic data suggest that the sp^2-bonded carbon segregates in graphite-like clusters which contain imbedded oxygen atoms and are interconnected by the sp^3-bonded carbon. The second subsurface layer results from PE oxidation after ion-beam treatment and is characterized by high contents of O-H and C=O groups, as well as ester and double bonds. Then the chemical composition is uniform and does not vary over the layer thickness of ca. 1.4 μm.

Actually, a recent theoretical study, performed with molecular dynamics simulation of the normal bombardment of bulk Polyethylene and Pentacene crystals, with 100 eV Ar^+ ions, was carried on by Yermolenko [47]. The model makes use of a many-body potential for hydrocarbons with description of covalent bonds. These simulations give as a result that, after ion implantation, a huge sputter of atomic Hydrogen is observed for both the samples but the Pentacene target is carbonized much more intensively than the Polyethylene target.

The carbonification effect is probably responsible of other effects: this three-dimensional crosslinking provided by sp^3 atoms may account for example for the high hardness, high density and microwear resistance observed for the carbon layer [42][48][44][49][45][50]. In the work of Tretinnikov [42], cited before, the nanoindentation measurements (see Figure 2.8) show that the hardness of the film increases till 25 times more than the non-implanted sample only in the superficial part (~100 nm).

It was observed that polymers turn opaque or change color as a result of ion beam induced carbonization at high doses [44][49][50].

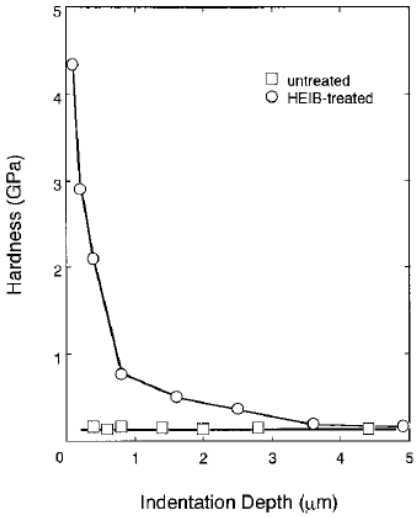

Figure 2.8: Dynamic microhardness of the untreated and HEIB-treated PE films as a function of indentation depth [(42)].

Probably the most interesting property observed on polymers after ion implantation is a huge increase of the conductivity of the material [(44)(51)(46)(52)(37)(45)]. The effect is related to the ion species, the ion dose and the beam energy. As the work of Li [(51)] proves, the increase of ion energy could increase the surface conductivity more effectively than that of ion dose (see Figure 2.9). The tests carried on by several researchers with different types of ions show that the conductivity increases from about 7-8 orders of magnitude for low energies (~50 keV)[(51)(49)], 14 orders for higher energies (~100 keV) [(44)(53)] up to 17 orders (2 MeV)(45). Thus, by ion implantation the organic materials can pass from insulators to real metal-like materials.

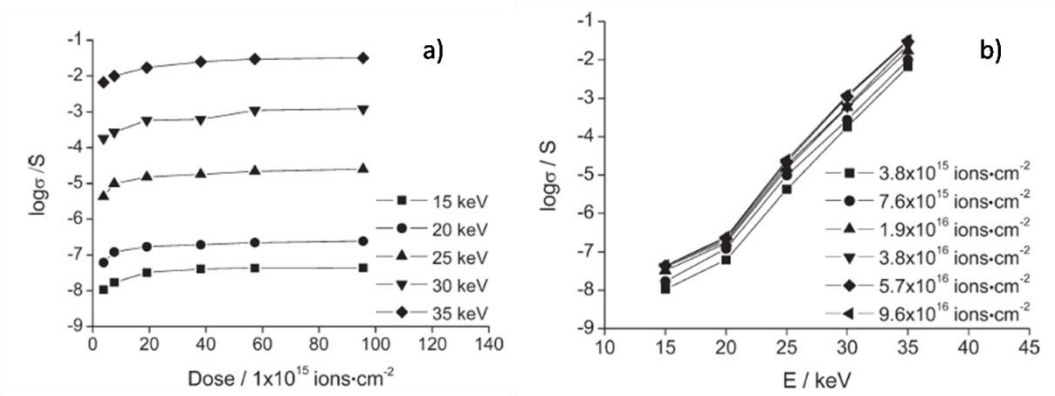

Figure 2.9: Effects a) of ion dose and b) of beam energy on surface conductivity of MMB-PPV film implanted with N^+ ions [(51)].

The explanation of this effect is still debated, one possible reason of the increased surface conductivity after ion implantation might be that the chemical bond

breaking of the organic material such as C-H bond breaking occurred during ion implantation and the localized polaron states in the HOMO band of the polymer produced to increase the carrier mobility resulting in the enhancement of the surface conductivity [51][42]. In Brock experiments with F^+ ions, implanted on PET films at 50-75 keV, this effect has a threshold dose (10^{14} ions/cm^2) upon which the conductivity increases. The presence of a threshold has been taken as evidence that structural disruptions rather than chemical changes are responsible for the enhanced conductivity [49].

Venkatesan [45], that studied Ar^+ implantation on PVC with 10^{17} ions/cm^2 at energy beam 2 MeV, reported the formation of amorphous, carbonaceous (sp^3 hybridized) as well as graphitic (sp^2 hybridized) materials depending on the implanted ion mass and ion energy. High energy ion beams tend to favour the formation of graphite-like phases (sp^2 hybridization of carbon) in contrast to deposition techniques assisted by low energy beams which produce mostly diamond-like phases (sp^3 hybridization of carbon)[52]. The enhanced conductivity through the charge carrier hopping conduction was explained in terms of formation of carbonaceous clusters, formed in the carbon-rich matrix described before. The presence of the latter was reported using neutron diffraction technique for mylar bombarded with 50 MeV B^+ [54] and Raman spectroscopy for polystyrene irradiated with 240 keV Ar^+ [55]. Fink [56] showed the onset of formation of carbonaceous clusters to be dependent on the energy density deposited in irradiated polymers as revealed by UV-VIS spectrometry, similar to that for the onset of induction of polymeric conductivity. These results are supported also by the experiments of Das [44] with N^+ ion implantation at 100 keV on PPO films.

Conductivity measurements repeated after one week and one month showed no significant changes [49][53]. Thus the enhanced stability of the ion-implanted polymers, appears stable to ambient conditions, a definite advantage over chemical doping.

Another effect presented by both organic and inorganic materials is the amorphous transition resulting after the ion implantation. Talking about polymers, the irradiation of polymeric chains with high energy (10 keV/amu-1.0 MeV/amu) ions gives rise to a complexity of phenomena related to the high value of energy deposited by the ion beams into electronic excitation and/or ionization processes. Typical ion-chain interaction involves crosslinks and scissions formation, which deeply affects the macromolecular structure. The molecular weight distribution of polystyrene suffers a continuous change with ion fluence until the sol-gel transition occurs. A statistical gel-theory allows to correlate these changes to the number of crosslinks per chains produced by ion irradiation [41]. Moreover the modifications in the chemical and morphological properties can be explained on the basis of the gel formation. In semicrystalline polymer the crosslinks formation is responsible of the change in the crystallite morphology: the lamellar structure is damaged up to a complete amorphization of the material. In polystyrene the production of excited and ionized species produces crosslinks

modifying the molecular weight distribution and the solubility of the polymer. In semicrystalline polymers, the formation of crosslinks and the subsequent bond rearrangement change the morphology of the target, which is transformed to a more disordered state up to a complete amorphization. The dependence of all these processes on the energy density is not the same for the different ions, showing that this parameter is not the only relevant factor in the polymer modifications. However, the efficiency of these processes (as chemical yield of crosslinks, damage efficiency in semicrystalline polymers, etc.) is lower for high energy ions than for low energy ions. These results have been explained in terms of the difference in the spatial distribution of energy deposition, which is more localized for a low energy ion. It has been shown that the chemical yield of crosslinks in polystyrene and the damage efficiency in semicrystalline polymers increases with the local energy density inside the ion track (D_e) and reaches a saturation at high D_e, values. These results indicated that the microscopic effects of an high energy ion in a polymer target cannot be explained by the energy loss and by the energy density of the ion, however, the local energy density, which is provided by the radial energy distribution, has to be taken in account. The effects induced in a polymer target at low irradiation dose seem to depend mainly on this parameter [41].

As regards the optical absorption, the common trend observed after ion implantation on polymers is that the optical absorption starts to increase gradually and quite linearly from higher wavelengths and also there is a decrease, up to a complete disappearance, of the first absorption peak as the dose increases. Li [51] absorption measurements on N^+ implanted MMB-PPV films as a function of the ion dose is shown in Figure 2.10. There is a broad optical absorption band in the range of 450–550 nm assigned to $\pi-\pi^*$ transition of p-conjugated structure in the spectrum of pristine film. After ion implantation, the UV-Visible absorption spectra exhibited that the optical absorption was raised gradually in the visible region followed by a red shift of optical absorption threshold with the increase of ion dose, while the absorption maximum (λ_{max}) at 499 nm was decreased relatively compared with the raised optical absorption. The λ_{max} disappeared completely when the ion dose was increased to $5.7 \cdot 10^{16}$ ions/cm^2. Ion implantation could cause the chemical bond breaking of MMB-PPV to form a lot of active free radicals in molecular chain and produce new nonconjugated molecular structure in MMB-PPV through the further interaction between the active free radicals, resulting in the destruction of original π-conjugated structure of MMB-PPV and the decrease of the absorption maximum at 499 nm. Moreover, the raised optical absorption in the visible region could be due to the production of defect levels in the band gap as a result of N^+ ion implantation effect.

UV-Vis absorption spectra of MMB-PPV films implanted by N^+ ion with the energy ranging from 15 to 35 keV at a dose of $5.7 \cdot 10^{16}$ ions/cm^2 are shown in Figure 2.11. It indicates that the variation of ion energy had less significant influence on the UV-Vis absorption of MMB-PPV film than that of ion dose [51].

The optical band gap, obtained by the absorption spectra, decreases rapidly with the increase of ion energy and dose. The decrease in optical band gap is an indication of enhancement in electrical conductivity. Das[44] attributes the progressive decrease in optical band gap to be associated with $\pi-\pi^*$ transitions of the carbon enriched graphite-like clusters as a function of increasing ion dose.

Despite the fact that numerous mechanisms for the observed wear of polymers have been suggested, including adhesive wear, abrasive wear, fatigue wear, delamination wear, brittle fracture wear, penetration wear, erosion wear and cavitation wear, adhesive wear, abrasive wear and fatigue wear have been identified as the basic wear mechanisms [39].

It should be pointed out that practical wear mechanisms frequently operate sequentially or even simultaneously. Although it is difficult to separate the individual contributions of the basic wear mechanisms quantitatively, it is known that wear resistance of polymers would be significantly improved if the abrasion and adhesion action could be addressed successfully. This is largely because the rate of fatigue wear is usually much lower than that of either adhesive wear or abrasive wear. Clearly, ion beam modifications have great potential in improving tribological behaviour of polymers through shifting the dominant wear mechanism from abrasive or adhesive wear to fatigue wear. This could be done by means of irradiation-induced cross-linking and chemical functionalization of the surface topography [39]:

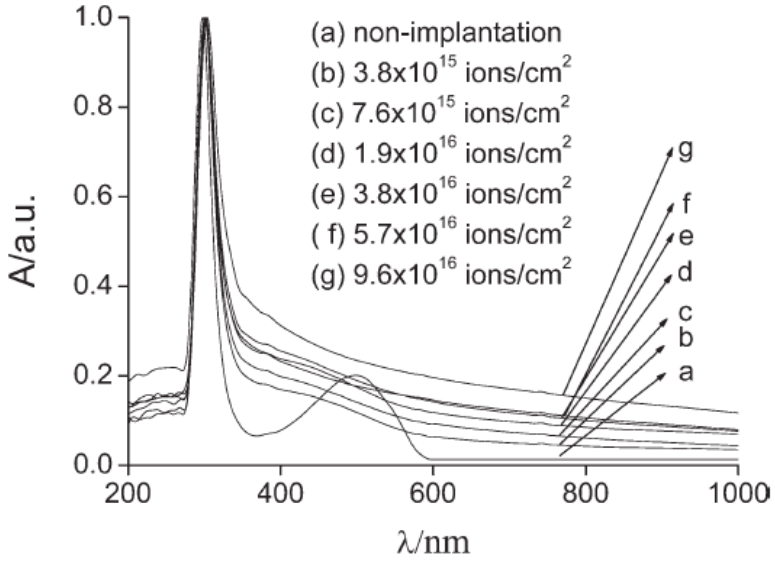

Figure 2.10: UV-Vis absorption spectra of MMB-PPV films implanted by N^+ ion with ion dose ranging from 0 to 9.6 ·10^{16} ions/cm^2 with an energy of 30 keV[51].

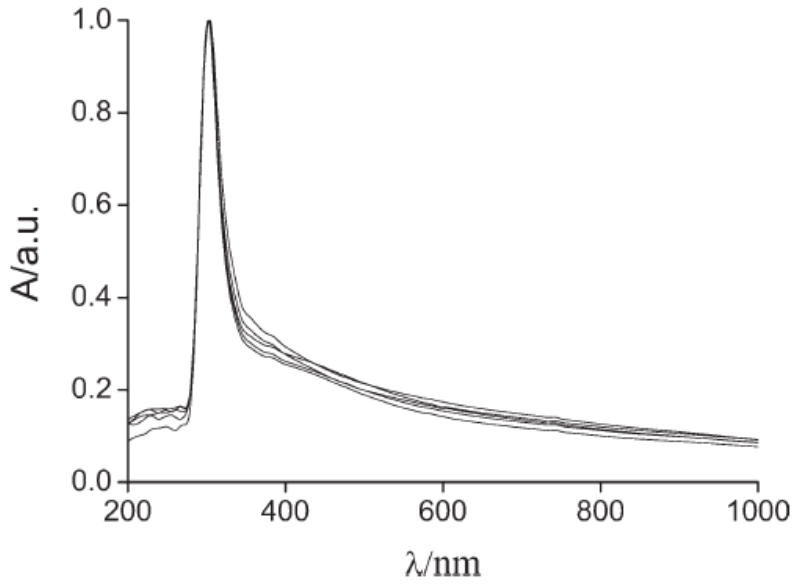

Figure 2.11: UV-Vis spectra of MMB-PPV films implanted by N^+ ion with ion energy ranging from 15 to 35 keV at a dose of $5.7 \cdot 10^{16}$ ions/cm^{2}[51].

Irradiation induced cross-linking can increase surface hardness (H) as well as stiffness (E), which would enhance abrasive wear resistance of polymers.

1. Cross-linked polymer usually exhibit a much lower E/H ratio than that of the pristine, which would limit plastic deformation and promote elastic deformation, thus conferring high adhesive resistance to ion beam modified polymeric surfaces.
2. Irradiation induced chemical functionalization or changes in surface topography can effectively enhance wettability of polymers, which would improve lubrication conditions between contact surfaces, thus leading to high adhesive wear resistance.

Therefore, a significantly improved tribological compatibility of the ion beam modified polymeric surfaces is expected.

2.5 Applications on organic materials

Ion implantation provides a mechanism for radically modifying the electronic and transport properties of a variety of polymers that are normally insulating. By using masks and tailoring the implanted species and ion energies, conducting paths in an insulating medium can be fabricated between specific reference points, an application of obvious relevance to the microelectronics industry. Specific results are reported for

modification of the structure, electrical conductivity, thermoelectric-power, optical transmission and electron spin resonance for several polymers under a variety of implantation conditions [57].

Actually polymer doping has not been fully successful yet, because of the considerable radiation damage accompanying ion implantation, which is a severe limitation for electronic transport. Thermal treatments, generally performed to recover the original order and to realize the chemical effects of impurities in semiconductors, cannot be applied in this case because organic films are instable at high temperatures.

As regards the application in the microlithography field, the ion beam lithography has two main features, i.e. the high resolution and sensibility. The resolution is intrinsically higher compared with the one of the electrons because the ion scattering is much lower and they produce secondary electrons of very low energy, reducing to a value of ~0.1 μm the spreading of exposure features in a polymeric resist. The sensibility of a polymer to ion irradiation is very high and with respect to electrons differs by several orders of magnitude [41].

A big improvement of the performance of devices as the OFETs could be reached with a passivation superficial layer, obtained by ion implantation, to avoid instability due to the atmospheric agents and leaving a not implanted organic material at the interface with the dielectric. My research intends to study and investigate the potential of ion implantation for this application and the results will be reported in chapter 6.

Another important feature that has important applicability is the improvement of the adhesion to the substrate. The adhesion performance of thin deposited films is of critical importance in many technological applications. These applications include metal/ceramic and metal/polymer structures for semiconductor packaging and contact fabrication, optical coatings on glass, and protective coatings on metals. In many such cases, film and substrate have no bulk chemical affinity. An interesting application regards the inkjet printed organic transistors or the organic electrochemical transistors (OECT), that will be discussed in chapter 7, for them it's important to obtain a good wettability and a good adhesion at the substrate as the organic semiconductor starts as a liquid drop that solidificate on the substrate and it's even in contact with a liquid electrolyte in the second case. However, strong and stable adhesion has been obtained by means of ion beam treatment to tailor the interface atomic structures for the purpose [58].

2.6 Plasma Source Ion Implantation

A fundamental limitation to more widespread use of ion implantation for large-area, high-dose applications is the time, expense, and complexity associated with conventional line-of-sight, accelerator-based techniques. For example, more than 56 hours are required to perform a $5 \cdot 10^{17}$ ions/cm^2 dose implant over a 5 m^2 surface with a 10 mA N_2 ion accelerator system. Amortized capital and ancillary equipment costs are of the order of one million US dollars [37]. Manipulation of large, complicated workpieces could be awkward. Plasma source ion implantation (also called plasma immersion ion implantation or plasma ion implantation) has the potential of overcoming these limitations by producing a high dose of ions in a simple, fast, efficient, and cost-effective manner.

The plasma source ion implantation (PSII) process is illustrated in Figure 2.12. A negative high-voltage pulse is applied to a workpiece which is immersed in a plasma. Plasma ions are accelerated by the electrical potential and are implanted into the surface of the workpiece. PSII offers several improvements over conventional techniques. Particle accelerators are eliminated; and PSII is a non-line-of-sight process, enabling conformal implantation, i.e., ions are accelerated from all directions simultaneously into all exposed surfaces of the workpiece. Consequently, cumbersome workpiece manipulation fixtures and beam rastering are unnecessary. System efficiencies can be improved since the perpendicular trajectories into the workpiece eliminate the need for masking. Implant times are short when compared with beam-line techniques since high-current, pulsed-power supplies compatible with this process can provide two-orders-of-magnitude higher average currents than conventional accelerators. Since large areas can be implanted concurrently, ion current densities to the workpiece can be kept low to avoid overheating problems sometimes encountered in beam-line implants [37].

PSII is an intrinsically pulsed process. The evolution of the plasma during the applied voltage pulse is depicted in Figure 2.13a. In a very short time after application of the voltage, typically several nanoseconds, plasma electrons are repelled away from a layer near the surface of the workpiece, uncovering plasma ions. This electron motion is a displacement current that charges a plasma capacitance. During this phase (Figure 2.13b), the ions remain essentially motionless because of their larger inertia. This initial uniform ion layer is called the ion matrix sheath. Just enough electrons are displaced so that the electrical potential at the outer edge of the sheath is near zero. The ion matrix sheath thickness, increases with applied voltage, V, and decreases with plasma density, n. For planar geometry, s_0 may be derived by integrating Gauss's law to obtain:

$$s_0 = (2\varepsilon_0 V/en)^{1/2} \qquad \text{[Eq. 33]}$$

where $\varepsilon_0 = 8.9 \cdot 10^{-12}$ F/m is the electric permittivity of free space, and $e = 1.6 \cdot 10^{-19}$ C is the elemental charge constant. For example, for a 100 kV applied voltage and 10^{10} cm^3 plasma density, the ion matrix sheath dimension will be 33 mm. On a longer time scale, usually several microseconds, plasma ions are accelerated across the sheath by the electrical potential and are driven into the workpiece surface. The characteristic transit time, τ_{tr} for ions to cross the sheath is estimated by integrating the ion equation of motion:

$$\tau_{tr} = 2(\varepsilon_0 M/ne^2)^{1/2} \quad \text{[Eq. 34]}$$

where M is the ion mass. This equation may be rewritten as $\tau_{tr} = 2/\omega_{pi}$, where $\omega_{pi} = (ne^2/\varepsilon_0 M)^{1/2}$ is the characteristic response frequency of ions to electrostatic perturbations in a plasma. After a few ion transit times (Figure 2.13c), quasi-steady ion current flow is established with space charge limited current density, j, across the sheath governed by the Child-Langmuir equation. For planar geometry, this equation is:

$$j_1(t) = (4\varepsilon_0/9)(2e/M)^{1/2}[V^{3/2}(s(t))^2] \quad \text{[Eq. 35]}$$

where s(t) is the time-dependent sheath thickness, which evolves as:

$$s(t) = so[(2/3)\omega_{pi}t + 1]^{1/3} \quad \text{[Eq. 36]}$$

As ions are implanted, charge imbalance repels more electrons away from the workpiece, thereby forcing the sheath to expand outward from the workpiece to uncover more ions (Figure 2.13d).

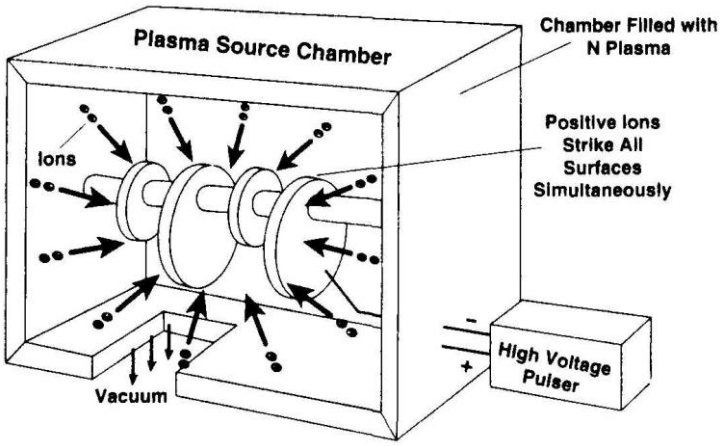

Figure 2.12: Schematic of the plasma source ion implantation (PSII) process [37].

The pulse length and the plasma ion density are usually adjusted so that the sheath remains contained inside the vacuum chamber, and the plasma load impedance matches the power supply. Typical pulse lengths last between 1 and 40 μs. Plasma densities are kept relatively low, usually varying between 10^8 and 10^{11} cm^{-3}. Between pulses, ions must be replenished near the workpiece by either diffusion or ionization,

since the workpiece, in effect, behaves like an ion pump. The plasma constitutes a small fraction of the background fill gas density, n_0, which is introduced into the evacuated processing chamber. Fill gas pressures, p_0 are kept low so that the ions will avoid collisional energy losses as they are accelerated across the sheath.

Development of adequate ion sources is required for large-scale Implementation of PSII [37]. Gaseous discharges with either thermionic, radiofrequency, or microwave ionization sources have been successfully used to produce ions. The production of large-scale, uniform, mass-separated plasmas is usually prohibitive. Consequently, PSII often produces a broadened implant profile due to the varied stopping ranges of the assorted ion masses that are usually present. For example, with typical N plasmas, the atomic ions implant deeper than the molecular ions. Non-gaseous sources, such as vacuum arc discharges, appear promising, although large, high-current steady-state sources must still be developed for a practical PSII system.

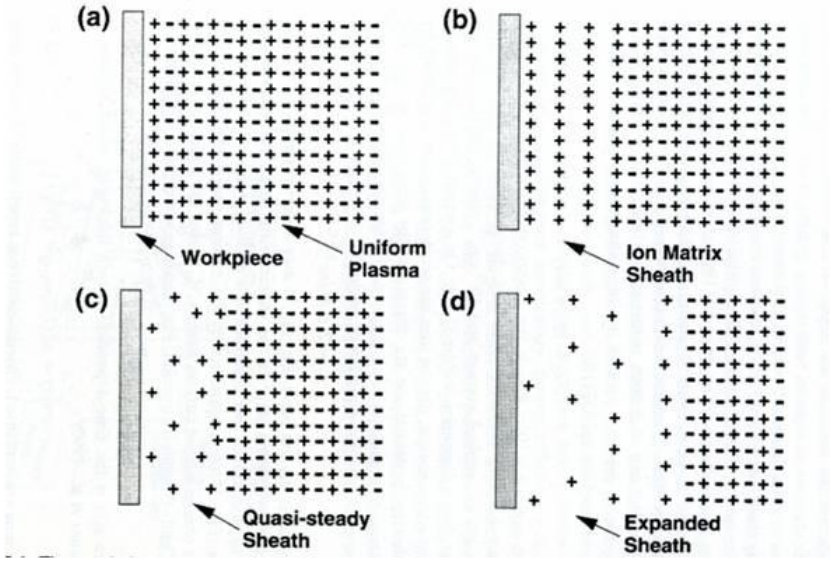

Figure 2.13: Time evolution of the plasma sheath during the PSII pulse: a) t=0, initial conditions; b) t ~ 5ns, repulsion of electrons near the workpiece to form the ion matrix; c) t ~ 1μs, quasi-steady, space charge limited ion flow across sheath; d) t ~ 10 μs, space charge limited flow in the expanding sheath [37].

3 Photocurrent spectroscopy

3.1 Theory

Photoconductivity is an important property of semiconductors by means of which the bulk conductivity of the sample changes due to incident light radiation (IR-Visible-UV). This property has been used advantageously in several branches of science and technology. Photoconduction, as the name suggests, comes from the generation and recombination of charge carriers and their transport to the electrodes. Obviously, the thermal carrier relaxation process, charge carrier statistics, effects of electrodes, and several mechanisms of recombination are involved in photoconduction. Above all, every mechanism mentioned here is a complicated one, and therefore photoconductivity in general is a very complex process. For interpretation purposes, complementary information from other experimental techniques is always needed, for example I will compare the data with optical absorption spectra. Detection of weak photosignals needs a careful selection of several parameters. It is necessary to know the change in the resistance of the sample caused by the incident radiation, the impedance of the measuring circuit, the response time, the capabilities and limitations of the photodetector, and sources of noise with their magnitudes. In spite of the complexity of the photoconductance process, Photocurrent Spectroscopy provides useful and valuable information about physical properties of materials and offers applications in photodetection and radiation measurements.

The basic principle involved in photoconductivity for semiconductors is can be stated in a very simple way. When photons of energy greater than that of the band gap of the semiconductor are incident upon a photoconductive material, electrons and holes are created in the conduction and valence bands, respectively, increasing the conductivity of the sample. But this statement is only partially true. In a doped semiconductor, for example, the photon of slightly less energy than that of the band gap is absorbed by the impurity atom and a free electron is created in the conduction band. In this case, photoresponse starts from the low-energy side of the band gap and photoconduction occurs due to excitation near the band edge. This is a general case and not an exception. It is also possible to observe photoconductivity when the energy of the incident photon is much smaller than that of the band gap. When the energy of the incident photons matches the ionization energy of the impurity atoms, they are ionized, creating extra electrons in the conduction band, and hence an increase in conductivity is observed. This phenomenon is called extrinsic photoconductivity and lies in the far-infrared region.

As regards photoconductivity in organic semiconductors, we have to consider that mobile charge carrier creation may take place not only by interband optical transitions across the higher occupied molecular orbit (HOMO) to lower unoccupied molecular orbit (LUMO) but also by extrinsic processes. These ones involve creation by light of *excitons* which may dissociate into mobile charge carriers. However, the nature of the *excitons* as well as the charge separation remain unclear and various optical spectroscopic studies have been dedicated to shine light on this issue. The spectral response of the photocurrent can be employed to study the energy distribution of the excited states of organic semiconductors, the charge carrier creation mechanism, and the identification of the optical transitions. It should be noted that, since in an organic molecule several anti-bonding orbitals are present (LUMO representing the lowest one), the absorption of radiation with energy higher than the bandgap corresponds to transitions between higher energy levels for an organic semiconductor.

A typical photocurrent spectra is obtained measuring the voltage drop across a load resistor used in series with a battery and the semiconductor, due to the change of conductivity of the last one in presence of a certain wavelength of light focused on it. The current that flows in this circuit is named *photocurrent*. The conductivity of a semiconductor in darkness condition can be expressed as function of electron end holes concentration, indicated with n_0 and p_0 respectively, as follows:

$$\sigma = e\left(n\mu_n + p\mu_p\right) \qquad \text{[Eq. 37]}$$

where e is the electronic charge and $\mu_{n/p}$ is the electrons/holes mobility. When the material is exposed to an electromagnetic radiation with an appropriate energy, the absorption of a photon results in the generation of an electron-hole pair and thus in an increase of the conductivity:

$$\sigma + \Delta\sigma = e\left[\left(n + \Delta n\right)\mu_n + \left(p + \Delta p\right)\mu_p\right] \qquad \text{[Eq. 38]}$$

Consequently, the current density $J = \sigma E$, where E is the electrical field applied, increases to the value:

$$J = \left(\sigma + \Delta\sigma\right)E = J_{bulk} + J_{ph} \qquad \text{[Eq. 39]}$$

Through the measurement of the variation of J in the sample is therefore possible to detect the light absorption by the material. Indeed, when a photon is absorbed by an organic semiconductor the formation of an electron-hole pair is not so easy as for inorganic materials. The main difference between organic semiconductors and inorganic semiconductors as photovoltaic materials is that optical excitations of organic semiconductors create bound electron-hole pairs (the already mentioned *excitons*) that are not effectively split by the electric field. To separate the bound electrons and holes, there must be a driving force to overcome the *exciton*-binding energy, typically 0.1–0.4 eV. *Excitons* in organic semiconductors that are not split eventually recombine either radiatively or non-radiatively, for example, reducing the quantum efficiency of a solar cell. In inorganic semiconductors the attraction between an electron-hole pair is less

than the thermal energy kT. Therefore, no additional driving force is required to generate separated carriers. Research has shown that *excitons* in organic semiconductors can be efficiently split at a heterojunction of two materials with dissimilar electron affinities or ionization potentials [59]. Also, once generated, the electron-hole pair has an average life time τ, at the end of which the charge carriers are not more available for conduction. τ is affected above all by recombination processes due to the presence of trap levels in the forbidden gap. The recombination processes can decrease until a critical value, under which no photocurrent signal can be detected. Also, traps can bond charge carrier only for a certain time but also in this case the macroscopic effect will be a decrease in the detectable photocurrent due to charge trapping. If the electron (or hole) falls into such a trap, it is, for a finite average time interval, no longer free and its probability of recombination with a carrier of opposite sign is greatly increased. However there is also a finite probability that the carrier may escape from the trap. Both of these probabilities depend on the energy level of the trap and the mean energy of the carrier. Traps are usually associated with crystal imperfections, dislocations, grain boundaries, and the surface of the material, as such, which allow the excess momentum of the electron hole pairs to be transferred to the lattice. The lifetime τ of a carrier may thus be written:

$$\tau = \frac{1}{vsn} \qquad \text{[Eq. 40]}$$

where v is the velocity of the charge carrier; s is the collision cross section of the trap, determined by its energy and called the *capture cross section*; and n is the concentration of the traps.
The photocurrent I_{ph} in a photoconductor is:

$$I_{ph} = \frac{eF\tau}{T_r} \qquad \text{[Eq. 41]}$$

where e is the electronic charge and F is the number of carriers photoelectrically excited into the conduction band per second and moving with a mobility μ, in a given specimen which has an electrode spacing d and to which a voltage V is applied. The *transit time* T_r is defined as:

$$T_r = \frac{d^2}{V\mu} \qquad \text{[Eq. 42]}$$

In Figure 3.1, a simple diagram of the photocurrent measure is shown. Let R_d and R_{i11} be the resistance of the sample in the dark and under uniform illumination conditions, respectively. The change in resistivity is linear with the intensity of illumination.

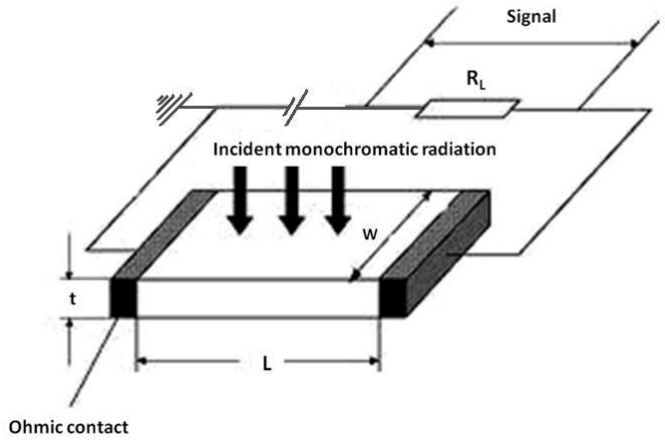

Figure 3.1: Schematic picture of the circuit for photocurrent measures.

Photocurrent is generally measured across a load resistance R_L introduced in the biasing circuit. Photovoltage across the resistance R_L can be calculated very easily by evaluating the difference between the voltages with and without radiation. When no radiation is incident on the sample, voltage is given by:

$$V_d = \frac{R_L V}{R_L + R_D} \qquad \text{[Eq. 43]}$$

Similarly, the voltage for an illuminated sample is given by:

$$V_{ill} = \frac{R_L V}{R_L + R_{ill}} \qquad \text{[Eq. 44]}$$

where V is the applied voltage. The difference between them is the signal response, which is given by:

$$S = R_L V\left(\frac{1}{R_L + R_{ill}} - \frac{1}{R_L + R_d}\right) = R_L V\left(\frac{\Delta R}{(R_L + R_{ill})(R_L + R_d)}\right) \qquad \text{[Eq. 45]}$$

where $\Delta R = R_d - R_{ill}$.

In the laboratory, one generally handles the values of the resistance in the dark, load resistance, matching impedance, and variation of conductance of the sample due to radiation, and therefore it is necessary to convert Eq. 45 to make all these terms visible. Conductance G (in ohms) is defined as the reciprocal of the resistance, and therefore G, the difference in the conductance caused by the radiation, is given by:

$$\Delta G = \frac{1}{R_{ill}} - \frac{1}{R_d} \qquad \text{[Eq. 46]}$$

Therefore,

$$\Delta R = \Delta G R_d R_{ill} \qquad \text{[Eq. 47]}$$

And hence Eq. 45 becomes:

$$S = \frac{V R_L R_d R_{ill} \Delta G}{(R_L + R_{ill})(R_L + R_d)} \qquad \text{[Eq. 48]}$$

Here we have assumed that the sample is illuminated uniformly, so that the variation in the conductance is uniform in the plane on which the radiation is incident. However, absorption cannot be uniform in the direction perpendicular to the plane, as the number of photons absorbed varies according to Lambert's law of absorption:

$$I(x) = I_0 \exp(-\alpha x) \qquad \text{[Eq. 49]}$$

where I_0 is the number of incident photons, α is the absorption coefficient, and x is the distance measured from the surface. Thus, the amount of radiation absorbed at each thin layer is different, and therefore the conductance is different. The total variation can be obtained by integrating over entire thickness of the sample:

$$\Delta G = \frac{W}{L} \int_0^{thickness} \Delta\sigma(x) dx \qquad \text{[Eq. 50]}$$

which can be estimated, as all the necessary parameters are known. Let us consider two limiting cases [60]:

1. Variation in the resistance with and without radiation is very small compared to the dark resistance R_d, that is, $R_d \approx R_{ill}$. Eq. 48 becomes:

$$S = \frac{V R_L {R_d}^2 \Delta G}{(R_L + R_{ill})^2} \qquad \text{[Eq. 51]}$$

of a given photoconductor except load resistance R_L. To a detector user, it is the only parameter that can be controlled to obtain the maximum photoresponse. The value of R_L that gives maximum response can be obtained by using $dS/dR_L = 0$ and is found to be $R_L = R_d$. This is the reason experimentalists use the load resistance equal to the dark resistance of the sample when the photosignal is weak.

2. In the case of high-resistivity material the dark current is low, which makes it very easy to measure photocurrent (or voltage) without any need to optimize the load resistance. On the contrary, if $R_L \ll R_d$, then the response time increases as a consequence of the circuit time constant ($RC = \tau$). As $R_L \ll R_d$, Eq. 48 can be written as:

$$S = V R_L \Delta G \qquad \text{[Eq. 52]}$$

As organic semiconductors are characterized by high resistivity I will use this last set up condition. Because of this, the response of the signal is very slow, as the impurity atom creates defect states, which may act as recombination centres. The recombination process reduces the lifetime of the charge carriers in the conduction or valence band, and therefore the intensity of the response is reduced. In addition, the traps retain electrons far a considerable time and hence the response becomes slow (seconds or even a few minutes).

As already said, to check the reliability of the photocurrent spectra to investigate the DOS of the organic semiconductors it's useful to correlate the data with optical absorption measures. For many organic semiconductors, the relationship between the photocurrent and absorption spectra can be classified as either symbatic or antibatic. If the maximum photocurrent coincides with the strongest photon absorption, the photocurrent response is said to be symbatic with the absorption spectrum. If the maximum of the photocurrent spectrum occurs at photon energy where absorption is weakest, i.e., the photocurrent and absorption are almost complementary, the photocurrent response is said to be antibatic.

In organic semiconductors, the absorption of photons in the visible range creates *excitons* rather than free carriers. In order to generate photocurrents, these *excitons* must dissociate into free carriers at the metal-organic interface due to surface enhancement (not in the bulk, which is often the case in inorganic or doped organic materials). So the *excitons* reach the metal-organic interface by diffusion and dissociate into free carriers there. Thus great importance is given to the geometry of the sample and the interfaces, as some researchers confirm studying the change of trend from symbatic to antibatic response due to the non homogeneous disposition of the contacts in the sample in reference to the incident light [(61)].

A crucial factor in the photocurrent generation process is the fraction of the photon flux F(x) penetrating the films. F(x) strongly depends on the light absorption (α) and the film thickness d. Figure 3.2[(62)] presents the profile of the variation of the relative photon flux, $F(x)/F_0$, as a function of the distance, x, from the top illuminated surface of a film, as is calculated from $F(x) = F_0\exp(-\alpha x)$ for different photon energies of the incident illumination. As it can be seen from Figure 3.2, the illumination of the higher photon energies, corresponding to low α values, is largely transmitted in the first part of the film and partially absorbed near the interface with the dielectric. By contrast, for lower photon energies, corresponding to the maxima of the absorption spectra (α), a strong light absorption takes place near the illuminated front surface of the organic semiconductor films whereas only a few photons are absorbed near the dielectric interface. Thus relatively few photons with low energy penetrate deeply in the bulk region of the thick films. Gorgolis[(62)] found that the antibatic response is observed in thick films of Pentacene ($d \geq 300$ nm) where the photocurrent is generated mainly by the photons absorbed near the surface, so the major contribute is not given by the dissociation of the excitons at the interface with the dielectric. This is not observed instead for thin films where the response is symbatic (see
Figure 3.3) cause the absorption occurs uniformly in the whole film. So a possible explanation is that in the antibatic behavior, the *excitons* are generated by the low-energy photons near the illuminated surface and difficulty they will interact with the substrate interface, this could be the main difference with the symbatic response that,

instead, arises from carriers generated by the interaction between *excitons* and the Pentacene-insulator interface.

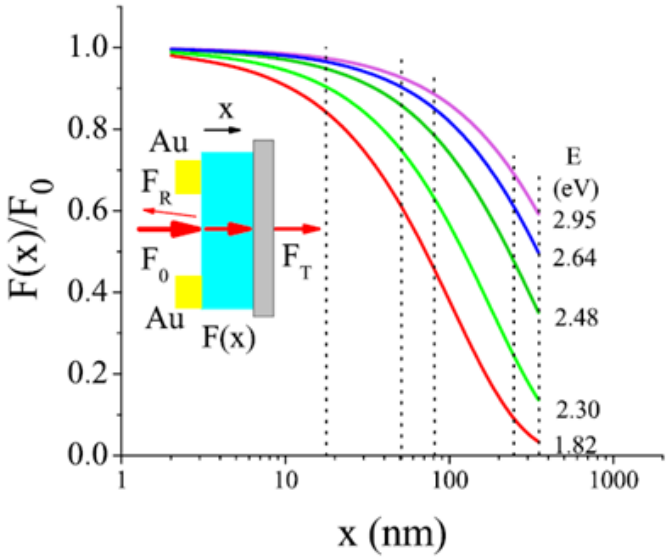

Figure 3.2: Calculated relative magnitude $F(x)/F_0$ of the light flux penetrating in the films as a function of the distance, x, from the top illuminated free surface (see inset) for the indicated photon energies. Vertical dotted lines indicate the position of the substrate of some Pentacene samples of different thicknesses [(62)].

Kotowski[(63)] focused its attention on the different concentration of traps at the substrate-semiconductor interface (H_0) and at the "non-substrate" interface (H_d). He argues that if the photon flux hits the non-substrate surface, the photocurrent is expressed by the following equation:

$$I_{ph} = \underbrace{\left[\frac{N_{eff} n_{t0} e \mu U a b}{L} (\eta \tau_0 \alpha \Phi)^{1-1/l}\right]}_{A} \underbrace{\left[\frac{e^{-\alpha d(1-1/l)}}{H_0} + \frac{1}{H_d}\right]}_{B} \qquad \text{[Eq. 53]}$$

where the term A describes photocurrent as a function of light intensity (Φ) and the absorption coefficient (α) and the term B describes the photocurrent dependence by the exponential of α and the thickness d of the sample[1].

[1] The other parameters are: N_{eff} is the effective density of the states, n_{t0} is the trapped charge carrier concentration, e is the elementary charge carrier, μ is the mobility of the charge carrier, U is the voltage applied to the sample and L is the distance between electrodes, a is the total thickness of the layer which contains the trapped charge carrier and b is the width of the layer in the active region for the charge carrier transport, η is the efficiency of charge carrier detrapping by *excitons*, τ_0 is the life time of *excitons*, and finally l is the parameter describing the energetic distribution of the traps.

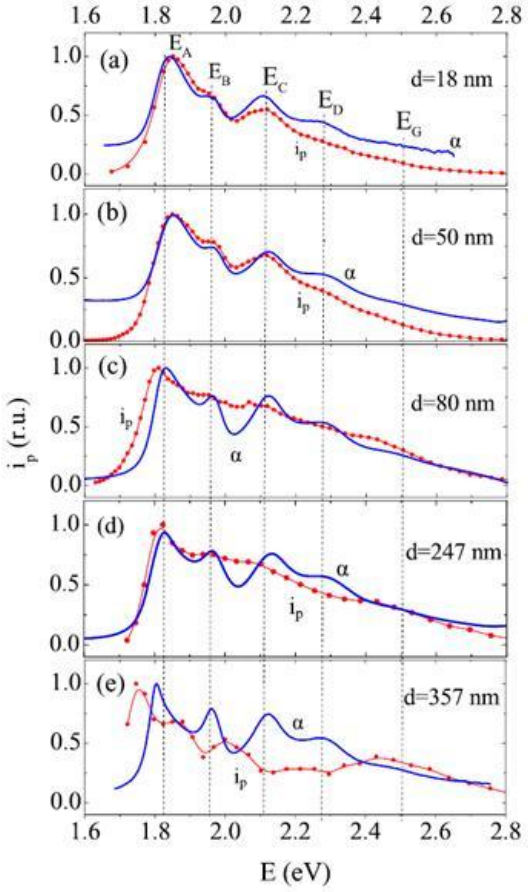

Figure 3.3: As measured photocurrent I_p (solid circles and lines) and optical absorption α (solid lines) spectra normalized to the first maximum around E_A of Pentacene films of d=18 nm in (a), d = 50 nm in (b), d= 80 nm in (c), d= 247 nm in (d) and d= 357 nm in (e) [(62)].

Taking into account traps concentration and analyzing Eq. 53 we can say that, if:

$$\frac{1}{H_d} >> \frac{e^{-\alpha d(1-1/l)}}{H_0} \qquad \text{[Eq. 54]}$$

the photocurrent is directly proportional to the light intensity and absorption coefficient ($I \sim (\Phi\alpha)^{1-1/l}$). This type of relationship is usually called as symbatic. So the symbatic behaviour of the photocurrent is possible when the concentration of traps is much smaller at non-substrate side than that at the substrate side of the sample ($H_d << H_0$).

To assess what type of behavior (symbatic vs antibatic) takes place in the PC analyses carried out in this thesis, I always compared photocurrent and optical absorption spectra confirming that I was always relying on symbatic response.

3.2 Photocurrent apparatus

Photocurrent spectroscopy were carried out in the common mode planar configuration in air and at room temperature. As samples I used OTFTs with the gate contact grounded, in fact photocurrent is a reliable measure that can be done with the right attention on several different devices. Before the measurements I made several tests to calibrate the instrument and optimize the response. The lamp used is a 150 W QTH (Quartz Tungsten Halogen), which has the characteristic of not presenting characteristic peaks of brightness, therefore is not necessary to use filters to eliminate the contribution of certain range of wavelengths. In my research the electromagnetic spectrum investigated starts from 450 nm to 800 nm. The lamp is coupled to a SPEX monochromator and mechanically chopped at low frequency (<20 Hz), then a current amplifier is connected to a digital lock-in amplifier (Stanford Research 850) that collects the signal and sends it to the PC with an on-line data acquisition (see Figure 3.4). The energy resolution is 0.01–2.40 eV. The diffraction grating is rotated by a step-by-step motor connected to a voltage generator. The monochromatic light passes through a slit, whose thickness is varied to search a good sensitivity and a strong signal. As we can see from Figure 3.5 the best choice is to use a slit 2 mm thick. The light beam is focused with a mirror and the collimation is performed manually by varying the distance sample-mirror, maximizing the current signal.

In its final configuration the circuit in which is inserted the transistor is shown in Figure 3.6. As said before, during the PC spectra acquisition, the OTFT gate was grounded, while a bias was applied between the source and drain contacts. The photocurrent signals obtained for three values of load resistance with constant voltage 1 V and 15 V are shown in Figure 3.7. In this case the photocurrent is expressed in Volt because the original signal is a voltage, otherwise to show the signal as a current it must be divided for the load resistance. The R_L is put in parallel with a capacitor of 4 nF, used as a filter for the background noise. Organic semiconductors are characterized by very high resistivity (for my samples $R_{dark} \div 10$ GΩ) so the choice is a compromise between a clean signal (low R_L), as expressed in the chapter before (Eq. 52), and a strong signal (high R_L).

In conclusion, considering these aspects and Figure 3.7, I chose $R_L = 100$ kΩ. To reduce the time constant τ and as a filter for the background noise, I used a capacitor C= 4nF in parallel with the resistor R_L, so that $\tau = 0{,}4$ ms. The bias voltage in the circuit was also varied at constant resistance of 100 kΩ to search for the best signal and the results lead to use low voltages (1,5 V) (see Figure 3.8).

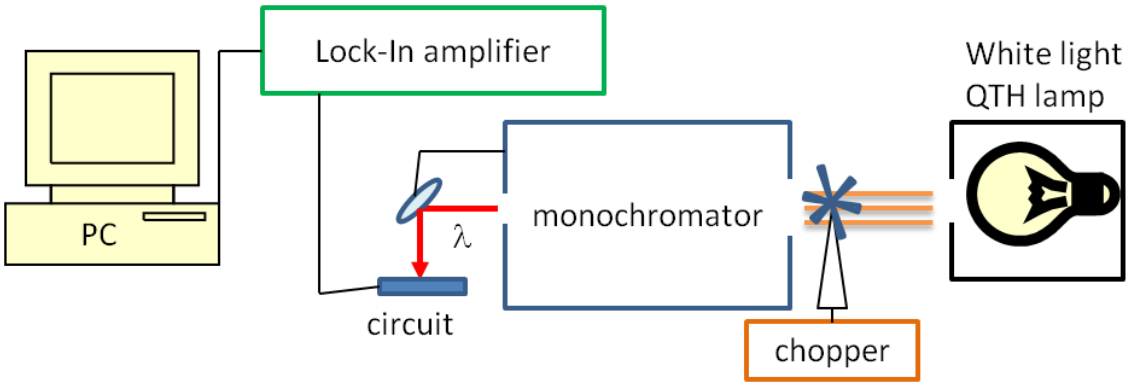

Figure 3.4: Apparatus for photocurrent measures.

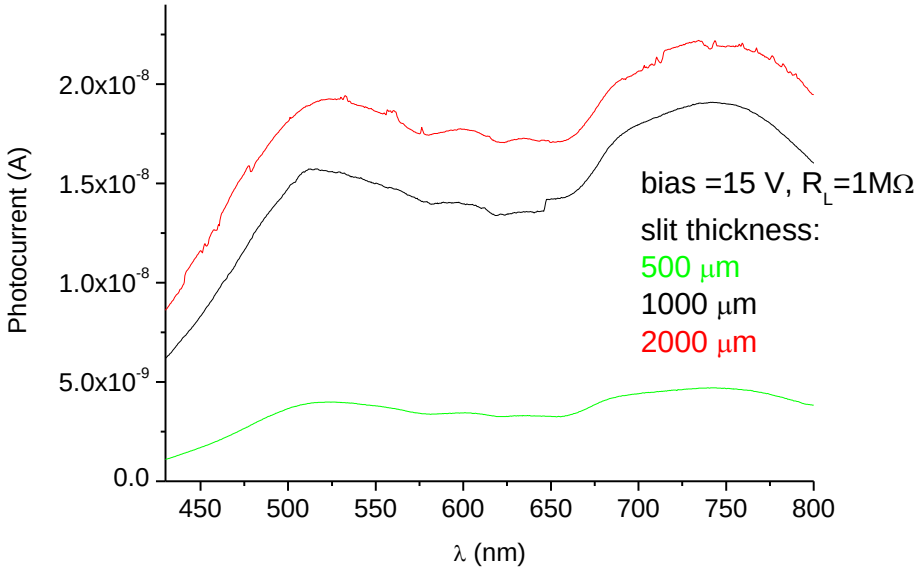

Figure 3.5: Photocurrent measures of a Pentacene OTFT for three different slit thicknesses with V_{SD}=15 V and R_L= 1MΩ..

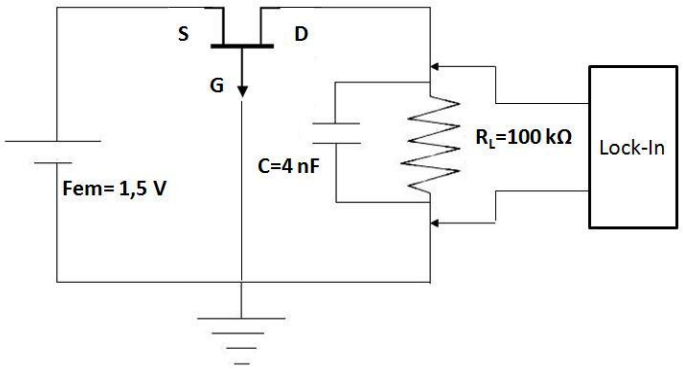

Figure 3.6: Electrical circuit for photocurrent measures.

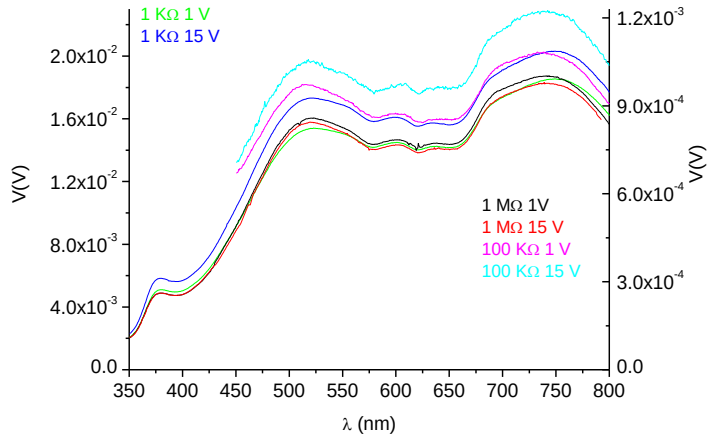

Figure 3.7: Photocurrent spectra (measured as a voltage) of a Pentacene OTFT for different values of load resistances R_L and bias V_{DS}=1V or 15V.

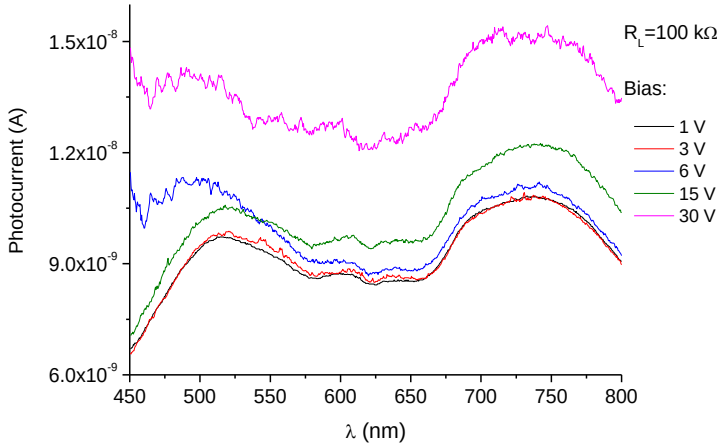

Figure 3.8: Photocurrent measures of a Pentacene OTFT for different values of bias V_{DS} and a constant load resistance R_L= 100 kΩ.

Photocurrent spectra have to be normalized, dividing for the intensity of incident light, as this changes with the wavelength. In Figure 3.9 the light intensity spectra (measured with a thermopile in Volt) as a function of the wavelength is reported for a slit thickness of 2 mm. Thermopile allows to measure the photon flux because it has a flat response in the wavelength range of interest. In Figure 3.10 thus, the photon flux incident on the sample per unit of area and time is shown. PC analyses were carried out under low-injection conditions ($1x10^{20}$ photons/cm^{2}s at λ = 450 nm) and no variations were observed in the PC spectra following exposure to the incident photon beam, as

assessed by comparing consecutively acquired spectra. Photon flux is obtained by the next equation:

$$\Phi = \frac{signal}{rA_{th}h\nu} \qquad \text{[Eq. 55]}$$

where r = 7,8 μV/μW is the thermopile responsivity, A_{th} = 0,0078 cm^2 is the thermopile area and hν is the photon energy.

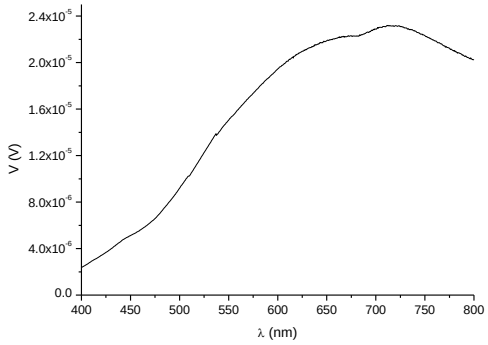

Figure 3.9: Calibration spectra of the light source with a slit width of 2 mm at the output of the monochromator.

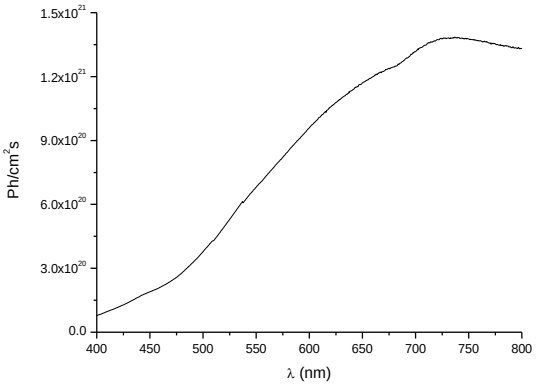

Figure 3.10: Photon flux of the QTH lamp incident to the sample as a function of the wavelength with a slit 2 mm thick.

4 Pentacene OTFTs

4.1 Characterization of Pentacene thin films in OTFTs

4.1.1 Electrical, structural and morphological properties

Pentacene ($C_{22}H_{14}$) has demonstrated the highest hole and electron mobility of organic small molecules. The material exhibits a strong tendency to form highly ordered films which depend on the growth conditions and the substrate. Bulk single crystals are not favorable for low cost electronics, because the fabrication is time consuming and the crystals are small, nevertheless they show higher mobility-e.g. Jurchescu found a extraordinary value of 35 cm^2/Vs [(64)]. Thin films are more favorable, because they can be fabricated on various low cost substrates. The hole mobility of thin film Pentacene is close to the intrinsic transport limit of bulk single crystals, and thin film transistors with mobility of ≥ 1 cm^2/Vs have been fabricated by several groups. Mobility is therefore comparable with that achieved by amorphous silicon TFTs and hence Pentacene TFTs might be considered for large area active matrix arrays.

The electrical parameters, especially the mobility, depends on the morphology and the structural properties of the OTFT. More specifically they are affected by the physical and chemical properties of the dielectric, the temperature and the rate of deposition of the organic film and its thickness. These features can be analyzed by XRD and AFM measures. With X-Ray Diffraction (XRD) we can state the crystalline structure and in particular the distance between the planes of the molecules. With Atomic Force Microscopy (AFM) we can map the topography of a surface discovering the grains size of polycrystalline films of Pentacene.

Before showing the typical XRD spectra, a description of the molecular packing of Pentacene films is necessary. In its crystalline bulk structure this semiconductor forms a triclinic lattice with a characteristic layered structure consisting of (001) planes. Within each layer the molecules are oriented upright and adopt a face-on-edge *herringbone* arrangement which is a common packing motive found in most planar polycyclic hydrocarbons. Related to this molecular structure also a pronounced anisotropy is obtained for the charge carrier mobility which has been attributed to differences in the orbital overlap of neighbored molecules along the various crystallographic directions [(65)]. The three different crystal structures of Pentacene (at 300 K) known are shown in Table 4.1 and in Figure 4.1:

Polymorph/phase	a, b, c (Å)	α, β, γ (°)	d (001)	$2\theta_{XRD}$
Bulk, Campbell [66]	6.06, 7.90, 14.88	96.74, 100.54, 94.20	14.502 Å	6.090°
Bulk, Siegrist [67]	6.27, 7.79, 14.51	76.65, 87.50, 84.61	14.116 Å	6.256°
Thin film [68]	5.60, 7.60, 15.61	81.25, 86.56, 89.80	15.400 Å	5.734°

Table 4.1: Pentacene molecules in the crystal structure [65].

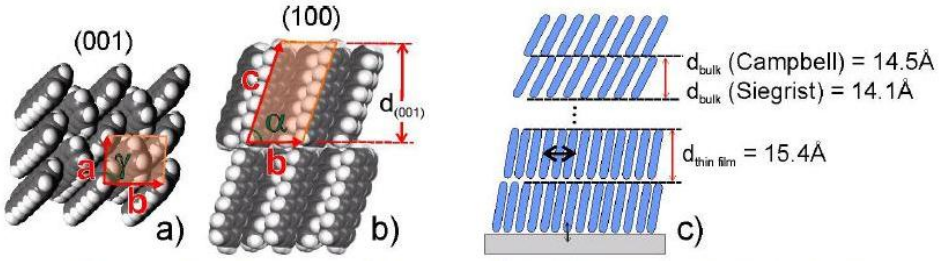

Figure 4.1: Pentacene crystal structure in a) top view and b) side view, schematic illustration of different d(001) spacings.

The charge carrier mobility and the resistivity are also highly anisotropic with the crystal structure directions: μ_a= 0,66 $cm^2V^{-1}s^{-1}$, μ_b = 2,3 $cm^2V^{-1}s^{-1}$ at 300 K, interlayer mobility in c-direction being much lower [69]; ρ_a= $1{,}3\cdot10^6$ Ωcm, ρ_b= $4{,}7\cdot10^5$ Ωcm and ρ_c= $2{,}1\cdot10^8$ Ωcm [64], while for the thin film phase ρ= $4{,}7\cdot10^4$ Ωcm has been found[70].

The numbers in Table 4.1 show that the thin film phase of Pentacene consists of molecules nearly perfectly upright with some empty space in between the layers yielding an overall smaller density. The difference between the two bulk structures is essentially the packing density in the layers: while there is less interlayer penetration for the Siegrist phase it nevertheless has the highest density and therefore must consist of perfectly closest packed molecules inside each layer. This means that in this case the penetration of molecules from the outer part (air agents for example) is more difficult.

My research is based on OTFTs of Pentacene grown on SiO_2, so in Figure 4.2 three groups of reflexes in XRD scans of Pentacene films evaporated on SiO_2 are reported: 5.73/6.09°, 11.46/12.25° and 17.25/18.43°, which can be assigned to the (00i) peaks in the thin film phase and Campbell bulk phase respectively. The corresponding interlayer spacings of 15.41 and 14.48 Å match closely to the d(001) spacings of the two crystal structures (compare Table 4.1).

The observation that both the thin film phase and the Campbell bulk phase are present on SiO_2 at intermediate film thicknesses has been made in numerous studies in

the literature. Thus, more detailed information is reviewed from these studies, revealing 3 stages of Pentacene film growth on SiO_2 [65]:

1- At low temperatures (<259 K) only amorphous films are present on SiO_2, yielding charge carrier mobilities hardly detectable. At 330 K evaporation of up to 50 nm leads to Pentacene in the thin film phase [71]. The thin film phase is also observed on other non-interacting substrates.

2- In the range of 60-80 nm Pentacene film thickness or at SiO_2 substrate temperature of above 335 K, a transition from the thin film phase to the Campbell bulk phase is observed, where both also increase the bulk fraction and overall crystallinity. Also smoother substrates will enhance the crystallinity of deposited Pentacene films on top, as well as more ordered SAMs. The transition interval shifts from 60-80 nm at 300 K to around 25 nm at 340 K, and also depends on the substrate chosen and the evaporation rate, as higher rates cause higher transition temperatures. A lower deposition rate increases the bulk percentage, while higher deposition rates above 150 Å/min fail to yield crystallinity at all, although rates between 150 and 360 Å/min produce the highest charge carrier mobilities. The transition is observed usually at lower temperature/ thicknesses for SAM-covered surfaces like OTS/SiO_2 [72].

3- For thicker films or higher SiO_2 substrate temperatures only the Campbell bulk phase is found [68].

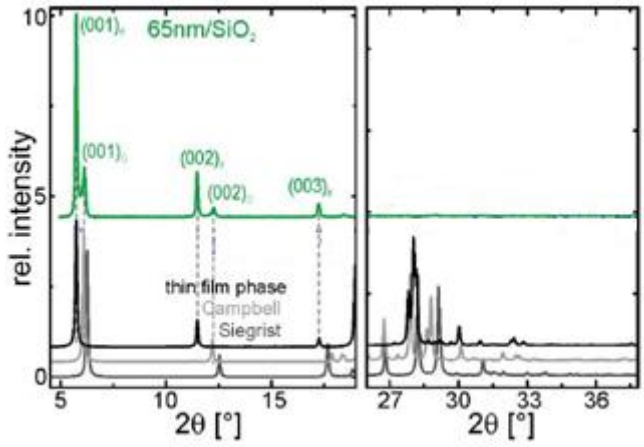

4-

5- *Figure 4.2: XRD patterns of 65 nm Pentacene on SiO_2 (300 K, 20 Å/min), together with the powder patterns of the 3 crystal structures for comparison* [65].

Together with the thin film phase, another parameter that influences the mobility of an OTFT of Pentacene is the grains size and we can measure this with AFM. Larger

grains constitute an ordered texture that make easier the conduction by hopping so the mobility increase (see Figure 4.3).

Several conditions influence the production of an ordered film with large grains. As shown in Figure 4.4 for example, the grains size (in this case of Octithiophene) change considerably with the temperature of the substrate, precisely at 125° C the grains are ~250 nm large and at room temperature the grains are ~50 nm large. In Figure 4.5 the mobility is represented for the two films as a function of the grains size [20]. So we can note that the mobility increases with the grains size, i.e. with the temperature of the substrate. The AFM maps reported in Figure 4.6, instead, show how the grain size of a Pentacene thin film changes considerably with the deposition rate [73].

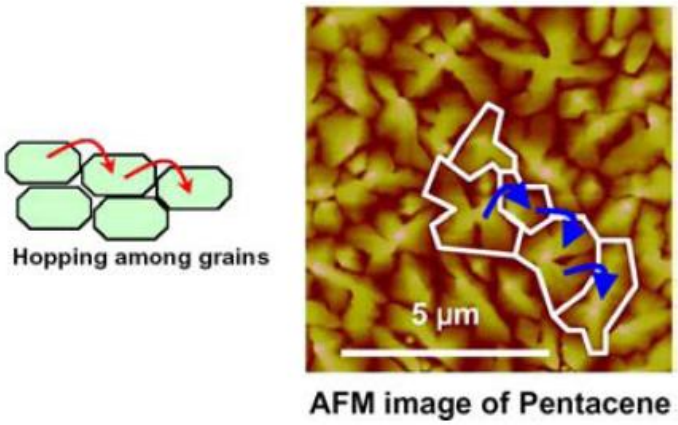

Figure 4.3: Sketch of the hopping of electrons/holes among the grains in a polycristalline film of Pentacene and related AFM image of a Pentacene film.

Material with similar morphology can be grown with different preparation conditions. Knipp [72] did some experiments and stated that at lower substrate temperatures (70 °C) a low deposition rate (0.5 Å/s) is required to grow material with large crystals (≥ 5 µm), whereas for higher substrate temperatures (90 °C) the deposition rate can be increased so large two-dimensional crystals will form. He observed increased surface mobility of the material at higher temperature, which resulted in faster formation of crystals. It's important to notice that the thin film and crystalline phase were both polycrystalline and highly ordered. The structural properties of thin Pentacene films were dominated by the thin film phase of the film. The change of the ratio of the XRD intensities in Figure 4.7 and Figure 4.8 reveals that an increase of the substrate temperature and film thickness results in a change of the volume fraction of the two-phase material. The composition of the two-phase material (thin film

phase and bulk crystalline phase) shifts towards the crystalline phase for higher temperatures.

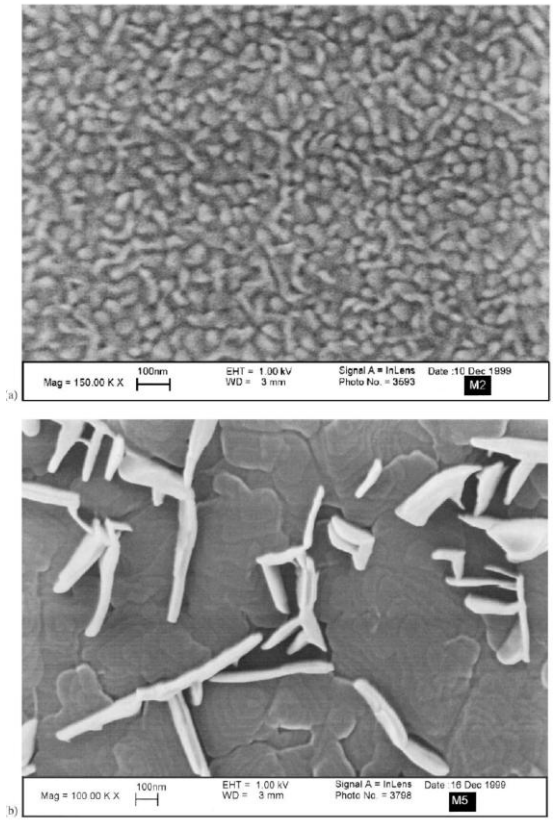

Figure 4.4: Scanning electron micrographs of Octithiophene evaporated films: (a) film deposited on a substrate at room temperature; (b) film deposited on a substrate held at 275°C [(20)].

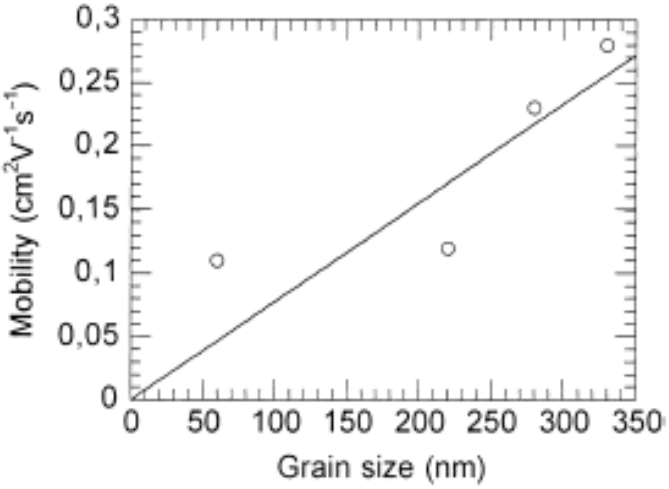

Figure 4.5: Variation of the mobility with grain size in octithiophene. The straight line is a least-square fit of the data to a linear function [(20)].

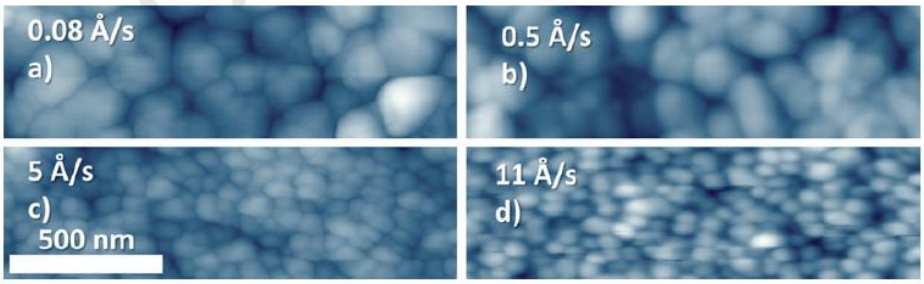

Figure 4.6: AFM maps of Pentacene deposited using different deposition rates, indicated on each image [73].

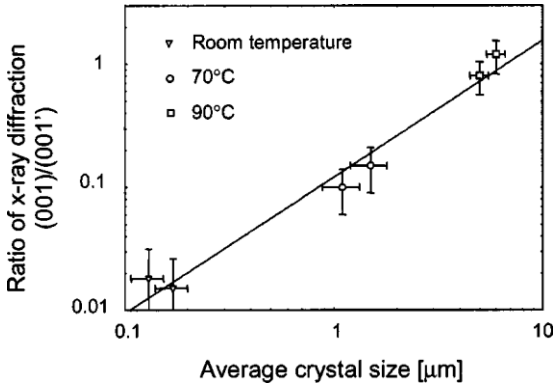

Figure 4.7: Ratio of x-ray diffraction peaks (001)/(001') of thermally evaporated Pentacene films on thermal oxide. The thickness of the film is 200 nm and the substrate temperature was varied from room temperature to 90° C [72].

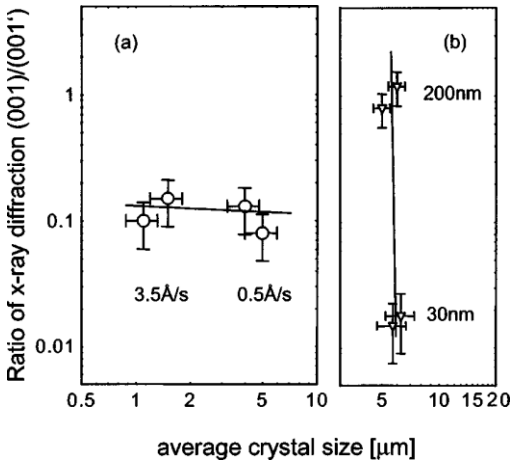

Figure 4.8: Ratio of x-ray diffraction peaks (001)/(001') of thermally evaporated Pentacene films on thermal oxide. (a) Influence of the deposition rate;(b) influence of the layer thickness [72].

Also the material used as the OTFT dielectric affects the morphology of the film, in Figure 4.9 the mobility as a function of the grains size is shown for different substrates [72]. We can see that some materials lead to a better mobility (for example Thermal Oxide) but also the same material treated with a solvent (OTS) can increase appreciably the electrical parameter despite the fact that the grains size is smaller. Thus the substrate properties strongly affect the morphology and the structural properties of Pentacene films not only for the physical properties of the dielectric (roughness) but also for the chemical ones (surface wetting).

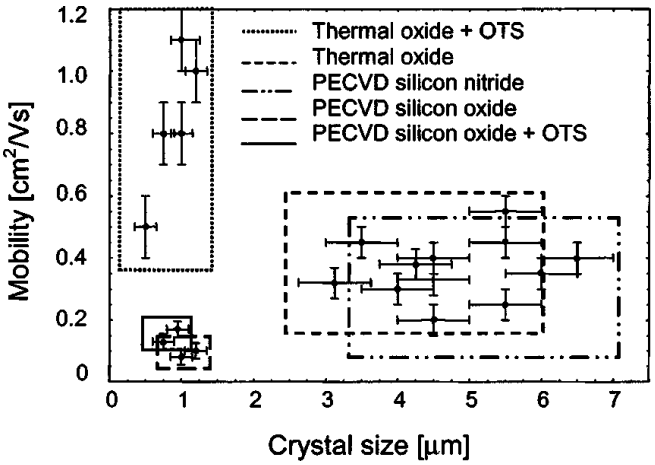

Figure 4.9: Mobility of thermally evaporated Pentacene thin film transistors on different inorganic dielectrics (thermal oxide with and without OTS, PECVD silicon oxide with and without OTS, and PECVD silicon nitride) as a function of the crystal size. The crystal size was determined by AFM measurements [72].

4.1.2 Experimental I: AFM, XRD, IV

After having described some of the features that affect Pentacene OTFTs electrical parameters, in this paragraph I will report the parameters and properties of the OTFTs I have characterized in this research [74]. My research was conducted in collaboration with the University of Cagliari (Department of Electrical and Electronic Engineering) where they fabricated OTFTs with an active Pentacene layer of different thicknesses (from 50 to 300 nm on highly conductive silicon substrate (acting as gate electrode) with a 500 nm thermally grown silicon dioxide layer, which acts as gate insulator. Pentacene appears, at ambient conditions, as a purple powder and it is typically deposited by means of thermal evaporation, since it shows insolubility in most common organic solvents. We used a sublimation temperature of 145° C, with an evaporation rate of about 0.3 Å/min, whereas the pressure in the evaporation *High Vacuum Chamber* was

$5 \cdot 10^{-5}$ torr. All devices have been realized using a bottom contact configuration with gold source and drain electrodes (W= 5 mm, L= 50 μm) as in Figure 4.10. Atomic Force Microscopy (AFM) measurements instead, were carried out in my laboratory in *tapping mode*[2] for a 300 nm thick Pentacene layer, evaporated on quartz slides [(75)]. In Figure 4.11, the 2-dimensional map of a 4.5 μm×4.5 μm area is shown. In the inset is represented the molecular packing (*herringbone*) and the structure of the Pentacene molecule. The map shows the small grains size (~0,1 μm) of the film and this will correspond also to a small mobility of the OTFT compared to the devices of other researchers. The map shown is extremely in good agreement also with the experimental results obtained by Gao for a Pentacene film 200 nm thick reported in Figure 4.12. AFM in *tapping mode*, can also be used to determine the thickness of the layer through a scan on an area crossed by a scratch appositely done to measure the profile of the film. I measured by this technique the thickness of two layers: 300 nm and 50 nm. In Figure 4.13 is shown the profile of the first sample crossed by a scratch: this one is about 25 μm large, and the two lateral barriers are 300 nm thick, as expected. In this figure is also drawn, as a suggestion, a distinction between the thin film phase and the bulk phase. The first phase is located at the interface with the substrate and usually is more or less 50 nm thick. The second phase instead start to dominate after a thickness of 150–200 nm.

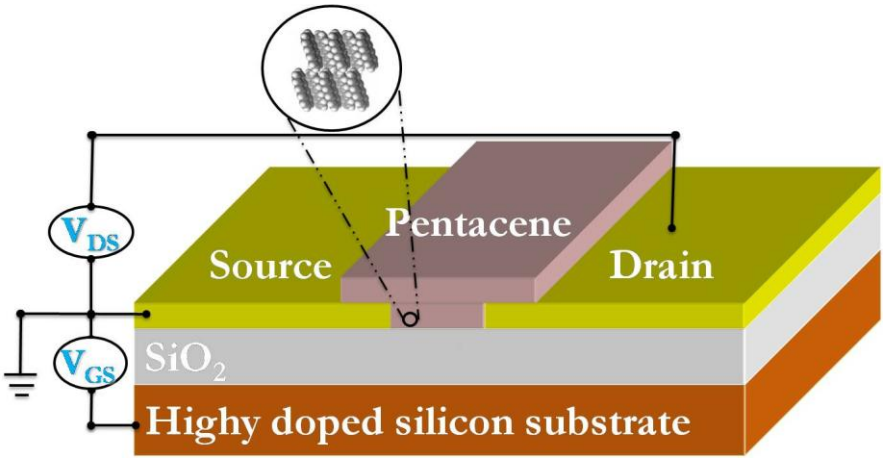

Figure 4.10: Schematic layout of a OTFT device[(74)].

To confirm the real presence of the two phases also XRD measures were carried out at the CNR of Bologna[3]. In Figure 4.14, we can see two patterns of the two Pentacene layers of 50 and 300 nm thick on quarz slides [(75)]. Comparing them with Figure 4.2 (even if there the substrate is SiO_2) we can admit the good match with these

[2] For technical specifications and theoretical description about AFM measurements see paragraph 5.1.6.
[3] For technical specifications and theoretical description of the XRD measurements see paragraph 5.1.5.

data and conclude that in the OTFT with a 50 nm layer thick the thin film phase is predominant, whereas in the 300 nm layer thick the thin film phase is present but the Campbell bulk phase is predominant.

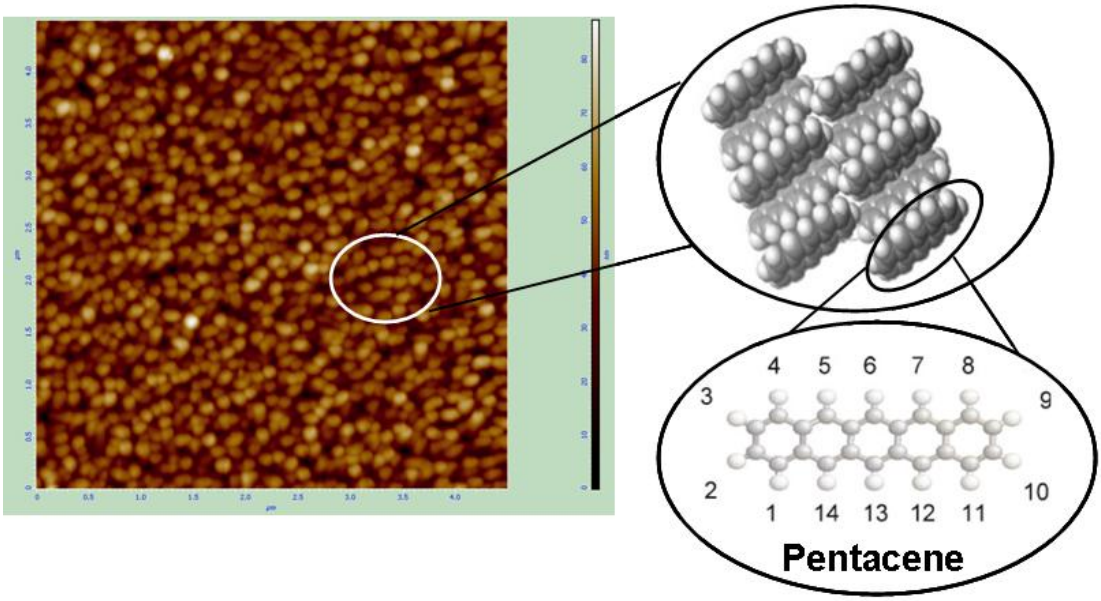

Figure 4.11: AFM map in contact-mode of a small surface (4.5 μm x 4.5 μm) of a Pentacene layer 300 nm thick. In the focus it is shown the typical molecular packing of Pentacene, called herringbone, and finally the structure of the Pentacene molecule ($C_{22}H_{14}$) [75].

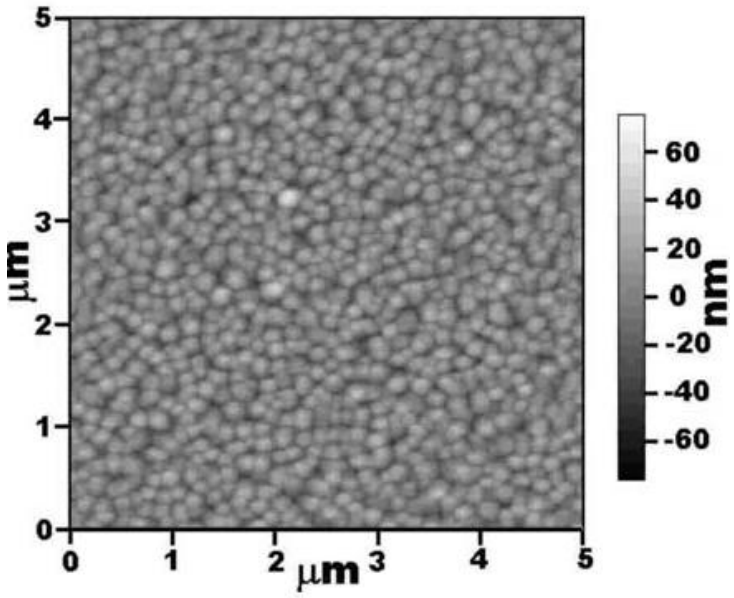

Figure 4.12: AFM map of the topography of a Pentacene layer 200 nm thick [76].

Figure 4.13: Profile of the edges of a scratch in a Pentacene layer 300 nm thick, measured by AFM in contact-mode. The separation in thin film phase and bulk phase is only appended to suggest the proportion of the two parts [75].

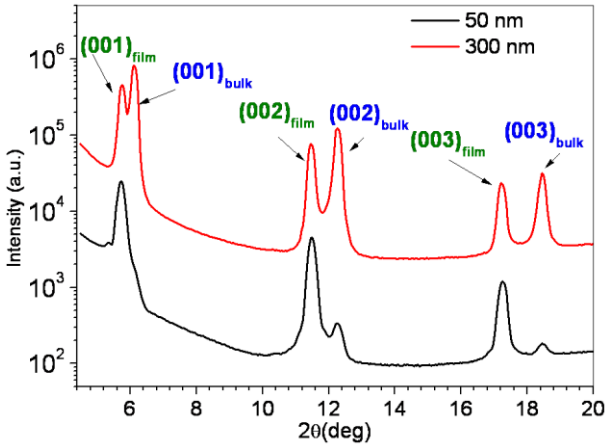

Figure 4.14: XRD patterns of Pentacene layers of 50 and 300 nm deposited on quartz substrates[75].

In Table 4.2 the average electrical parameters of these OTFTs are shown [74]. The I-V measures were carried out in air and at room temperature. As can be noticed, charge mobility and threshold voltage do not seem to be strongly influenced by the active layer thickness, whereas one order of magnitude lower I_{ON}/I_{OFF} has been obtained for thicker Pentacene OTFTs; this effect is usually ascribed to an increment in the I_{OFF} values for thicker layers, correlated with the increase in the bulk conductance of the active layer.

Pentacene thickness (nm)	μ (cm^2/Vs)	V_{TH} (V)	$I_{ON/OFF}$
300	$2 \cdot 10^{-2} \pm 2 \cdot 10^{-3}$	-12 ± 2	10^5
50	$3 \cdot 10^{-2} \pm 3 \cdot 10^{-3}$	-16 ± 2	10^6

Table 4.2: Typical electrical transport parameters of Pentacene OTFTs with different active layer thickness [(74)(75)].

4.1.3 Experimental II: Photocurrent spectroscopy

I have carried out photocurrent spectroscopy analyses on OTFTs with Pentacene layers of different thicknesses (from 50 to 300 nm) with the apparatus described in paragraph 3.2 and typical PC spectra are shown in Figure 4.15(a). The observed evolution in the shape of the PC spectra as a function of the film thickness can be associated to the different structural phases present in the film: in the 50 nm thick one, the "thin-film" phase is supposed to dominate, while in the 300 nm thick one, the "bulk" phase should prevail. Four major bands can be identified in both samples and similar bands have been experimentally observed by optical spectroscopy [(77)(78)], by PC analyses[(79)(80)] and theoretically modeled by *ab initio* calculations [(81)] on the optical properties of different Pentacene polymorphs. They are located at about 1.85, 1.97, 2.12, and 2.26 eV and have been associated to inter- and intramolecular excitons, even if their attribution is still widely debated [(62)(80)(77)(78)(79)]. In order to assess the reliability of PC spectroscopy when applied on working OTFT devices, I have carried out optical absorption spectroscopy on Pentacene thin films of the same thickness (50 to 300 nm, evaporated on quartz slides at the same time of the active layer of the OTFTs' structures). Figure 4.15(b) shows a comparison of an optical absorption and a photocurrent spectrum obtained on a 300 nm thick film. It is evident that PC spectroscopy provides exactly the same information as optical absorption.

We will focus the attention on the first two lower energy peaks in each spectrum, that constitute the first absorption band. It is well known that amorphous Pentacene shows a thickness-independent single optical absorption band at about 1.87 eV. This optical absorption band splits into two peaks for crystalline samples, located at about 1.84 eV and 1.96 eV, respectively. The split has been observed by optical absorption analyses and reported to enhance for layers with thickness growing from 40 to 280 nm, passing from about 0.11 to 0.14 eV (see Figure 4.16)(77)[(78)(62)]. It has been associated to the changes in the internal film structure induced by its growing thickness, i.e., by the shift from the dominant role of the "thin-film" phase to the "bulk" phase. Such splitting was explained as Davydov splitting[(62)(78)] and was confirmed by micro-Raman spectroscopy analyses of Pentacene OTFTs that undergo a structural modification after

a long-term bias stress. Davydov splitting is thought to arise from dipole-dipole interactions of the vibration related dynamic dipole moments of the molecules in the unit cell and is related to the strength of the intermolecular forces. For thick Pentacene films (150 nm) where the bulk phase dominates, the molecular spacing is smaller than in thin films (100 nm), characterized by "thin-film" phase, and the coupling of intermolecular π-electron system becomes more effective, thus enhancing the Davydov splitting of the first absorption band.

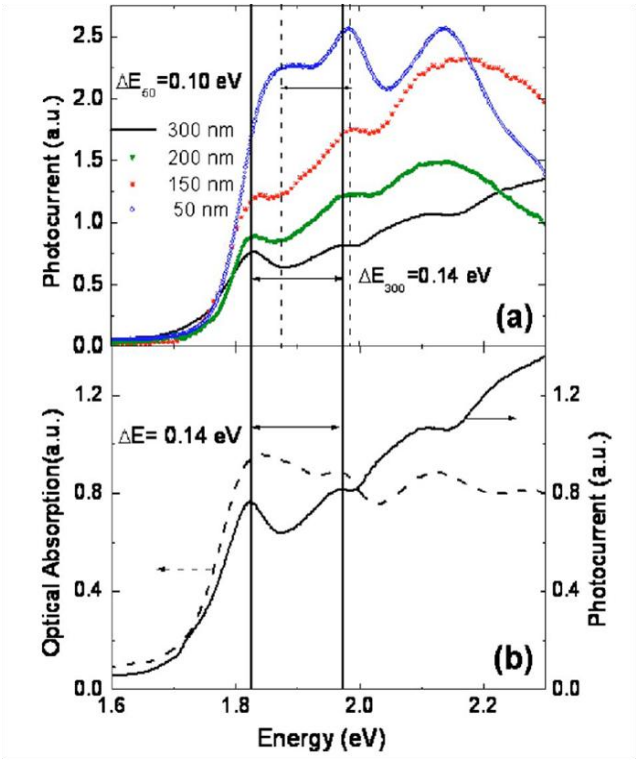

Figure 4.15: (a) Photocurrent spectra of OTFTs with different active Pentacene layer thickness: 50 nm (open circles), 150 nm (stars), 200 nm (solid triangles) and 300 nm (solid squares), for V_G=0 V; (b) Photocurrent (solid squares) and optical absorption (dashed line) spectra of a Pentacene thin film 300 nm thick [(74)].

PC results (Figure 4.15(a)) clearly show the enhancement of the Davydov splitting occurring in the first absorption band for Pentacene layers of increasing thickness, from 50 to 300 nm. The energy separation between the first two peaks in 50 nm and 300 nm thick films varies from 0.10 eV to 0.14 eV, respectively, in very good quantitative agreement with data previously reported by optical absorption analyses [(78)].

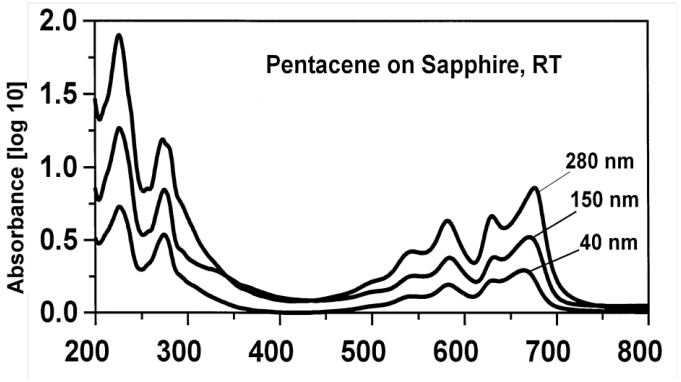

Figure 4.16: Absorption spectra of Pentacene films in dependence on average film thickness at ambient temperature [(78)].

OTFTs have intentionally been characterized in air in order to assess the potentiality of PC spectroscopy as a tool to be applied in atmosphere and on fully operational devices. On the contrary, XRD analysis cannot be done directly on the OTFT. It is noteworthy that PC spectra on the same OTFT do not change after one week of exposure to air and repeated analyses, even if the transport parameters of the device (mobility and threshold voltage) slightly varied. This confirms that the shape of the PC spectrum is not directly affected by the minor changes measured in the device macroscopic transport parameters and provides a "fingerprint" of the distribution of the electronic states in the material. Photocurrent spectroscopy is a new tool able to investigate DOS and molecular packing at the same time and directly on the device.

4.2 Aging of Pentacene OTFTs

In this paragraph, I will discuss the problem of aging of Pentacene OTFTs making use of PC spectroscopy and electrical characterization, with the goal of studying the aging of the device and providing a new tool, the photocurrent measurements, to assess the formation of deep electrically active states within the band-gap after prolonged operation in atmosphere and with exposure to light or darkness. To this aim, OTFTs were fabricated with an active Pentacene layer 50nm thick, in the same conditions explained in the paragraph before. Then they were measured by Photocurrent and IV characterization at room temperature and in air. The measures of PC were made with the apparatus described in chapter 3.2. The electrical measurements on OTFTs were carried out using two Keithley 2600 source meters controlled by Labview software. One OTFT was kept in air in a dark room whereas the other in air with exposure to solar light, the effects of aging where studied for 10 months. Photocurrent spectroscopy were carried out several times to control the changes of the DOS distribution in the course of

time. Also IV measures were made to control, after several months, the effect of aging on the main parameters (measurements of mobility and threshold voltage).

Photocurrent spectra obtained as a function of time of the two OTFTs are shown in Figure 4.17. We can clearly see the degradation of the intensity of the spectra after 10 months for both the OTFTs and in particular the presence of a bump before the band edge for the OTFT kept with light. The atomistic model proposed in chapter 1.4 describes the formation of gap states in polycrystalline Pentacene, suggesting that acceptor-like states are formed at 0.29 eV above the valence band following exposure to oxygen and moisture and are electrically activated by the application of a gate bias voltage. The light have the effect of activate the process [25]. This result, as already said, is confirmed also by other researches [16][26][27]. My experimental results well correlate with this model, in fact the bump before the band edge is located at 1,68 eV (band edge = 1,97 eV for a 50 nm layer of Pentacene [74]), so I have a $\Delta E \sim 0{,}29$ eV. This is an indication of how PC analyses can provide useful information on the formation of electrically active deep states in OTFTs.

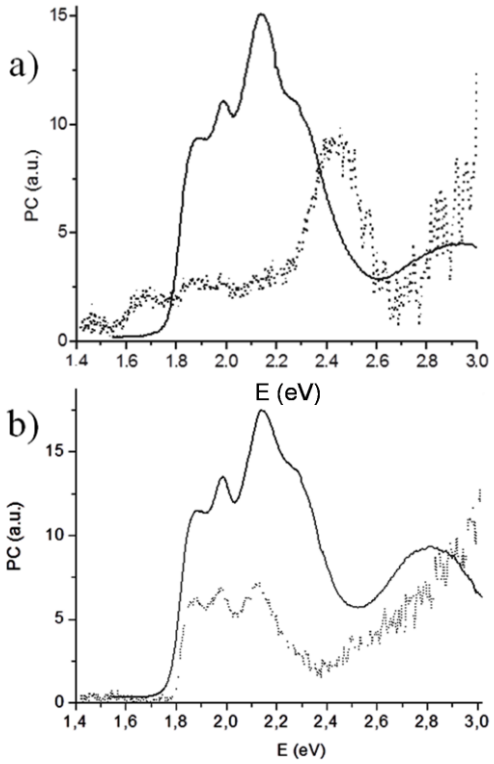

Figure 4.17: Photocurrent spectra of two Pentacene OTFTs with an active layer of 50 nm: a) as deposited (solid line) and after 10 months exposure to ambient light (dotted line); b) as deposited (solid line) and after 10 months in the dark (dotted line).

The typical electrical performance of my Pentacene OTFTs is described by the major transport parameters (carrier mobility and threshold voltage) reported in Table 4.3. After 10 months of aging the performance of the OTFTs strongly degrades for each device measured, as clearly shown by the significant reduction in the carrier mobility (see also Figure 4.18) and the important V_{TH} shift toward positive voltage. The results are concordant with the aging and bias effects discussed in paragraph 1.4.

OTFTs (Pentacene layer: 50 nm)	**Aging**	**μ (V/cm^{2}s)**	**V_{TH} (V)**
OTFT 1	as deposited	$7x10^{-2} \pm 7 \cdot 10^{-3}$	-18 ± 2
	aging: air + light	$1x10^{-3} \pm 1 \cdot 10^{-4}$	22 ± 2
OTFT 2	as deposited	$9x10^{-2} \pm 9 \cdot 10^{-3}$	-23 ± 2
	aging: air + dark	$4x10^{-3} \pm 4 \cdot 10^{-4}$	8 ± 2

Table 4.3: Electrical transport parameters of Pentacene OTFTs with different active layer thickness and different conditions of aging.

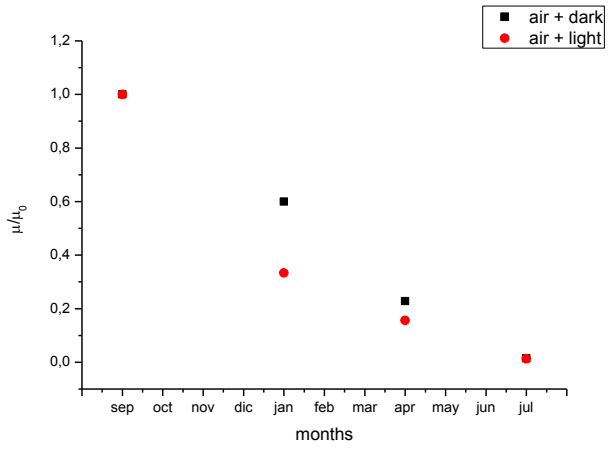

Figure 4.18: Mobility trend as a function of time for two OTFTs with Pentacene layer 50 nm thick, exposed to solar light (red circles) or in dark room (black squares).

The drop of the mobility happened in presence of air and is accelerate by the effect of light in an irreversible way even though it is not sudden [(16)]. This is the confirmation that there is the absolute need to find a way to avoid this aging effect, if we want to have efficient and reliable devices in the course of time.

Other experiments have been carried out on OTFTs with an active layer of Pentacene 300 nm thick. These devices were kept in air and light and measured with PC

and IV at room temperature as in the previous experiment. After five months, as no variation could be seen in the DOS shape in the PC spectra, I applied a bias stress (I_{DS} with V_{DS} varying from 0 V to -60 V and fixed V_G =-100 V, for 10 times). After three months the effect of aging was clearly visible in the PC spectra, both for the great lost in intensity and also for the different DOS. In Figure 4.19, the comparison between a OTFT with Pentacene layer 300 nm thick as grown and after aging is shown. In particular, the bump localized at the energy of about 1.69 eV before the band edge (1.97 eV for a Pentacene layer 300 nm thick), can be attributed to a deep level created by the interaction between the Pentacene and the constituents of the air mediated by a bias stress effect. So there is correlation again with the atomistic model we used previously for the OTFT with active layer 300 nm thick. But this effect cannot be explained only by the aging due to air and light because if it was, the bump should be appeared in the thicker layer after than the thinner layer, instead 8 months were enough for the 300 nm OTFT whereas 10 months for the 50 nm OTFT. It is known that Oxygen and water diffuse in the Pentacene layer till they reach the dielectric interface and create defects, but for a thicker layer the time of diffusion should be more than for the thinner layer [65].

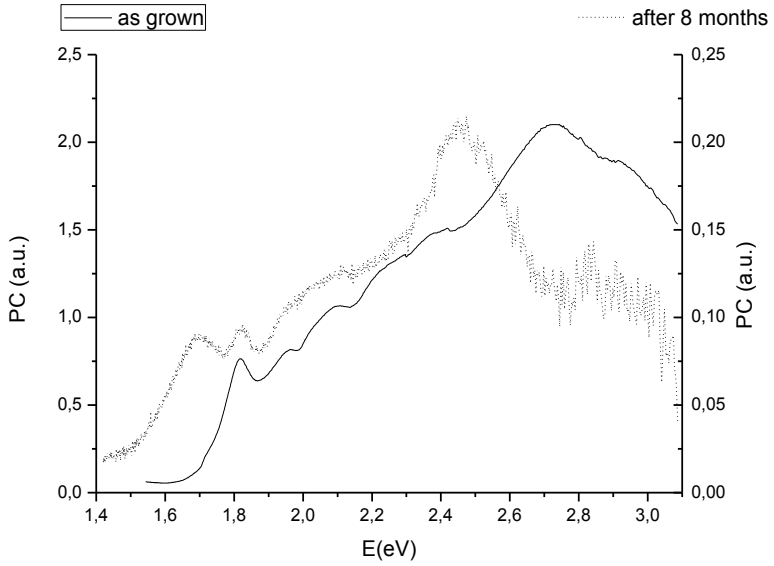

Figure 4.19: Photocurrent spectra of Pentacene OFET with an active layer 300 nm as grown (solid line) and after 8 months exposure to ambient light and bias stress (dotted line).

In conclusion, I applied PC spectroscopy to Pentacene OTFTs to investigate the effects on the density of states distribution induced by a prolonged exposure to air and bias stress. I detected the formation of a deep band of traps at about 1.68 eV, associated to the degradation of the OTFT performance following exposure to air, light and time or

bias stress, thus assessing the reliability of PC analyses as a non-destructive tool to characterize the electrical properties of organic thin films and devices. Finally I checked the degradation of the electrical parameters (mobility and threshold voltage) by electrical measurements after aging.

5 Ion implanted Pentacene thin films

The focus of the research I carried on in this thesis work is the analyses of the effects of ion implantation on thin films of organic semiconductors or, as I will discuss in the next chapter, on fully operational OTFTs. In this chapter we will see that the controlled ion implantation of some species of ions will modify thin Pentacene layers, giving as primary results: the formation of a surface encapsulation layer, the possibility of increasing the conductivity of the semiconductor and furthermore the possibility to implant stable charged species to modify the electrical characteristics of the layer. The comprehension of these effects is extremely interesting both for the knowledge of the properties of the organic semiconductors themselves and even more for the possibility to modify their electrical and structural properties in order to achieve improved and reliable devices.

The first implanted ion species I will discuss are N^+ or Ne^+, these two species were chosen for the their very different chemical properties and reactivity. The energy of the beam is relatively low (÷ 30 keV) because we want to preserve a undamaged Pentacene layer at the interface with the substrate and to contain the damage of the implantation in the superficial part of the layer. The doses and energies more suitable were chosen with SRIM simulations as explained in the next paragraph. However to analyze the effects of the implantation as a function of the energy, some tests were carried out with several energies of the beam. The doses of ions implanted also were varied at constant beam energy for several test samples to understand the effects of the implantation as a function of the dose.

Ion implantation was performed on Varian CF-3000 ion implanter at Ion Beam Materials Laboratory in Los Alamos National Laboratory on Pentacene thin films 300 nm thick evaporated on SiO_2. To minimize the sample exposure to the environment during the transportation, samples before and after the implantation were either packed under dry nitrogen atmosphere or sealed under vacuum. The implantation was performed under room temperature with different ion species (N^+ and Ne^+) to various fluencies. The beam flux was kept at a fixed value so that the flux effect is not a concern in these sets of experiments. The maximum ion energy was chosen so as not to completely damage the Pentacene layer (see Figure 5.1).

Previously reported results on ion irradiation of polymers, showed that a controlled damage induced by the implanted ions can induce strong chemical and structural modifications of the material, altering its mechanical and electrical properties (see paragraph 2.4). In this research I will describe how the consequences of ion implantation described before are observed also on a an organic semiconductor, made of single molecules, as Pentacene, deposed in thin films. The effects studied are mainly three:

1. Carbonification and loss of Hydrogen in the film, induced by a controlled implantation of both ions (N^+ and Ne^+), that also lead to an increase of the hardness and to a different texture of the film.
2. Enhancement of the conductivity of the organic film due to the ion implantation clearly described by the *four-contacts* measurements. N^+ ions show a variability of the conductivity as a function of dose and energy whereas Ne^+ doesn't. Furthermore a huge change of the optical spectra is present that means a DOS distribution completely altered.
3. Formation of stable charged chemical species, following implantation only with N^+ ions, that chemically react with the organic matrix, thus assessing the potentiality of employing this ion implantation to permanently modify the electrical transport properties of organic thin films.

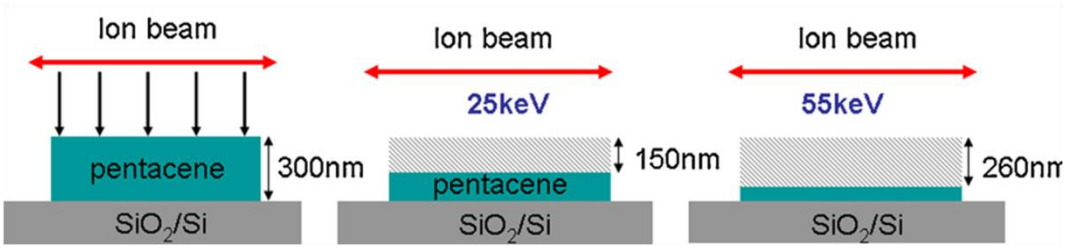

Figure 5.1: Schematic layout of the ion implantation process of Pentacene thin films [82].

5.1 Structural characterization

5.1.1 Ion penetration: SRIM simulations

Monte Carlo SRIM code (paragraph 2.2) was used in my research to estimate ion beam parameters that would produce the required damage thickness and ion profile in the Pentacene film. According to these simulations, the thickness of the damaged layer is slightly thinner than the depth profile of the implanted ions. Looking at Figure 5.2, under 25 keV of N^+ ion bombardment, the damaged layer thickness in the Pentacene is approximately 100 nm for both the two doses ($1\cdot10^{16}$ or $5\cdot10^{16}$ ions/cm^2), while the tail of the implanted N^+ ions goes as deep as 130 nm. As the energy beam grows the penetration depth grows, for example at 65 keV (110 keV) it becomes 290 nm (420 nm). As the doses vary the number of displacements varies, for $1\cdot10^{16}$ ions/cm^2 of N^+ ions at 25 keV there are $2\cdot10^{18}$ atoms/cm^2 displaced from their initial position in the material, whereas for $5\cdot10^{16}$ ions/cm^2 of N^+ ions at 25 keV there are $1\cdot10^{19}$

displacements. An analogue reasoning can be followed for the Ne^+ ions with a similar penetration depth and a lightly higher number of displacements, in the same conditions.

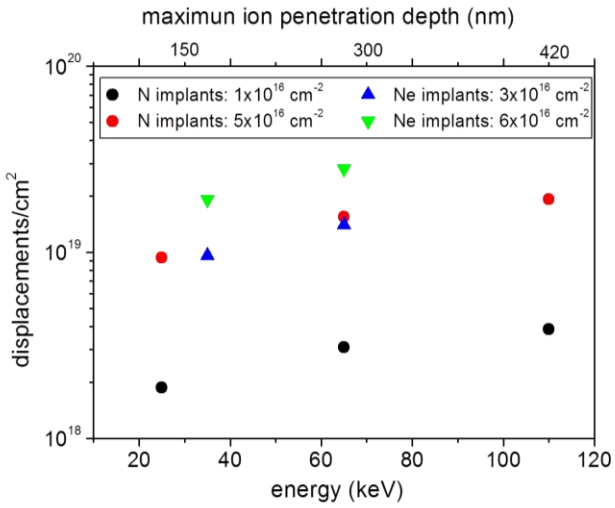

Figure 5.2: Simulation of the ion displacements/cm^2 as a function of the beam energy, or similarly as a function of the maximum ion penetration depth, for different ion doses of N^+ and Ne^+.

The SRIM simulation of the number of the collision events per ion per Å and of the ion ranges as a function of the target depth are reported in Figure 5.3a and in Figure 5.3b for a Pentacene film N^+ implanted at 65keV. In Figure 5.3b also the other moments: Straggle (or standard deviation), Skewness, and Kurtosis, were reported (see paragraph 2.1). Looking at Figure 5.3a, the most of the displacements, or collision events, happen at an average depth of about 170 nm whereas, as Figure 5.3b shows, the ion range is about 200 nm. The same distributions are shown in Figure 5.4 and Figure 5.5 respectively for N^+ implantation at 110 keV and for Ne^+ implantation at 65 keV.

Comparing the first two figures (N^+ implants) we can see that the implantation with higher energy produce a higher penetration depth and a higher number of displacements/ion. At energy beam equal to 110 kev the whole film, 300 nm thick, is completely modified by the implantation as the ion range is about 310 nm and also the highest number of displacements/ion have its average peak at that depth. Comparing Figure 5.3 and Figure 5.5, considering the area covered by the two distributions, Ne^+ implant shows more displacements/ion, so more damage, at the same penetration depth, compared with N^+ implant. The beam energy values and the doses have been chosen, following SRIM simulations, in order to limit the damage to the top portion of the active layer.

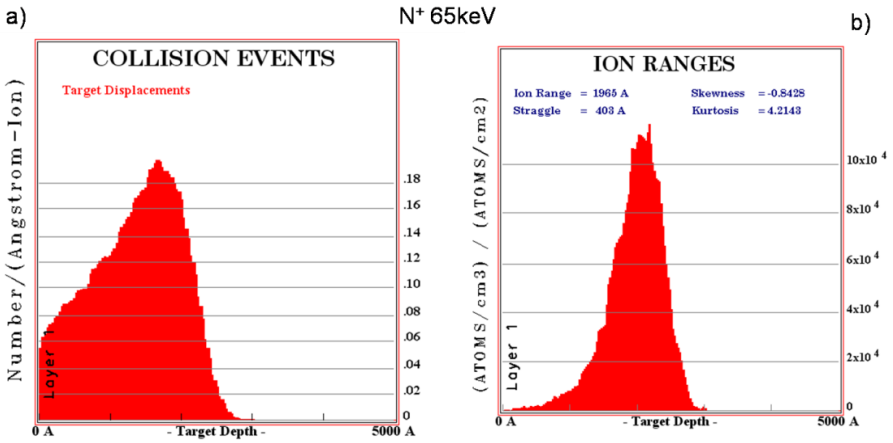

Figure 5.3: SRIM simulation for a Pentacene film N^+ implanted at 65keV a) Collision events and b) ion ranges as a function of the target depth.

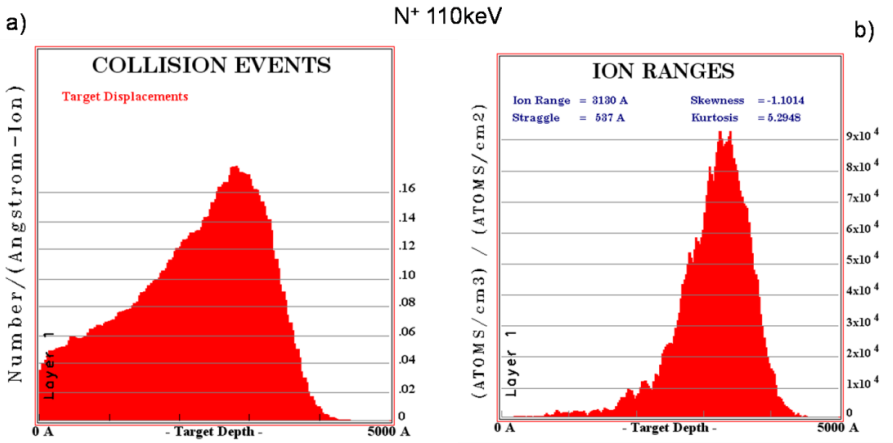

Figure 5.4: SRIM simulation for a Pentacene film N^+ implanted at 110 keV a) Collision events and b) ion ranges as a function of the target depth.

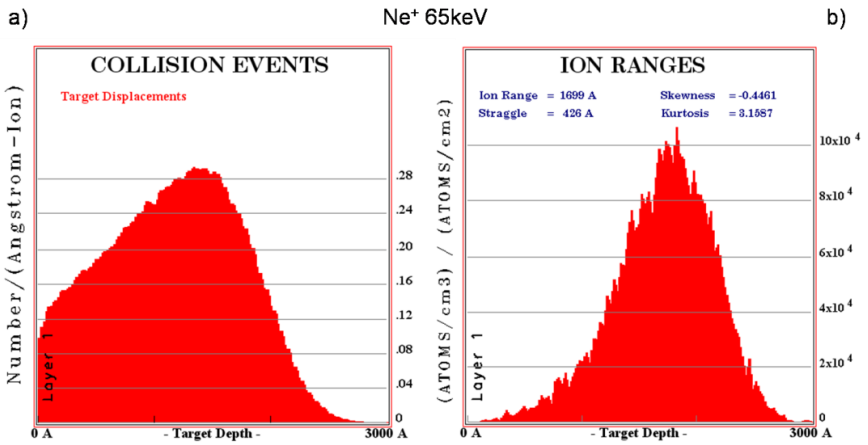

Figure 5.5: SRIM simulation for a Pentacene film Ne^+ implanted at 65keV a) Collision events and b) ion ranges as a function of the target depth.

5.1.2 Fourier transform infrared (FTIR) spectroscopy

Fourier transform infrared (FTIR) spectroscopy is a technique largely used to analyze the organic semiconductors and sometimes inorganic ones. The infrared wave number range goes from the 14000 to 20 cm^{-1} and is divided in three main parts: near-IR (14000-4000 cm^{-1}), medium-IR (4000-500 cm^{-1}) and far-IR (500-20 cm^{-1}). In Figure 5.6 the three regions of the infra-red spectra of the E.M. radiation is reported with an example of a FTIR spectra collected in the medium-IR. This technique measures the absorption of the material in the infra-red range of wavelengths. The absorption of IR radiation produces characteristic vibrational motions of the molecules called *stretching* and *bending*. As illustrated in Figure 5.7a the *stretching* of the molecules present a continuous variation of the distance between the two atoms bonded, the *stretching* can be symmetric or asymmetric. The *bending* instead regards the angle of the bonds of three or more atoms that can be in plane or out of plane (see Figure 5.7b). The quantity of energy necessary to produce these kind of motions are related to the strength and the polarity of the bonds among the atoms in the molecules considered. So this measure can give information about the rearrangement of the molecular bonds and about the modification of the crystal structure, for example, due to the ion implantation.

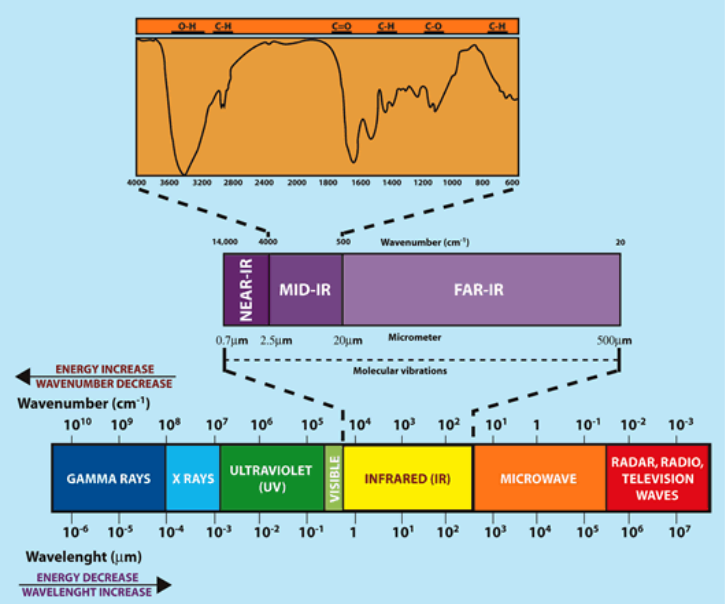

Figure 5.6:Spectral regions of the electromagnetic radiation with an expansion of the infra-red part. Above a typical FTIR spectra.

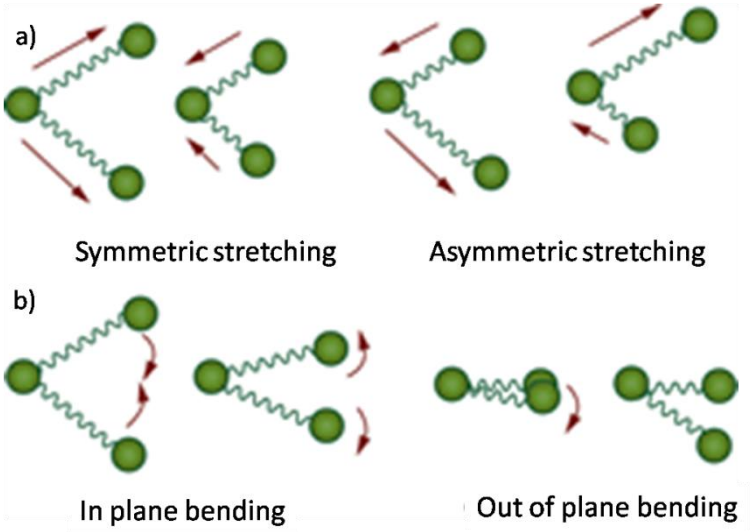

Figure 5.7: Vibrational motions of the atoms inside a molecule: a) stretching symmetric and asymmetric; b) bending in plane and out of plane.

In this research, Fourier transform infrared (FTIR) spectroscopy was performed to study the modification of Pentacene film by N^+ or Ne^+ ions. In order to enhance the signal-to-noise in the IR data, and therefore enhance signal resolution, Multiple Internal Reflection IR (MIR-IR) (also called Attenuated Total Reflectance or ATR), where the IR beam repeatedly interacts with the sample, was employed. The data were acquired under the maximum resolution of 2 cm^{-1} and each spectrum is the average of 400 scans. In Figure 5.8 and Figure 5.9, three characteristic peaks from virgin film of Pentacene are clearly visible at 732, 906 and 1299 cm^{-1} (also reported in Table 5.1). The first two peaks correspond to a C–H out of plane bending mode, while the peak at 1299 cm^{-1} is associated to a C–C stretching mode. The intensities of the two C–H related peaks decrease after either N^+ or Ne^+ implantation while the peak at 1299 cm^{-1} increases. Figure 5.10 shows the trend of the C–H/C–C peak ratio as a function of the increasing dose and indicates how C–H bonds in Pentacene are easily broken by ion implantation[83]. The resulting free hydrogen diffuses out of the irradiated region, leading to the formation of a hydrogen-depleted carbon-rich matrix. These results well correlate with the ERD data, discussed in the following paragraph, that indicate the occurrence of hydrogen loss after N^+ or Ne^+ implantation. The modification of Pentacene by ion implantation becomes more significant with increasing implantation dose. The bond breaking discussed here is in complete agreement with the results reported in paragraph 2.4.

Wavenumber (cm^{-1})	Identification
732	C–H out of plane bending
906	C–H out of plane bending
960	C–H out of plane bending
1299	Aromatic C–C stretching

Table 5.1: Wavenumber and identification of the principle IR peaks of Pentacene.

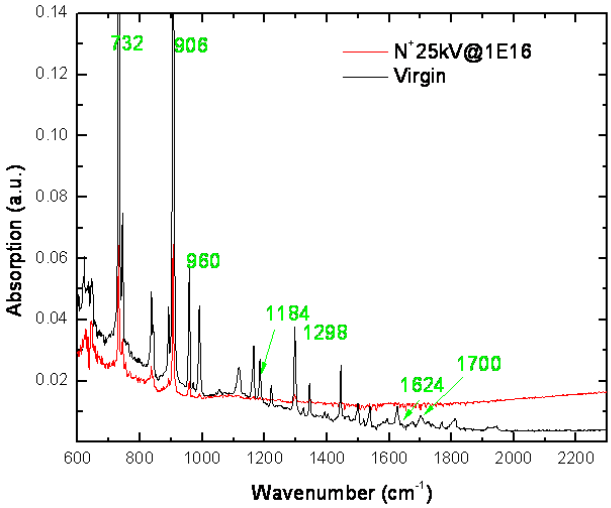

Figure 5.8: FTIR measurements of a Pentacene film virgin (black) and implanted with $1x10^{16}$ N^{+} ions with beam energy 25 keV.

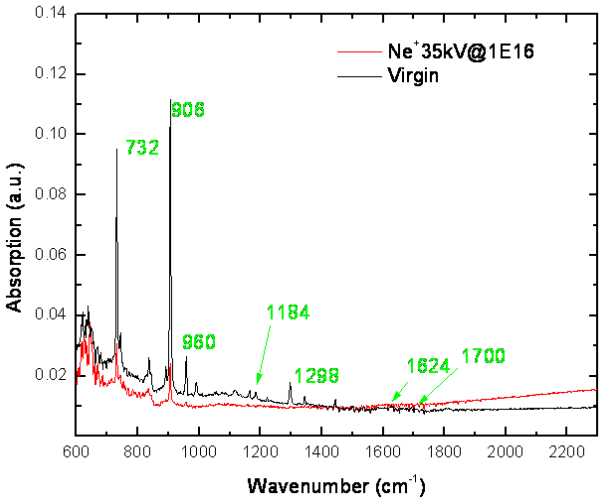

Figure 5.9: FTIR measurements of a Pentacene film virgin (black) and implanted with $1x10^{16}$ Ne^{+} ions with beam energy 35 keV.

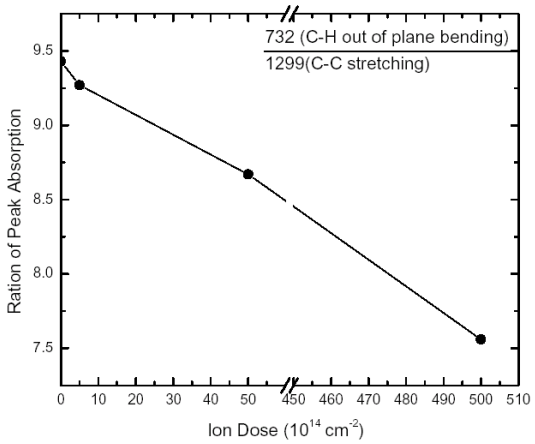

Figure 5.10: FTIR analyses of N^+ and Ne^+ implanted Pentacene films, showing the modifications induced in the C–H and C–C molecular bonds[83].

5.1.3 Elastic recoil detection (ERD)

In elastic recoil detection (ERD) one determines the yield and energy of particles ejected out of the surface region of samples under MeV ion bombardment. By application of this surface and thin film analysis technique one can obtain quantitative information concerning the depth distribution of light elements in a sample to be analysed. The quantitativity and the depth resolving power are based on knowledge of the recoil cross section and the stopping power of high-energy ions in matter [84].

One of the most popular methods among numerous analysing techniques is Rutherford Backscattering Spectrometry (RBS)**.** This technique makes use of high-energy (MeV) ion beams and is based on the process of elastic scattering and the energy loss of the energetic primary and backscattered ions. In RBS light ions, usually He or H, with energies ranging from 0.5-3 MeV impinge on a target while the number and energy of ions backscattered in the direction of a detector are determined. Since the collisions with the target nuclei are elastic, one can derive the mass of the scattering centres from the measured energies, making use of the laws of conservation of energy and momentum. The excellent ability of this method to extract quantitative data about abundancies of elements is due to the precise knowledge of the Rutherford scattering cross sections.

A consequence of the conservation laws is that the energy of the other participant in the collision, which is not detected in RBS, i.e. the atom initially residing in the target, contains the same kind of information. The technique that evaluates these secondary particles is called elastic recoil detection (ERD). One of the main drawbacks of RBS is its poor sensitivity for light elements present in a heavier matrix This is caused by the relatively low value of the cross section σ for backscattering at light

elements ($\sigma_{RBS} \sim Z^2$ where Z is the atomic number) and the fact that the energy of a particle will be low when it is backscattered from a light atom. The features corresponding to light elements in a heavy matrix therefore tend to drown in a background representing the presence of matrix atoms at a certain depth. Since backscattering from hydrogen is not possible, this element cannot be detected at all by RBS.

In ERD one makes use of the fact that the information about the target is carried by the target nuclei themselves and not by the backscattered primaries as in RBS. This enables us to identify the particles under investigation. Detection in ERD essentially occurs in a forward scattering geometry, and therefore both scattered and recoiled particles will move in the direction of the detector. In conventional ERD heavy primary ions are used. An absorber foil in front of a silicon surface barrier detector (SSBD) is employed to stop these particles. The stopping power in the foil decreases substantially with decreasing mass of the moving particle. Therefore the thickness of the foil can be chosen such that the light energetic recoils are allowed to reach the detector, while the heavy primary particles are completely stopped. From an analysis point of view, the most interesting situation occurs when investigations focus on atoms that are light with respect to the matrix or substrate atoms. This is the situation for which RBS is inconvenient. If we apply primary ions of approximately the same mass as the matrix or substrate atoms the optimal conditions for this type of analysis are achieved. The absorber foil will stop both the primary and the heavy recoiled particles. In this way the lighter atoms can be detected without any background. In Figure 5.11 we can see the typical geometry of the system for ERD measurements.

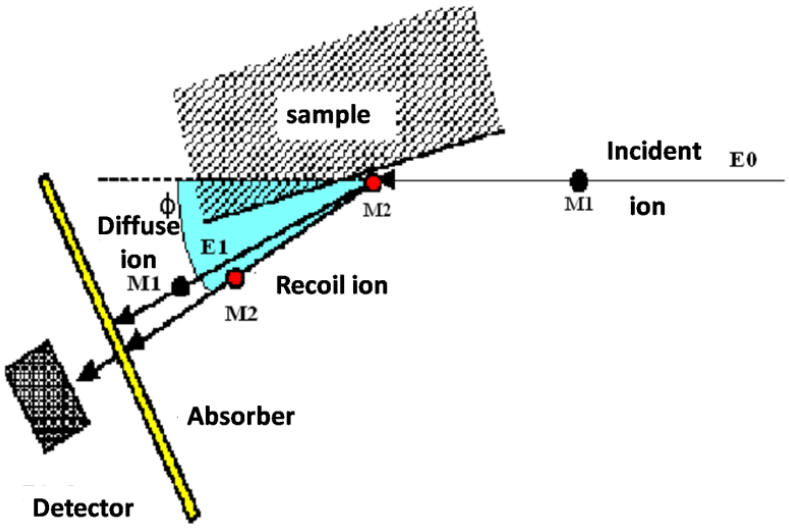

Figure 5.11: Geometry of the system for the ERD analyses.

Elastic recoil detection (ERD) was used to measure hydrogen content in the Pentacene films before and after the ion implantation with N^+ ions at 25 keV with different doses. During the measurement, 3 MeV $^4He^+$ ion beam from a 3.0 MV Pelletron tandem accelerator was incident on the film sample at a 75° angle (between the beam and the sample normal). The elastically recoiled hydrogen atoms by the incident ^4He particles were detected by a silicon surface barrier detector at 30° angle (between the beam and the detection direction). A 14 μm thick of mylar foil was placed in front of the detector to filter out the forward scattering ^4He particles from the target so only hydrogen signal is recorded in the detector. Both small beam current (~8 nA) and small collected charge (2 μC) were used so that the hydrogen loss during the ERD measurement is negligible. Integration of the hydrogen signals over the entire film thickness provides the total amount of hydrogen remaining in the film before and after the different ion doses (as shown in Figure 5.12). This figure indicates that the hydrogen loss increases with the implantation dose, but the rate of the hydrogen loss decreases with the dose, presumably due to the fact that less and less H–C covalent bonds are remaining in the film as a result of the initial ion bombardment [83]. The results obtained are supported by the other results obtained on polymers and reported in paragraph 2.4.

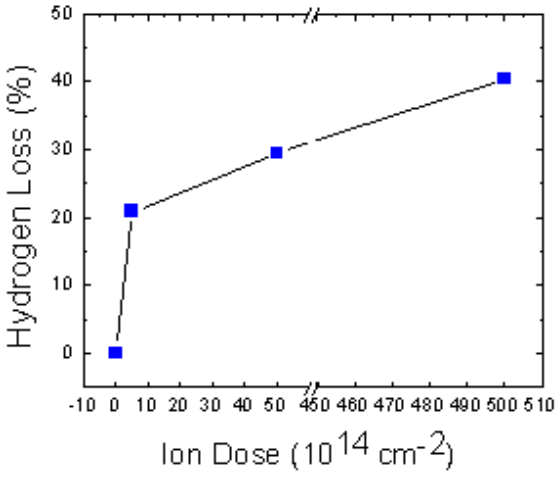

Figure 5.12: ERD analyses on N^+ implanted OTFTs, showing the hydrogen loss as a function of the ion dose (the ion energy is 25keV)[83].

5.1.4 Nanoindentation

Depth-sensing indentation devices allow the amount of penetration of an indenter into a material to be measured as a function of applied load. The objective of micro- and nanoindentation testing using these devices is to produce absolute measurements of material properties under indentation loading. Further, the ability of

these devices to measure the responses of microscopic regions can be a key to understanding mechanical behavior of technologically important material systems [85].

The atomic force microscope (AFM) is useful for evaluating polymeric materials on a sub-micrometer scale. AFM images are produced by scanning a probe, consisting of a sharp tip (nominal tip radius on the order of 10 nm) located near the end of a cantilever beam, across a sample surface using piezoelectric scanners. The AFM can also be operated in a non-imaging mode, called force mode, to perform indentation tests. A force curve is produced, which is a plot of tip deflection as a function of the vertical motion of the scanner. This curve can be analyzed to provide information on the local mechanical response. Also, the spring constant of the cantilever probe can be chosen such that small differences in response can be detected between polymers that have a certain range of stiffness. AFM indentation measurements are relative measurements, largely due to the lack of information regarding the tip shape of the AFM probes. Also, current tip shape calibration procedures used in depth-sensing indentation rely on indentation results from a reference material, and the reproducibility of these methods has been poor in a recent interlaboratory comparison[86].

In my research Nanoindentation measurements were carried out to evaluate the changement in hardness of the implanted Pentacene film. The measures were done in Los Alamos National Research laboratory. In Figure 5.13 we can see that the hardness of the Pentacene film, implanted with N^+ ions at 25 keV of energy, increases as a function of the dose of ions implanted in the film. The increase of the hardness of the organic compounds is a consequence of ion implantation present also in the literature (see paragraph 2.4)

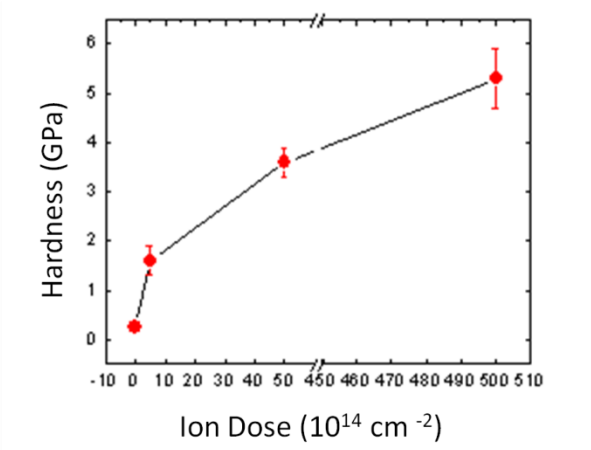

Figure 5.13: The hardness of the Pentacene film increases when the ion doses increase, for N^+ ions implanted with 25 keV of energy.

5.1.5 XRD analyses

X-Ray Diffraction (XRD) is a non-destructive technique widely used to investigate the crystallographic structure and chemical composition of materials and thin films. The samples can be both crystalline materials (SC-XRD, Single *Crystal X-Ray Diffraction*) and polycrystalline or powdered solid samples (XRPD, *X-Ray Powder Diffraction*). Since XRPD is the most commonly used, usually it is called simply XRD.

The analysis is based on the observation of the scattered intensity pattern produced by the diffraction of an incident X-ray hitting the sample. The diffraction spectra depends on the wavelength of the incident radiation and on the crystallographic structure of the investigated sample. In 1913 Sir W. H. Bragg and his son Sir W. L. Bragg explained the formation of the diffraction pattern from the scattering of a X-ray hitting on a crystalline material developing the notorious relationship, known as the *Bragg's Law:*

$$n\lambda = 2dsen\theta \qquad \text{[Eq. 56]}$$

where: θ is the angle of incidence, λ is the wavelength of the incident X-Ray radiation, d is the distance between atomic layers in a crystal and n is an integer. For the determination of the crystal structure of NaCl, ZnS and diamond in 1915 the Braggs was awarded with the Nobel Prize in physics.

In Figure 5.14 a schematic visualization of the Bragg's law is reported. When a monochromatic radiation (or subatomic particle wave) with a wavelength λ comparable to atomic spacing d is incident on a crystalline sample at an angle θ, the Bragg diffraction occurs only when the path length of the rays reflected from successive planes differs by an integer number n of wavelengths. This condition of constructive interference (maximum scattered intensity) is satisfied, varying the incidence angle θ, by different *d*-spacing in polycrystalline materials, thus allowing to understand the crystallographic structure of the investigated material. The intensity of the diffraction peaks plotted in function of θ constitutes the *diffractogram*, a graph which characterizes the sample.

A typical diffractometer consists of a source of radiation, a monochromator to choose the wavelength, slits to adjust the shape of the beam, the sample and a detector. Also a goniometer is used for fine adjustment of the sample and the detector positions. The most used kind of diffractometer for thin film and powdered sample investigation is the *θ-2θ diffractometer*. In such system the sample is located in the centre of the instrument, the x-ray beam is directed on the sample surface with an incidence angle θ and at the same angle the detector monitors the scattered radiation.

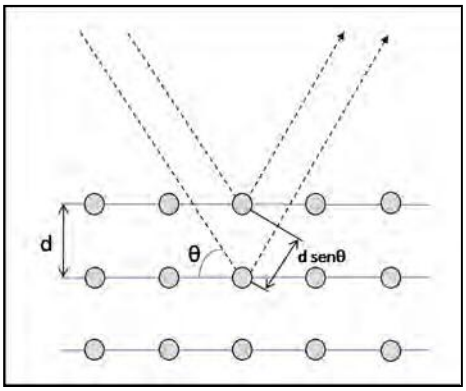

Figure 5.14: Schematic visualization of Bragg's diffraction. The condition for constructive interference, i.e. for maximum scattered intensity, is satisfied only when the distance travelled by the rays reflected from successive planes differs by an integer number n of λ.

Such a kind of diffractometer operates in two different scan configurations, which differs in the mutual position and angular velocity of the source/sample and the detector: in the *θ-2θ scan configuration* the sample and the detector move with an angular velocity of ω and 2ω respectively, while in the *θ-θ scan configuration* the source and the detector move with the same angular velocity ω. The rotations are performed by the goniometer, which is the central part of a diffractometer. Typically the sample is mounted on the rotational axis, while the detector and/or x-ray source move along the periphery, but both axes of rotation coincide [(87)].

X-Ray diffraction (XRD) measurements were done on Pentacene films 300 nm thick, grown on quartz slides, virgin and N^+ ion implanted. XRD (θ-2θ scan) were carried out with a diffractometer equipped by a rotating anode source (SmartLab-Rigaku). A focus line x-ray beam (Cu Kα) was collimated by a parabolic graded multilayer mirror placed in front of the sample and a double slits were mounted before the detector to achieve the required angular resolution.

Related to XRD, another technique that we used is X-Ray Reflectivity, sometimes known as X-ray specular reflectivity, X-ray reflectometry, or XRR, is a surface-sensitive analytical technique used to characterize surfaces, thin films and multilayers. The basic idea behind the technique is to reflect a beam of x-rays from a flat surface and to then measure the intensity of x-rays reflected in the specular direction (reflected angle equal to incident angle) as in Figure 5.15. If the interface is not perfectly sharp and smooth then the reflected intensity will deviate from that predicted by the law of Fresnel reflectivity. The deviations can then be analyzed to obtain the density profile of the interface normal to the surface.

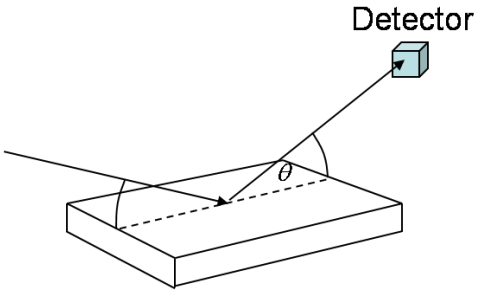

Figure 5.15 Diagram of x-ray specular reflection (XRR)

The basic mathematical relationship which describes specular reflectivity is fairly straightforward. When an interface is not perfectly sharp, but has an average electron density profile given by $\rho_e(z)$, then the x-ray reflectivity can be approximated by [88]:

$$R(Q)/R_F(Q) = \left| \frac{1}{\rho_\infty} \int_{-\infty}^{\infty} e^{iQz} \left(\frac{d\rho_e}{dz} \right) dz \right|^2 \qquad \text{[Eq. 57]}$$

Here *R(Q)* is the reflectivity, $Q = 4\pi \sin\theta / \lambda$, ρ_∞ is the density deep within the material, λ is the x-ray wavelength, and θ is the angle of incidence. Typically one can then use this formula to compare parameterized models of the average density profile in the z-direction with the measured x-ray reflectivity and then vary the parameters until the theoretical profile matches the measurement. For films with multiple layers, X-ray reflectivity may show oscillations with wavelength, analogous to the Fabry-Pérot effect. These oscillations can be used to infer layer thicknesses and other properties, for example using the Abeles matrix formalism [89].

From the X-ray diffraction spectra with specular geometry, shown in Figure 5.16, we can see that the intensity of Pentacene reflections decreases with the dose but still some crystalline phase persists; this is clear for the (001) plane but less evident for the (002) one. So there is a considerable amorphization of the layer as reported also in the results described in paragraph 2.4.

From the measures of the X-Ray Reflectivity (XRR), shown in Figure 5.17, we can say that the film thickness does not change with the implantation process because there are the same fringes frequency in the spectra.

Rocking Curves are a useful way to study perfection in thin films and bulk single crystals. By fixing the detector at the center of the expected Bragg reflection and following the diffracted intensity as the sample is independently rotated (or “rocked”), one can gain valuable information. The plot of a rocking curve is the X ray intensity as a function of ω. The full width at half maximum intensity (FWHM) is related to the

dislocation density in the film and to the curvature of the sample. High Resolution variations of the method also allow us to determine misfit strain, the periodicity in artificial superlattices, the quality of the interfacial region, layer thickness, composition, and degree of mosaicity[90]. In a similar way, Rocking Curves can also be used to study polycrystalline materials. Key characteristic information that can be obtained are the size of the coherently diffracting domain (sometimes called the "particle" or "grain" size) and the degree of deformation in ductile materials.

The Rocking Curve measurements were done only on the reference sample and they suggest that there is a misorientation of several degrees of the crystallites around the preferential orientation, given by the FWHM of the Rocking curves (see Figure 5.18).

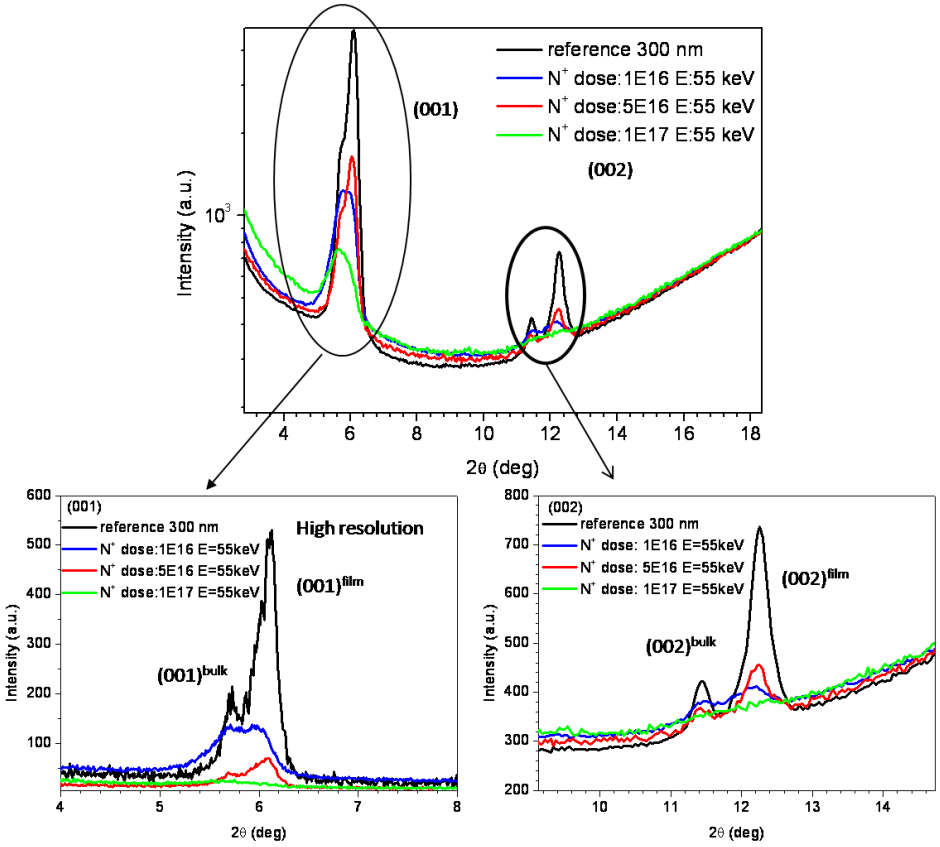

Figure 5.16: X-ray diffraction spectra with specular geometry. The two figures in the bottom part are the amplification of the angular ranges that describe the planes (001) and (002).

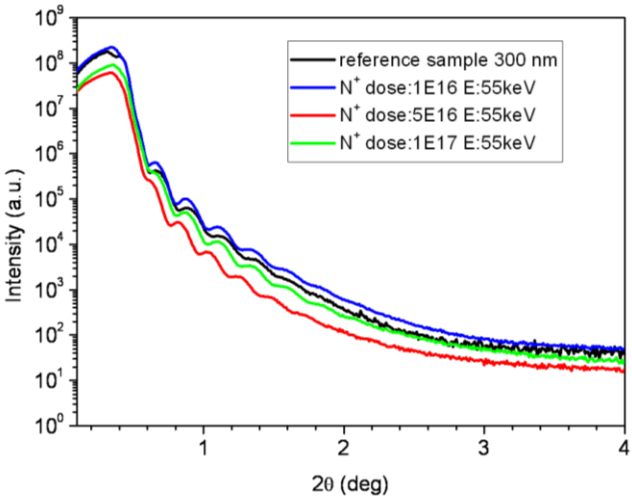

Figure 5.17: X-Ray Reflectivity measurements of OTFTs of Pentacene 300 nm thick, virgin and implanted with N^+ ions at different doses and with beam energy 55 keV.

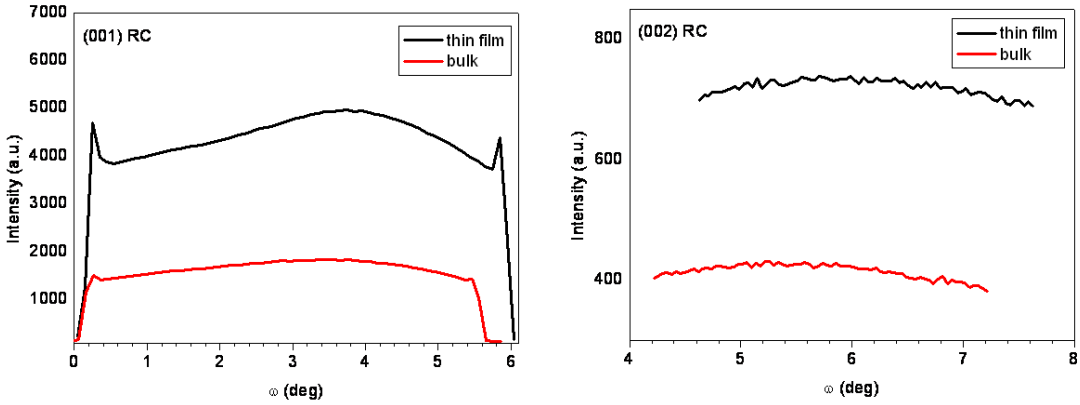

Figure 5.18: Rocking Curve measurements for the reference sample, a Pentacene film 300 nm thick.

5.1.6 AFM measures

In atomic force microscopy (AFM) or scanning force microscopy (SFM) a cantilever is scanned over the sample and its bending is detected with a laser beam deflected from it. On the cantilever a pyramidal tip of Silicon with a curvature radius of about 10 nm is mounted on its edge. The cantilever obeys Hook's law ($\Delta F = k\Delta Z$), thus a detection of very small short-ranging Van der Waals forces up to the nN range and of stronger long-range electrostatical forces is possible. The reflected laser light is detected by a position-sensitive photo-detector (4-field diode), allowing to measure the normal

force using difference currents in the vertical segments ($\Delta I_{top\text{-}bottom}$) and to measure the lateral force using the horizontal segments ($\Delta I_{right\text{-}left}$). The latter one arises through torsion of the cantilever caused by friction. A diagram of the AFM apparatus is drawn in Figure 5.19a. A dynamical feed-back system with tube-shaped piezo elements in z-axis (and x,y) not only pure height measurements but also constant-height operation with pm precision. Thus, the AFM can be operated in different modes (see also Figure 5.19b) [65]:

- In *contact mode*: the tip has direct contact to the sample and feels the repulsive part of the potential curve, i.e. the repulsion of the electron density sticking out of the sample surface decaying with r^{-6}. The height is kept constant at constant bending or constant force under feed-back control. A severe disadvantage of this mode is the possibility of easy destruction of the sample surface.
- In *tapping mode*: the cantilever oscillates at its resonance frequency $\omega_0=(k/m)^{1/2}$ in the range of 10^5 Hz with a turning point just at the sample surface. This mode is slower but less destructive and yields additional information by measuring the amplitude of the resonance frequency. For both modes a topographic contrast is formed.
- In *phase imaging mode*: the phase difference between the cantilever oscillation in tapping mode relative to the signal sent to the cantilever's piezo driver is recorded, creating a contrast due to the composition, adhesion, friction and viscoelastic properties.
- In *non-contact* or *intermittent mode*: the cantilever oscillates near its resonance frequency but its turning point is found 20-30 Å above the sample surface, avoiding the repulsive part of the potential curve, still showing topographic contrast.
- In *friction* or *lateral force mode*: the torsion of the cantilever is measured upon scanning in contact-mode allowing a friction-dependant imaging of the sample surface.

I carried on the AFM measurements in *tapping mode*, to avoid the damage of the surface of the Pentacene thin films. The cantilever I used has a length of 95 $\pm$ 10 μm a width of 30 $\pm$ 5 μm is used. Typical resonant frequency of this cantilever is around 240 kHz. It consists of a sharp pyramidal tip of Silicon with a curvature radius of 10 nm mounted on its edge (NSG10 by NT-MDT). The backside is coated with gold to increase the laser deflection yield. The vertical resolution, which depends on the z-piezo movement is around < 0.5 Angstrom. The lateral resolution would depend on the pyramidal tip curvature radius, so, for this tip, we can approximate it as ~ 10 nm.

In Figure 5.20 we can see the AFM topography maps (4x4 μm) for the sample virgin Pentacene film 300 nm thick and for the same film but implanted with N^+ ions at 55 keV with $3\cdot10^{17}$ ions/cm^2. A huge modification of the texture is visible from the

comparison of the two maps: the implanted sample shows a more dense structure formed by several conglomerates of molecules, it's visible also a deformation of the shape and dimension of the Pentacene molecules. This measure is in good agreement with the electrical measurements I will describe in paragraph 5.4, in fact we will see that the implantation brings to an enhancement of the conductivity of the film. We can suppose that this film becomes more conductive as the molecules are closer or more packed one with each other as shown in the AFM map. Furthermore the increase of the grain size brings to a decrease of the grain boundaries fraction, increasing the electron mean free path and thereby the electrical conductivity of the film. This is also in agreement with the description of Das[44] described in paragraph 2.4.

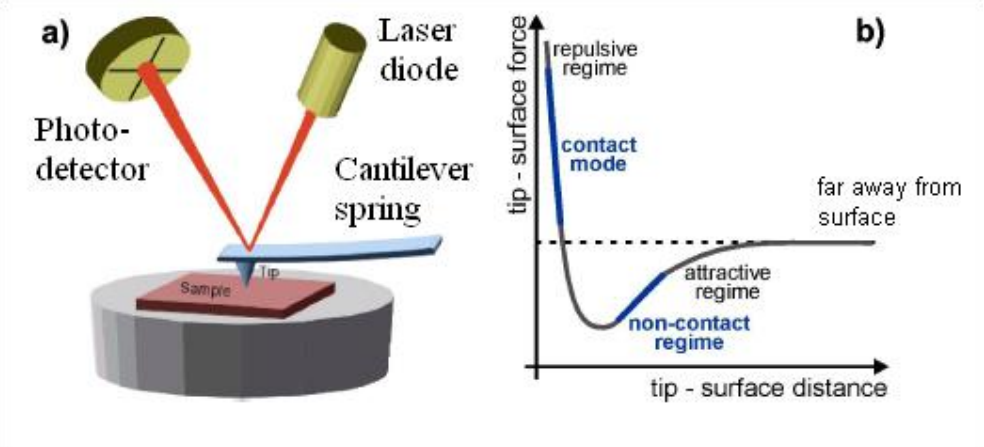

Figure 5.19: a) working principle of an AFM, b) force-distance curve.

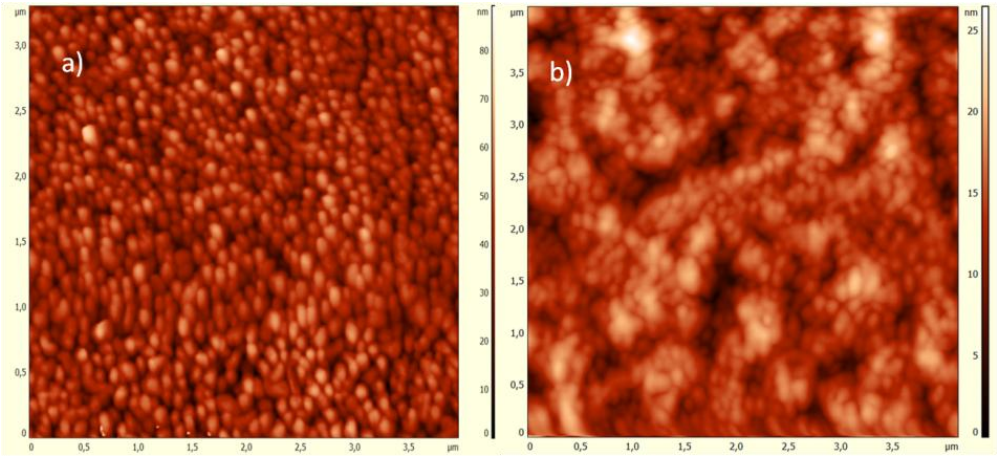

Figure 5.20: AFM 4 x 4 μm^2 maps of Pentacene film 300 nm thick a) virgin and b) implanted with $3 \cdot 10^{17}$ ions of N^+ with beam energy 55 keV.

5.2 Optical characterization

A material's absorption spectrum is the fraction of incident radiation absorbed by the material over a range of frequencies. The absorption spectrum is primarily determined by the atomic and molecular composition of the material. Radiation is more likely to be absorbed at frequencies that match the energy difference between two quantum mechanical states of the molecules. The absorption that occurs due to a transition between two states is referred to as an absorption line and a spectrum is typically composed of many lines or peaks.

The wavelengths where absorption lines occur, as well as their relative intensities, primarily depend on the electronic and molecular structure of the molecule. The wavelengths will also depend on the interactions between molecules in the sample, the crystal structure in solids, and on several environmental factors (e.g., temperature, pressure, electromagnetic field). The lines will also have a width and shape that are primarily determined by the spectral density or the density of states of the system.

The most straightforward approach to absorption spectroscopy is to generate radiation with a source, measure a reference spectrum of that radiation with a detector and then re-measure the sample spectrum after placing the material of interest in between the source and detector. The two measured spectra can then be combined to determine the material's absorption spectrum. The sample spectrum alone is not sufficient to determine the absorption spectrum because it will be affected by the experimental conditions (the spectrum of the source, the absorption spectra of other materials in between the source and detector and the wavelength dependent characteristics of the detector). The reference spectrum will be affected in the same way, though, by these experimental conditions and therefore the combination yields the absorption spectrum of the material alone. Optical absorption analyses were carried out in the transmission mode in air and at room temperature. The apparatus used for the measure is completely similar to the photocurrent system described in paragraph 3.2a part from pyroelectric detector that was used to measure the transmitted light with a energy resolution of 0.01 at 2.40 eV.

To assess the modification in the density of the states (DOS) of the sample following the ion implantation, we carried on the Optical Absorption spectroscopy on some of the implanted samples. We decide to study the films implanted with N^+ ions at the highest doses as they show the most important modification of the conductivity. The samples are still made of Pentacene 300 nm thick, deposited on quartz slides and implanted at constant energy of 55 keV with different doses: $1 \cdot 10^{16}$, $5 \cdot 10^{16}$ and $1 \cdot 10^{17}$ ions/cm^2.

As we can see in Figure 5.21, there is a huge modification in the spectra of the implanted samples compared with the reference sample (Pentacene film 300 nm thick). The spectra show an intensity of the absorption increasing with the ion dose, probably because there are more defects due to the implantation so an higher trapping and absorption of the photons. In the case of the implant with low doses ($1 \cdot 10^{16}$ ions/cm^2) the spectra seems even without any particular shape. Actually the spectra of all the implanted samples are probably the overlap of the Pentacene spectra and another material, as the characteristic peaks of Pentacene are still visible in the higher implants, even if masked by another high signal. Furthermore, they show the typical Davydov splitting of a 50 nm Pentacene layer, probably the only layer, near the quartz interface, that is still pure Pentacene. This is extremely important if we want to build an OFET because it needs a channel of pure Pentacene with no ion implanted inside to work properly as a transistor.

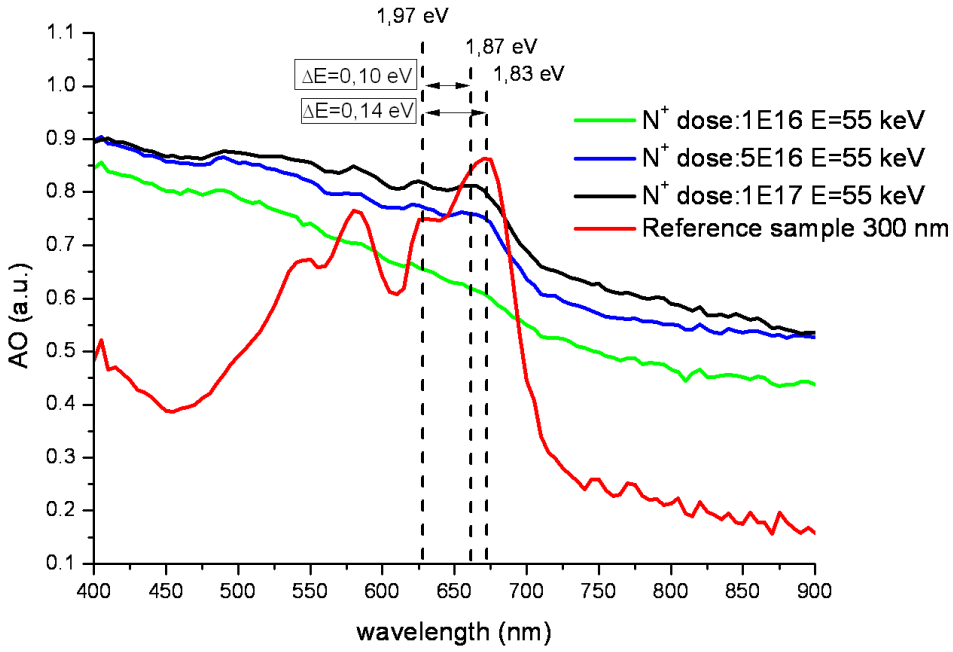

Figure 5.21: Optical absorption as a function of the wavelength for Pentacene films 300 nm thick: reference sample and implanted with different doses of N^+ ions with beam energy 55 keV. The arrows show the Davydov splitting for reference (ΔE=0,14 eV) and the most implanted sample (ΔE=0,10 eV).

It's interesting to notice that the spectra of the implanted ones show a behavior more similar to a conductor, i.e. the absorption decreases linearly as the wavelength of the photons increases. This will be in good agreement with the proved increase of the conductivity described in paragraph 5.4. The optical absorption was carried on also for

higher wavelengths (till 1500 nm) to verify if other structures that could be correlated to other materials were present in the spectra, but actually any other peak was observed (see Figure 5.22).

The optical spectra obtained are in very good agreement with the measurements obtained by Li[51] and Das[44] described in paragraph 2.4.

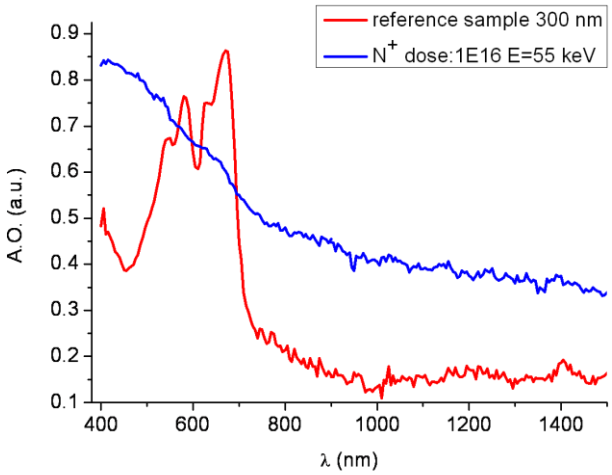

Figure 5.22: Optical absorption in the range 400-1500 nm of the reference sample (Pentacene 300 nm thick) and of one implanted film (N^+ ions with dose= $1 \cdot 10^{16}$ at 55 keV of energy beam).

5.3 Charged species: XPS measures

X-ray photoelectron spectroscopy (XPS) is a quantitative spectroscopic technique that measures the elemental composition, empirical formula, chemical state and electronic state of the elements that exist within a material. XPS spectra are obtained by irradiating a material with a beam of X-rays while simultaneously measuring the kinetic energy and number of electrons that escape from the top (1 to 10 nm) of the material being analyzed (see Figure 5.23). XPS requires ultra-high vacuum (UHV) conditions because electron counting detectors in XPS instruments are typically one meter away from the material irradiated with X-rays. XPS is a surface chemical analysis technique that can be used to analyze the surface chemistry of a material in its "as received" state, or after some treatment, in the case of our research after the exposure to ion implantation.

A typical XPS spectrum is a plot of the number of electrons detected as a function of the binding energy of the electrons detected. Each element produces a

characteristic set of XPS peaks at characteristic binding energy values that directly identify each element that exists in or on the surface of the material being analyzed. These characteristic peaks correspond to the electron configuration of the electrons within the atoms, e.g., 1s, 2s, 2p, 3s, etc. The number of detected electrons in each of the characteristic peaks is directly related to the amount of element within the area (volume) irradiated. To generate atomic percentage values, each raw XPS signal must be corrected by dividing its signal intensity (number of electrons detected) by a "relative sensitivity factor" (RSF) and normalized over all of the elements detected. It is important to note that XPS detects only those electrons that have actually escaped into the vacuum of the instrument. The photo-emitted electrons that have escaped into the vacuum of the instrument are those that originated from within the top 10 to 12 nm of the material. All of the deeper photo-emitted electrons, which were generated as the X-rays penetrated 1– 5 micrometers of the material, are either recaptured or trapped in various excited states within the material. For most applications, it is, in effect, a non-destructive technique that measures the surface chemistry of any material.

X-ray photoelectron spectroscopy and ion sputter depth profiling analyses were done with a Physical Electronics 5600ci multi-technique surface science system at the Los Alamos National Research laboratory. In profile mode XPS data was collected in medium energy resolution in order to increase signal intensity, and for the core level photoemission spectra shown here in high resolution (better than the intrinsic chemical linewidths) for more careful chemical analysis and assignments. Ion sputtering for the depth profile analysis was done using 4 keV Ar^+ ions at an approximate rate of 2 nm/minute erosion rate. XPS data acquisition was alternated with ion sputtering to obtain depth resolved information for the profile. Standard relativity sensitivity factors specific to the instrument were used to convert XPS peak area intensity to relative atomic concentration.

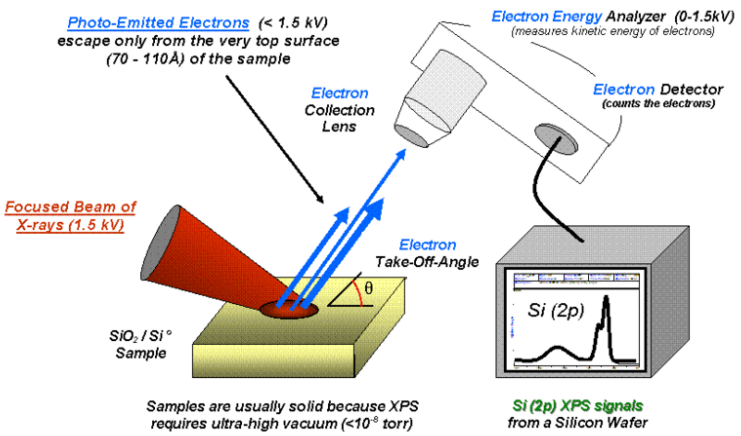

Figure 5.23: Working principles and basic components of a XPS system.

We have carried out depth-resolved XPS analyses to assess the chemical structure of N^+ and Ne^+ implanted samples and the Pentacene matrix layers by alternating XPS analyses with Ar ion sputter etching (4 keV) to form a sputter depth profile. Extensive XPS investigations were performed on both untreated and ion-implant treated specimens. This included replicate analysis, angle resolved XPS measurements in order to look for chemical differences in the near surface region (<10 nm) with depth into the material, and sputter ion XPS depth profiles to understand chemistry and elemental concentration through the thickness of the film, from the top, air exposed surface, through to the substrate where the primary electronic characteristics are active.

The data shown in Figure 5.24 and Figure 5.25 are representative of various XPS analysis performed on the thin film Pentacene system, and show unusual detail in the chemical composition of the film as a function of depth. As shown in Figure 5.24a, no Ne^+ signal was detectable with sputter profile XPS analyses on Ne-implanted samples, indicating (as expected) that implanted Ne^+ did not form bonds with the hydrocarbon matrix, and was thus lost into vacuum prior to, or during, XPS analyses. Figure 5.24b shows the XPS depth profile for a N^+ implanted layer (25 keV and $5 \cdot 10^{14}$ cm^{-2} dose). The concentration of the implanted N^+ in the Pentacene is maximized at 4.5% atomic concentration (relative to carbon) at a depth of about 76 nm from the top surface in a Gaussian-like distribution as expected from the implant simulations (paragraph 5.1.1). We have identified the presence of two main N-related chemical states, consistent with –C–N– (398.1 eV), and –C≡N (nitrile functional 399.7 eV) functional terminations on the aromatic rings (Figure 5.25a)[(91)]. A minor third component at higher binding energy is indicative of the presence of $–NH_3^+$. This higher binding energy is consistent with ionic ammonium-like functionality. These observations confirm that N^+ reacts with the hydrocarbon matrix and induces the activation/formation of both additional dipole layers (relative to virgin Pentacene) and stable positive charge groups within the Pentacene layer. The observed broadening of the C1s peak to higher binding energy when N^+ is present in the organic matrix (Figure 5.25a), is consistent with the activation of a C–N functionality. The only difference in the two C1s XPS traces in Figure 5.25a is the presence (red trace) or absence (green trace) of implanted N in the virgin Pentacene. An equivalent depth profile of the virgin Pentacene does not show these differences, and as such, the differences are clearly due to chemical interaction (bonding) of N with C in the structure of Pentacene. The N1s spectrum at the same depth (Figure 5.25b) also corroborates this by showing various chemical functionalities of N interacted with the C in the structure of Pentacene. It is clear that the differences are due to N incorporation chemically with the Pentacene matrix. These modifications lead to a different polarizability with respect to the pure Pentacene that affects the resistivity of the material.

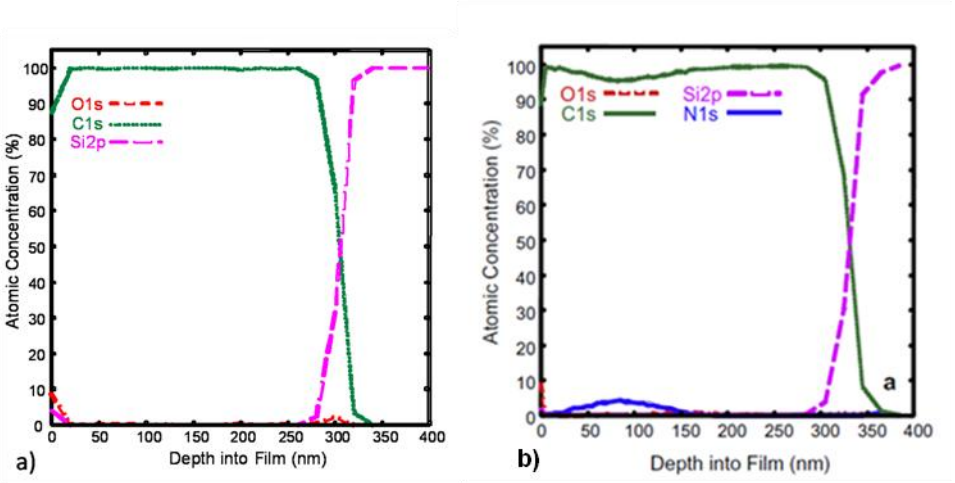

Figure 5.24: Depth-resolved X-ray photoelectron spectroscopy (XPS) analyses for Pentacene thin films, 300 nm thick, a) N^+ implanted and b) Ne^+ ion implanted at 35 keV with a dose of $1 \cdot 10^{14}$ ions/cm^{2} [83].

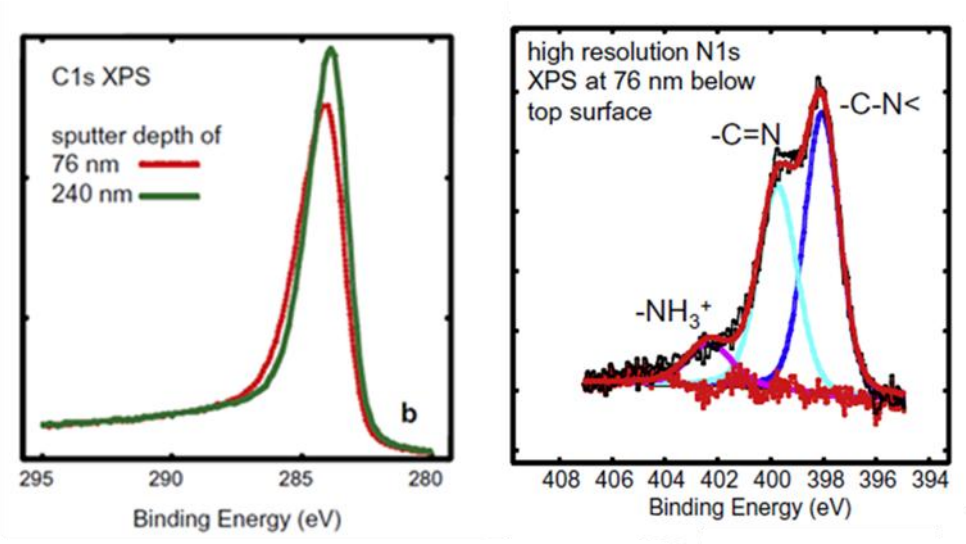

Figure 5.25: Depth-resolved X-ray photoelectron spectroscopy (XPS) analyses for N^+ implanted OTFTs (ion energy 25 keV, dose $5 \cdot 10^{14}$ cm^{-2}). a) shows the modification in the chemical environment of C in the presence of N (depth of 76 nm). b) shows the deconvolution into the three main chemical components of the N1s peak at a film depth of 76 nm [83].

5.4 Enhancement of conductivity

The electrical characterization was carried on with the *four-contacts* method (see Figure 5.26), to avoid contact resistances, in air at room temperature. The results showed a very interesting effect: the resistivity (the reciprocal of the conductivity) of

the film has a huge decrease both for N^+ and Ne^+ ions compared to the not implanted sample. This consequence is present also in the literature of ion implantation of polymers (see paragraph 2.4). In particular we discovered also that N^+ ion implantation shows a huge change increasing the dose of ions implanted or the energy beam.

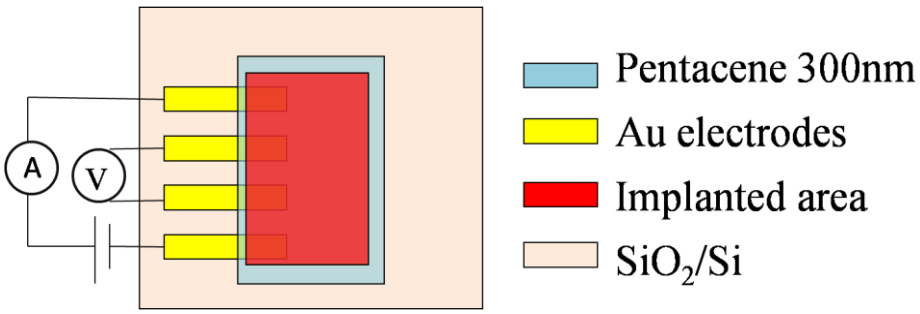

Figure 5.26: Left: schematic circuit for the four-contacts measurements. Right: the colored rectangles represent a legend of the materials of the layers.

In Figure 5.27 the logarithmic plot of ρ/d is reported, where ρ is the resistivity and d is the thickness of the Pentacene layer. We decided to plot ρ/d instead of R because the devices had different geometries (contacts length and distance) and in this way the obtain a parameter comparable for each sample. The decrease of ρ/d, when we implant N^+ ions at 25 keV, compared to reference sample, goes from 4 to even 7 orders of magnitude respectively for $1 \cdot 10^{16}$ ions/cm^2 or $5 \cdot 10^{16}$ ions/cm^2, whereas at 65 keV the decrease goes from 7 to 9 orders of magnitude compared to not implanted one. Finally at the highest energy of 110 keV, with a dose of N^+ equal to $5 \cdot 10^{16}$ ions/cm^2, the ratio ρ/d decreases of near 10 orders of magnitude compared to reference sample. As regards Ne^+ ion implantation, at 35 keV there is a decrease of 5 orders of magnitude compared to reference sample, but the interesting effect is that there are quite similar results for the two different doses $3 \cdot 10^{16}$ and $6 \cdot 10^{16}$ ions/cm^2 and also with higher energy (65 keV). An hypothesis to explain this behavior is described in paragraph 5.3. The parameter ρ/d remains stable during time for at least 800 hours, as show the results reported in Figure 5.28.

Thus, in conclusion, these experiments show that:

1- N^+ and Ne^+ ion implantation create the same damage on Pentacene (see paragraph 5.1.1) and so the conductivity change as explained in paragraph 2.4 similarly to the implantation on polymers.
2- N^+ ions change the conductivity much more than Ne^+ ions because there is an additional effect due to the implantation of stable charged species, like a doping effect, observed only for N^+ ions.

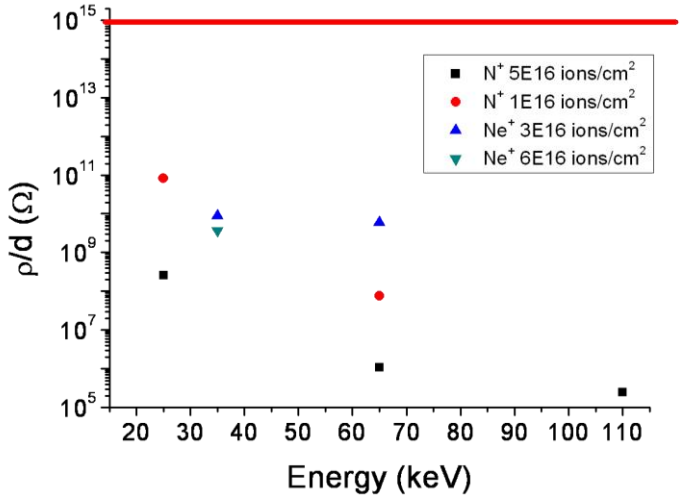

Figure 5.27: Logarithmic plot of the resistance as a function of energy beam and doses of ions N^+ or Ne^+. The red line is indicative of the sample of Pentacene not implanted (300 nm thick).

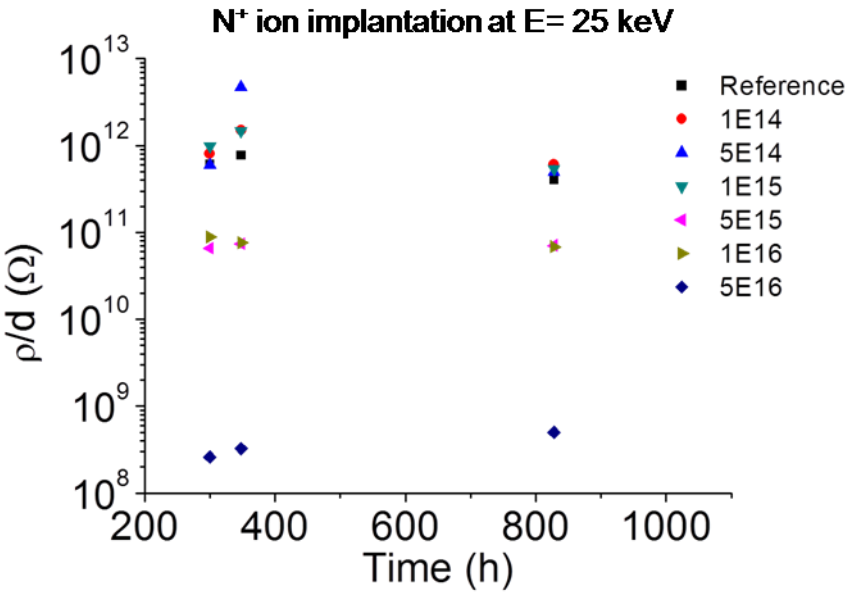

Figure 5.28: Evolution in time of the parameter ρ/d, as a function of the ion dose (ions/cm^2), for N^+ ion implantation at energy beam 25 keV of Pentacene films 300 nm thick.

6 Ion implanted Pentacene OTFTs

The results obtained by Feng[92] demonstrated that ion implantation not only changed the electrical conductivity of polyaniline but also significantly reduced its degradation to the moisture exposure by creating a dense, hermetic layer near the polyaniline surface through ion–polymer interactions. However, the effects of ion implantation have never been investigated neither on small molecule organic semiconductors, such as Pentacene, widely studied thanks to its excellent transport performance, nor on fully operating organic devices. So, in collaboration with the University of Cagliari (Department of Electrical and Electronic Engineering) and with the Los Alamos National Research laboratory, this hypothesis to find a stabilization of OTFTs of Pentacene implanted with ions was carried on, as we will see, in this chapter. A photograph of the typical OTFTs used in my research is reported in Figure 6.1a. The channel width of the OTFT is 5 mm and the length is 50 μm, as in the magnified photograph of one of the transistor reported in Figure 6.1b.

The results described in the paragraph 6.1 investigate the single ion implantation on OTFT of Pentacene 300 nm thick; in particular paragraph 6.1.1 focus on the lifetime-enhancing effects induced on Pentacene OTFTs by a controlled low-energy implantation of Ne^+, N^+ ions. These effects concern the main transport parameters of the material, such as its carrier mobility and threshold voltage, that are not only preserved after ion implantation but even stabilized on a longer time scale. The interesting consequence is that the mobility is stabilized by Ne^+ ions and the threshold voltage by N^+ ions. In fact, the modifications induced by Ne^+ or N^+ ion implantation positively affect the stability of only one of this two electronic parameters of the device.

In paragraph 6.1.2, I will link the XPS measurements, already shown in chapter 5.3 for a Pentacene film, to this interesting consequence of pinning of the device threshold voltage to high voltage in a Pentacene OTFT, due to a controlled ion implantation of N^+ ions that generate charged species inside the Pentacene layer (as in chapter 5.3).

Other two types of ions were implanted on OTFTs, F^+ or S^+ ions (paragraph 6.1.3). A very high and stable mobility is achieved with F^+ ions whereas no good effects are visible on the threshold voltage; as regard S^+ ions no improvements of the device were obtained, in fact, even if it allows the stabilization of the threshold voltage, the value of V_t will change considerably from the initial value Vt_0. To explain this behavior the same line of reasoning used in paragraph 6.1.2 could be followed also for S^+ ion implantation effects on V_t.

Finally, in paragraph 6.2 it's described the extremely positive effect of the co-implantations of the ions N^+ and Ne^+ and expecially of N_2^+ and Ne^+. The last one, in

fact, allows the best solution against aging effects due to the great stability at the same time of both the parameters: mobility and threshold voltage.

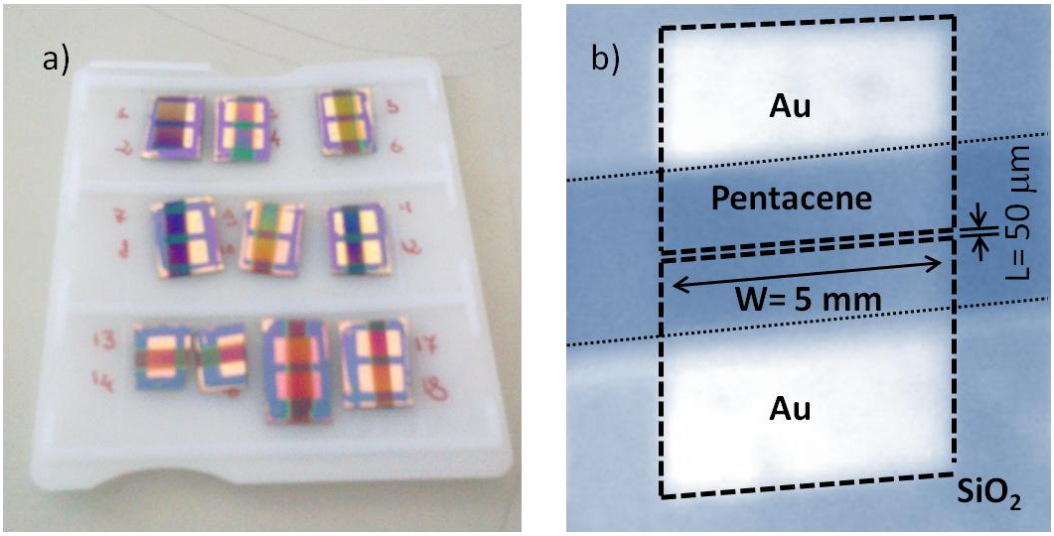

Figure 6.1: a) OTFTs with Pentacene layer 300 nm thick, virgin and ion implanted; b) magnified image of an OTFT with the dimensions of the channel and a description of the areas: SiO_2 substrate, two Au pads and overall a Pentacene strip.

6.1 Single Ion implantation

The variations induced by ion implantation in the OTFT main electrical transport parameters, such as charge carrier mobility and threshold voltage, have been measured for several samples implanted with different types of ions at different doses and different beam energies. The first electrical and optical measurements were carried on with OTFTs implanted with N^+ or Ne^+ ions, after doing all the structural measurements described in chapter 5. At a later stage a second batch of samples was built, they are OTFTs implanted with new ion species: F^+ and S^+. These two types of ions give different electrical and optical results: F^+ implants have led to a very stable and high mobility, whereas S^+ implants gave a stable V_t but with a huge initial shift at low voltage compared with V_{t0} before implantation. For these samples the structural characterization isn't carried out yet. In conclusion, the samples used to check the effect of ion implantation on the electrical parameters of the OTFTS are reported in Table 6.1. The configuration of the OTFTs is the same described in Figure 4.10 and all of them are made of a Pentacene layer 300 nm thick, implanted as in Figure 5.1.

6.1.1 N^+ or Ne^+ ion implantation

Figure 6.2 and Figure 6.3 report the values for the relative mobility (μ/μ_0) and the relative threshold voltage ($Vt\text{-}Vt_0$) obtained as a function of the dose for N^+ ions at 25 keV and for Ne^+ ions at 35 keV. The effects of N^+ ions as a function of increasing energy are reported instead in Figure 6.4. The average carrier mobility and threshold voltage measured over 50 OTFTs before implantation were $\mu_0 = 0.02 \pm 0.01$ cm^2/Vs and $V_{t0} = -21 \pm 10$ V, respectively.

Despite the large spread in μ_0 and V_{t0}, it is noteworthy that devices with very different starting in μ_0 and V_{t0} values but implanted with the same dose/energy behave in a very reproducible way (as shown in more detail in Table 6.2 and Table 6.3). On the contrary, if we implant with a different ion dose (more than two orders of magnitude) two samples with an very similar initial mobility value, we record a huge difference in the mobility degradation (see Figure 6.2a and Figure 6.3a). These observations clearly indicate that the effects induced by ion implantation override the existing morphological/functional differences in the starting OTFT devices.

a)

Ion	Dose (ions/cm^2)	Beam Energy (KeV)
N^+	$1x10^{14}$	25
N^+	$5x10^{14}$	25
N^+	$1x10^{15}$	25
N^+	$5x10^{15}$	25
N^+	$1x10^{16}$	25
N^+	$5x10^{16}$	25
N^+	$1x10^{17}$	25

b)

Ion	Dose (ions/cm^2)	Beam Energy (KeV)
N^+	$5x10^{15}$	25
N^+	$5x10^{15}$	35
N^+	$5x10^{15}$	45
N^+	$5x10^{15}$	55

c)

Ion	Dose (ions/cm^2)	Beam Energy (KeV)
Ne^+	$6x10^{13}$	35
Ne^+	$3x10^{14}$	35
Ne^+	$6x10^{14}$	35
Ne^+	$3x10^{15}$	35
Ne^+	$6x10^{15}$	35
Ne^+	$3x10^{16}$	35
Ne^+	$6x10^{16}$	35

d)

Ion	Dose (ions/cm^2)	Beam Energy (KeV)
Ne^+	$3x10^{14}$	35
Ne^+	$3x10^{14}$	45
Ne^+	$3x10^{14}$	55
Ne^+	$3x10^{14}$	65
Ne^+	$3x10^{16}$	35
Ne^+	$3x10^{16}$	65

e)

Ion	Dose (ions/cm2)	Beam Energy (KeV)
F^+	30	3.83E13
F^+	30	3.83E14

f)

Ion	Dose (ions/cm2)	Beam Energy (KeV)
S^+	1.98E14	50 keV

Table 6.1: Implants parameters of the samples: OTFTs implanted with N^+ ions a) at different doses and b) at different beam energies Ne^+ ions c) at different doses and d) at different energies; OTFTs implanted e) with F^+ ions at different doses and f) with S^+.

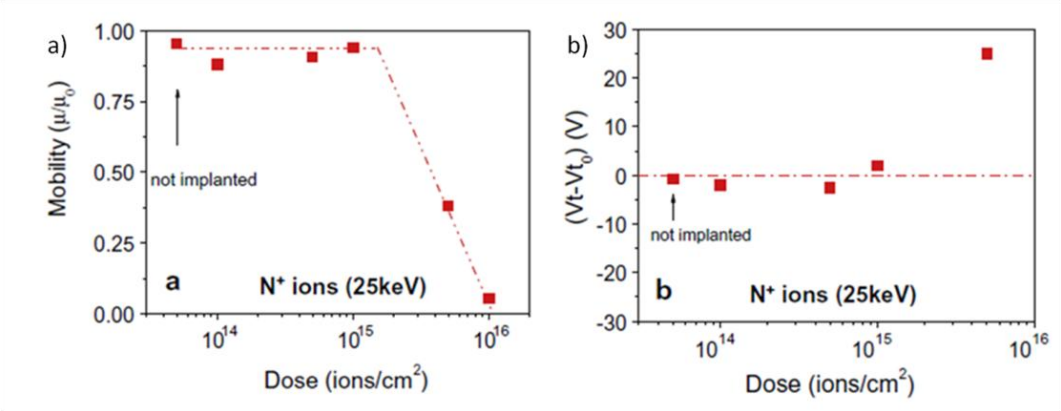

Figure 6.2: Relative modification in a) the charge carrier mobility (μ) and b) the threshold voltage (V_t) of OTFTs implanted with 25 keV N^+ ions as a function of the ion dose [82] [83].

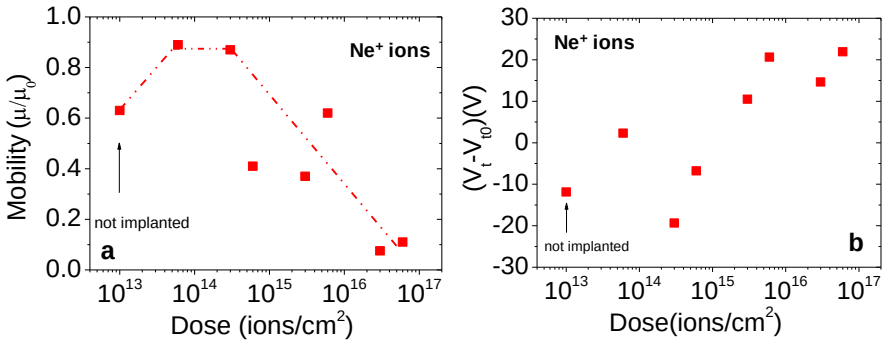

Figure 6.3: Variations induced on the OTFT main transport parameters (mobility μ and threshold voltage V_t) after 35 keV Ne^+ implantation at different doses [83].

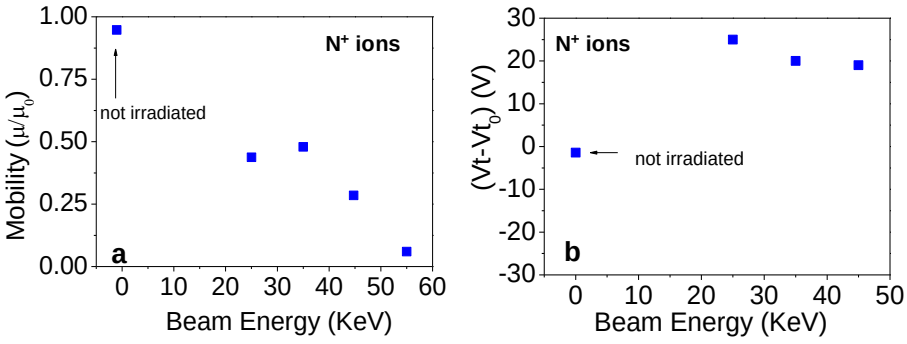

Figure 6.4: Variations induced on the OTFT main transport parameters (mobility μ and threshold voltage V_t) after N^+ implantation at a dose $5x10^{15}cm^{-2}$ [82] [83].

Ne^+ doses (cm^{-2})	μ_0 (cm^2/Vs)	μ_1 after implantation	μ_1/μ_0	μ_2 after 492 h	μ_2/μ_0	μ_3 after 1200 h	μ_3/μ_0
Reference	$3.5x10^{-2}$	$2.2x10^{-2}$	0.64	$1.5x10^{-2}$	0.43	$1.6x10^{-2}$	0.46
$6x10^{13}$	$6.5x10^{-3}$	$5.6x10^{-3}$	0.86	$4.2x10^{-3}$	0.65	$5.0x10^{-3}$	0.77
$1x10^{14}$	$1.4x10^{-2}$	$1.1x10^{-2}$	0.78	$1.0x10^{-2}$	0.72	$8.0x10^{-3}$	0.57

Table 6.2: Variations in the mobility of OTFTs devices with different starting μ_0 values after implantation with the a similar dose of 35keV Ne^+ ions [(83)].

Ne^+ doses (cm^{-2})	μ_0 (cm^2/Vs)	μ_1 after implantation	μ_1/μ_0	μ_2 after 492 h	μ_2/μ_0	μ_3 after 1200 h	μ_3/μ_0
Reference	$3.5x10^{-2}$	$2.2x10^{-2}$	0.64	$1.5x10^{-2}$	0.43	$1.6x10^{-2}$	0.46
$6x10^{13}$	$6.5x10^{-3}$	$5.6x10^{-3}$	0.86	$4.2x10^{-3}$	0.65	$5.0x10^{-3}$	0.77
$6x10^{15}$	$6.5x10^{-3}$	$4.0x10^{-3}$	0.61	$3.3x10^{-3}$	0.51	$2.4x10^{-3}$	0.37

Table 6.3: Variations in the mobility of OTFTs devices with very similar starting μ_0 values after implantation with very different doses ($6x10^{13}$ cm^{-2} and $6x10^{15}$ cm^{-2}) of 35keV Ne^+ ions [(83)].

The first value of the relative mobility of the not-implanted reference samples differs from one in Figure 6.2a since it is determined using the mobility value of the reference samples re-measured after all the other samples had been exposed to ion implantation (there is a sizeable time-lag between the fabrication of the devices, their implantation and the measurement of their mobility). In this way, the mobility used to determine the first data point of Figure 6.2a has been measured at the same time, both for the reference and the implanted ones. The same considerations apply to the non-zero value of the first data point for the not-implanted devices in Figure 6.2b. The interesting result is that the OTFT performance is seriously affected only for doses higher than $5 \cdot 10^{14}$ ions cm^{-2} for both types of ions. No particular trend can be detected in the mobility and threshold voltage variation as a function of the beam energy for N^+ implantation. The energy plots are not available for Ne^+ ions since for beam energies higher than 35 keV, the devices lose their field effect transistors behaviour, indicating that these conditions severely damage the device active channel.

The molecular electronic density of states distribution has been investigated by photocurrent (PC) spectroscopy analyses to assess the modifications induced at the molecular level on the electronic transport properties. PC analyses were carried out on all OTFTs except on those that have been implanted at the highest doses/energies and that, therefore, had completely lost their device behavior. PC spectra of OTFTs

implanted with 25 keV N^+ ions at different doses are shown in Figure 6.6 and provide a clear indication of the presence of an undamaged active Pentacene film. The same behaviour is followed by the OTFT implanted with 35 keV Ne^+ at different doses (Figure 6.7). In fact, as already said in chapter 4.1, two phases coexist in Pentacene films, called the thin-film phase, characterized by a molecular spacing of 15.5 Å and dominant for thicknesses below 50 nm, and the bulk phase, characterized by a spacing of 14.5 Å and dominant for films over 150 nm thick. The different molecular spacing derives from the different tilt angle of the molecular *herringbone* packing structure, which induces a different coupling of intermolecular p-electron systems.

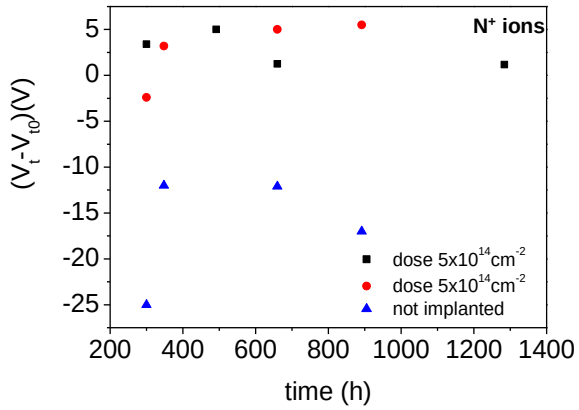

Figure 6.5: Evolution with time of the threshold voltage V_t for OTFTs with different V_{t0}, implanted with identical conditions (25 keV N^+ ions, dose of $5x10^{14}cm^{-2}$)[83].

The density of states distribution obtained from PC spectra can provide information on the dominant phase of the Pentacene film by assessing the Davydov splitting of the first absorption band. The Davydov splitting of the first absorption band is correlated to modifications in the film molecular structure and packing and it increases when passing from the thin film to the bulk phase (see chapter 4.1.3).

Our measurements (Figure 6.6, Figure 6.7) indicate that, as the implantation doses increase, the active layer passes from a bulk phase dominated (i.e. a film >150 nm thick) to a thin-film phase dominated structure (i.e. about 50 nm thick). Figure 6.6a shows the gradual decrease in the Davydov splitting with increasing implantation dose starting from the reference non-implanted sample (300 nm thick); its further evolution is highlighted in Figure 6.6b, where the PC spectra of OTFTs implanted at the highest tested doses are compared with a non-implanted, 50 nm thick, reference sample.

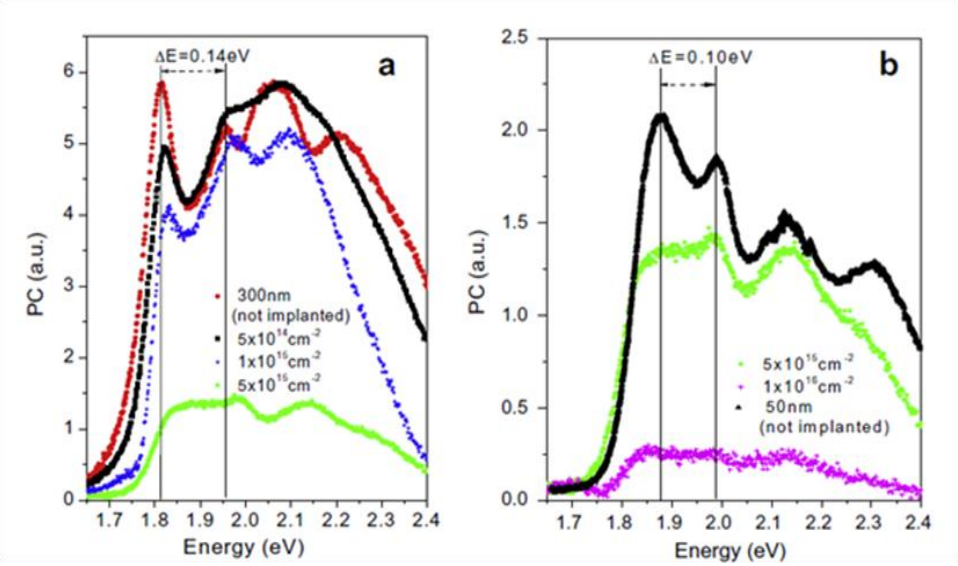

Figure 6.6: Photocurrent spectra of OTFTs implanted at different N^+ ion doses. The ion energy is 25 keV. The spectrum of a not-implanted 300 nm thick reference sample is reported in (a) and the spectrum of a not-implanted 50 nm thick reference in (b). The reduction in the Davydov splitting as the Pentacene layer thickness decreases is highlighted [(82)(83)].

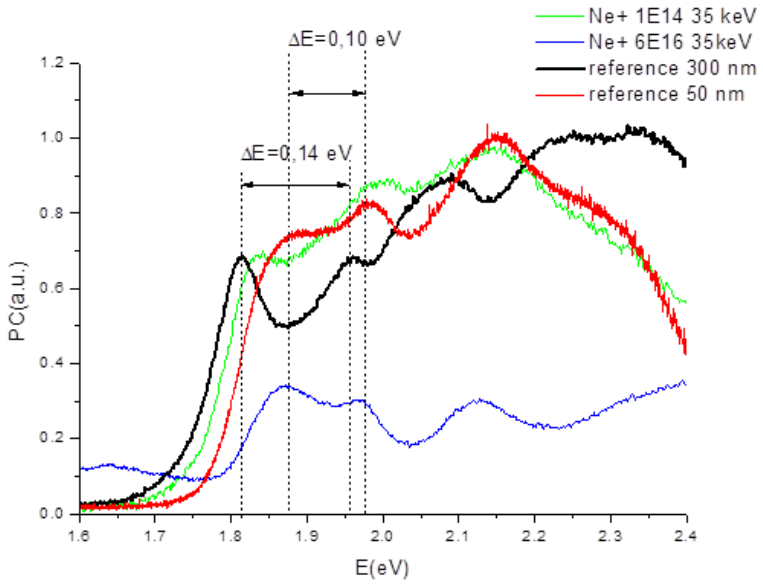

Figure 6.7: Photocurrent spectra of OTFTs implanted at different Ne^+ ion doses. The ion energy is 35 keV. The spectra of a not implanted 300 nm and 50 nm thick reference samples are reported. The Davydov splitting of the reference samples is highlighted to identify the intermediate behaviour of the implanted OTFTs.

In Figure 6.7, the 35 keV Ne^+ implanted OTFTs at different doses are compared with the reference samples 300 nm and 50 nm thick, and as before there is a gradual decrease of the Davydov splitting from the lowest dose to the highest one. Similarly, also the mobility and threshold voltage are preserved. It is noteworthy that the PC spectrum of the highest dose N^+ implanted sample ($1 \cdot 10^{16}$ ions cm^{-2}) has an extremely poor quality and, correspondingly, the OTFT device functionality is completely lost. The same dose instead don't have a negative effect when the ion implanted is Ne^+, at $6 \cdot 10^{16}$ ions/cm^2, in fact, the PC spectra is very similar to a 50 nm thick Pentacene OTFT. Nevertheless the mobility decays to one by ten, probably due to a defect created by the exposure to atmosphere before the implantation as indicated by the bump inside the gap. These PC results indicate that a thin undamaged layer of Pentacene can still be preserved under the damaged top layer after ion implantation with selected doses and energies, and this layer grants the full functionality of the implanted OTFTs. Therefore, PC measurements confirm that it is possible to preserve the full functionality of the OTFT device by properly choosing ion implantation conditions. It is noteworthy that PC spectroscopy, that provides a ″fingerprint″ of the density of states distribution on the Pentacene film, allows identifying the actual thickness of the electrically active layer left undamaged after ion implantation, without affecting the operation of the device. Other techniques usually applied to obtain information on Pentacene phases, such as X-ray diffraction, could not be easily applied to fully operational OTFTs that have also undergone ion implantation leaving their performance unaffected.

We have then monitored the evolution of the transport parameters with time in ion implanted OTFTs to test the effects of the irradiation process on the aging and degradation of the device performance. The results are extremely promising since: (i) there is a clear stabilization effect induced on carrier mobility and/or in threshold voltage for at least up to 2000 h after the implantation process; (ii) implantation with N^+ or with Ne^+ ions induces different effects. In particular, low implantation doses (up to $3 \cdot 10^{14}$ cm^{-2}) of 35 keV Ne^+ ions stabilize the carrier mobility (μ) (Figure 6.8), while implantation with selected doses and energies of N^+ ions induce a stabilization of the OTFT threshold voltage (V_t) (Figure 6.9). The stabilization of V_t is optimized (i.e. almost no V_t variations can be detected) for 25 keV ions and for doses up to $1 \cdot 10^{15}$ cm^{-2}.

It is noteworthy that higher doses and energies also induce a stabilization of V_t, even if it occurs at values that are largely shifted with respect to the reference, non-implanted device. This effect will be explained in chapter 6.1.2.

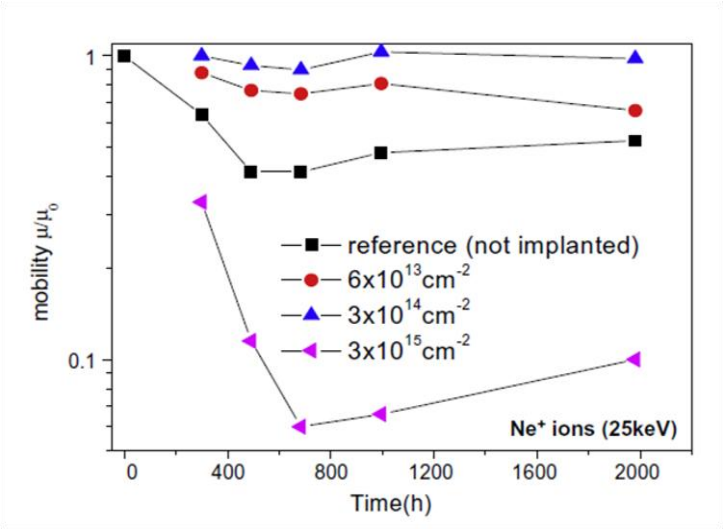

Figure 6.8: Evolution with time of the relative charge carrier mobility (μ/μ_0) in Ne^+ implanted OTFTs (ion energy 35 keV), for different ion doses[83].

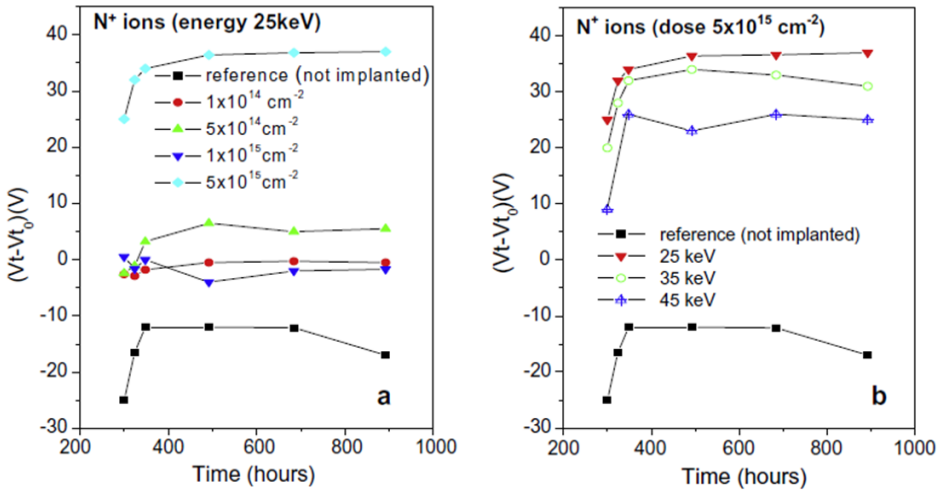

Figure 6.9: Evolution with time of the relative threshold voltage (V_t - V_{t0}) in N^+ implanted OTFTs: a) for different ion doses and same energy (25 keV); b) for different ion energy and same dose ($5 \cdot 10^{15}$ cm^{-2}) [83].

To complement the results reported in Figure 6.8 and Figure 6.9, I report here the behaviour of the threshold voltage V_t for Ne^+ implanted devices (Figure 6.10) and of the mobility μ for N^+ implanted OTFTs in Figure 6.11 as a function of time. No clear stabilization of these parameters is evident in these conditions, as opposed to what observed and reported in Figure 6.8 and Figure 6.9.

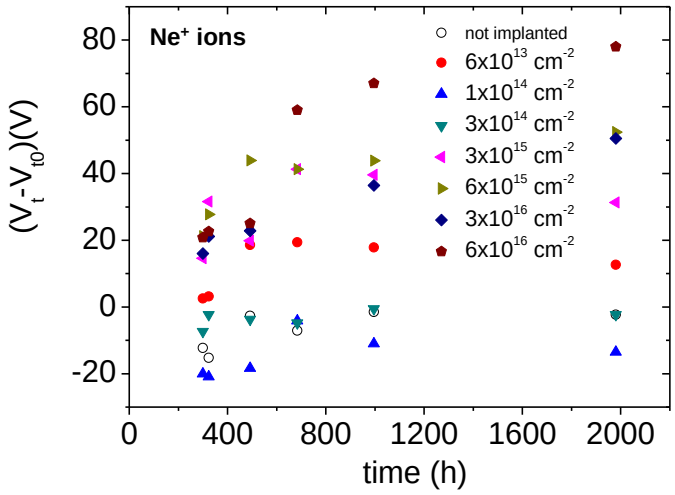

Figure 6.10: Evolution with time of the threshold voltage V_T for 35 keV Ne^+ implanted OTFTs, for different implant doses [83].

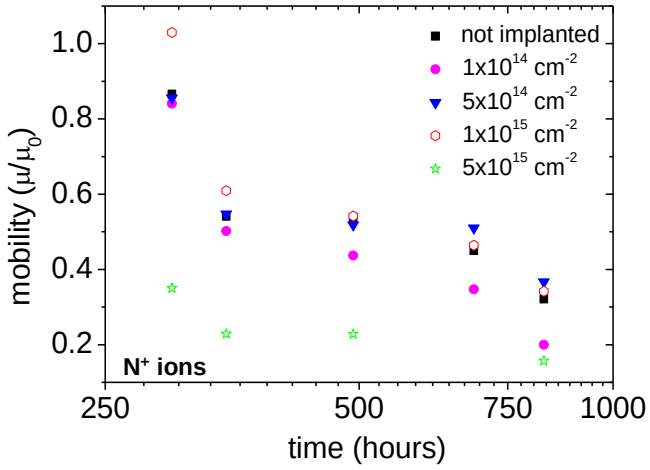

Figure 6.11: Evolution with time of mobility μ for 25 keV N^+ implanted OTFTs, for different implant doses [83].

6.1.2 Charged species: effects on V_t

The reason for the different behavior induced by implantation with N^+ or with Ne^+ ions can be ascribed to the different reactivity of the two elements. In fact, Neon is not expected to chemically interact with the organic matrix, while Nitrogenum has a high probability of reacting with the organic matrix of Pentacene once implanted within the film, as already said in chapter 5.3. Further interesting observations can be drawn from the V_t evolution with time; it is known that V_t in unaltered Pentacene progressively degrades with time due to charge trapping effects at the semiconductor/dielectric

interface. Many recent studies attribute this effect to the chemical surface structure of most dielectric layer (e.g. -OH terminations in SiO_2) [93]. In the investigated implanted devices, V_t does not significantly degrade with time (Figure 6.9), indicating that these trapping effects could possibly be neutralized or masked by another effect. Since the semiconductor/dielectric interface in itself is not directly affected by the implantation process, a possible/reasonable explanation could rely on the effects induced on the OTFT active channel by the presence of charges or modification of the material polarizability, as suggested by XPS (see chapter 5.3). In particular, our XPS results indicate that N implantation gives rise to a positively charged layer that reaches different depths, controlled by the implant energy. The measured threshold voltage shift seems to be proportional to the thickness of the undamaged layer (Figure 6.9b), i.e. to the difference between the film thickness and the implant depth. A simple effect can be invoked to qualitatively explain these data. The implanted charged layer induces an electric field that superposes to the gate field, thus pushing holes towards the insulating layer, i.e. into the device channel. As a consequence, it is necessary to apply a positive gate voltage in order to deplete the channel and to switch the device off. The same effect can also be obtained by keeping the energy constant (i.e. the implantation depth) and varying the dose (i.e. the density of the charges in the layer), as shown in Figure 6.9a. The trend in V_t shift can be again quantified by considering the ratio between the implanted charge density and the undamaged layer capacitance. More interestingly, Figure 6.9a shows how low doses ($1\cdot10^{14}$ cm^{-2}, $5\cdot10^{14}$ cm^{-2}, $1\cdot10^{15}$ cm^{-2}) induce a clear stabilization effect on V_t and, on the contrary to what happens to the reference sample and to samples implanted with higher ion doses, V_t does not differ much from V_{t0} (the value before implantation). The stabilization effect on V_t, observed also in non V_t - shifted devices, suggests that it is this superposed electric field rather than the interface charged states that determines the effective charge carrier concentration and, as a consequence, the threshold voltage.

6.1.3 F^+ or S^+ ion implantation

In the second batch of OTFTs we implanted F^+ or S^+ ions to investigate the effects on the electrical behaviour followed by those species of ions, intermediate in the periodic table between N^+ and Ne^+. The doses and energies used were decided using SRIM simulations with the purpose to avoid an excessive damage of the Pentacene layer. In Figure 6.12 we can see the trend of the mobility as a function of time for F^+ implants. It's impressive that the implantation at $4\cdot10^{13}$ ions/cm^2 (black scatters) keeps the mobility constant in time for at least 1500 hours with no decrease from the value before the implantation μ_0. The dose $4\cdot10^{14}$, instead, seems to be too high because the

value of mobility decreases compared to μ_0, even if then continues with a constant value in time.

In Figure 6.13 the evolution with time of the threshold voltage for OTFTs F^+ implanted is reported. We can notice that the stability is not completely obtained as it is instead for N^+ implants. However we can conclude that both F^+ or Ne^+ implants have a similar behaviour as they stabilize the mobility for a long time and with no substantial difference from μ_0 but they do not stabilize the threshold voltage.

As regards S^+ implants, the evolution in time of the two main electrical parameters is shown in Figure 6.14 and Figure 6.15. From the first figure we can deduct that the mobility doesn't follow a constant trend as time goes by and from the second one, we can see that there is a strong stabilization of the threshold voltage but at very much lower values than V_{t0}. A similar trend was observed also for N^+ implants (Figure 6.9), even if, in this case, the threshold voltage was stabilized at higher values than V_{t0}. A possible explanation to understand this effect is proposed in paragraph 6.1.2, i.e. the stable formation of highly electronegative fixed charges, but the XPS measurements necessary to verify the hypothesis weren't carried out yet.

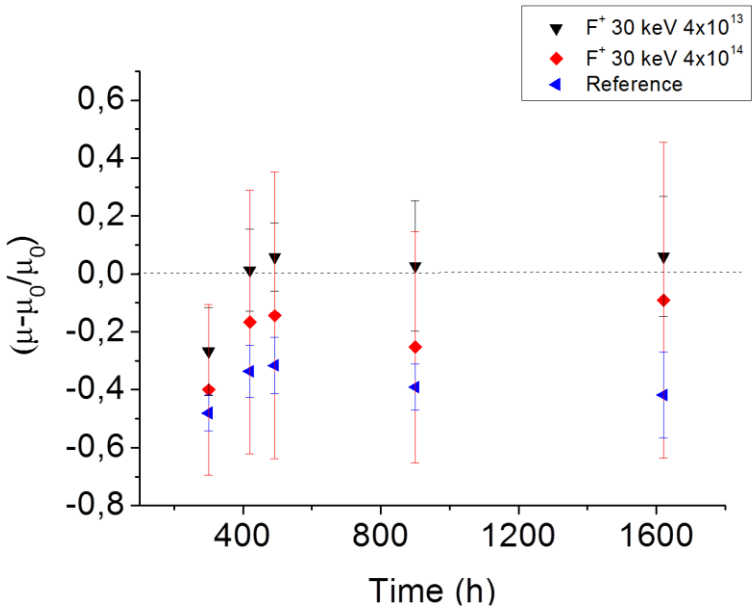

Figure 6.12: Evolution with time of the relative charge carrier mobility ($\mu-\mu_0/\mu_0$) in F^+ implanted OTFTs (ion energy 30 keV), for different ion doses.

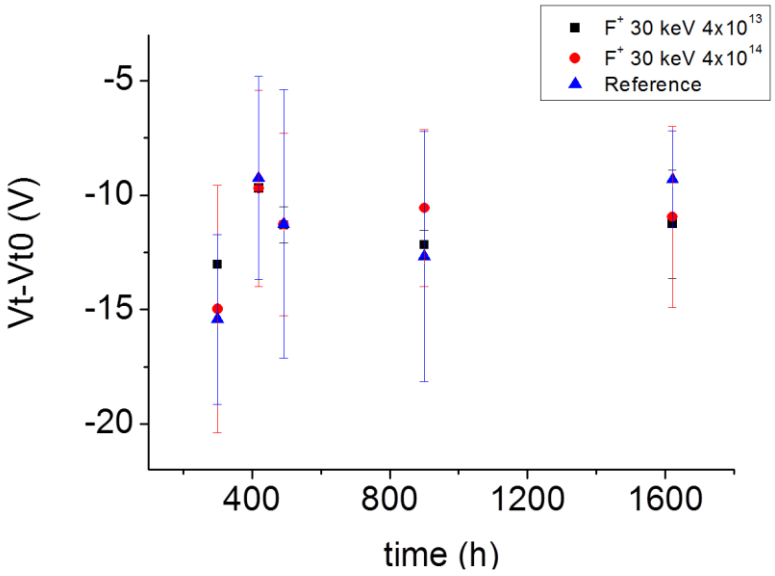

Figure 6.13: Evolution with time of the relative threshold voltage (V_t -V_{t0}) in F^+ implanted OTFTs (ion energy 30 keV), for different ion doses.

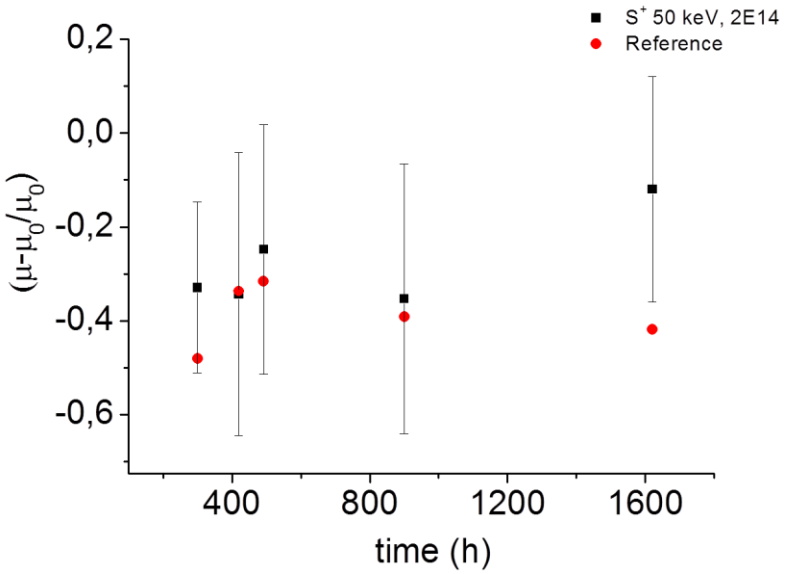

Figure 6.14: Evolution with time of the relative charge carrier mobility ($\mu-\mu_0/\mu_0$) in S^+ implanted OTFTs (ion energy 50 keV), for different ion doses.

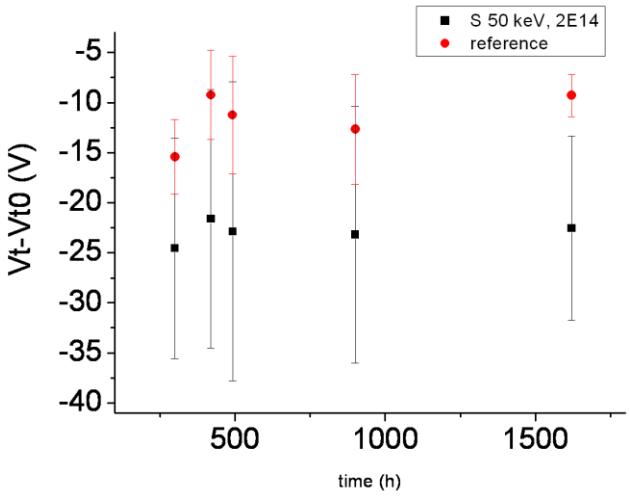

Figure 6.15: Evolution with time of the relative threshold voltage (V_t -V_{t0}) in S^+ implanted OTFTs (ion energy 50 keV), for different ion doses.

After the electrical characterization, the photocurrent spectra were carried on to state if there was a DOS modification after the implantation. In Figure 6.16 the spectra of the OTFTs implanted with F^+ and S^+ are shown and they are compared with a reference OTFT of Pentacene 50 nm thick.

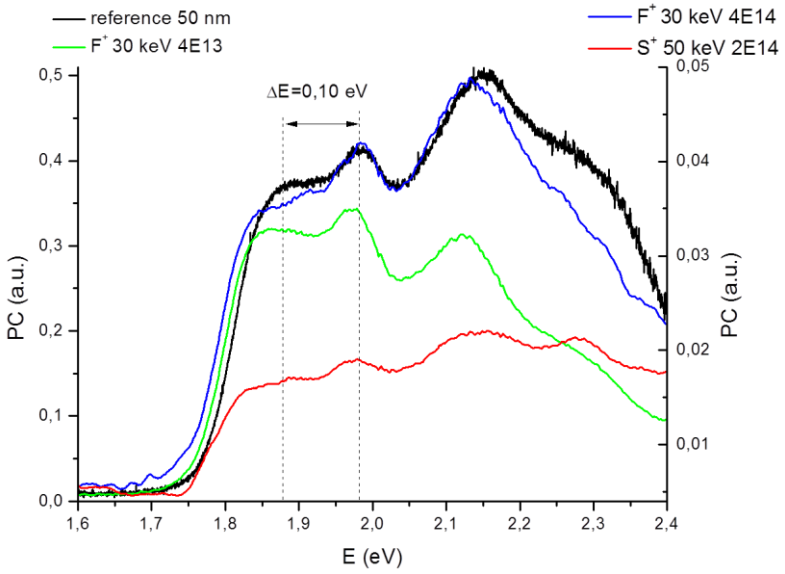

Figure 6.16: Photocurrent spectra of OTFTs implanted with F^+ (at two different doses) and with S^+ ions. For comparison a reference OTFT with Pentacene 50 nm thick is shown. The spectra of S^+ and F^+ (at high dose) OTFTs are in a different scale as they report one order of magnitude less of PC intensity.

As we can see the spectra of S^+ and F^+ (at high dose) OTFTs are in a different scale as they report one order of magnitude less of PC intensity, this is due probably to the high level of damage due to the implant. All the OTFT implanted with F^+ or S^+ ions, show a PC spectra similar in the shape to the reference sample of Pentacene 50 nm thick and have also the same Davydov splitting, as in the implants at high energies or doses described in paragraph 6.1.1. this means that there is a huge modification of the top portion of the Pentacene layer that brings to have only a thin film phase left of pure Pentacene of 50 nm, upon the 300 nm of thickness before the implantation process.

6.2 Co-implantation

Another batch of OTFTs with Pentacene 300 nm thick were co-implanted with N^+ and Ne^+ ions in order to obtain the simultaneous stability of both the electrical main parameters μ and V_t. The samples studied with their implant parameters are reported in Table 6.4: the difference between sample 1 and 2 is the order of implantation, the co-implantation of the sample 3, instead, is formed by a new ion N_2^+ and then Ne^+. The energy beam and the doses chosen are the best obtained from the previous results.

Sample	Ion	Dose (ions/cm^2)	Beam Energy (KeV)
1	N^+	25 keV	5,00E+14
	Ne^+	35 keV	1,00E+14
2	Ne^+	35 keV	1,00E+14
	N^+	25 keV	5,00E+14
3	N_2^+	25 keV	5,00E+14
	Ne^+	25 keV	2,00E+14

Table 6.4: Implant parameters of the OTFTs irradiated with N^+ and Ne^+ ions in a different order of implantation (sample 1-2) and with N_2^+ and Ne^+ (sample 3).

In Figure 6.17 and Figure 6.18 we can see the results obtained with the electrical characterization for the mobility and threshold voltage of these OTFTs as a function of time. The data show that all the solution proposed give a better result for both the parameters in comparison with the reference sample. For a clearer comparison between the samples performances, the exact numeric parameters studied, $(\mu-\mu_0)/\mu_0$ and $Vt-Vt_0$, are written in Table 6.5 and Table 6.6 as a function of time. At the end of the tables the average values of the parameters considered for each sample is reported, this information is important to see what sample has μ or Vt less degraded compared to the initial value, that means that, to have a good implant, the average value of this parameter has to be as near to zero as possible. In the last line the deviation standard σ

is reported to describe the deviation from the average value, i.e. the instability of the parameter during time, so also σ must be near to zero as much as possible to have good stability.

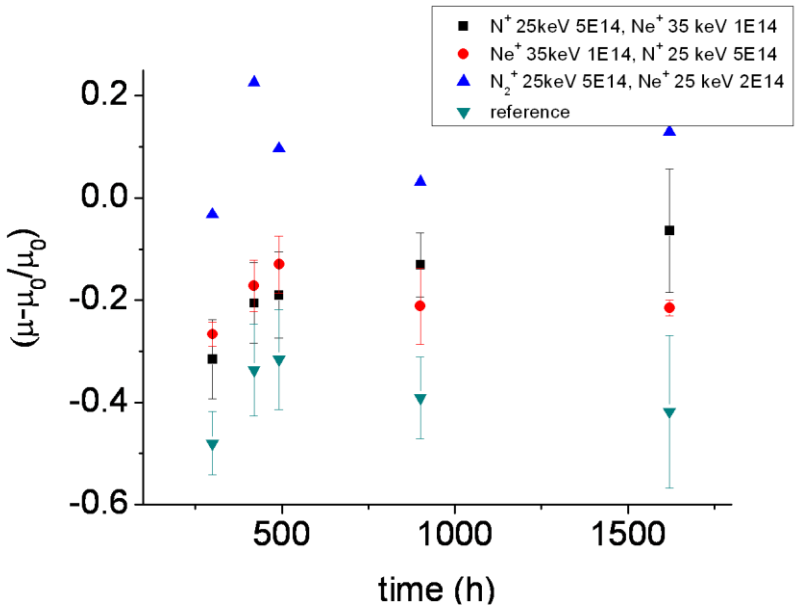

Figure 6.17: Evolution with time of the relative charge carrier mobility ($\mu-\mu_0/\mu_0$) in co-implanted OTFTs.

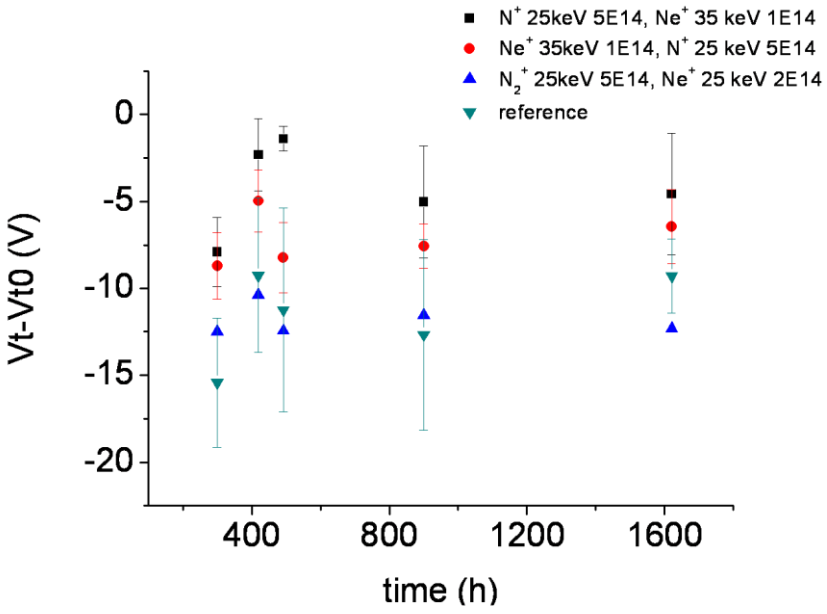

Figure 6.18: Evolution with time of the threshold voltage V_t -V_{t0} for co-implanted OTFTs.

Looking at Figure 6.17 and Table 6.5, the average value of $(\mu-\mu_0)/\mu_0$ nearer to zero is for sample 3, that means that for this sample we have the highest mobility after implantation; instead, the lower σ value is obtained for sample 2, that means that this sample has the best stability. Actually I have to underline that σ of sample 3 is not so different from σ of the sample 2.

	$(\mu-\mu_0)/\mu_0$			
Time (h)	**Sample 1 N^++Ne^+**	**Sample 2 Ne^++N^+**	**Sample 3 N_2^++Ne^+**	**Reference 300 nm**
300	-0.315	-0.267	-0.032	-0.480
420	-0.205	-0.172	0.226	-0.337
492	-0.190	-0.130	0.097	-0.316
900	-0.131	-0.212	0.032	-0.391
1620	-0.064	-0.215	0.129	-0.418
average	-0.181	-0.199	0.090	-0.388
σ	0.093	0.051	0.098	0.066

Table 6.5: Relative charge carrier mobility compared to the value μ_0 (before implantation) of implanted OTFTs and a reference sample with pure Pentacene 300 nm thick, as a function of time. In the last two lines the average values and the deviation standard σ of $(\mu-\mu_0)/\mu_0$ are expressed for all the samples. The colored boxes want to underline the lowest absolute values.

	$Vt-Vt_0$			
Time (h)	**Sample 1 N^++Ne^+**	**Sample 2 Ne^++N^+**	**Sample 3 N_2^++Ne^+**	**Reference 300 nm**
300	-7.9	-8.705	-12.48	-15.425
420	-2.31	-4.975	-10.37	-9.25
492	-1.38	-8.225	-12.44	-11.25
900	-5.025	-7.56	-11.54	-12.675
1620	-4.56	-6.45	-12.31	-9.3
Average	-4.235	-7.183	-11.828	-11.58
σ	2.550	1.496	0.900	2.585

Table 6.6: $Vt-Vt_0$, i.e. the difference between threshold voltage Vt and Vt_0 (before implantation) of implanted OTFTs and of a reference sample with pure Pentacene 300 nm thick, as a function of time. In the last two lines the average values and the deviation standard σ of $Vt-Vt_0$ are expressed for all the samples. The colored boxes want to underline the lowest absolute values.

As regard the threshold voltage (Figure 6.18 and Table 6.6), the average value nearer to zero is achieved with sample 1, that means that the Vt after implantation is not so different compared with the value before the implantation. Nevertheless the lower σ value, that means stabilization of Vt, is obtained with sample 3 with a consistent difference compared to the other samples.

I want to point the attention on the need of the stability of the threshold voltage, as this parameter has to be set for a OTFT device and that this condition is more important than the modification from the initial value Vt_0 induced by the implantation (described by the average value). On the contrary, the mobility needs to be high (so similar to the beginning value) to have an efficient OTFT and stable. In conclusion the sample with the best optimization of both the parameters, μ and Vt, is sample 3, i.e.: N_2^+ (25 keV, $5 \cdot 10^{14}$) + Ne^+ (25 keV, $2 \cdot 10^{14}$).

After the electrical characterization, also the photocurrent measurements were implemented to understand the DOS distribution and the molecular packing resulting after the co-implantation. As we can see in Figure 6.19 the PC spectra give interesting information:

1. Sample 1 has a spectra similar to the reference sample 50 nm thick, i.e. a spectra with a considerable modification of the superficial layer that preserves a pure Pentacene layer of about 50 nm at the interface with SiO_2.
2. Sample 2 presents the first peak of the Davydov splitting corresponding to the reference sample 50 nm thick but the second peak is a bit shifted to high energies. So the Davydov splitting of the implanted OTFT will be higher than that of the reference (ΔE=0,10 eV) and thus the thickness preserved of pure Pentacene could be higher than 50 nm.
3. Sample 3 shows a spectra very different from sample 1 and 2 but more similar to the reference of 300 nm. As this sample show the best performance for stabily of the parameters and less degrade of the mobility, we can say that we need an implantation that doesn't penetrate so much in the semiconductor layer leaving a thickness of pure Pentacene with an intermediate value between 300 nm and 50 nm.

To strengthen this hypothesis, a comparison with the PC spectra of the single implants with the best electrical performances shown in paragraph 6.1.1 (N^+ with energy beam: 25 keV, dose: $5 \cdot 10^{14}$ ions/cm^2 or Ne^+ with energy beam: 35 keV and dose: $1 \cdot 10^{14}$ ions/cm^2), are reported together with the spectra of sample 3 and of the reference OTFT (with Pentacene layer 300 nm thick) in Figure 6.20. It's evident the similar behavior of the spectra of the implanted OTFTs, presenting a Davydov splitting intermediate between a 300 nm and a 50 nm Pentacene layer and with a intense first peak. I want to recall that N^+ implanted OTFT stabilizes the threshold voltage, whereas Ne^+ implanted OTFT stabilizes the mobility, the co-implantation used for sample 3,

instead, allow a constant trend for both the parameters. We can see an intermediate behavior of sample 3 also in the PC spectra, as the first peak of this OTFT lies in between of the two first peaks of the other two OTFTs, i.e. also the thickness of the pure Pentacene layer at the interface with the dielectric of this OTFT must be intermediate between those of the other OTFTs.

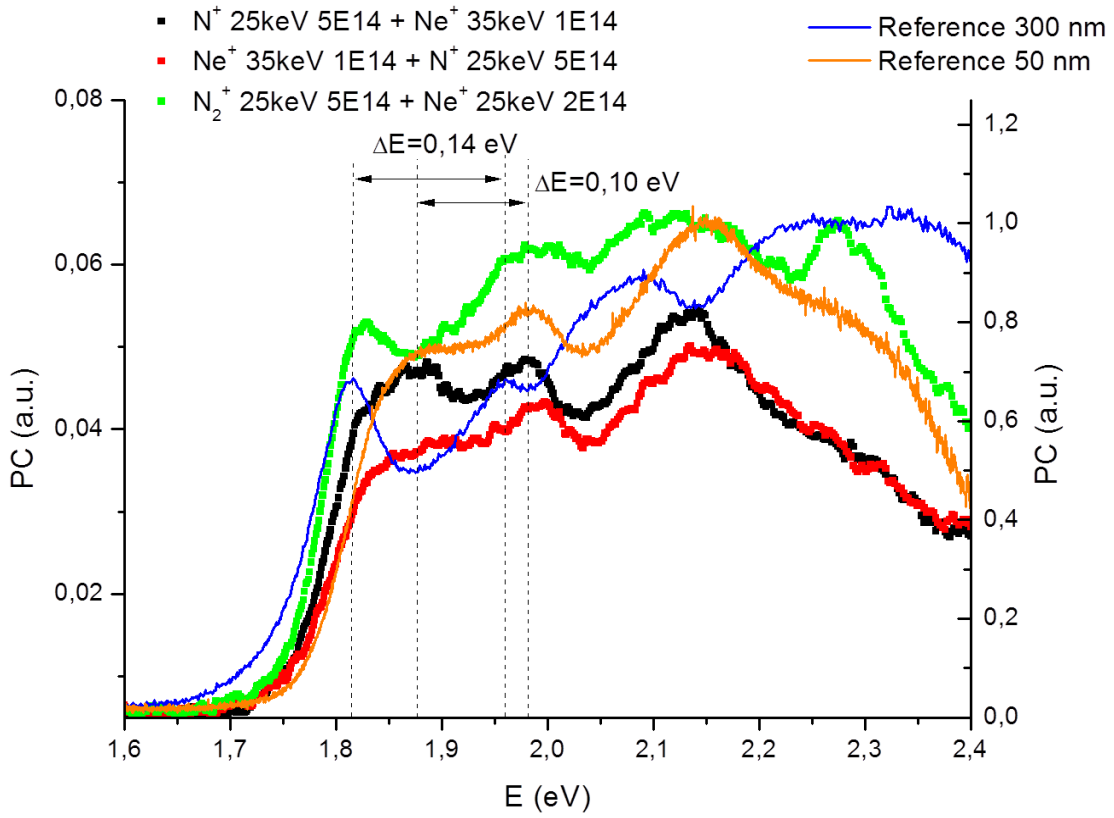

Figure 6.19: Photocurrent spectra of OTFTs co-implanted (Table 6.4) compared with reference OTFTs of Pentacene 300 nm and 50 nm thick. The spectra are reported on two different scales as the PC spectra of the implanted samples shows one order of magnitude less intensity.

By the other hand, all the other spectra presented in my research show a Davydov splitting typical of a 50 nm Pentacene layer (see paragraph 6.1); so probably the damage caused by the implantation is too high, leaving only a very thin layer of 50 nm of pure Pentacene at the interface with the dielectric that doesn't bring to a better stability of the OTFT.

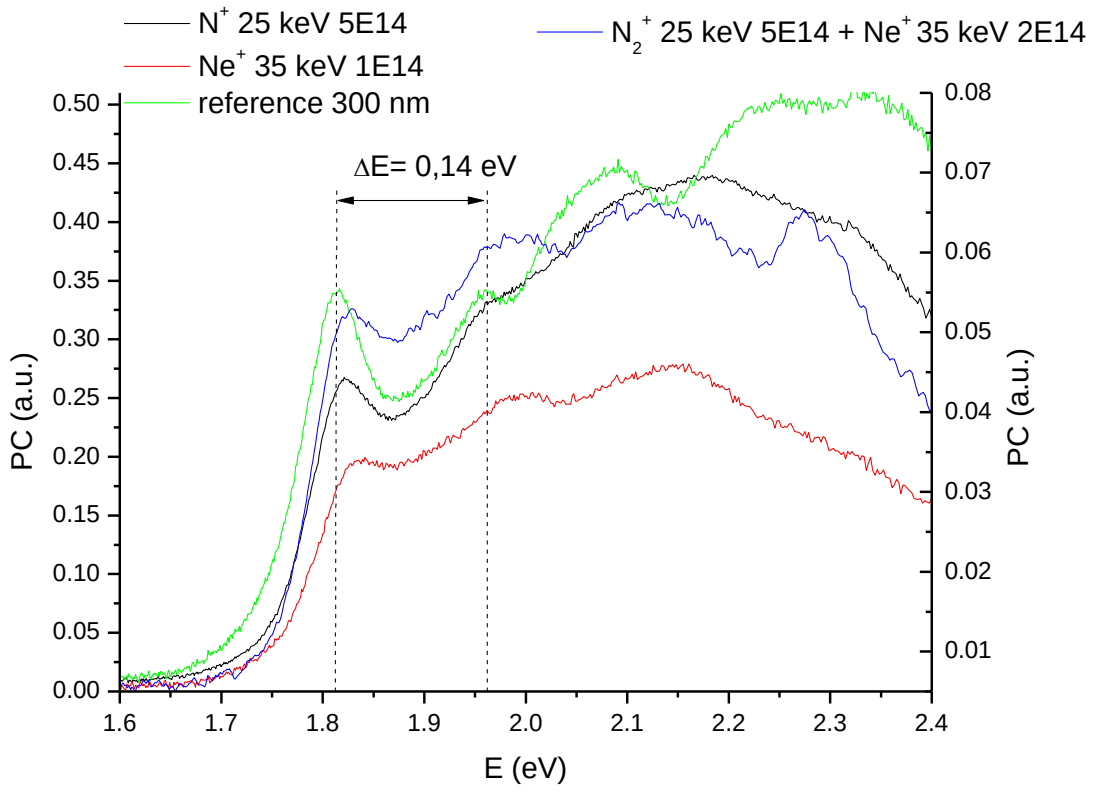

Figure 6.20: Photocurrent spectra of implanted OTFTs and of a reference sample with Pentacene layer 300 nm thick. The implanted OTFTs are the single implants N^+ or Ne^+ and the co-implant N_2^++Ne^+. This last OTFT shows a spectra with a PC intensity of one order of magnitude less than the others, so it is reported on another scale. The Davydov splitting of the reference sample is shown with the dashed lines and arrows.

In conclusion, the best solution to obtain stable electrical parameters for OTFTs of Pentacene with ion implantation is to co-implant N_2^+ ions with energy beam: 25 keV and dose: $5 \cdot 10^{14}$ ions/cm^2 and then Ne^+ ions with energy beam=25 keV and dose= $2 \cdot 10^{14}$ ions/cm^2. Thus, as the photocurrent spectra assesses, the implantation damage, necessary to encapsulate the OTFT, doesn't penetrate to much in depth but remains superficial and keeps a layer of pure Pentacene with thickness intermediate between 50 and 300 nm.

Further XPS measurements are going to be done in order to verify the presence of charged species also with these types of implants and co-implants.

7 Inkjet printed organic transistors

Solution-based processing is the key to enabling ultralow-cost circuit fabrication. This processing eliminates the need for lithography, subtractive processing, and vacuum-based film deposition. Recently, there has been great interest in the development of printed organic electronics technologies since these technologies allow the use of spin coating, drop casting, ink jet printing, spray coating, nanoimprinting, or the screen printing process. These technologies are expected to be used in low-cost, flexible displays and disposable electronics applications. As a consequence, extensive research by many groups has been actively carried out to improve the charge carrier mobility and the current modulation. Among the several possible devices, Organic ElectroChemical Transistors (OECTs) [(94)], as a subset of OFETs, have attracted particular interest for their simple fabrication and low operating voltages. Also, the capability of working in aqueous environments make OECTs suitable for biological and chemical sensing application.

In this chapter I will describe in the first paragraph the inkjet printed OTFTs made with a functionalized molecule of Pentacene, named TIPS-Pentacene, and in the second paragraph I will discuss the production of ElectroChemical Transistors, created with PEDOT-PSS as organic semiconductor.

7.1 Inkjet TIPS-Pentacene OTFTs

Pentacene unprocessability in liquid phase represents a huge limitation in terms of its deposition by means of low cost techniques as inkjet printing. Also, Pentacene has a crystalline order, often referred to as *herringbone* packing (depicted in Figure 7.2a), with only minimal π-stacking which results in a poor dispersion of the electronic bands in the solid, implying that Pentacene transport properties may be limited by its crystal packing. In order to overcome the insolubility issue, several Pentacene derivatives have been developed by substitution with different functional groups. By means of such functionalizations, also the tuning of electronic properties, such as charge injection barriers, HOMO-LUMO gaps, charge transfer rates, and molecular ordering of Pentacene can be accomplished.

Among the Pentacene derivatives developed *triisopropylsilylethynyl-substituted* (TIPS) Pentacene is the most popular and appropriate for its use in thin-film transistors[(95)]. It has sufficient solubility in common organic solvents (e.g. Toluene, Chlorobenzene, Tetrahydrofuran and Chloroform) and, in addition, the bulky functionalized groups in TIPS-Pentacene efficiently maximize π-orbital overlap. In fact,

the bulky group substitution on the central aromatic ring disrupts aromatic edge-to-face interactions, preventing the adoption of the *herringbone* packing motif, typical of the unsubstituted Pentacene crystals: the triple bond between the carbon atoms (see Figure 7.1) allows adjacent molecules to interact in a face-to-face π-stacking orientation, since the substituents are hold away from the aromatic surface. This inter-molecular interaction improves π-orbital coupling and potentially increases the carrier mobility. In Figure 7.2 the molecular packing arrangements with average distances between the π-faces in the solid state Pentacene (a) and TIPS-Pentacene (b) are shown.

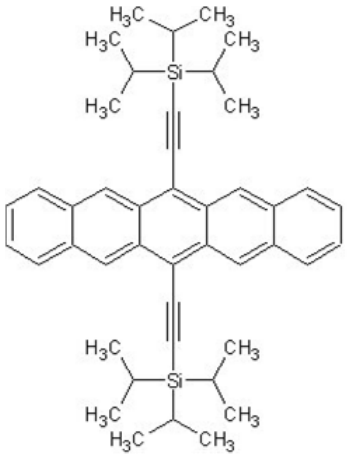

Figure 7.1: Chemical structure of TIPS Pentacene.

Thanks to its solubility in a wide range of organic solvents, TIPS-Pentacene is commonly spin coated, drop cast and inkjet printed in order to constitute the active layer in OTFTs. The electrical characteristics of such devices were found to be highly dependent on processing conditions i.e. the solvent used, the post processing treatment and the deposition method, since they determine the morphology of the deposited semiconductor film. The highest electrical performances have been found in transistor with single crystal TIPS-Pentacene semiconductor because they are free of grain boundaries and molecular disorder which limit the charge transport through the material. Generally using high boiling point solvent and drop casting allow slower solvent evaporation leading to highly ordered films. Mobilities up to 1.8 cm^2/Vs in drop cast TIPS-pentacene OTFTs are reported in literature [87].

The optimization of the process to fabricate inkjet printed Pentacene-TIPS OTFTs is still a work in progress. This research was carried on by the Department of Electrical and Electronic Engineering of the University of Cagliari with the collaboration of the University of Bologna. Several trials were done in order to obtain good mobility of the devices: changing the TIPS-Pentacene concentration in the

solution, the drop spacing, the channel length, the frequency of injection, the material used for the electrodes, the chemical treatments of the substrate and the real number of drops that cover the channel.

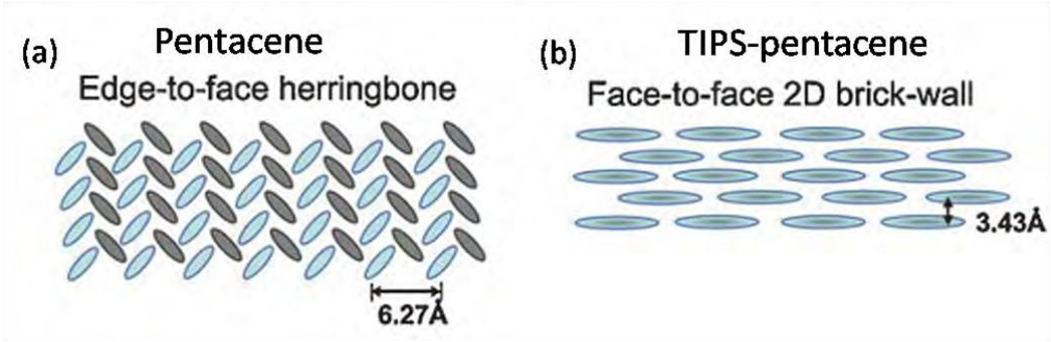

Figure 7.2: Molecular packing arrangements with average distances between the π-faces in the solid state (a) Pentacene and (b) TIPS-Pentacene [(87)].

For a complete description of all the surveys implemented see Basiricò studies [(87)]. I will focus here my attention only on the differences between *single drop* and *multiple droplets* approaches. The first consists in single-droplet printing where each droplet acts as an individual functional deposit [(96)]; conversely, the second is based on printing multiple droplets which form a continuous film covering the whole area between the source and the drain electrodes in forming the OTFT channel [(97)(98)]. Both methods present advantages and drawbacks. With the first, high ordering is easily achievable controlling the hydrodynamic flows in the drying droplet which forms the channel (e.g. using a mixed solvent system or varying the surface energy of the substrate), leading to hole mobilities up to 0.2 cm^2/Vs for pure TIPS-Pentacene inks and up to 1 cm^2/Vs for inks containing TIPS-Pentacene blended with insulating or other semiconductive polymers [(96)]. On the other hand, printing multiple droplets could be more effective in forming an uniform thin film over a large area if the spot produced by one single droplet does not cover the channel region (e.g. if the channel length is greater than the droplet diameter); printing of several separate single drops in fact can lead to interfaces between droplets which negatively affect the uniformity of the printed active layer [(97)].

Employing this latter printing method mobilities up to 0.24 cm^2/Vs for pure TIPS-Pentacene[(98)] and up to 0.11 cm^2/Vs in devices were TIPS blended with polystyrene was employed [(97)] were reported.

The solution prepared has a concentration of 5 wt.% of TIPS-Pentacene (provided by Sigma-Aldrich company) prepared in Toluene. Before deposition each solution was stirred for 1 h at 90° C on a hot plate and subjected to ultrasonic bath for 15 min before filling a DMP-11610 cartridge. The solutions were deposited without

filtering. During deposition, the substrate (Parylene C) was kept at a constant temperature of 60° C in order to promote fast solvent evaporation and subsequently to obtain a better crystallization of the semiconductor [99].

Figure 7.3a shows an example of the transparent and flexible matrix of transistors that we created printing TIPS-Pentacene solution and silver electrodes on Parylene; Figure 7.3b instead shows a magnified image of one transistor; it is made with a different configuration from the ones we used in the other chapters, the geometry is an interdigitated channel structures and employs more tracks as electrodes to achieve more signal, beneath two tracks there is a channel length of 50 μm whereas the width of the transistor is 5 mm as shown in Figure 7.4. In other matrices instead, other transistors always with the configuration of interdigitated channel structures were built with other channel length and other electrodes materials, all the parameters of the transistors studied are reported in Table 7.1.

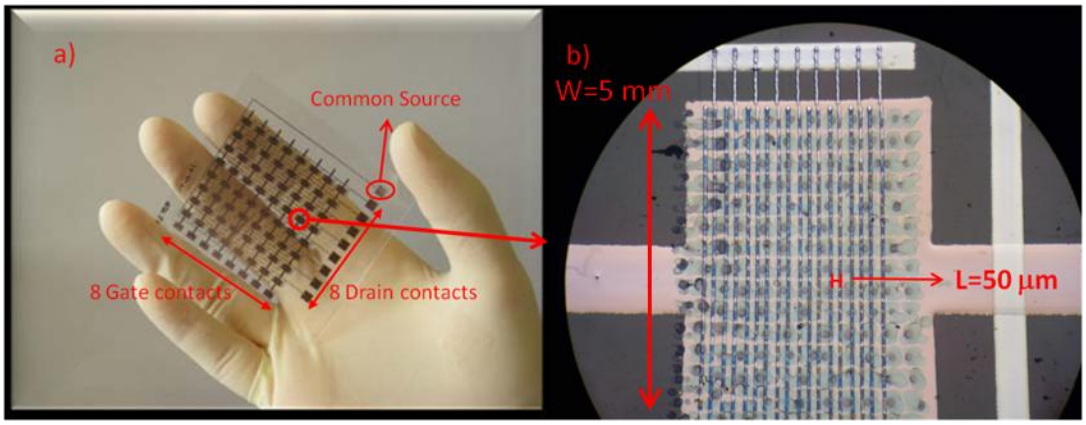

Figure 7.3: a) First prototype of matrix realized: 64 transistors with a common Source, 8 Drain and 8 Gate contacts, b) the magnified image of one transistors with specified the channel length between the tracks.

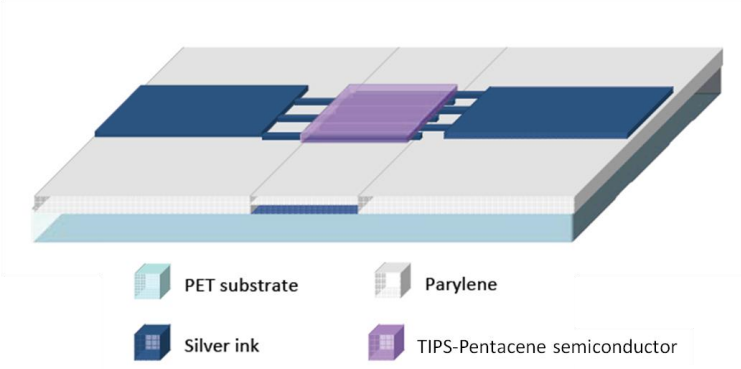

Figure 7.4: Transistor outline for inkjet printed TIPS-Pentacene devices.

Sample	# drops	Drop spacing	Approach	Width = # drops*ϕ_{drop} (ϕ_{drop}=50 μm)	Channel Length
1	-	50 μm	Multiple droplets on Ar	5 mm	50 μm
2	12	120 μm	Single drop on Ar	600 μm	60 μm
3	28	120 μm	Single drop on Ar	1400 μm	60 μm
4	48	200 μm	Single drop on Au	2400 μm	30 μm

Table 7.1: List of the inkjet printed transistors with their specifications: numbers of droplets, drop spacing, approach used, channel width and length.

The multiple drops approach presents difficulties in obtaining the order necessary to cover appropriately the channel, in Figure 7.5, the TIPS-Pentacene solution is inkjet printed with drop spacing 50 μm and channel length also 50 μm. As is shown in the figure, multiple-droplets method led to superimposition between adjacent printed drops, which diameter is of about 50 μm. The printing parameters used in both the approaches are listed in Table 7.2. It should be noted that single drop patterns have to be printed with one single nozzle jetting (instead of two as in multiple droplets approach) at frequency of 1 kHz (the lowest limit of the printer); printing with higher frequency values in fact could lead to chaotic and uncontrolled droplets deposition. The optimal drop spacing which has to be used in order to obtain ordered separate droplets with a jetting frequency of 1 kHz is 150 μm. Through the optimization of printing parameters it is possible to print ordered separate droplets in a controlled way, but if the transistor has a channel larger than the drop diameter, one drop will not be able to cover the distance between source and drain electrode and, consequently, two or more partially superimposed droplets have to be printed anyway in order to form the active layer of the device.

At first, a procedure was developed to realize short channel (L= 30 μm) devices, with inkjet printed silver electrodes and a single row of single drops. Unfortunately for most of these transistors we measured a short circuit between source and drain electrodes; moreover, the thickness of the silver electrodes does not allow a good wettability of both source and drain electrodes with only one drop and the channel can be formed again by at least two partially overlapped drops. Therefore, devices with gold electrodes patterned through common photolitography with a channel length of 30 μm were realized in order to finally test the performances of TIPS-Pentacene where actually one single droplet acts as an individual functional unit to form the channel, without discontinuity and grain boundaries in the active layer.

Main Settings	Multiple droplets	Single drop
Firing voltages range	20-25 V	12-15 V
Cartridge Print Heigh	1 mm	1 mm
Platen Temperature	60° C	60° C
Cartridge Temperature	RT	RT
Maximum Jetting Frequency range	25 kHz	1 kHz
Drop spacing	< 90 mm	> 120 mm
Number of jetting nozzles	2	1

Table 7.2: Main cartridge and printer settings used in printing TIPS-Pentacene based ink with multiple-droplets and single-drop approach [(87)].

An example of such cases is depicted in Figure 7.6 for sample 2, 3 and 4, the comparison shows: (a) the channel formed by two rows of partially superimposed drops disordered and (b) ordered and (c) the channel is formed by a single row of separate drops. In the first two cases the drop diameter (around 50 μm) is smaller than the distance between source and drain electrodes (60 μm), while in the third case it is larger (since the distance between source and drain electrodes is 30 μm).

The electrical characteristics for all the samples are reported in Figure 7.7. Considering the different geometric parameters the mobilities of the devices were calculated and reported in Table 7.3. As we can see, the multiple droplets approach doesn't provide an high mobility, whereas the single drop in a single row shows the highest mobility. So the mobility trend seems strictly related to the inkjet process, in particular a more ordered deposition of the droplets gives better performances. The explanation of this phenomena can be understood keeping in mind how the mobility decreases with a higher number of grain boundaries [(100)(101)].

Figure 7.5: Optical images (magnification 5x) of the TIPS-Pentacene solution with concentration of 5 wt. % inkjet printed using a drop spacing of 50 μm [(87)].

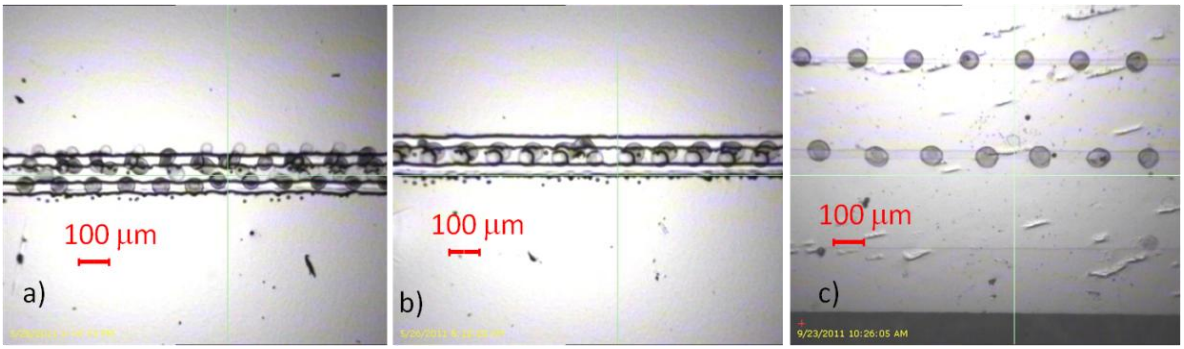

Figure 7.6: Optical images taken by means of the Fiducial Camera of samples 2, 3 and 4 of Table 7.1. a) disordered and partially superimposed TIPS droplets, b) two rows of partially superimposed TIPS droplets, c) a single row of separate TIPS droplets [(87)].

Sample	Drop spacing	Approach	Mobility (cm^2/Vs)
1	50 µm	Multiple droplets on Ar	$7{,}9 \cdot 10^{-5}$
2	120 µm	Single drop on Ar	$1{,}45 \cdot 10^{-3}$
3	120 µm	Single drop on Ar	$2{,}38 \cdot 10^{-3}$
4	200 µm	Single drop on Au	$5{,}88 \cdot 10^{-3}$

Table 7.3: Mobilities and other device parameters of inkjet printed OTFTs with TIPS-Pentacene.

Photocurrent measurements were also carried out to find a correlation between mobility and crystalline order. Ostroverkhova[(102)] found that for TIPS-Pentacene thin films there is a red-shift of the first optical absorption peak when the sample is more crystalline and, vice versa, there is a small blue-shift of this peak when the samples are more amorphous or more similar to a liquid. As we can see in Figure 7.8 also in the spectra of the samples of Table 7.3 we observe a shift of the first photocurrent peak. In particular sample 1 shows a red-shift compared with sample 2, whereas sample 3 and 4 a blu-shift. We can see that the shift of the first peak of the photocurrent spectra follows the same trend of the mobility, presenting an higher crystalline structure for the device with lowest mobility. This fact could be thought as a contradiction with the dissertation done in the chapters before (par. 4.1.1), actually we can find a clearer view of the results looking at the XRD spectra that we carried out.

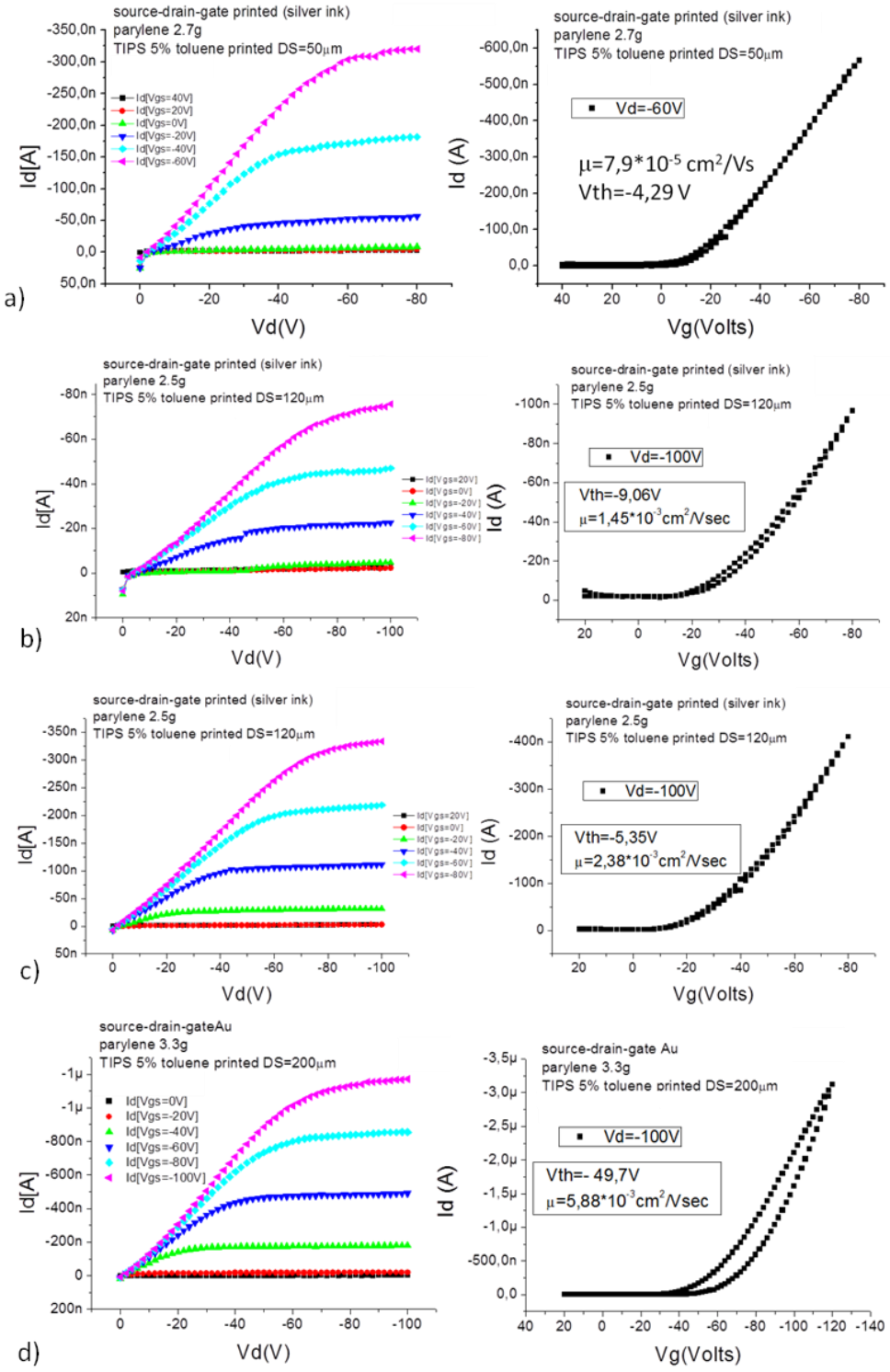

Figure 7.7: Electrical characteristics and transfer characteristics of the inkjet printed TIPS OTFTs reported in Table 7.1: I_d-V_d on the left, I_d-V_g on the right [87].

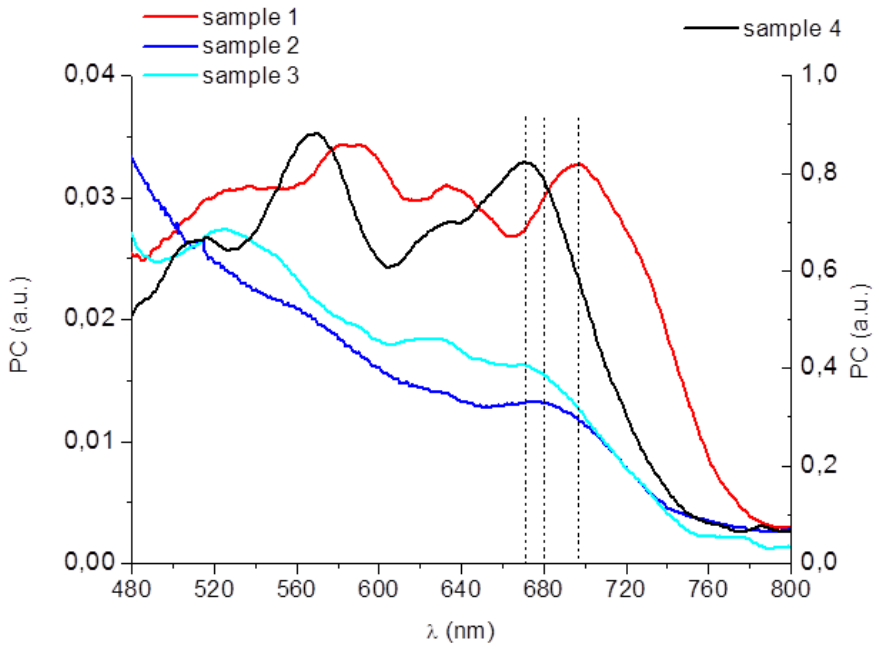

Figure 7.8: Photocurrent spectra for inkjet printed OTFTs with TIPS-Pentacene semiconductor listed in Table 7.3. Sample 4 is plotted in a second scale as it presents an intensity of the signal higher of about one order of magnitude.

X-ray diffraction measurements were employed on other three correlated samples inkjet printed on Parylene substrate with a solution made of TIPS-Pentacene 5 wt.% in Toluene repeating the same approaches said before: multiple drops (drop spacing 50 μm), and single drop (drop spacing of 120 μm and 200 μm). The XRD spectra (Figure 7.9) shows that all the samples are crystalline, even if the first sample (multiple droplets) is more crystalline than the others. This is probably due to an amount of thicker material crystallized in the place of the grain boundaries, that are more present in this sample. These measurements agree with those reported by Sele [(103)], for dip-coated TIPS-Pentacene films onto silicon wafers from a Toluene solution containing 1 wt.% TIPS-Pentacene. However, we observed another peak (about 12. 5°) in the first sample, and to a lesser extent in the sample with 120 μm of drop spacing, which could be due either to the presence of crystallites with a different orientation or to material not completely dissolved in the solution. Furthermore the molecular orientation (π–π stacking) of all the samples is perpendicular to the surface as requested for a good horizontal charge transport.

In conclusion a higher crystalline structure is not always referred to an higher mobility as in this case where the higher amount of crystalline material creates a barrier for the conduction of the charge carriers instead to make easier the conduction (see Figure 7.10).

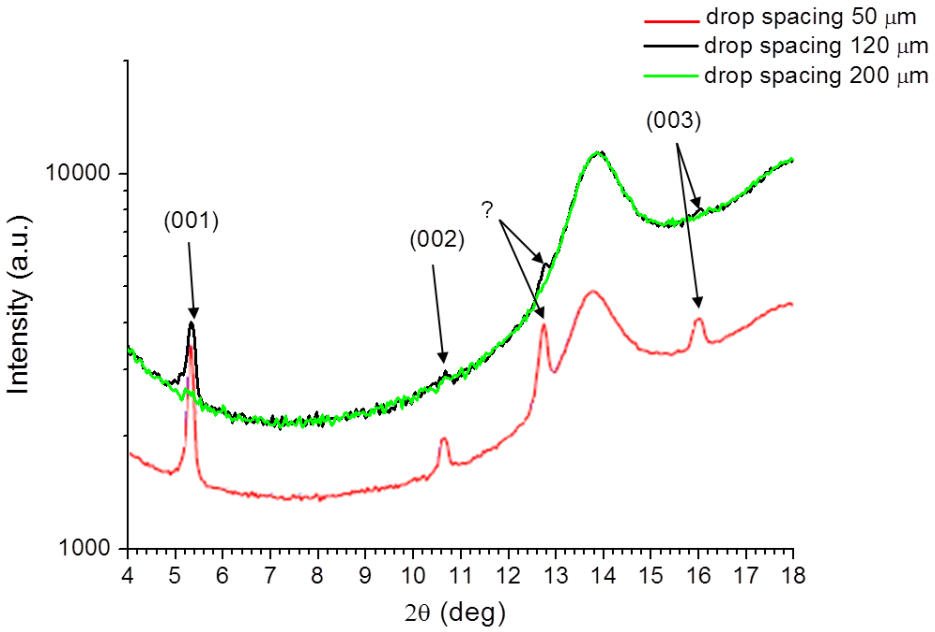

Figure 7.9: XRD spectra in specular geometry for samples of TIPS-Pentacene 5 wt. % in Toluene inkjet printed with drop spacing: 50 μm (multiple droplets),120 μm and 200 μm (single drop) [87].

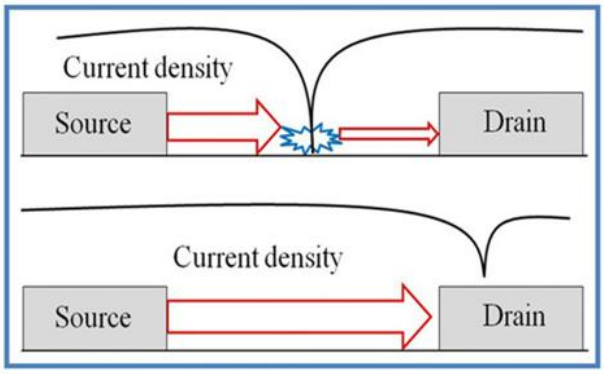

Figure 7.10: Influence of a grain boundary on the channel current [101].

7.2 Inkjet Organic Electrochemical Transistors (OECT)

Organic electrochemical Transistors (OECTs) exploit the ability of organic semiconductors to conduct ionic in addition to electronic charge and are of great interest for chemo-sensing and bio-sensing applications as they can operate in liquid environment. They are also used for the fabrication of simple circuitry that, if fabricated

at low enough cost, could become disposable. OECTs have a simpler geometry than OTFTs (see Figure 7.11), as they may have a planar, monolayer structure, composed by a channel, usually made of poly(3,4-ethylenedioxythiophene) doped with poly(styrene sulfonic acid) (PEDOT:PSS), and a gate contact realized close to the channel, that can be fabricated employing a variety of conducting materials. The gate contact can also be made by PEDOT:PSS, thus enabling an even simpler structure (as only one material is used) that can be printed, as PEDOT:PSS inks are commercially available.

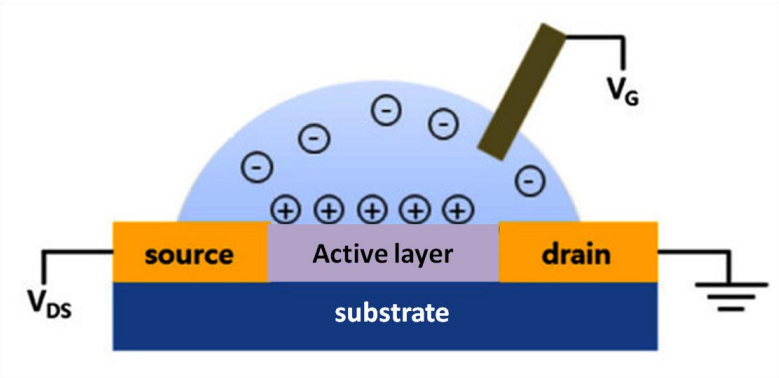

Figure 7.11: Schematic view of an OECT.

Recently, Kaihovirta [104] presented all-polymer electrochemical transistors and memory elements fabricated by means of flexography, which is a roll-to-roll manufacturing technique. This is an extremely interesting example of OECT realized with a high throughput manufacturing technique. However, ink-jet printing offers a great flexibility in the choice of the substrates to print. A first example of an ink-jet printed OECT was presented by Mannerbro [105] who adapted a conventional desktop thermal ink-jet printer to the deposition of an aqueous dispersion of PEDOT:PSS onto photo-paper. The present work deals with the realization of Organic ElectroChemical Transistors made with a piezoelectric, drop-on-demand, ink-jet printing technique that, in principle, has looser constraints than thermal printing in terms of ink composition and properties

The goal of the present work [106], focused on the realization of devices entirely made of PEDOT:PSS, is: (i) to show that inkjet printing is a simple and reliable printing procedure for obtaining robust working devices and (ii) to demonstrate that their working range (i.e. the gate voltage range in which they can operate) may be predictably varied by changing the ratio between the gate and the channel areas. With this aim, we fabricated all-organic, semitransparent devices by ink-jet printing PEDOT:PSS electrodes on plastic substrates. Thanks to a treatment with Ethylene Glycol (EG), that can be done as a final fabrication step after the printing, not only a clear increase in the conductivity, but also a significant improvement in the mechanical robustness of the final PEDOT:PSS films was achieved. In this way, several runs of measurements can be

performed on the same device without problems of delamination, which is typical for PEDOT:PSS devices when measured in liquid environment.

7.2.1 Materials and methods

The transistors realized were created, and in part characterized, by the Department of Electrical and Electronic Engineering of the University of Cagliari, the electrical and optical measurements, instead, were done at the University of Bologna. All-PEDOT:PSS OECTs were fabricated on transparent and flexible 175 μm thick poly(ethyleneterephthalate) (PET) sheets by means of inkjet printing. Substrates were cleaned by subsequent 15 min ultrasonic baths both in acetone and in isopropyl alcohol, then washed in deionized water and finally dried under nitrogen flow. The devices have been entirely ink-jet printed in air by means of Fujifilm Dimatix Material Printer (DMP) 2800, a piezoelectric, drop on demand, ink-jet printer widely used for organic electronic applications, using a DMC-11610 cartridge. This cartridge contains 16 nozzles with a diameter of 21.5 μm and each nozzle generates 10 pl drops of ink. For all electrodes, we employed an aqueous dispersion of PEDOT:PSS (Clevios P Jet HC provided from H.C. Starck), made of sub-micrometer sized gel particles, which after solvent drying and thermal annealing, form a continuous and transparent conducting film. Before filling the cartridge, PEDOT:PSS based ink has been sonicated for 15 min and then filtered with a 0.2 μm nylon filter to avoid nozzle clogging. During printing, substrates have been kept at a constant temperature of 60° C to help fast solvent evaporation. Electrodes were fabricated superimposing 2, 3 or 4 printed layers, waiting for 60 s in printing two subsequent layers with a drop spacing of 20 μm in order to minimize ink spreading on the substrate. After printing, samples were annealed on a hot plate at 60° C for 8 h. After annealing, EG was deposited on the structure by means of spin coating, then the devices were dried in an oven at 60° C for 12 h. Between gate and source-drain electrodes, a 6 μL drop of aqueous PBS (Phosphate Buffered Saline) 0.01 M electrolytic solution (NaCl - 0.138 M; KCl - 0.0027 M provided by Sigma-Aldrich) was deposited only a few seconds before the electrical characterization was performed. The electrical measurements were carried out in air, at room temperature, using two Keithley 2600 SourceMeters controlled by Labview software.

7.2.2 Results and discussion

We have first carried out a complete characterization of printed PEDOT:PSS lines, in order to establish printing quality, electrical conductivity properties and optical transparency. By printing PEDOT:PSS ink with a suitable choice of drop spacing, it is

possible to obtain uniform layers formed by the superposition of several single drops (Figure 7.12a,b) being the total thickness on one layer about 200 nm (Figure 7.12c). With three printed layers (including the final post treatment with EG), more than 80% of radiation in the range between 400 and 800 nm is transmitted through the PEDOT:PSS layer (Figure 7.12a), thus ensuring a high level of transparency of the final devices. This value is comparable with that of a spin-coated layer with a similar thickness according to the datasheet of the PEDOT:PSS compound. Transparency is useful for bio-sensing applications as it could allow to optically inspect devices with conventional optical transmission microscopy.

As for the conductivity, our results show the typical resistive behavior [107] displayed by a conducting polymer as shown in Figure 7.13b by a R vs. T curve.

After this initial characterization step, we proceeded with the fabrication of all-PEDOT:PSS OECTs. As mentioned, the printed structures have been treated with Ethylene Glycol (EG), after the printing process. A direct mixing of EG into the PEDOT:PSS ink has been attempted but it had a detrimental effect to the quality of the printed layers. The treatment with EG is known to increase the conductivity of PEDOT:PSS [108] and also contributes to increasing the robustness of the printed devices. As a matter of fact, printed devices tend to delaminate from plastic substrates (as PET) or at least to severely degrade even after one operation. This does not occur for EG-treated devices as shown in Figure 7.14 where it is evident that the current vs. drain voltage curve does not change at all before and after washing with deionized water, and drying under nitrogen flow. Figure 7.15 shows an output curve, i.e. I_{DS} vs. V_{DS}, measured in one of these devices. The current modulation due to the applied voltages is explained according to the usual operational model [109]: the drain current is due to hole drift in the PEDOT:PSS channel, induced by the drain voltage.

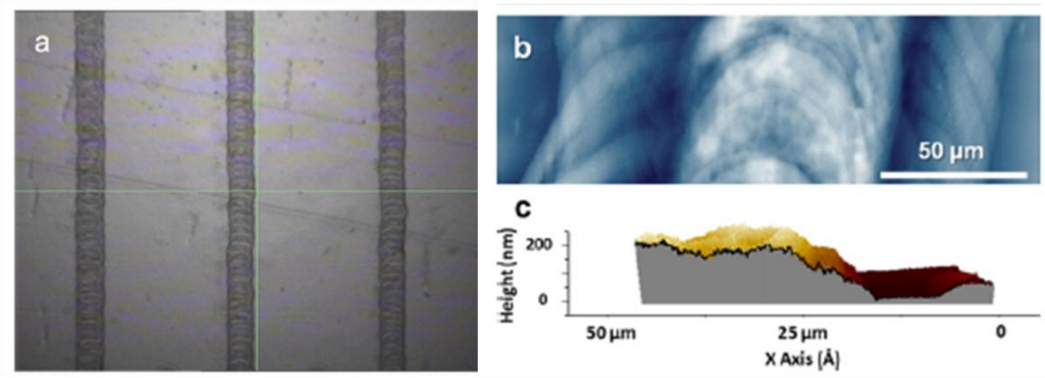

Figure 7.12: (a) Optical image of PEDOT:PSS lines ink-jet printed on top of a PET substrate. (b) AFM image of a double layer of PEDOT:PSS printed on top of a PET substrate. (c) The profile of a single layer of PEDOT:PSS obtained with a drop spacing of 20 µm [106].

When a positive gate voltage (V_G) is applied, cations from the electrolyte enter into the channel, de-dope it and reduce the drain current. After a certain value of V_G, called V_{OFF}, the channel current drops to zero (off-state) indicating a complete de-doping of the channel.

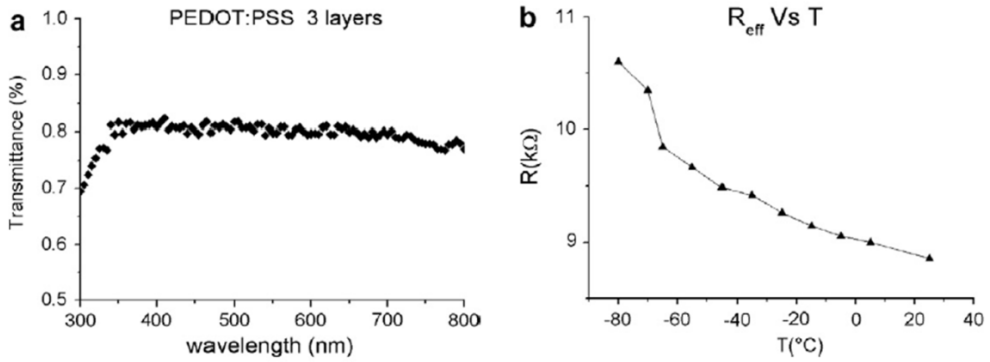

Figure 7.13: (a) Transmittance of a triple layer of PEDOT:PSS printed on a PET substrate. The values are normalized with respect to PET. More or less 80% of the radiation is transmitted for all wavelengths in the visible range. (b) Resistance vs. temperature of a printed line with three layers [(106)].

The effect of the device geometry may be observed in Figure 7.16A that reports two measurements of I_{DS} vs. V_{DS} taken on the same asymmetric structure (see the top portion of the figure), by exchanging channel and gate. Currents are normalized with respect to the channel width. Basically, in the type 1 configuration (top left portion of Figure 7.16A), the smallest structure is taken as the channel and the largest as the gate (therefore Ag/Ach > 1) while in the type 2 configuration (top right), the largest structure is taken as the channel and the smallest as the gate (therefore Ag/Ach < 1).

It is clear that the transconductance (fitting lines in the bottom portion of Figure 7.16A) is different in the two devices, showing that it is possible to tune the transistor characteristics (i.e. not only current by also the operative voltage range) by tuning device geometry. This feature is further confirmed in Figure 7.16B, where the curves of three different devices with the same channel dimensions and different gate dimensions are shown. This feature is very useful in the design of biosensors, where the transconductance relates to sensitivity, as well as in the design of electronic circuitry. It should also be noted that the device may be operated also with negative value of V_G and the channel current continues to increase in this regime. This indicates that the application of negative V_G leads to further doping of the PEDOT:PSS in the channel.

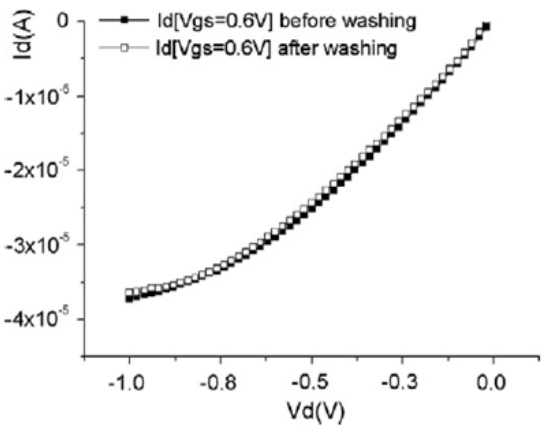

Figure 7.14: The effect of washing on the behaviour of a device printed with PEDOT:PSS and then treated with Ethylene Glycol. It is clear that the current of the device is perfectly stable and no difference is appreciable between measurements before and after washing [106].

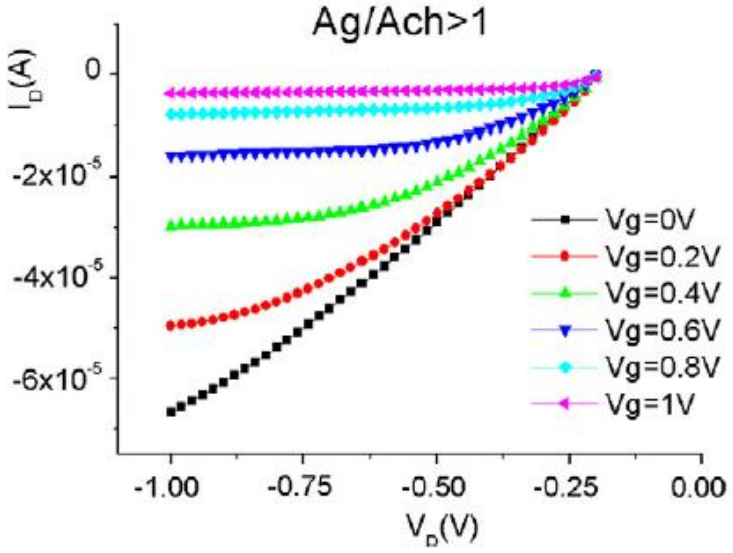

Figure 7.15: I_{DS} vs. V_{DS} curves taken on a device with the gate area larger than the channel area [106].

When a certain (negative) value of V_G is reached, the drain current saturates. This may be because on one hand, the channel reaches its maximum doping limit and on the other hand, because the gate itself is de-doped and a fraction of the gate voltage is dropped across the gate electrode rather than being applied across the solution. The effect of saturation is more defined in type 1 devices. It is also noticeable that no permanent degradation is caused on the device by the cyclic application of this voltage range (see Figure 7.17). Previous studies showed that OECTs utilizing Pt gates

(operated with positive gate voltages), showed a similar dependence of transfer characteristics on geometry, while OECTs utilizing Ag/AgCl gates did not [110]. This was attributed to the fact that the potential drop at the interface between a polarizable electrode like Pt and an electrolyte varies with the area of the electrode. In an OECT with a large gate and a small channel, the potential applied at the gate will drop mainly at the electrolyte/channel interface and result into efficient gating, hence a large transconductance. The opposite is true when the channel is larger than the gate. On the other hand, in OECTs with a gate electrode that is non-polarizable (such as Ag/AgCl), the potential applied at the gate always drops at the electrolyte/channel interface. Our results indicate that PEDOT:PSS is closer to the first limit, hence it exhibits characteristics similar to those of a polarizable electrode. However, it should be noted that ions are able to interact with the active PEDOT:PSS film (after all, this is the basis of the OECT operation), hence an "effective" capacitance model is appropriate for the gate electrode/electrolyte interface, with a capacitance larger than that of a polarizable electrode [109].

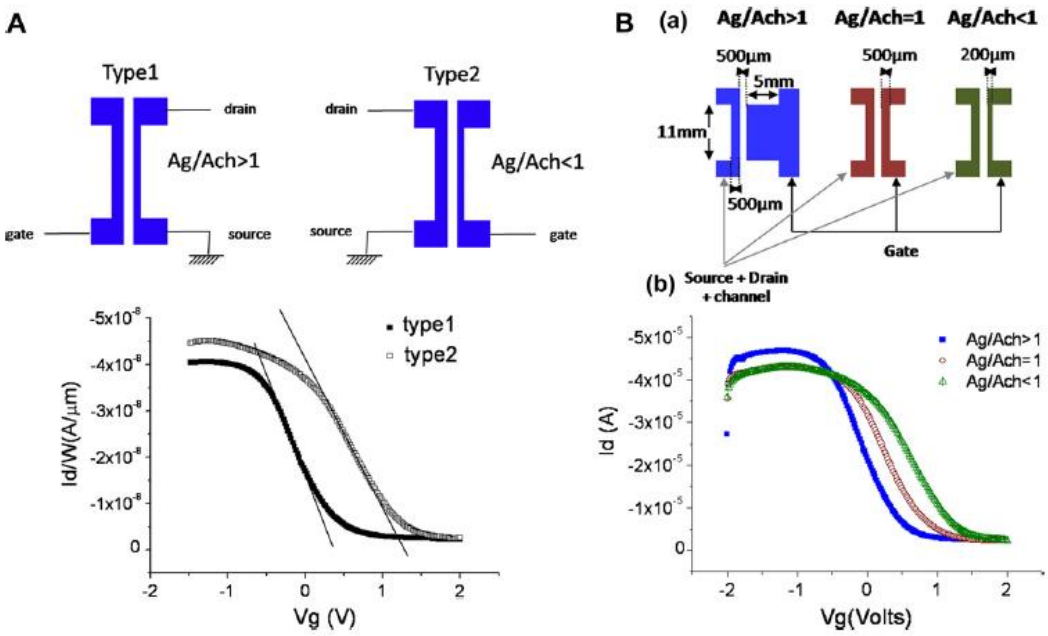

Figure 7.16: (A) Schematic representation of the employed asymmetric geometry in which by exchanging the channel and the gate it is possible to modify the Ag/Ach ratio (top); I_d vs. V_g curves taken on the same device by exchanging the channel and the gate (bottom). The solid lines define the different transconductances exhibited in the two cases. The dimensions of gate width are 500 and 200 μm for type 1 and type 2 devices, respectively. (B) The effect of three different geometries on the transfer characteristic curve of the device. The channel dimension is always the same, while the gate dimension is changing [106].

In conclusion, we demonstrated the possibility of using inkjet printing to fabricate all-PEDOT:PSS Organic Electro-Chemical Transistors, that are reproducible and robust enough for biosensors and low-cost circuitry. We also demonstrated that the working range of such devices can be controlled by varying the device geometry (i.e. the ratio between the gate and the channel areas) as in the case of structures with the gate acting as a polarizable electrode.

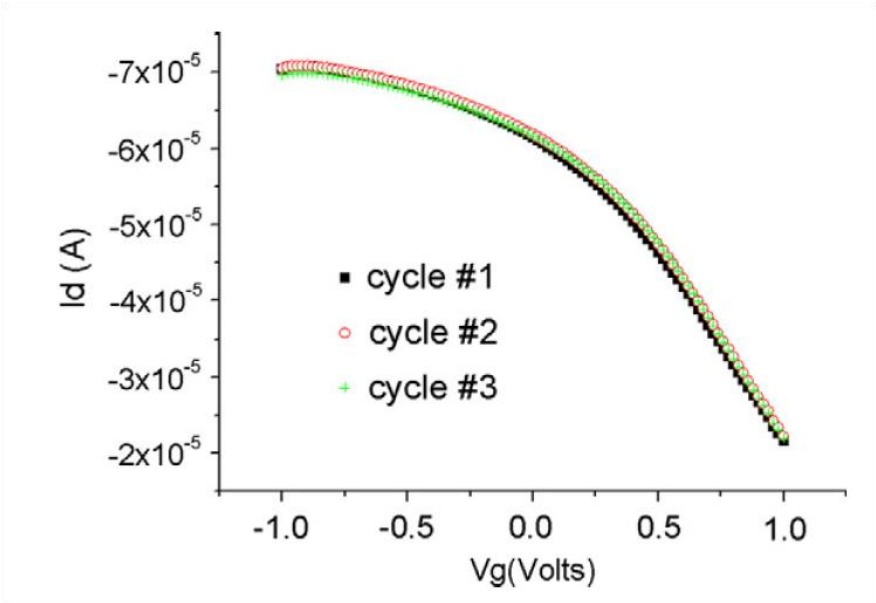

Figure 7.17: Effect of multiple cycles of application of V_G, also in the negative range. As it can be noticed, the curves are perfectly identical [106].

Conclusions

During my work of thesis the characterization of organic thin films and organic thin film transistors (OTFTs) was carried on with several experiments. In particular, I analyzed the structural properties, the morphology and the optical behavior of Pentacene thin films. Among the techniques used, Photocurrent Spectroscopy was found to be a very practical tool to analyze DOS distribution and molecular packing of organic thin films even in OTFTs whereas other techniques cannot be easily employed with a working transistor [74][75].

A very important issue of my thesis is the analysis of the effects of ion implantation on Pentacene thin films in order to assess the modifications induced by the irradiation with the aim to obtain structural, electrical and optical properties useful to build reliable and efficient OTFTs, in particular:

1. modification of the electrical conductivity (paragraph 5.4);
2. introduction of stable charged species, electrically active with organic thin films (paragraph 5.3);
3. stabilization of transport parameters: mobility and threshold voltage (chapter 6).

The ion species implanted on Pentacene layers were initially two: N^+ and Ne^+, chosen appositely with a different reactivity with the matrix to compare their different behaviour. These studies, carried on as a function of the ion dose and of the energy beam, reported very favorable effects with both the ions. The most important features are: higher hardness of the superficial Pentacene layer and higher conductivity due to the damage created by ion implantation (for both the ions). This later effect can also be due to the introduction of stable charged species inside the organic film, which in turn leads to a higher conductivity of 10 orders of magnitude (this effect was observed only for N^+ ions).

After these promising experiments, ion implantation was employed on working Pentacene OTFTs. A controlled damage induced by the ions in the superficial part of the Pentacene layer (300 nm thick) permits to create an encapsulation layer and, under that, to keep a fresh and pure layer of Pentacene at the interface with the transistor dielectric [82]. The superficial implanted layer (about 50 nm thick) is able to keep stable the electrical parameters of the OTFT, i.e. the mobility and the threshold voltage, and to preserve them by the atmospheric agents for at least 2000 hours [83]. The ions used for the implantation during the research were several: N^+, Ne^+, F^+ and S^+, but the more efficient conditions for the stability was verified to be the co-implantation of two different ions: N_2^+ and Ne^+. The improvement of the OTFTs doesn't damage at all the special good properties of organic semiconductors as transparency, flexibility and bio-compatibility.

Furthermore the introduction of stable charged species, due to ion implantation, is able to modify appositely the threshold voltage of the organic transistor. The possibility to increase the conductivity at high doses of ions, instead, allows the possible future application to create completely organic transistors, building the electrical contacts directly on the organic semiconductor with ion implantation at high doses, masking particular areas of the sample.

Among the several ion beam systems existing by now, there is Plasma Source Ion Implantation, that has the possibility to industrialize the process of implantation of large surfaces thanks to the immersion of the sample inside a plasma of accelerated ions. This technique allows to preserve the cheaper costs of organic semiconductors, which are used most of all for large surfaces like, for example, solar cells.

The intent to produce always new, low-cost and efficient organic devices bring me to study the so called inkjet printed organic transistors. These transistors can be built in very simple way with a inkjet printer and with an organic semiconductor as a ink. In particular I studied two different inkjet printed devices: the first was a TIPS-Pentacene inkjet printed transistor, the second, particularly indicated for biological applications, was an inkjet electrochemical transistor with PEDOT-PSS as semiconductor [(106)]. I started with their structural, electrical and optical characterization and further work will be carried out in the future to continue the research on ion implantation also of these devices to obtain stable electrical parameters.

Ion implantation has proven to be an efficient and reliable tool in the fabrication of OTFTs, allowing to achieve unprecedented properties, very useful in the development and improvement of organic devices.

Bibliography

1. **D. C. Northrop, O. Simpson.** Electronic properties of aromatic hydrocarbons. I. Electrical conductivity. *Proc. R. Soc. Lond. A.* 1956, Vol. 234, pp. 124-135.

2. **C. K. Chiang, C. R. Fincher, Jr., Y. W. Park, A. J. Heeger, H. Shirakawa, E. J. Louis, S. C. Gau.** *Phys. Rev. Lett.* 1977, Vol. 39.

3. **Brutting, W.** *Introduction to the Physics of Organic Semiconductors.* Weinheim : Wiley-VCH Verlag GmbH & Co. KGaA, 2005.

4. **Koch, N.** Organic Electronic Devices and Their Functional Interfaces. *Chem. Phys. Chem.* 2007, Vol. 8, pp. 1438 – 1455.

5. **G. Horowitz, R. Hajlaoui, H. Bouchriha, R. Bourguiga, M. Hajlaoui.** *Adv. Mater.* 1998, Vol. 10.

6. **C. R. Newman, C. D. Frisbie, D. A. da Silva Filho, J. L. Bredas, P. C. Ewbank, K. R. Mann.** *Chem. Mater.* 2004, Vol. 16.

7. **L. L. Chua, J. Zaumseil, J. F. Chang, E. C. W. Ou, P. K. H. Ho, H. Sirringhaus, R. H. Friend.** *Nature.* 2005, Vol. 434.

8. **T. B. Singh, F. Meghdadi, S. Gunes, N. Marjanovic, G. Horowitz, P. Lang, S. Bauer, N. S. Sariciftci.** *Adv. Mater.* 2005, Vol. 17.

9. **M.-H. Yoon, C. Kim, A. Facchetti, T. J. Marks.** *J. Am. Chem. Soc.* 2006, Vol. 128.

10. **S.R. Saudari, Y.J. Lin, Y. Lai, C.R. Kagan.** Device Configurations for Ambipolar Transport in Flexible, Pentacene Transistors. *Adv. Mat.* 2010, Vol. 22, pp. 5063-5068.

11. **G. Horovitz, R. Hajlaoui, P.Delannoy.** Trapping in Organic Field Effect Transistors. *J.Phys.III.* 1995, Vol. 5, p. 355.

12. **Street, R. A.** Thin-Film Transistors. *Adv. Mat.* 2009, Vol. 21, pp. 1-16.

13. **C.D. Dimitrakopoulus, D.J. Mascaro.** Organic Thin film Transistors: A review of recent advances. *J. Res. & Dev.* 2001, Vol. 45.

14. **C.D. Dimitrakopoulus, A.R. Brown, A. Pomp.** Molecular Beam Deposited Thin Films of Pentacene for Organic Thin Film Transistor Applications. *J. Appl. Phys.* 1996, Vol. 80, p. 2501.

15. **Karl, N.** Charge carrier transport in organic semiconductors. *Synth. Met.* 2003, Vols. 133-134, pp. 649-657.

16. **W. L. Kalb, K. Mattenberger, B. Batlogg.** Oxigen-related traps in Pentacene thin films: Energetic position and implications for transistor performance. *Phys. Rev. B.* 2008, Vol. 78, p. 035334.

17. **G. Horovitz, M.E. Hajlaoui, R. Hajlaoui.** Temperature and Gate voltage dependence of hole mobility in polycrystalline oligothiophene thin film transistors. *J. Appl. Phys.* 2000, Vol. 87.

18. **V. I. Arkhipov, P. Heremans, E. V. Emelianova, G.J. Adriaensens, H. Bassler.** *Appl. Phys. Lett.* 2003, Vol. 82, p. 3245.

19. IEEE Standard Test Methods for the Characterization of Organic Transistors and Materials. 3 Park Avenue, New York, NY 10016-5997, USA : The Institute of Electrical and Electronics Engineers, Inc., 2004. ISBN 0-7381-3993-9 SS95210.
20. **G. Horowitz, M. E. Hajlaoui.** Grain size dependent mobility in polycrystalline organic field-effect transistors. *Synth. Met.* 2001, Vol. 122, pp. 185-189.
21. **W. L. Kalb, F. Meier, K. Mattenberger, B. Batlogg.** Defect healing at room temperature in pentacene thin films and improved transistor performance. *Phys. Rev. B.* 2007, Vol. 76, p. 184112.
22. **D. Knipp, A. Benor, V. Wagner, t. Muck.** 2007, J. Appl. Phys., Vol. 101, p. 044504.
23. **D. Kumaki, M. Yahiro,Y. Inoue, S. Tokito.** 2007, Appl. Phys. Lett., Vol. 90, p. 133511.
24. **A. Sharma, S. G. J. Mathijssen, M. Kemerink, D. M. D. M. de Leeuw, P. A. Bobbert.** proton migration mechanism for the instability of organic field-effect transistors. *Appl. Phys. lett.* 2009, Vol. 95, p. 253305.
25. **D. Knipp, J. E. Northrup.** Electric-Field-Induced Gap States in Pentacene. *Adv. Mater.* 2009, Vol. 21, pp. 1-5.
26. **J. Puigdollers, A. Marsal, S. Cheylan, C. Voz, R.Alcubilla.** Density-of-states in Pentacene from the electrical characteristics of thin-film transistors. *Org. Electron.* 2010, Vol. 11, pp. 1333-1337.
27. **D. Simeone, M. Rapisarda, G. Fortunato, A. Valletta, L. Mariucci.** Influence of structural properties on enviromental stability of Pentacene thin film transistors. *Org. Electron.* 2011, Vol. 1126.
28. **S. D. Wang, T. Miyadera, T. Minari, Y. Aoyagi, K. Tsukagoshi.** Correlation between grain size and device parameters in pentacene thin. *Appl. Phys. Lett.* 2008, Vol. 93, p. 043311.
29. **O. D. Jurchescu, J. Baas, T. T. M. Palstra.** Electronic transport properties of pentacene single crystals upon exposure to air. *Appl. Phys. Lett.* 2005, Vol. 87, p. 052102.
30. **A. Vollmer, O. D. Jurchescu, I. Arafoui, I. Salzmann, T. T. M. Palstra, P. Rudolf, J. Niemax, J. Pflaum, J. P. Rabe, N. Koch.** The effect of Oxygen exposure on Pentacene electronic structure. *Eur. Phys. J. E.* 2005, Vol. 17, pp. 339-343.
31. **Z. Zhu, J. T. Mason, R. Dieckmann, G. Malliaras.** Humidity sensors based on pentacene thin-film transistors. *Appl. Phys. Lett.* 2002, Vol. 81.
32. **J. Li, H. Lin, F. Zhou, W. Zhu, X. Jiang, Z. Zhang.** Suppression of bias stress-induced degradation of pentacene-TFT using MoOx. *Curr Appl. Phys.* 2012, Vol. 12, pp. 280-283.
33. **X. Cheng, M. Caironi, Y. Noh, J. Wang, C. Newman, H. Yan, A. Facchetti, H. Sirringhaus.** Air stable Cross-Linked Cytop ultrathin gate dielectric for high yield low-

voltage top-gate organic field effect transistors. *Chem. Mater.* 2010, Vol. 22, pp. 1559-1566.
34. **T.Umeda, D. Kumaki, S. Tokito.** High air stability of threshold voltage on gate bias stress in Pentacene TFTs with a hydroxyl-free and amorphous fluoropolymer as gate insulator. *Org. Electron.* 2008, Vol. 9, pp. 545-549.
35. **S. Cho, K. Lee, A. J. Heeger.** Extended lifetime of Organic Field-Effect Transistors encapsulated with Titanium Sub-Oxide as an 'active' passivation/barrier layer. *Adv. Mat.* 2009, Vol. 21, pp. 1-4.
36. **W. J. Kim, W. H. Koo, S. J. Jo, C. S. Kim, H. K. Baik, J. Lee, S. Im.** Enhancement of long-term stability of pentacene thin-film. *Appl. Surf. Science.* 2005, Vol. 252, pp. 1332-1338.
37. **M. Nastasi, J. W. Mayer, J. K. Hirvonen.** Ion-Solid Interactions- Fundamentals and applications. Cambridge : Cambridge University Press, 1996.
38. **J. Ziegler, J. Biersack, U. Littmark.** The Stopping and Range of Ions in Solids. New York : Pergamon Press, 1985.
39. **H. Dong, T. Bell.** State-of-the-art overview: ion beam surface modification of polymers towards improving tribological properties. *Surface and Coatings Technology.* 1999, Vol. 111, pp. 29–40.
40. **Chapiro, A.** Radiation Chemistry of Polymeric Systems. London : Interscience Publisher, 1962, Vol. 354.
41. **Calcagno, L.** Ion-chains interaction in polymers. *Nuclear Instruments and Methods in Physics Research B.* 1995, Vol. 105, pp. 63-70.
42. **O. N. Tretinnikov, Y. Ikada.** Surface Characterization of Ion-Implanted Polyethylene. *Journal of Polymer Science: Part B: Polymer Physics.* 1998, Vol. 36, pp. 715–725.
43. **G. Dlubeck, F. Borner, R. Buchhold, K. Sahre, R. Krause-Rehberg, K.-J. Eichhorn.** Damage-Depth Profiling of Ion-Irradiated Polyimide Films Damage-Depth Profiling of Ion-Irradiated Polyimide Films. *Journal of Polymer Science: Part B: Polymer Physics.* 2000, Vol. 38, pp. 3062–3069.
44. **A. Das, S. Dhara, A. Patnaik.** N+ ion-target interactions in PPO polymer: A structural characterization. *Nucl. Instrum. Methods B.* 1999, Vol. 149, pp. 53-60.
45. **Venkatesan, T.** High energy ion beam modification of polymer films. *Nucl. Instrum. Methods B.* 1985, Vols. 7-8, pp. 461-467.
46. **I.H. Loh, R. W. Oliver, P. Sioshansi.** Conducting polymers by ion implantation. *Nucl. Instrum. Methods B.* 1988, Vol. 34, pp. 337-346.
47. **O. A. Yermolenko, G. V. Kornich, G. Betz.** Molecular Dynamics Simulation of the Interaction of Low-Energy Ar Ions with Polyethylene and Pentacene Surfaces. *Bulletin of the Russian Academy of Sciences: Physics.* 2008, Vol. 72, pp. 579–582.
48. **E. H. Lee, G. R. Rao, M. B. Lewis, and L. K. Mansur.** *Nucl. Instrum. Methods B.* 1993, Vol. 74, p. 326.

49. **S. Brock, S. P. Hersh, P. L. Grady, J. J. Wortman.** Enhanced Electrical Conductivity of Poly(ethylene Terephthalate) Implanted with Fluorine Ions. *Journal of Polymer Science: Polymer Physics Edition.* 1984, Vol. 22, pp. 1349-1352.
50. **N. Shekhawat, S. Aggarwal, A. Sharma, S. K. Sharma, S. K. Deshpande et al.** Surface disordering and its correlations with properties in argon implanted CR-39 polymer. *J. Appl. Phys.* 2011, Vol. 109, p. 083513.
51. **B. Li, L. Cheng, Y. Zheng.** Conductive and Optical Properties of PPV Modified by N+ Ion Implantation. *Journal of Polymer Science: Part B: Polymer Physics.* 2010, Vol. 48, pp. 2072–2077.
52. **J. Davenas, P. Thevenard, G. Boiteux, M. Fallavier, X. L. Lu.** Hydrogenated carbon layers produced by ion beam irradiation of PMMA and polystyrene films. *Nucl. Instr. and Meth. in Phys. Res. B.* 1990, Vol. 46, pp. 317–323.
53. **J .S. Abel, H. Mazurek, D.R. Day, E.W. Maby, S.D. Senturia, G. Dresselhaus, M.S. Dresselhaus.** Electrical properties of ion implanted Poly (P-Phenylene Sulfide). *MRS Proceedings.* 1981, Vol. 27.
54. **D. Fink, K. Ibel, P. Goppelt, J.P. Biersack, L. Wang, M. Behar.** Ion beam induced carbon clusters in polymers. *Nucl. Instr. and Meth. B.* 1990, Vol. 46, p. 342.
55. **D. Xu, X.L. Xu, S.C. Zou.** Correlation between ion-beam-modified polyimide conductivity and implantation condition: A Raman spectroscopic approach. *Mater. Lett.* 1991, Vol. 12, p. 12.
56. **D. Fink, W.H. Chung, R. Klett, A. Schmoldt, J. Cardoso,R. Montiel, M.H. Vazquez, L. Wang, F. Hosoi, H.Omichi, P. Gopppelt-Langer.** *Radiat. Eff. Def. Solids.* 1995, Vol. 133, p. 193.
57. **M. S. Dresselhaus, B. Wasserman, G. E. Wneck.** Ion implantation of polymers. *MRS Proceedings.* 1983, Vol. 27.
58. **Baglin, J. E. E.** Interface tailoring for adhesion using ion beams. *Nucl. Instr.Meth. Phys. Res. B.* 1989, Vol. 39, pp. 764–768.
59. **C. Goh, M. D. McGehee.** Organic Semiconductors for low cost solar cells. *The bridge.* 2005, Vol. 35, 4.
60. **Joshi, N.V.** *Photoconductivity. Art, science and technology.* 1990, pp. 36-51.
61. **C. L. Yang, Z. K. Tang, W. K. Ge, J. N. Wang,Z. L. Zhang, X. Y. Jian.** Exciton diffusion in light-emitting organic thin films studied by photocurrent spectra. *Appl. Phys. Lett.* 2003, Vol. 83.
62. **S. Gorgolis, A. Giannopoulou, D. Anastassopoulos, P. Kounavis.** Impact of pentacene film thickness on the photoresponse spectra: Determination of the photocarrier generation mechanism. *J. Appl. Phys.* 2012, Vol. 112, p. 013101.
63. **D. Kotowski, B. Kutrzeba-Kotowska, M. Obarowska,R. Signerski, J. Godlewski.** Surface photocurrents in tetracene layers. *Org. Electron.* 2005, Vol. 6, pp. 193–199.

64. **O. D. Jurchescu, J. Baas, T.T. M. Palstra.** Effect of impurities on the mobility of single crystal pentacene. *Appl. Phys. Lett.* 2004, Vol. 84.
65. **Kafer, D.** Characterization and optimization of growth and electronic structure of organic thin films for applications in organic electronics. *PhD Thesis.* 2008.
66. **R. B. Campbell, J. M. Robertson, J. Trotter.** The crystal structure of Hexacene, and a revision of the crystallographic data for Tetracene and Pentacene. *Acta Cryst.* 1962, Vol. 15, p. 289.
67. **T. Siegrist, C. Kloc, J. H. Schon, B. Batlogg, R. C. Haddon, S. Berg, G. A. Thomas.** Enhanced physical properties in a Pentacene polymorph. *Angew. Chem. Int. Ed.* 2001, Vol. 40, 9, p. 1732.
68. **H. Yoshida, K. Inaba, N. Sato.** X-ray diffraction reciprocal space mapping study of the thin-film phase of Pentacene. *Appl. Phys. Lett.* 2007, Vol. 90, p. 181930.
69. **V. Coropceanu, J. Cornil, D. A. da Silva Filho, Y. Olivier, R. Silbey, J. Bredas.** Charge Transport in Organic Semiconductors. *Chem. Rev.* 2007, Vol. 107, pp. 926-952.
70. **P. Parisse, S. Picozzi, M. Passacantando, L. Ottaviano.** Experiments and theory on pentacene in the thin film phase: structural, electronic, transport properties, and gas response to oxygen, nitrogen, and ambient air. *Thin Solid Films.* 2007, Vol. 515, pp. 8316-8321.
71. **C. C. Mattheus, A. B. Dros, J. Baas, G. T. Oostergetel, A. Meetsma, J. L. de Boer, T. T.M. Palstra.** Identification of polymorphs of pentacene. *Synt. Met.* 2003, Vol. 138, pp. 475–481.
72. **D. Knipp, R. A. Street, A. Volkel, J. Ho.** Pentacene thin film transistors on inorganic dielectrics: Morphology, structural properties, and electronic transport. *J. Appl. Phys.* 2003, Vol. 93.
73. **P. Cosseddu, G. Tiddia, S. Milita, A. Bonfiglio.** Continuous tuning of the mechanical sensitivity of Pentacene OTFTs on flexible substrates: From strain sensors to deformable transistors. *Organ. Electr.* 2013, Vol. 14, pp. 206-211.
74. **B. Fraboni, A. Scidà, A. Cavallini, P. Cosseddu, A. Bonfiglio, S. Milita, M. Nastasi.** Spectroscopic investigation of the semiconductor molecular packing in fully operational organic thin-film transistors. *Appl. Phys. Lett.* 2010, Vol. 96, p. 163302.
75. **Scidà, A.** Spectroscopic analyses of molecular packing in Pentacene thin films. *Il Nuovo Cimento C.* 2011, Vol. 34.
76. **J. Gao, F. A. Hegmann.** Bulk photoconductive gain in pentacene thin films. *Appl. Phys. Lett.* 2008, Vol. 93, p. 223306.
77. **D. Faltermeier, B. Gompf, M. Dressel, A. K. Tripathi, J. Pflaum.** Optical properties of Pentacene thin films and single crystals. *Phys. Rev. B.* 2006, Vol. 74, p. 125416.
78. **T. Jentzsch, H. Juepner, K. Brzezinka, and A. Lau.** Efficiency of optical second harmonic generation from pentacene films of different morphology and structure. *Thin Solid Films.* 1998, Vol. 315, p. 273.

79. **M. Breban, D. Romero, S. Mezhenny, V. Ballarotto, E. Williams.** Photocurrent probe of field-dependent mobility in organic thin-film transistors . *Appl. Phys. Lett.* 2005, Vol. 87, p. 203503.
80. **B. Fraboni, A. Matteucci, A. Cavallini, E. Orgiu, A. Bonfiglio.** Photocurrent studies of stress and aging in pentacene thin film transistors. *Appl. Phys. Lett.* 2006, Vol. 89, p. 222112 .
81. **M. Tiago, J. Northrup, S. Louie.** *Phys. Rev. B.* 2003, Vol. 67, p. 115212 .
82. **B. Fraboni, A. Scidà, A. Cavallini, S. Milita, P. Cosseddu, A. Bonfiglio, Y. Wange, M. Nastasi.** Photocurrent spectroscopy of ion-implanted organic thin film transistors. *Synthetic Metals.* 2012, Vol. 161, pp. 2585– 2588.
83. **B. Fraboni, P. Cosseddu, Y.Q. Wang, R.K. Schulze, Z.F. Di, A. Cavallini, M. Nastasi.** Aging control of organic thin film transistors via ion-implantation. *Org. Electron.* 2011, Vol. 12, pp. 1552–1559.
84. **W. M. A. Bik, F. H. P. M. Habraken.** Elastic recoil detection. *Rep. Prog. Phys.* 1993, Vol. 56, p. 859 .
85. **M. R. VanLandingham, J. S. Villarrubia, G. F. Meyers.** Nanoindentation of Polymers: Overview. *ACS Polymer Preprints.* 2000, Vol. 41, 2, pp. 1412-1413.
86. **N. M. Jennet, J. Meneve.** Fundamentals of Nanoindentation and Nanotribology. 1998, Vol. 522, p. 239.
87. **Basiricò, L.** Inkjet Printing of Organic Transistor devices. *PhD Thesis.* 2012.
88. **J. Als-Nielsen, D. McMorrow.** Elements of Modern X-Ray Physics. s.l. : Wiley, 2001, p. 83.
89. **M. Born, E. Wolf.** Principles of optics: electromagnetic theory of propagation, interference and diffraction of light. Oxford : Pergamon Press, 1964.
90. **C. R. Wie, T. A. Tombrello, T. Vreeland.** Dynamical x-ray diffraction from nonuniform crystalline films: Application to x-ray rocking curve analysis. 1986, Vol. 59, pp. 3743 - 3746 .
91. **J.F. Moulder, W.F. Stickle, P.E. Sobol, K.D. Bomben.** Handbook of X-Ray Photoelectron Spectroscopy. [ed.] J. Chastain. Eden Prairie : Perkin Elmer Corporation, Physical Electronics Division, 1992.
92. **Y.P. Feng, D. Robey, Y. Wang, R. Giedd.** Conductivity and stability in ion-implanted polyaniline. *Mater. Lett.* 1993, Vol. 17, p. 167.
93. **L.-L. Chua, R. Friend, P. Ho.** General observation of n-type field-effect behaviour in organic semiconductors. *Nature.* 2005, Vol. 434, p. 194.
94. **H. S. White, G. P. Kittlesen, M. S. Wrighton.** *J. Am. Chem. Soc.* 1984, Vol. 106, p. 5375.
95. **O. L. Griffith, J. E. Anthony, A. G. Jones, D. L. Lichtenberger.** Electronic Properties of Pentacene versus Triisopropylsilylethynyl-Substituted Pentacene: Environment-Dependent Effects of the Silyl Substituent. *J. Am. Chem. Soc.* 2010, Vol. 132, pp. 580-586.

96. **X. Li, W. T. T. Smaal, C. Kjellander, B. van der Putten, K. Gualandris, E. C. P. Smits, J.Anthony, D. J. Broer, P. W. M. Blom, J. Genoe, G. Gelinck.** *Org. Electron.* 2011, Vol. 12, pp. 1319-1327.
97. **M-B. Madec, P. J. Smith, A. Malandraki, N. Wang, J. G. Korvink, S. G. Yeates.** *J. Mater. Chem.* 2010, Vol. 20, pp. 9155-9160.
98. **S. H. Lee, M. H. Choi, S. H. Han, D. J. Choo, J. Jang, S. K. Kwon.** *Org. Electron.* 2008, Vol. 9, pp. 721-726.
99. **J. A. Lim, J-H. Kim, L. Qiu, W. H. Lee, H. S. Lee, D. Kwak, K. Cho.** *Adv. Funct. Mater.* 2010, Vol. 20, pp. 3292-3297.
100. **S. K. Park, T. N. Jackson, J. E. Anthony, D. A. Mourey.** High mobility solution processed 6,13-bis(triisopropyl-silylethynyl) pentacene organic thin film transistors. *Appl. Phys. Lett.* 2007, Vol. 91, p. 063514.
101. **M. W. Lee, G. S. Ryu, Y. U. Lee, C. Pearson, M. C. Petty, C. K. Song.** Control of droplet morphology for inkjet-printed TIPS-pentacene transistors. *Microelectronic Engineering.* 2012, Vol. 95, pp. 1–4.
102. **O. Ostroverkhova, S. Shcherbyna, D. G. Cooke, R. F. Egerton, F. A. Hegmann, R. R. Tykwinski, S. R. Parkin, J. E. Anthony.** Optical and transient photoconductive properties of Pentacene and functionalized Pentacene thin films: Dependence on film morphology. *J. Appl. Phys.* 2005, Vol. 98, p. 033701.
103. **C. W. Sele, B. K. C. Kjellander, B. Niesen, M. J. Thornton, J. Bas P. H. van der Putten, K. Myny,H. J. Wondergem, A. Moser, R. Resel, A. J. J. M. van Breemen, N. van Aerle, P. Heremans, J., E. Anthony, G. H. Gelinck.** Controlled Deposition of Highly Ordered Soluble Acene Thin Films: Effect of Morphology and Crystal Orientation on Transistor Performance. *Adv. Mater.* 2009, Vol. 21, pp. 4926-4931.
104. **N. Kaihovirta, T. Makela, X. He, C.-J. Wikman, C.-E. Wilen, R. Osterbacka.** Printed all-polymer electrochemical transistors on patterned ion conducting membranes. *Org. Electron.* 2010, Vol. 11, pp. 1207–1211.
105. **Richard Mannerbro, Martin Ranlof, Nathaniel Robinson, Robert Forchheimer.** Inkjet printed electrochemical organic electronics. *Synth. Met.* 2008, Vol. 158, pp. 556–560.
106. **L. Basiricò, P. Cosseddu, A. Scidà, B. Fraboni, G.G. Malliaras, A. Bonfiglio.** Electrical characteristics of ink-jet printed, all-polymer electrochemical transistors. *Organic Electronics.* 2012, Vol. 13, pp. 244–248.
107. **A. Mantovani Nardes, M. Kemerink, R.A.J. Janssen, J.A.M. Bastiaansen,N.N.M. Kiggen, B.M.W. Langeveld, A.J.J.M. Van Bremen, M.M. de Kok.** Microscopic understanding of the anisotropic conductivity of PEDOT:PSS thin films. *Adv. Mater.* 2007, Vol. 19, pp. 1196–1200.

108. **J. Ouyang, Q. Xu, C. Chu, Y. Yang, G. Li, J. Shinar.** On the mechanism of conductivity enhancement in PEDOT:PSS films through solvent treatment. *Polymer.* 2004, Vol. 45, pp. 8443–8450.
109. **D.A. Bernards, G. Malliaras.** Steady-state and transient behavior of organic electrochemical transistors. *Adv. Funct. Mater.* 2007, Vol. 17, pp. 3538–3544.
110. **G. Tarabella, C. Santato, S.Y. Yang, S. Iannotta, G.G. Malliaras, F.Cicoira.** Effect of the gate electrode on the response of organic electrochemical transistors. *Appl. Phys. Lett.* 2010, Vol. 97, pp. 123304–123307.
111. **T. A. Skotheim, R. L. Elsembaumer, and J. R. Reynolds (eds.).** *Handbook of Conducting Polymers.* New York : Marcel Dekker, 1998.
112. **Weiss, P. M. Borsenberger and D. S.** *Organic Photoreceptors for Imaging Systems.* New York : Marcel Dekker, 1993.
113. **G. Horowitz, D. Fichou, X. Z. Peng, Z. Xu, and F. Garnier.** *Solid State Commun.* 1989, Vol. 72.
114. **H. Koezuka, A. Tsumara, and T. Ando,.** *Synth. Met.* 1987, Vol. 18.
115. **J. H. Burroughes, C. A. Jones, and R. H. Friend.** *Nature.* 1988, Vol. 355.
116. **J. H. Burroughes, D. D. C. Bradley, A. R. Brown, R. N. Marks, K. Mackay, R. H. Friend, P. L.** *Nature.* 1990, Vol. 347.
117. **Tang, C. W.** *Appl. Phys. Lett.* 1986, Vol. 48.
118. **VanSlyke, C. W. Tang and S. A.** *Appl. Phys. Lett.* 1987, Vol. 51.
119. **L. Sebastian, G. Weiser, H. Bässler.** Charge transfer transitions in solid tetracene and pentacene studied by electroabsorption. 1981, Vol. 61, pp. 125-135.
120. **Y.Q. Wang, L. Bridwell, R. Giedd.** Modification of Polymers by Ion Implantation. *ACS Book Publisher.* s.l. : R. Arshady, 1997, pp. 371–404.
121. **Kleiman, J.** Surface modification technologies for durable space polymers. *MRS Bull.* 2010, Vol. 35, p. 55.
122. **J-F. Chang, J. Clark, N. Zhao, H. Sirringhaus, D. W. Breiby, J.W. Andreasen, M. M. Nielsen,M. Giles, M. Heeney, I. McCulloch.** *Phys. Rev. B.* 2006, Vol. 74, p. 115318.

List of publications related to the Thesis

- "Spectroscopic investigation of the semiconductor molecular packing in fully operational organic thin-film transistors"
  B. Fraboni, A. Scidà, A. Cavallini, P. Cosseddu, A. Bonfiglio, S. Milita, M. Nastasi
  Applied Physics Letters, **96** (2010) 163302

- "Spectroscopic analyses of molecular packing in pentacene thin films"
  A. Scidà
  Nuovo Cimento C, **34** (2011) 103

- "Electrical characteristics of ink-jet printed, all-polymer electrochemical transistors"
  L. Basiricò, P. Cosseddu, A. Scidà, B. Fraboni, G.G. Malliaras, A. Bonfiglio
  Organic Electronics, **13** (2012) 244-248

- "Photocurrent spectroscopy of ion-implanted organic thin film transistors"
  B. Fraboni, A. Scidà, A. Cavallini, S. Milita, P. Cosseddu, A. Bonfiglio, Y. Wang, M. Nastasi
  Synthetic Metals, **161**, (2012) 2585– 2588

- "Enhancement of conductivity due to ion implantation on Pentacene Organic Thin Film Transistors"
  B. Fraboni, A. Scidà, A. Cavallini, S. Milita, P. Cosseddu, A. Bonfiglio, Y. Wang, M. Nastasi
  Submitted

- "Investigation on inkjet printing conditions of TIPS-pentacene as active layer for organic thin film transistors"
  L. Basiricò, P. Cosseddu, B. Fraboni, A. Scidà, S. Milita, A. Bonfiglio
  Submitted

Acknowledgements

I'd like to thank my supervisor Prof. Beatrice Fraboni for the fundamental contribution in this research and for her support and understanding all these years.

Still concerning the Department of Physics and Astronomy of Bologna, I would like to thank also Prof. Anna Cavallini, Dr. Daniela Cavalcoli and Mr. Antonio Castaldini for the assistance during my research work.

From the University of Cagliari I would like to thank Prof. Annalisa Bonfiglio, Dr. Piero Cosseddu, Dr. Laura Basiricò and Dr. Silvia Milita (CNR of Bologna) for the substantial collaboration (preparation of the samples, electrical characterization and XRD analyses) and for the valuable discussions.

A particular thanks also to our collaborators, Prof. Michael Nastasi and Prof. Yongqiang Wang of the Los Alamos National Research Laboratory, for their essential work: ion implantation of the samples, SRIM simulations, XPS, FTIR, ERD and Nanoindentation measurements.

Finally, a special thanks to my colleagues: Lucia, Andrea, Albert, Saurabh, Alberto, Stefania and Martina for their sustain, scientific and not, all these three years.